Numerical simulation of compressible viscoelastic flows.

Keshtiban, Ibrahim Jalili

Numerical Simulation of Compressible Viscoelastic Flows

by

IBRAHIM JALILI KESHTIBAN

B.Sc., M.Sc.

THESIS SUBMITTED TO THE UNIVERSITY OF WALES
IN CANDIDATURE FOR THE DEGREE OF
PHILOSOPHIAE DOCTOR
INSTITUTE OF NON-NEWTONIAN FLUID MECHANICS

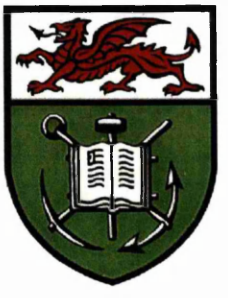

DEPARTMENT OF COMPUTER SCIENCE

UNIVERSITY OF WALES SWANSEA

NOVEMBER 2004

DEDICATION

To my motherland, Azerbaijan,

To my sister, Leyla,
To my grandparents,
To my mother, Tuti, and my father, Aziz
To my brother and his family,

and

To all of my friends

I dedicate this work.

Declaration

I declare that this work has not already been accepted in substance for any degree, and is not being concurrently submitted in candidature for any degree

(Candidate)

Statement 1

This thesis is the result of my own investigations, except where otherwise stated. Other sources are acknowledged by footnotes giving explicit references. A bibliography is appended.

(Candidate)

Statement 2

I hereby give consent for my thesis, if accepted, to be available for photocopying and for inter-library loan, and for the title and summary to be made available to outside organisations.

(Candidate)

.....28/02/05.....

Date

Acknowledgements

I wish to express my sincere appreciation to my supervisor Prof. M. F. Webster whose encouragement, guidance and suggestions helped me during the course of this research.

I acknowledge assistance and contribution of Dr. F. Belblidia whose continuous consultation has already proved most helpful.

My special thanks go to Dr. D. Ding who helped me in the first year of my PhD. programme.

I would like to give my gratitude to my former supervisor Dr. M.N. Famili who for the first time opened the door for me to study complex fluid flows. Also, thanks goes to Dr. Towfiqi and his family who supported me thoroughly during my course study.

Also, I strongly wish to thank Dr. M.T. Manzari, who was the encouragement and cause for my educational career in UK.

The author wishes to acknowledge helpful discussion and valuable hints provided by Dr. M. Aboubacar, Dr. H. Matallah, Dr. H. R. Tamddon-Jahromi, Dr. M.S. Chandio, Dr. K. S. Sujata and Dr. D. Harlan.

Finally, special thanks go to Mr. J. Banaai , Dr. F. Nasiri, Dr. B. Tayfeh-Rezaie and Mr. J. Harvey, my close friends.

Abstract

This thesis is concerned with the numerical simulation of both compressible and incompressible viscoelastic/viscous flows. This is a pioneering study in computations of compressible viscoelastic flows. The study retains novelty in analysing the impact of compressibility within the performance properties of numerical methods (stability, accuracy, convergence and consistency), along with flow characteristics such as vortex activities and stress boundary layers. The developed algorithm leads to classification of a unified scheme for both compressible and incompressible viscoelastic flows.

In this work, we first present a brief introduction to flow at low Mach numbers, followed by rheological constitutive equation and equations of state for dense materials. Subsequently, we provide the background theory over several difficult issues encountered by compressible schemes, at low Mach numbers (singular limit of compressible flows). This would include key modifications employed to rectify density-based schemes and extending pressure-based incompressible algorithms for dealing with compressible flows.

To accommodate weakly-compressible viscoelastic/viscous flows at low Mach numbers, a high-order time-marching pressure-correction algorithm has been adopted, in semi-implicit form. For discretisation of velocity and pressure equations, over the fractional stages of this pressure correction scheme, a Galerkin finite element was employed. To accommodate stress equations (considered here in Oldroyd-B form) two spatial discretisation alternatives are adopted. This encompasses a mixed finite element formulation in SUPG form, with a quadratic stress and velocity interpolations. The second scheme involves a sub-cell finite volume implementation, a hybrid *fe/fv* scheme for the full system. For both scheme variants, enhanced velocity gradients are acquired, via a recovery technique.

Two discrete representations are proposed to interpolate density: a piecewise-constant form with gradient recovery and a linear interpolation form, akin to that on pressure. Validation on a number of classical benchmark problems bears out the high quality of performance of both compressible flow implementations, at low to vanishing Mach

number. Neither linear, nor constant density interpolation schemes degrade the second-order accuracy of the original incompressible fractional-staged pressure-correction scheme. The piecewise-constant interpolation scheme, efficient in implementation, is advocated as a viable method of choice, with its advantages of order retention.

In the viscous context, we conduct several tests on cavity and contraction flows (both Cartesian and cylindrical coordinates) for both compressible and incompressible flow settings. To validate results of our original incompressible scheme, for the cavity test problem, we compare and contrast predicted velocity fields with those in the literature. For this test problem, the effect of singularity in boundary conditions is investigated on spatial accuracy for both incompressible and compressible flows with the two density interpolations. On contraction flows, consistency is confirmed according to the two different forms of density interpolation. Capability of the scheme in dealing with very low Mach number flows is demonstrated, via adjusting Tait parameters. The scheme responses well as Mach number approaches zero (incompressible limit), and there is no obvious minimum threshold on Mach number for this scheme. We have conducted several tests, under the compressible settings on the effect of system eigenvalues on convergence patterns.

In the viscoelastic context with the mixed finite element method, the scheme is applied to contraction flows for Oldroyd-B model fluids. Stability and performance characteristic of the new algorithm implementation are highlighted. Solutions are provided for a range of compressible settings approaching incompressible limit at vanishing Mach number. The stabilisation effect of time-step scaling is also addressed.

Similar studies are conducted for the alternative spatial approximation, with the hybrid *fe/fv* schemes, where we present stress approximations over sub-cell finite volume implementation. Critical attainable Weissenberg numbers are addressed, with both stress discretisation alternatives for compressible and incompressible flows. In addition, close examination is conducted on flow patterns, particularly around the contraction point and in vortex activity.

Finally, we present stabilised solutions in the settings discussed above. This is conducted through extensive studies upon the hybrid *fe/fv* scheme variant. The key issues involved deal with: *i*) minimising splitting-errors in the application of fractional-staged pressure-correction schemes for the couple system of pressure-velocity-stress, *ii*) improving satisfaction of the inf-sup conditions through enhancing spatial representations of velocity gradients, *iii*) incorporating ellipticity into the equation system, appending elliptic dissipation into the momentum equation, *iv*) some miscellaneous considerations relating the treatment of capturing discontinuities and steep stress gradients. We conduct several tests to embark on various aspects of stabilisation within the flow field and upon vortex activity. Employing stabilised schemes enables us to achieve solutions at higher Weissenberg numbers and consequently presenting vortex activity on highly elastic flows, illuminating the significant influence that stabilisation has on this context.

Glossary of terms

CBS	Characteristic Based Splitting
CFl	Courant Friedrichs Lewy
CT0	See page 155
CT2	See page155
CT3	See page 155
De	Deborah number
DG	Discrete Galerkin
EVSS	Elastic Viscous Splitting Stress
FD	Fluctuation Distribution
fe	Finite Element
fe/fv	Finite Element/Finite Volume
fv	Finite Volume
GFEM	Galerkin Finite Element Method
GLS	Galerkin Least Square
HWNP	High Weissenberg Number Problem
LBB	Ladisenskaïa-Babuska-Brezzi
LCM	Lower Convected Model
LDA	Lower Diffusion A
LDB	Lower Diffusion B
Ma	Mach number
MDC	Median Dual Cell
PC	Pressure-Correction
RCI	Reduced Corner Integration
Re	Reynolds
SBL	Stress Boundary Layer
SIMPLE	Semi Implicit Pressure Linked Equations
SRS	Strain Rate Stabilisation
SU	Streamline Upwinding
SUPG	Streamline Upwinding Petrov Galerkin
TGPC	Taylor Galerkin Pressure Correction
TSS	Time Step Scaling
TVD	Total Variation Diminishing
UCM	Upper Convected Maxwell
We	Weissenberg number
We_{crit}	*We* critical

Contents

CHAPTER 1

Introduction

In this thesis, one is concerned with the compressible flow of highly viscous/viscoelastic materials. This type of flow generally arises in low Reynolds number (*Re*) situations corresponding to high pressure-drops. The question immediately arises as to where and when compressibility in such flow has significance. The circumstances under which this is the case are discussed below.

1.1 Molecular theory of compressibility

Consider a system of a cylinder and a piston as shown in Figure 1.1. The confined volume is filled with fluid, either a gas or liquid. To elucidate the mechanisms of compressibility, first, we introduce some concepts within kinetic theory. The fluid is considered to be a composition of self-similar rigid molecules held within a state of continuous random motion. Usually there are significant distances between the rigid molecules, so that molecules travel in straight lines between abrupt collisions at the walls and between each other. These collisions randomise the motion. The mean-free-path is defined as the average distance travelled by a molecule between successive collisions. The mean free-path is assumed to be far larger than the diameter of the molecules. Density for a heterogeneous system is directly proportional to the number of molecules in a particular volume. Accordingly, the pressure exerted by a fluid on the wall is attributed to the impact of the fluid molecules upon it. Therefore, pressure is not only a function of impact frequency (density), but also of the energy within such impacts (described through temperature change). It must be noted that, temperature is a macroscopic thermodynamic property defined upon the "zeroth-law" of

thermodynamics [7]. The microscopic representation of temperature may be attributed to the kinetic energy of molecules.

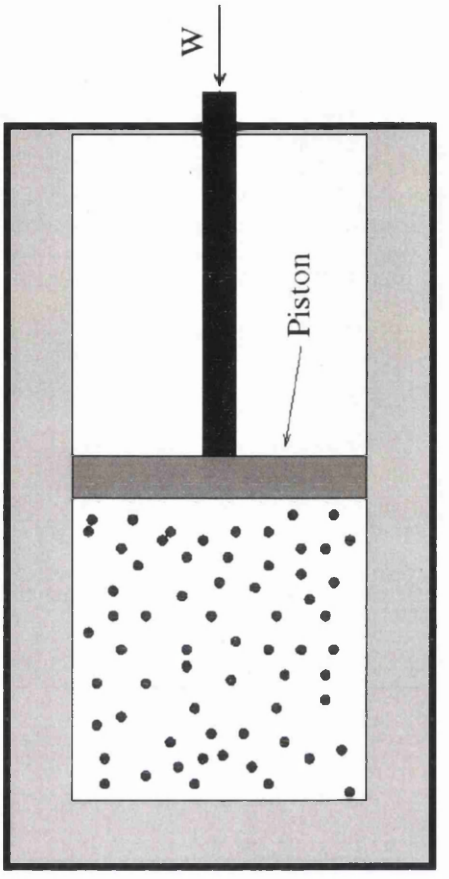

Figure 1.1: System of cylinder and piston

The cylinder-piston system is initially taken into consideration in the thermodynamic equilibrium state. There is a balance between the weight of the piston and the force exerted by the pressure inside the cylinder. If this system deviates from the initial state, by loading an extremely small weight upon the piston, the system will undergo a transition to eventually reach an equilibrium state. During this process, the piston will start to descend, which will reduce the average distance between the molecules (density increases). Hence, intermolecular forces will rise (causing pressure increase). The pressure rise will continue until an equilibrium state is reached. This process can be analysed from both a thermodynamic (steady-state) and a fluid mechanical (time-dependent) viewpoint. In a thermodynamic sense, both the density and temperature are subject to increase. From a fluid mechanical point of view, the thermodynamic description gives way to a local and time-dependent alternative. This is an essential

basis upon which to describe phenomena in fluid mechanics. In addition, molecular kinetic theory[†] provides facilities to analyse this process throughout time, appealing to simple physical laws. When the piston starts to move, the mean distance among the molecules adjacent to the piston decreases, and hence, local pressure will rise. Since any external force is finite and molecules have some mass, it will take a specific period of time for molecules to move and interact. The macroscopic representation of the propagation of pressure waves is termed the speed of sound (c). As such, any effect of pressure change will be transmitted at the speed of sound. In liquids, the mean distance between molecules is miniscule. Therefore, any change in pressure can be transmitted through much smaller movements, and hence, at a speed much faster than that experienced within gases. The propagation speeds of travelling waves are characteristic of the media in which they travel, and in general are not dependent upon other wave characteristics, such as frequency, period, and amplitude. The speed of sound in air and other gases, liquids, and solids may be estimated from the density and elastic properties of the media (bulk modulus). In a volume medium, the wave speed takes the general form:

$$c = \sqrt{\frac{elastic\ property}{inertial\ property}} = \sqrt{\frac{B}{\rho}} \tag{1.1}$$

where, B represents the bulk modulus and ρ the density of the material occupying the volume. This relationship predicts the speed of sound for air as 334 m/s (at 25 °C), for water as 1483 m/s (at 20 °C) and for structural steel as 4512 m/s (at 20 °C). The bulk elastic properties of a material determine how much that material will compress under a given amount of external pressure. The ratio of change in pressure to the fractional volume compression is termed the bulk modulus of the material, where

$$B = \frac{\Delta p}{\Delta V/V}. \tag{1.2}$$

[†] Molecular kinetic theory is an important tool for interpreting physical and chemical phenomena. The aim of molecular kinetic theory is to account for the thermodynamic and kinetic behaviour of matter. That is in terms of the concept of the chemical composition of matter in consisting of molecules and atoms, using mechanical laws derived from a study of the equilibrium and motion of large bodies. Nevertheless, the scope of molecular kinetic theory is broader than that of thermodynamics, as kinetic theory may extend to interpret phenomena involving time, such as diffusion, the rate of chemical reaction, and the dynamics of fluid flow. Although density is a macroscopic property of a thermodynamic system, to analyse the effects of compressibility, it is essential to adopt a molecular viewpoint.

In the above expression, p and V equate to the pressure and fluid volume, respectively. The reciprocal of the bulk modulus is termed the compressibility of the substance. The amount of compression supported by solids and liquids is normally observed to be miniscule.

In analysing a particular physical phenomenon, if the time-scale of that process is sufficiently large compared to the time-scale of propagation of pressure-waves ($1/c$), one may neglect the effect of pressure waves in the transient analysis. The time-scale for flow of a fluid is proportional to $1/u$, where u is the fluid particle velocity. The Mach number ($Ma = \frac{u}{c}$) is employed to characterise compressibility effects within a flow. When the Mach number is low, the effects of compressibility will be minimal. When the time-scale of a phenomenon is comparable to the time-scale of pressure-wave propagation, compressibility should be taken into account. For example, consider fuel ignition within an enclosed cylinder, the time-scale of reaction is miniscule, and therefore, compressibility is an important factor. Note, the rate of reaction, especially in a gaseous phase, is a function of density (concentration). Then, if the time-scale is sufficiently small, propagation of pressure-waves will play a more significant role. This is the case for combustion processes, for example, where density fluctuations arise due to thermal gas expansion upon the conversion of chemical energy. In the presence of flame fronts, that are thin in comparison with a characteristic length of the flow, density fluctuations may reflect steep gradients [129]. With respect to bubble dynamics and cavitation, an important aspect relevant in many industrial applications, we quote from the study of Brujan [21]:

> "...the assumption of liquid incompressibility has been made based on the idea that only a small fraction of the energy of the bubble motion is radiated away as sound. However, for conditions similar to cavitation, the later stages of bubble collapse proceeded so quickly that the velocity of the bubble interface can be compared to the speed of sound in the liquid and the compressibility of the liquid can no longer be ignored."

In essence, compressibility should be considered based upon the conditions a system is exposed to (fluid mechanical viewpoint), rather than simply its physical properties alone (a thermodynamic stance).

1.2 Low Mach limit

Numerical computation of compressible flows in low Mach number situations (say Ma <0.3), is a difficult setting to resolve. This is a singular limit for compressible flow, at which compressible flow solvers begin to lose their efficiency and accuracy. In low Mach number (LMN) regimes, compressible fluids reflect similar patterns of response as those under incompressible flow. Panton [110] quoted:

> "The layman is usually surprised to learn that the pattern of the flow of air can be similar to that of water. From a thermodynamic standpoint, gases and liquids have quite different characteristics. As we know, liquids are often modelled as incompressible fluids. However, 'incompressible fluid' is a thermodynamic term whereas 'incompressible flow' is a fluid-mechanical term. We can have incompressible flow of a compressible fluid."

One may regard flow at LMN as being at the centre of fluid dynamics, by virtue of its fundamental nature and its vast practical importance. In quantitative terms for LMN flows, the speed of sound for air at 25°C and sea level is about 334 m/s. Therefore, the speed of a fluid particle at Ma=0.3 will be around 100 m/s (360 km/h). Thus, from general observation, one notes that the majority of fluid phenomena arising within nature occur at low Mach numbers. The speed of tornadoes rarely reaches this level. Likewise, everyday phenomena, such as talking, breathing and flow of air around vehicles, may be considered as examples of LMN regimes.

Even the fluids we classify as incompressible may in fact display some compressible response. The density of liquids is a weak function of pressure, temperature and concentration. The incompressible assumption taken for a liquid is valid within a specific range of these variables. Free convection takes place as a result of variation of density due to temperature gradients, and general circulation within the oceans is mainly driven by salinity and temperature gradients. In many industrial processes, flow may encounter regions of high pressure-difference. This is the case for most flows in polymer processing. In such scenarios, density discrepancies arise due to large pressure-differences and variations in temperature. In some special types of flow, such as jet-cutting, the speed of fluid particles (say 400 m/s) is comparable to the speed of sound (for water, 1423 m/s). Compressibility should be taken into account when the Mach number for this process is around 0.3. This is an interesting example for a

material such as water, commonly considered as incompressible, which indicates some compressible and elastic effects within the jet-cutting process.

Injection moulding involves two distinct phases. The first involves melt generation, mixing, and pressurisation, conducted within the injection unit of the moulding machine. The second phase is that of product shaping, which takes place within the mould cavity. In the second filling stage, the polymer melt is injected into the cavity through the sprue, runner and gate. In the packing stage, additional polymer melt must be pushed into the cavity, in order to compensate for shrinkage caused by material cooling. During these phases, residual stress is produced due to the high pressures generated, temperature changes, and there is relaxation of the polymer chains. This results in shrinkage and warpage of the moulded part. In the filling stage, molten polymers of high viscosity are pressed through narrow channels in very short times. Consequently, pressures increase dramatically which affect density changes. Therefore, the Mach number for flow in this stage may reach a level at which compressibility becomes significant. Density adjusts within the packing and cooling stages due to the large variations in temperature and pressure. This has a crucial influence upon the quality and mechanical properties of the moulded parts, especially where optical properties are important. If the density is sensitive to the variation in pressure, then, the amount of melt injected should be increased within the filling stage. This will compensate to some degree for shrinkage, due to variations in density caused through that in temperature. Accordingly for realism, simulations for injection moulding should take compressibility into account.

In this thesis, one is concerned particularly with the development of algorithms for the computation of compressible viscoelastic flows under LMN regimes. As such, discussion is presented for the numerical difficulties that are introduced.

CHAPTER 2

Rheology and basic equations

2.1 Overview

Rheology is a fundamental interdisciplinary science, concerned with the study of the internal response of physical materials to stress. A definition of rheology is provided by Professor Bingham (Lafayette college, Indiana) as *"The study of the deformation and flow of matter"*, who inaugurated its name in 1929, when the American Society of Rheology was founded. In literal terms, rheology means the study of flow (from the Greek words $\rho\varepsilon'\tilde{\omega}$ - to flow, and $\lambda o'\gamma o\zeta$, science). The scope of modern rheology, however, is much broader than it would appear from its name. It is concerned with almost all aspects of deformation of physical bodies under the influence of external stress.

In view of the definition of rheology, the question arises as to what is the relationship between rheology and the traditional branches of mechanics, such as the theory of elasticity or flow of ideal viscous fluids. In fact, rheology is concerned with the description of the flow behaviour of all types of matter. Nonetheless, these disciplines (ideal elastic and viscous) are concerned with idealised bodies, which obey particular physical laws exactly. From a practical point of view, these two approaches would appear to be fully justified. Often, for a given class of materials and a considered range of variables, some flow/material properties are dominant and can be approximated by one of these classical extremes. However, every real material, whose properties may be approximated under specific conditions by one of the classical models, may exhibit alternative behaviour under other conditions. In addition, there are many materials

which cannot adequately be described by any of classical models, even under normal conditions. Rheology is especially concerned with these materials and by convention, the primary interest of rheologists is restricted to phenomena where materials exhibit intermediate properties, lying between those of ideal solids and liquids. Therefore, the word "rheology" normally refers to the flow and deformation of "non-classical" materials such as rubber, molten plastics, polymer solutions, slurries and pastes, electrorheological fluids, blood, muscle, composites, soils and paints. These materials can exhibit varied and distinct rheological properties that classical fluid mechanics and elasticity fail to describe.

The most spectacular examples of rheological complex materials occur in the case of solutions and melts of macromolecules, that is, polymeric materials and biological systems. These complex materials play an important role in nature and modern life. Production of rheologically complex materials reaches many millions of tones per year. A thriving trade is involved in the production and processing of such materials. The need for rheological research is evident from the modernisation of technological processes and the improvement of product standards.

2.2 Elastic, viscous and viscoelastic responses

In solid materials, the intermolecular bond forces are strong enough to hold molecules in their lattice state positions. The response of such a structure to a (small) external stress is deformation, and returning to into the original state upon removal of the stress. In solid materials, under the influence of deformation resulting from external forces, the stretching of intermolecular bonds occurs and the resulting internal stress balances that imposed externally. Because the deformation is extremely fast and the bonds can be stretched rapidly by an imposed stress, hence, little motion from lattice points is involved. Consequently, equilibrium deformation is established in an infinitely short time. This response of solids is termed "Elasticity".

In contrast, molecules of fluids in an ideal state move in a random motion with high mobility. When external (anisotropic) stress is imposed, a fluid will deform and continues to do so as long as the stress is applied. In addition, removal of the stress will not result in a return of the fluid to into the original undeformed state. The Brownian motion of fluid molecules is rapid and the internal frictional forces retard the rate-of-

deformation. This leads to an equilibrium state. Consequently, the work done during deformation will be dissipated. The ideal viscous limit for liquids is reached when all of the work has been dissipated.

Rheological behaviour may be characterised by a dimensionless number, named the 'Deborah number', introduced by Professor Reiner to measure the elasticity of materials. The Deborah number *De* represents a ratio of a characteristic time of the material, t, to a characteristic time of the deformation, T. The natural time of materials varies throughout a broad range (say, from $10^{-13}s$ to $10^{13}s$) [44]. For a Newtonian fluid, time t vanishes, whilst it tends to infinity for an ideal elastic solid. Typically, $t=10^{-12}s$ for water, $10^{-5}s$ for lubricating oils; it can be of the order of a few seconds for polymer melts, and for glass is 10^{5}s [137]. Consequently, a purely viscous fluid expressing a phenomenon with a small characteristic time, for example skimming, will display the response of a solid. In contrast, a material such as glass in a long time can demonstrate flowing effects.

These elastic and viscous responses to the external stress represent two extremes. In between, there can be an infinite number of intermediate responses. Rheology is especially concerned with more complex materials, which exhibit some elastic and some viscous effects simultaneously. These are termed viscoelastic substances.

It is important to express a terminology for the definition of the above responses. In principle, when external forces perform a certain amount of work (W), some part of the work can be stored as elastic energy (E), whilst the remainder can be dissipated irreversibly (D). Introduction of the quantities E and D allows one to classify the various materials as follow; if on deformation, $E \neq 0$ and $D=0$, the response is ideally elastic. If $E=0$ and $D \neq 0$, the response is ideally viscous. Finally, if $E \neq 0$ and $D \neq 0$, the response is viscoelastic.

From a historical perspective, the first quantitative explanation for rheological phenomena emerged through the introduction of elasticity theory, which essentially states: "if you double the tension, you double the extension" [66]. Nine years after the publication of Hooke's paper, Issac Newton addressed the problem of steady shear flow in a fluid and "The Principia" contains the famous hypothesis: "the resistance which arises from the lack of slipperiness of the parts of the liquid, other things being equal, is

proportional to the velocity with which the parts of the liquid are separated from one another". This 'lack of slipperiness' is what we now term viscosity.

These two relationships formed the basis of the development and foundation of mechanics. In time, rheologists encountered many phenomena which could not be described through the above relationships. Weber (1835) noticed that the elasticity of silk fibres in tension was not perfect. The materials displayed some viscous and some elastic effects, simultaneously. Initial study into viscoelasticity was primarily targeted towards creep and relaxation response of metals, prior to the explosive growth of the polymer industry and the application of macromolecules.

Table 2.1. Significant rheological works prior to formal inception of rheology in 1929

LUIDS/MODELS CLASS		KEY TIME	REPRESENTATIVE WORKS
Ideal materials	a) Perfect, rigid bodies	Antiquity	Archimedes (~250 BCE), Newton (1687)
	b) Ideal elastic solids	1600's	Boyle (1660), Hooke (1678), Young (1807), Cauchy (1827)
	c) Inviscid fluids	1700's	Pascal (1663), Bernoulli (1738), Euler (1755)
	d) Newtonian Liquids	Early 1800's	Newton (1678), Navier (1823), Stokes (1845), Hagen (1839), Poiseuille (1841), Weidemann (1856)
Linear Visvoelasticity		Mid 1800s	Weber (1835), Kohlrausch (1863), Wiechert (1893), Maxwell (1867), Boltzmann (1878), Poynting & Thomson (1902)
Generalised Newtonian (viscous) liquids		Late 1800s Early 1900s	Schwedoff (1890), Trouton & Andrews (1904), Hatchek (1867), Bingham (1922), Ostwald (1925), de Waele (1923), Herschel & Bulkley (1926)
Non-linear viscoelasticity		Early 1900s	Poynting (1913), Zaremba (1903), Jaumann (1905), Hencky (1992)
Key material descriptions	a) Suspensions	Early 1900s	Einstein (1906), Jeffrey (1992)
	b) Polymers		Schonbein (1847), Baekeland (1909), Staudinger (1920), Carothers (1929)
	c) Extensional viscosity		Banus (1893), Trouton (1906), Fano (1908), Tamman & Jenckel (1930)
The genesis of Rheology		1929	Bingham, Reiner and others

Rheology is a multidisciplinary science. From the chemical or mechanical engineering point of view, one may split it into three main research areas: theory, experiment and simulation. Theoretical aspects involve the study of the physics governing fluid behaviour and constitutive equations. Experimentation may be categorised under viscometry (measurement of viscosity) and rheometry (measurement of other rheological properties). Computer simulation is concerned with computation through mathematical modelling and visualisation. The lists in Tables 2.1 and 2.2 (taken

from [39]), represent the catalogue of such work from the earliest times to the present day.

Table 2.2. Rheology since its inception in 1929

#	AREA OF ACTIVITY		REPRESENTATIVE WORKS
1	Constitutive equations	a) Differential models	Oldroyd (1950), Truesdell (1952), Rivlin and Ericksen (1955), Giesekus (1962), White-Metzner (1961)
		b)Integral models	Green & Rivlin (1957), Coleman and Noll (1961)
		c)Network models	Green and Tobolsky (1946), Lodge (1956), Yamamoto (1956), Kaye (1962), Bernstein et al. (1963)
		d) Reptation models	Edwards (1967), De Gemmes (1971), Doi & Edwards (1978, 1986)
		e) Molecular models	Kuhn (1934), Rouse (1953), Zimm (1956), Kirkwood (1967), Bird et al. (1987)
2	Experimental advances and rheological descriptions	a) Shear flows and the no-slip boundary condition	Eisenschitz et al. (1929), Mooney (1931, 1936), Schofield & Blair (1930), Pearson & Petrie (1968), Grassley (1977), Ramamurthy (1986).
		b) Normal stresses and rod-climbing effects	Lander (1945), Weissenberg (1947), Markowitz (1957), Philippoff (1957), Ginn & Metzner (1969), Binnington & Boger (1985)
		c) Dynamic studies	Eisenschitz & Philippoff (1933), Schofield & Scott Blair (1932), Leaderman (1943), Cox-Merz (1958), Doraiswamy et al. (1991)
		d) Thixotropy	Freudrich & Bircumshaw (1926), Cheng & Evens (1965), Mewis (1979), Barnes (1997)
		e) Flow instabilities	Nason (1945), Tordella (1958), Petrie & Denn (1976), Bousfield et al. (1986)
		f) Turbulent drag reduction	Toms (1949), Agoston et al. (1954), Herahey & Zakin (1967), Seyer & Metzner (1967)
		g) Optical studies/ birefringence	Adams et al. (1965), Carothers & Hill (1932), Hermans & Platzek (1939), Janeschitz-Kriegl (1983), Fuller (1985)
		h)Time-temp. superposition	Williams et al. (1955), Ferry (1970)
		i) Extensional behaviour	Merrington (1943), Treolar (1944), Ballman (1965), Cogswell (1969), Metzner (1968), Meissner (1969), Dealy et al. (1976), Spearot & Metzner (1972), Laun & Mundstedt (1978), Sridar & Gupta (1985)
3	Advanced materials	a) LCPs	Leslie (1968)-Ericksen (1961), Doi (1981), Wissbun (1985), Doraiswamy & Metzner (1986), Marucci & Greco (1992)
		b) Composites and two-phase systems	Taylor (1934), Krieger-Dougherty (1959), Rumscheidt & Mason (1961), Leal (1975), Batchelor (1977), Folgar & Tucker (1984), Heller & Kuntamukkula (1987), Khan & Armstrong (1986), Acrivos & Shaqfeh (1988), Mewis et al. (1989), Dennis et al. (2001)
		c) ER/MR fluids	Winslow (1949), Parthasarthy & Klingenberg (1996)
4	Computational Rheology	a) Continuum simulations	Turner et al. (1956), Gottlieb & Orzag (1977), Cruise & Risso (1968), Yoo & Joseph (1985), Beris et al. (1987), Walters & Tanner (1992), Crochet & Walters (1993)
		b) Molecular dynamic simulations	Adler & Wainright (1957), Ashrust & Hoover (1975), Evans & Morriss (1988), Davis & Todd (1998)

2.3 Basic equations

Rheology is concerned with the study of the deformation and flow of matter. The principal theoretical concepts are kinematics, dealing with geometrical aspects of deformation and flow; conservation laws, dealing with force, stress, and energy interchange, and constitutive relations. The constitutive relations serve to link motion and force to complete the description of the flow process.

All real materials possess a microstructure at the molecular, crystal or higher level. In mechanics, one is often not interested in specifying the material in such detail, as the large-scale phenomena of interest usually involve the amalgamated behaviour of a large number of units of the microstructure. Thus, it is convenient to work with an ideal continuum model for the material, whose microstructure is unspecified. This means that any small volume fluid element is always taken to be sufficiently large that it contains a huge number of molecules. Accordingly, when one speaks of the infinitely small, that implies miniscule when compared with the volume of the body under consideration, but large compared to the distance between molecules. The expressions fluid particle and fluid point are to be understood in a similar sense. The governing equations of fluid motion are expressed through the conservation of mass, transport of momentum (second law of Newton) and energy (first law of thermodynamics)[†]. These equations in differential form can be expressed as:

$$\frac{\partial \rho}{\partial t} + \nabla \cdot (\rho u) = 0, \tag{2.1}$$

$$\rho \frac{\partial u}{\partial t} + \rho u \cdot \nabla u = \nabla \cdot \pi + f, \tag{2.2}$$

where the notation ρ, u, π and f represent density, velocity, total stress and external body force, respectively. These quantities are, in general, functions of spatial coordinates (x, y, z), and time, t. $u(x,y,z,t)$ represents the velocity of the fluid at a given point, (x,y,z), in space, and at a given time, t. The total stress, π, is split into an isotropic pressure, p, and stress tensor, σ,

$$\pi = \sigma - pI, \qquad I \text{ is the unit tensor.} \tag{2.3}$$

[†] For the phenomena of interest here, the energy equation can be decoupled from mass and momentum balances and solved separately, without disturbing the generality of the algorithm. As such, in this study, the effect of temperature in neglected.

It is necessary to introduce equations to describe the link between pressure, stress, density and velocity. By convention the equations describing such a relationship for pressure and stress are termed the *constitutive equations* (section 2.5) and the *equation of state* (section 2.4), respectively.

2.4 Equation of state

The state of a sample of a homogeneous[‡] substance is defined by its physical properties, and two thermodynamic quantities. The state of a pure gas, for example, is specified by giving the values of its specific volume, V, pressure, p, and temperature, T. It has been established as an experimental fact that any substance is described by an *equation of state*, an equation that interrelates these three variables. Here, it is sufficient to specify only two such variables, as then, the third is fixed. For a prefect gas, the equation of state may be expressed as $pV = RT$, where R is a universal constant. Real gases display deviation from the prefect gas law due to inter-molecular interaction. Repulsion forces between molecules assist expansion and attraction forces assist compression. Repulsion forces are significant only when molecules are almost in contact: they are short-range interactions, even on a scale measured in molecular diameters. As these forces are short-range interactions, repulsion can be expected to be important when the molecules are sufficiently close together on average. This is the case for condensed matter (gases under high pressure and for liquids) when a large number of molecules occupy a small volume. On the other hand, attraction intermolecular forces have a relatively long range and are effective over several molecular diameters. Intermolecular forces are important when molecules are fairly close together but not necessary touching. Attraction forces are ineffective when the molecules are far apart. When the molecules are on average close together (liquids or gases at high pressure and/or low temperature) the repulsion forces dominate and the fluid can be expected to

[‡] A homogeneous system is one with uniform properties throughout in space; that is, a property such as density has the same value from one location to another, in a macroscopic sense. For a homogenous phase with fixed composition, the 'phase-rule' defines the number of degrees of freedom as two [116]. Therefore, to define the intensive-state of such a system, one must specify two additional thermodynamic quantities. These are commonly taken as temperature and pressure, whose control and measurement are simpler than is the case for other variables, such as entropy.

be less compressible. Then, the forces assist in driving the molecules apart. For more details see [116].

The pressure-volume-temperature (*pVT*) relationships for polymeric materials have been treated as a subject of some importance to polymer scientists and engineers, particularly from a process design standpoint. It has been necessary to establish an equation of state that adequately describe this behaviour over a wide range of temperature and pressure. The equation of state is important in rheology in linking density to the computed variables. In addition, this law is significant in fluid phase equilibria to predict the properties of blends and solutions. The equation of state for polymeric materials can be categorised as empirical and theoretically based. Numerous theoretical equations of state for polymeric liquids have been developed (see [122] and relevant references there). These fall into three main groups: a cubic equation of state (for example, Peng-Robinson) with an excess free energy-based mixing rule [109], hard sphere chain-based theories, and lattice fluid-based models [75]. It would appear that practically all equations of state for polymeric liquids provide a reasonably good fit to the *pVT* data, especially under low pressure conditions [122]. However, there is a major difference between the various equations in their abilities to fit *pVT* data over a wide range of pressure, and to predict thermodynamic properties of polymer blends and solutions, particularly concerning phase separation behaviour. The parameters of the equation of state are related to intermolecular forces. Describing these interactions for different molecules is essential to develop mixing rules for parameters and this is the main subject in the theoretical methods. In material processing, the study of phases is not the principal interest. As such, the well-known empirical Tait equation of state [136], has been employed widely in this area (see for example [40]). The Tait equation may be expressed in the following form [136]:

$$\frac{\tilde{p}+B}{\tilde{p}_0+B}=\left(\frac{\rho}{\rho_0}\right)^m, \text{ with the augmented pressure } \tilde{p}=-\frac{1}{3}trace(\pi), \tag{2.4}$$

where, m and B are parameters and $\tilde{p}_o$, ρ_o represent reference values for pressure and density, respectively. This empirical equation of state is suitable for dense materials, such as polymer melts and solutions, water and other liquids ([49,67] under linear approximation (m=1), see also,[120]). Generally, m and B are dependent on temperature and are independent of entropy [21]. Rodgers [122] catalogued the parameters for the

Tait equation of state as a function of temperature for more than fifty six polymers. Han and Im [60] did likewise for *PP* in for different arrangements of the Tait equation.

2.5 Constitutive equations

One of the main objectives of rheology is to establish the relationships between the state of stress, strain, and rate-of-strain ($f(\sigma,\gamma,\dot{\gamma})=0$) experienced by a body. Equations that give such relations are termed the rheological equations of state or constitutive laws. Rheological equations of state are a mathematical reflection, or mathematical model, of the actual properties of the material. For constitutive equations it is necessity to adhere to certain general axioms. In this section, the major requirements are outlined which are expected to be satisfied by these constitutive laws.

First, the function $f(\sigma,\gamma,\dot{\gamma})=0$ is taken to represent a physical law, and to reflect the properties of the material. These properties are independent of the manner in which the law is formally expressed. This gives rise to the first principle, the requirement of the invariance of the physical law with respect to change in coordinate system. Tensor component values may adjust with rotation of axes, yet this does not entail change in material properties, nor in the physical relations that reflect these properties. As such, the physical features of strain must be expressed through the invariants of the respective tensors, and these must be independent of choice of coordinate system. For this reason, the constitutive equation must accommodate invariance under coordinate transformation. The converse is also true: if the constitutive equation is expressed in an invariant form, then, this may be represented through the relationships between the components of the corresponding tensors. From this relationship, it follows that the scalar quantities that enter the constitutive equations cannot be arbitrary functions of the components of strain or stress (tensors). Instead, there must be dependence on the invariants of such tensors; otherwise the requirement of coordinate invariance of the physical law would be violated [148]. These scalar quantities are coefficients characterising the particular properties of the material.

The second requirement is the principle of kinematic invariance. This principle implies that when relationships are established amongst various quantities, they must be referenced to the same point in the body, or in space. As such, if the time derivative of any quantity is encountered in the rheological equations of state, it should be calculated

taking into account the displacements of the body in space. This implies that account must be taken of the body motion as a whole, and the rotation of the elements of the body in the neighbourhood of the point in question. This requires not only the inclusion of partial time derivatives in the constitutive equations, but also those derivatives taken with respect to coordinate transformations in time. Examples of such derivatives are the Oldroyd and Jaumann operators.

The third principle, introduced by Oldroyd, is that only the neighbouring particles in a material should be involved in determining the stress at a particular location. This is consistent with the notion of short-range forces amongst the molecules of a physical material. At the same time, this excludes long-range forces, such as those of an electrostatic origin, included as body forces [137]. The assumption made here, that the stress in a given fluid particle depends on the kinematic history of that particle alone (and not on the kinematic history of the neighbouring particles) appears to have found universal acceptance, without requirement of appealing to a higher level of complexity [16]. With these principles, and some simplifying mathematical approximations and assumptions, one can establish reasonably general continuum mechanical constitutive equations, without appealing further to deeper molecular theory.

2.6 Constitutive models

2.6.1 Newtonian model

For an inelastic fluid, the constitutive equation may be expressed in the form of $f(\sigma,\dot{\gamma})$. The Newtonian constitutive equation is the most common form of this type of equation and is expressed viz.

$$\sigma_{ij} = 2\mu D_{ij} + \mu\left(\frac{k}{\mu} - \frac{2}{3}\right)(\nabla \cdot u)\delta_{ij} \tag{2.5}$$

where, D and δ represent the rate-of-deformation and Kronecker delta (tensors), respectively. Here, $2D_{ij} = \left(L_{ij} + L_{ij}^{T}\right)$ and $L^{T} = \nabla u$. The material parameters of k and μ represent bulk viscosity and shear viscosity, respectively. Bulk viscosity arises as a consequence of active rotational and vibrational modes at the polyatomic molecular level, relevant in compressible gas or granular matter flow.

2.6.2 Maxwell models

An early rheological model for viscoelastic fluids emerged from the proposals of Maxwell, who speculated that gases may be viscoelastic. This seminal notion was never actually adopted for gases, yet it did become the central basis for the development of viscoelastic models applicable for liquids and solids. Maxwell proposed the linear equation,

$$\sigma + \lambda \frac{\partial \sigma}{\partial t} = G\lambda\dot{\gamma}, \tag{2.6}$$

which has an elastic limit, $\sigma = G\gamma$, for rapid deformation and a viscous limit, $\sigma = G\lambda\dot{\gamma}$, for slow deformation. In the above equation, G and $G\lambda$ are the elastic modulus and viscosity, respectively. Oldroyd realised that this linear model did not obey the mathematical principle of objectivity. He established in this landmark paper [107], that for large strains, the rate-of-change of stress as well as deformation rate, must be objective, and hence, non-linear. Oldroyd proposed that frame invariance could be recovered by expressing the constitutive equation in a frame of reference convected or deformed with the material elements (second principle). To do so, one must reinterpret the time derivative in the Maxwell equation as a time derivative in a convected coordinate system:

$$\sigma + \lambda \frac{\delta \sigma}{\delta t} = 2\mu D. \tag{2.7}$$

There are two common convected coordinate systems. First, the base coordinate vectors, which are parallel to the material lines, are stretched and rotated with the material lines [88]. This gives rise to the set of contravariant base-vectors, and the convected time derivative

$$\frac{\delta \sigma}{\delta t} = \overset{\nabla}{\sigma} \equiv \frac{\partial \sigma}{\partial t} + v \cdot \nabla \sigma - \nabla v^T \cdot \sigma - \sigma \cdot \nabla v, \tag{2.8}$$

termed the upper-convected derivative. The second is a set of base-vectors that are normal to material planes. With this set of covariant base-vectors, the convected time derivative is,

$$\frac{\delta\sigma}{\delta t} = \overset{\Delta}{\sigma} \equiv \frac{\partial\sigma}{\partial t} + v\cdot\nabla\sigma + \nabla v^T\cdot\sigma + \sigma\cdot\nabla v \tag{2.9}$$

termed the lower-convected time derivative. The associated terminology, upper-convected and lower-convected, originally attributed as superscripts, was used for contravaraint base-vectors and subscript for covariant base-vectors [88]. These two choices, when imposed upon the Maxwell equation in frame-invariant form, lead to:

$$\sigma + \lambda\overset{\nabla}{\sigma} = 2\mu D \qquad \text{(UCM)} \tag{2.10}$$

$$\sigma + \lambda\overset{\Delta}{\sigma} = 2\mu D \qquad \text{(LCM)} \tag{2.11}$$

The equations (2.10) and (2.11) represent the upper-convected Maxwell (UCM) and the lower-convected Maxwell (LCM) equations, respectively. The UCM enjoys a molecular basis, whilst the LCM does not [88].

2.6.3 Oldroyd models

Oldroyd proposed employing the frame invariant form of the Jeffrey equation, a more generalised version than the Maxwell equation,

$$\sigma + \lambda\frac{\delta\sigma}{\delta t} = 2\mu\left(D + \lambda_2\frac{\delta D}{\delta t}\right). \tag{2.12}$$

The last term can be regarded as arising from stress in the solvent. As above, the two invariant forms of the Oldroyd equation become:

$$\sigma + \lambda\overset{\nabla}{\sigma} = 2\mu\left(D + \lambda_2\overset{\nabla}{D}\right) \qquad \text{(Oldroyd-B)} \tag{2.13}$$

$$\sigma + \lambda\overset{\Delta}{\sigma} = 2\mu\left(D + \lambda_2\overset{\Delta}{D}\right) \qquad \text{(Oldroyd-A).} \tag{2.14}$$

With the Oldroyd-B model, the stress tensor σ can be split into *polymeric stress* and *solvent stress*. This avoids additional numerical discretisation error encountered under the approximation of higher-order derivatives. Such a stress-splitting can be expressed through an extra-stress, τ, in the following form:

$$\sigma = \tau + 2\mu_s D, \tag{2.15}$$

from which the Oldroyd-B equation yields:

$$\tau + \lambda \overset{\nabla}{\tau} = 2\mu_e D . \tag{2.16}$$

Here, μ_s, μ_p represent the polymeric and solvent viscosity contributions, respectively. The total viscosity, μ, and retardation time, λ_2, may be recovered through the following relationships:

$$\mu = \mu_s + \mu_e \tag{2.17}$$

$$\lambda_2 = \frac{\lambda \mu_s}{\mu} . \tag{2.18}$$

Here, to satisfy the "second law of thermodynamics", the above equations must satisfy the constraint $\lambda \geq \lambda_2 \geq 0$. In order to reproduce the dependency of shear stress on shear rate in steady simple shear experiments, Crochet and Keunings, in a finite element context, proposed a viscosity ratio of Newtonian solvent to polymeric solute $\left(\frac{\mu_s}{\mu_e}\right)$ of $\frac{1}{8}$, and a retardation to relaxation time ratio $\left(\frac{\lambda_2}{\lambda}\right)$ of $\frac{1}{9}$. The Oldroyd-B model provides a constant shear viscosity, which is suitable for the study of (realistic) Boger fluids at moderate shear-rates. To a good approximation, in steady simple shear flow, these fluids (highly dilute solutions of a high molecular weight polymer in a highly viscous solvent) reflect a constant viscosity and a quadratic first normal stress difference over a reasonable range of shear rates. As such, these fluids, were used in experiments to separate shear-thinning from elastic effects. Over many years, the Oldroyd-B model has been thought of as a useful first approximation for such fluids, since the vsicometric functions for this model are broadly consistent with experimental observations [138].

In contrast, the extensional viscosity μ_e, of the Oldroyd-B model is not constant. For a uniaxial extensional flow, the extensional viscosity can be expressed as a function of extensional rate, $\dot{\varepsilon}$, viz,

$$\mu_{ex}(\dot{\varepsilon}) = 2\mu\frac{(1-2\lambda_2\dot{\varepsilon})}{(1-2\lambda\dot{\varepsilon})} + \mu\frac{(1+\lambda_2\dot{\varepsilon})}{(1+\lambda\dot{\varepsilon})}. \tag{2.19}$$

A drawback to the Oldroyd model is that at a finite extension rate, $\dot{\varepsilon} = \frac{1}{2\lambda}$, the extensional viscosity becomes infinite, which is unphysical. Nonetheless, the property of constant shear viscosity makes the Oldroyd-B an attractive model in investigating the performance of numerical algorithms and shall be used in this thesis study throughout.

CHAPTER 3

Numerical Algorithm and Finite Element Method

This chapter addresses the need to predict solutions for weakly-compressible highly-viscous/viscoelastic polymeric liquid flows, with attention to both accuracy and efficiency. The approach commences from a framework adopted for incompressible flow and viscoelastic fluids, upon which compressibility is imposed. Here, viscous/viscoelastic dominant fluids are considered, so that inertial effects are low to moderate, yet viscosities/viscoelasticities may be high. In such a context, the level of corresponding Reynolds number is low (typically, $\mathrm{Re} \approx O(1)$), diffusion dominates and convection terms may be resolved without difficulty. This lies in contrast to the aerodynamic high-convection regime (inertial, low-viscosity, high-speed), which gives rise to shocks and where characteristic-based methods are relevant. Here, such issues do not emerge. To address *viscoelastic flows*, where convection of stress (fluid-memory) is important, a suitable form of upwinding is demanded. To this end two different forms of upwinding based on Petrov-Galerkin [98] and fluctuation distribution [151,152] are adopted.

3.1 Governing equations

The governing equations for viscoelastic flows are represented by the conservation laws for mass and momentum, in conjunction with equations of state for stress and

density (compressible flow). The non-dimensional form of continuity and momentum balance equations for isothermal compressible flows respectively may be expressed, viz.

$$\frac{\partial \rho}{\partial t} + \nabla \cdot (\rho u) = 0, \tag{3.1}$$

$$\mathrm{Re}\,\rho \frac{\partial u}{\partial t} = \nabla \cdot (\tau_s + \tau) - \mathrm{Re}\, u \cdot \nabla u - \nabla p, \tag{3.2}$$

where, ρ, u, p and τ represent density, velocity vector, hydrodynamic pressure and extra-stress tensor respectively. The viscous stress τ_s is defined based on Eq.(2.5). The relationship between the solvent and polymeric viscosity implies $\mu = \mu_e + \mu_s$. When $\mu_s = 0$, the system describes the Maxwell model. Henceforth, we refer to $\mu_e^* = \mu_e/\mu = 8/9$ and $\mu_s^* = \mu_s/\mu = 1/9$.

The Oldroyd-B constitutive equation is given by

$$\tau + We \frac{\partial \tau}{\partial t} = -We u \cdot \nabla \tau + We\left(L \cdot \tau + \tau \cdot L^T\right) + 2\mu_e^* D. \tag{3.3}$$

The Reynolds (*Re*) and Weissenberg (*We*) non-dimensional group numbers are defined according to convention as,

$$\mathrm{Re} = \frac{\hat{\rho}\hat{U}l}{\mu}, \quad We = \frac{\lambda \hat{U}}{l}, \tag{3.4}$$

where, $\hat{\rho}$, μ and λ denote selected reference density, total viscosity and relaxation time; $\hat{U}$, l are characteristic velocity and length scales (channel exit half-width) of the flow. By convention, for the 4:1 contraction flow problem (see chapter four), a characteristic velocity for incompressible flow may be assumed as based on the maximum velocity at the channel outlet. Generally, this is calculated via the continuity equation from fully-developed outlet flow considerations. For incompressible flow, density is constant and only inlet mass flow-rate is calculated, via imposed boundary conditions on velocity. In contrast, for compressible flow, density at the inlet is a dependent variable. Consequently, the characteristic velocity remains a dependent variable. Therefore, within our study for compressible flow, the characteristic velocity is adopted of its incompressible counterpart.

To close the set of equations it is necessary to introduce an equation of state to link density to pressure. In this regard, the Tait equation of state (see chapter two) has been extensively employed in polymer processing to describe the relationship between density, pressure and temperature. The equation can be expressed in a simplified form,

$$\tilde{P} + B = B\rho^m \text{ where augmented pressure, } \tilde{P} = P - \frac{1}{3} trace\left(\tau_s + \tau\right). \tag{3.5}$$

Here, B represents a non-dimensional shift for pressure and m a dimensionless exponent (a function of temperature).

For clarity, the (*) notation on viscosity fractions is implied, yet discarded.

3.2 Background theory

Compressibility effects occur in both liquids and gases through the variation of density. Density itself depends on temperature, pressure and concentration levels. Flows of liquid materials, at moderate pressure levels, can be considered as incompressible. Nevertheless, at large pressure-differences, such flows may display some mild compressibility effects. The Mach number, the ratio of fluid velocity to the speed of sound ($Ma = u / c$), characterises the influence of compressibility on a flow field. Flows at low Mach number (LMN) may be described as incompressible, whilst for those at moderate to high Mach number, compressibility effects will be prominent. The incompressible limit of a compressible flow is approached, under suitable constraints, as the Mach number vanishes [103]. Under such circumstances, the speed of sound is much larger than the velocity of the liquid, resulting in fast pressure waves, where rapid pressure equalization takes place.

LMN flows play an important role, occurring widely in nature and industrial processes. Circulation within the oceans is driven mainly by density gradients, which arise via variation of salinity and temperature. Common human bodily functions, such as, singing, whistling, breathing and talking, all represent examples of LMN flow regimes. In addition, some industrial gas flow configurations take place at LMN. Free convection and combustion are yet further examples, where flow occurs driven under the variation of density with temperature. Compressibility has some impact upon applications such as in: liquid impact, jet cutting and liquid impact erosion, in steam turbine for example [45,78]; polymer extrusion [49]; injection molding with polymer

melts [60]; recovery and exploration of petroleum [160]. Compressibility should be incorporated in order to rigorously investigate such phenomena as cavitation [21], instabilities [49], and shrinkage and warpage [60], liquid impact erosion [72,78]. Moreover, in capillary rheometry, compressibility may have a significant influence on features such as the time-dependent pressure changes within a system (see piston-driven flows, [120].

Much attention has been devoted towards the computational solution of flows that manifest compressibility effects. Today, sophisticated numerical solvers can handle high Reynolds number compressible flow computations. To solve such scenarios, different methodologies have emerged under finite element and finite volume approaches. Within finite elements, this gives rise to various Streamline-Upwind/Petrov-Galerkin (SUPG) algorithms, with stabilization techniques such as Galerkin Least-Square (GLS) [70]. Equivalently, in the finite volume context, some high-performance counterpart algorithms have emerged [76,77,102]. Nonetheless, Wong *et al.* [159], state that some SUPG compressible-based algorithms may fail to yield adequate numerical solutions for flows that approach the incompressible limit. Degradation in the solution has been observed in several studies [143,159]. Here, the key difficulties are addressed associated with the computation of weakly-compressible liquid flows.

3.2.1 Switch of equation type

One of the key difficulties arises from the fact that the governing equations switch in type. The equations for viscous compressible flow form a hyperbolic-parabolic system with finite waves-speed (inviscid case, hyperbolic), whilst those for incompressible viscous flow assume an elliptic-parabolic system with infinite propagation rates. In addition, for viscoelastic flows, a sub-system of hyperbolic form may augment the whole. Switch in type of the governing equations may render ill-posedness in flow computation, due to boundary conditions and solution strategy.

3.2.2 Pressure decoupling

In the LMN situation, where density becomes almost constant, the role of pressure is to act on velocity through continuity, so that conservation of mass is satisfied. In these situations, when density changes are small, density-pressure coupling becomes weak [77]. As a result, the continuity equation is decoupled from the momentum equations

and can no longer be considered as the equation for density [102]. Rather, continuity acts as a constraint on the velocity field. Thus, for sequential solution of equations, it is necessary to devise a mechanism to couple the continuity and momentum equations through the pressure field. In compressible flow situations, the pressure takes on a dual role to act on both density and velocity through the equation of state and momentum conservation, respectively, so that mass conservation is satisfied. The choice of whether pressure has a major effect on density or velocity depends upon the flow regime, Mach and Reynolds numbers. This will be discussed in detail later for the case of present interest, where Mach and Reynolds numbers are generally low. The above reveals that for any numerical method to be capable of predicting both incompressible and compressible fluid flow, the pressure should always be allowed to play its dual role, to act on both velocity and density to satisfy continuity.

3.2.3 Large disparity in waves speed and efficiency

The main difficulty in solving the compressible equations for LMN is associated with large disparity of the waves-speed which are present in the system [143,159]. Acoustic waves travel much faster than entropy waves, which are convected at the fluid velocity. In LMN flows, the largest eigenvalues of the system (λ_{max}) tend toward the speed of sound and the smallest (λ_{min}) provides the speed of the fluid. Thus, the condition number of the system (κ), the ratio of largest to smallest eigenvalues, goes larger, as the Mach number tends to zero.

$$\kappa = \frac{\lambda_{max}}{\lambda_{min}} = \frac{u+c}{u} = 1 + \frac{1}{Ma}. \tag{3.6}$$

This effect increases the stiffness in the system [125,141]. Consequently, for compressible implicit schemes, iterative solution of the algebraic equation system is slow and expensive. On the other hand, the explicit time-marching schemes for numerical stability considerations are restricted to obey the CFL (Courant-Friedrichs-Lewy) condition. This states simply that the numerical domain of dependence must be at least as large as the physical domain of dependence (see [65]). In other words, the CFL condition states that the numerical scheme must be such that the solution at some point i at time level $t+\Delta t$ must depend on all points at time level t whose characteristic variables affect point i. This places a limit on the size of time-step Δt, which may be taken. Therefore, explicit time-marching schemes suffer from the lack of efficiency due

to excessively small time-steps to satisfy CFL conditions, which impose, the following restriction on time-step selection:

$$\Delta t_{com} \le a\frac{\Delta x}{u+c} \tag{3.7}$$

where, a is a constant of order unity, Δx the mesh length-scale, and $(u+c)$ the speed of the acoustic mode. For the incompressible counterpart, the stability restriction is less severe:

$$\Delta t_{inc} \le a\frac{\Delta x}{u} \tag{3.8}$$

where, the time-step is in balance with the physical time-scale. One can obtain

$$\frac{\Delta t_{com}}{\Delta t_{inc}} = \frac{Ma}{Ma+1} \to 0 \qquad \text{for} \quad Ma \to 0\,. \tag{3.9}$$

Thus, for LMN and explicit schemes, the acoustic waves impose a time-step much smaller than the physical time-step. Therefore, conventional compressible solvers for LMN flows, either in explicit or implicit form, become inefficient and impractical without modification for Mach numbers lower than about 0.3 [58,123]. The problem can be quantified on the following grounds: The speed of sound for air at room temperature is around 333 m/s [94]. Therefore at Ma=0.3, the speed of the fluid will be approximately 100 m/s. Nevertheless, the speed of sound for compressible liquids is much larger than the speed of sound in air (say five times). In applications such as polymer processing, velocity levels are generally low (order of unity). Therefore, condition numbers in compressible liquid flows are normally smaller, by order of magnitudes, compare to those for compressible low-Mach gas dynamic applications. This is why computation of compressible liquid flows generally is associated with much more severe conditions than gas flows. Therefore, the accurate solution of nearly incompressible flows is difficult to obtain [159].

3.2.4 Consistency and error cancellation

Stiffness of the equations is not the only problem that besets standard compressible flow computing methods at low speed. Actually, in addition to convergence and round-off error difficulties, the approximation of compressible fluid flow equations suffers from accuracy and consistency problems in the LMN limit [58]. There is experimental

evidence to show that on a fixed mesh, the discretised solution of the compressible fluid flow equations is not an accurate approximation of the incompressible equations [58,143]. Viozat analysed the Roe scheme in the LMN regime and quoted "when the mesh size h and the Mach number Ma tend to zero, the truncation error of the first-order Roe scheme applicable to the momentum equations, is only $O\left(\frac{h}{Ma}\right)$". Therefore, this scheme in the LMN limit is inconsistent. Sesterhenn *et. al.* [129] have shown that cancellation errors play a significant role in calculating LMN flows. They have shown precisely the role of computer accuracy and numerical cancellation for this problem. When a stiff system is solved by carrying out the required large number of small time-steps, often incorrect results are obtained for LMN problems [158].

3.3 Numerical methods

The need for algorithmic developments to handle the LMN flow regime may be justified on a number of grounds. For example, there are many natural phenomena, where accurate simulation in this scenario is demanded. In some instances, flow problems may exhibit mixed-type (compressible/incompressible), where some sections of the flow are incompressible with locally LMN, whilst other zones are significantly compressible. Under such circumstances, if the incompressible region is sufficiently small, compared to the compressible section, there is little loss of accuracy when incompressibility is neglected. However, there are flow regimes, such as in aerodynamics (high-speed/low-viscosity), where large regions of LMN coexist alongside supersonic flow regions. This arises in aerofoil high angle-of-attack configurations, where the solution will degrade if based solely on a compressible description. Moreover, acoustics in gases and liquids is not only a daily experience, but also has great scientific and technological significances. Aerodynamic noise regulations become more restrictive due to public demands caused by increased transport of persons and goods and by increased environmental sensitivity. Thus, aerodynamics has become a key issue in the design of airplanes, cars, engines and in general, everything that can produce acoustic waves. In addition, in some material processing instances, such as for polymers during the filling stage of injection moulding and in extrusion, there are some locally compressible regions, whilst most of the flow remains incompressible.

Therefore, it is both desirable and necessary to develop algorithms that can handle both regimes, concurrently.

Computational methods to solve flow problems fall into two main categories: (a) methods for compressible flows and (b) methods for incompressible flows [77,100,102]. These two classes of methods are quite different from each other with respect to the choice of variables, issues related to numerical stability and choice of solvers and boundary conditions [100]. Compressible schemes are characterised by employing density as the primary dependent variable, extractable from the continuity equation, and hence, pressure being determined from solution variables via an equation of state. These schemes are called density-based methods. For incompressible schemes (pressure-based) continuity is utilized as a constraint on velocity and is combined with momentum to form a Poisson-like equation for pressure. Each of these methods is appropriate for a specific range of Mach number values.

Density-based methods have been employed as a natural choice for computation of compressible flows. Turkel *et al.* [143] and Guillard and Viozat [58] have identified that, in the LMN limit, the discretised solution of the compressible flow equations may fail to provide an accurate approximation to the incompressible equations (quoting Guillard and Viozat [58] in particular). As a 'rule-of-thumb', compressible schemes without modification become impractical for Mach numbers lower than around 0.3 [123]. In contrast, pressure-based methods were originally conceived to solve incompressible flows, adopting pressure as a primary variable. With this approach, pressure variation remains finite, irrespective of Mach number, rendering computation tractable throughout the entire spectrum of Mach number [77], hence circumventing the shortcomings of density-based methods.

Therefore, from a numerical perspective, conventional approaches to handle LMN flows can be subjugated into two main categories: *density-based* schemes and *pressure-based* schemes [77,102].

3.3.1 Density-based methods

Density-based methods represent a large class of schemes adopted for compressible flows. Time-marching density-based schemes are employed widely in computational fluid dynamics for computation of steady and transient transonic, supersonic and hypersonic flows, where switch of type occurs here, as *Ma* passes through unity. In the

subsonic regime, when the magnitude of the flow velocity is small, in comparison with the acoustic wave-speed, computation of weakly-compressible flow in a standard density-based compressible formulation gives rise to loss of accuracy and consistency due to weak coupling between pressure and density and loss of efficiency due to the stiffness of the system of equations, when the Mach number is below 0.3 [144].

Two distinct techniques have been proposed to capture solution convergence for LMN regimes, preconditioning and asymptotic. Both techniques achieve rescaling of system condition numbers. The first technique is to pre-multiply time-derivatives by a suitable preconditioning matrix. Effectively, this scales the eigenvalues of the system to similar orders of magnitude and removes the disparity in wave-speeds, leading to a well-conditioned system [143]. The second technique introduces a perturbed form of the equations. This is known as the asymptotic method. Here, specific terms are discarded, so that the physical acoustic waves are replaced by pseudo-acoustic modes.

3.3.1.1 Preconditioning schemes

Chorin [27] proposed the method of artificial compressibility to solve the incompressible Navier-Stokes equations when a steady-state solution is sought. This led to attempts to solve the compressible equations over a large range of Mach numbers. This method consists of adding an artificial density time derivative term to the continuity equation in order to restore the hyperbolic type in this equation and thus to convert a system of mixed elliptic/parabolic type to a totally hyperbolic system. With this artificial term the resultant scheme is a symmetric hyperbolic system for the inviscid terms. Thus, the system is well-posed and a numerical method for hyperbolic systems can be used to advance this system in time [142]. The temporal derivative of density is replaced by an artificial state equation in form $\rho = \beta p$, where the adjustable parameter β is called the artificial compressibility. Therefore, the continuity equation reduces to the following form

$$\beta \frac{\partial p}{\partial t} + \nabla \cdot (u) = 0. \tag{3.10}$$

This method is not consistent in time, yet this has no consequences when one is interested in steady-state solutions only. The modified equations have only steady-state solutions in common with the original system (hence, are devoid of true transients). The equation is advanced in time until a steady limiting solution of the incompressible

equation is reached. When the steady-state is reached the above artificial form of continuity, is equivalent with the original continuity equation, but the time dependence of the solution is falsified.

This seminal idea of artificial compressibility can be generalised by pre-multiplying temporal terms of the system of equations with a *preconditioning* matrix. Turkel [141] extended artificial compressibility method by adding pressure time-derivatives to the momentum equations and not just the continuity equation. The preconditioner can be derived by using different sets of variables and different methods. Therefore, there can be a family of preconditioners to improve the conditioning of fluid flow equations in different circumstances. For a review on preconditioning schemes, one can refer to [142].

The preconditioning can be utilised for either compressible or incompressible flows, to accelerate convergence towards a steady-state. Indeed, the system of incompressible Euler equations, in which terms have been introduced as factors of the time derivatives, form a totally hyperbolic system, i.e. it is of the same type as the system of the compressible equations. Thus, the problem of solving the incompressible equations and the one of solving the compressible equations at LMN meet and can be solved with the same method when a steady-state solution is sought. Turkel [141] has introduced a family of preconditioners for low Mach-number flows. Similarly, Van Leer *et al.* [146] derived a symmetric preconditioner for the two-dimensional Euler equations. The main drawback of preconditioning methods is the lack of robustness near stagnation points (where the velocity field is slow). This may be due to artificial dissipation, where solution eigenvectors become almost parallel [33,159]. For the application of these methods to time-dependent problems, the 'dual-time-stepping' technique has emerged, where the physical time-derivative terms are treated as source terms. During each physical time-step, the system of pseudo-temporal equations is advanced in artificial time to reach a pseudo-steady-state, so that ultimately, a divergence-free constraint on the velocity field is satisfied [92].

Efficiency in preconditioner performance is known to be highly affected by the eigenvalue spectrum of the system, which must be taken into account within the design of the preconditioner. This arises for example, when simulating combustion problems at low Mach numbers. However, finding suitable preconditioners with optimised

properties for complex problems is far from straightforward. Darmofal and Schmid [33] analysed the influence of eigenvector properties on the effectiveness of some preconditioners. Both theoretically and numerically, Darmofal and Schmid have demonstrated, that due to the lack of eigenvector orthogonality, small perturbations in the linearised evolution problem could be significantly amplified over short time-scales. The long-time or asymptotic behaviour of the linearised system is governed by the eigenvalue spectrum. However, for practical applications to nonlinear problems, this short-time non-normal growth may completely alter the mean-state, to the extent that the predicted long-time asymptotic behaviour may be lost. Darmofal and Schmid have demonstrated, through nonlinear preconditioned Euler predictions, that non-normal amplification does arise, and in practice, generates a significant lack of robustness, particularly near stagnation points.

3.3.1.2 Asymptotic schemes

With the second technique, the asymptotic or perturbation approach, a perturbed form of the equations is employed to eliminate system stiffness. Here, a Taylor series expansion of variables in powers of the Mach number is introduced. This decouples the physical acoustic waves from the equations, replacing them by a set of pseudo-acoustic forms, whose speeds are comparable to the fluid velocity [26,140]. Application of perturbation methods to extend compressible flow solvers to slightly compressible instances is straightforward, particularly for reactive flows. One may consider, for example the combustion setting where, due to the transient reactive terms, preconditioning schemes require a complex analysis. Although perturbation procedures are highly robust and applicable for both viscous and inviscid flows, the nature of the perturbation limits their usage, particularly with respect to mixed compressible-incompressible flows.

A LMN asymptotic scheme is used by Klainerman and Majda [86] for the Euler equations and by Kreiss *et al.* [87] for the Navier-Stokes equations to prove the convergence of the compressible flow solutions for zero Mach number limiting solutions under certain conditions. The basic philosophy behind asymptotic methods is to decrease the numerical representation of the speed of sound artificially, by subtracting a constant pressure p_o across the entire domain. In modifying away from the true speed of sound, the numerical scheme may enjoy larger time steps (for more

details see [74]). From a theoretical point of view, the situation is now well-understood in the inviscid limit: if the initial pressure field p scales with the square of the Mach number Ma, $p(x,0) = p_0 + Ma^2\, p_2(x)$. Additionally, if the initial velocity field (at $t = 0$) is almost solenoidal: $u(x,0) = u_0 + Ma\, u_1(x)$ with $div(u_0) = 0$; then, the compressible flow solution remains uniformly bounded as the Mach number tends to zero. In the $(Ma \to 0)$ limit, the solution satisfies the 'reduced' equation system for the incompressible state [123].

A significant source of error at LMN arises due to the fact that the pressure term is of order $1/Ma^2$, which introduces considerable inaccuracy as the Mach number approaches zero. In this regime, compressibility effects have little influence on momentum transfer, since, pressure becomes only a weak function of density. To prevent inaccuracy in the computation of pressure-gradients within the momentum equation, the pressure can be decomposed into two contributions [26,140]: $p(x,t) = p_o(t) + p'(x,t)$, with $p_o(t)/p_o = O(1)$ and $p'(x,t)/p_o = O(Ma^2)$. Here, $p_o(t)$ and $p'(x,t)$ are termed the 'thermodynamic pressure' and the 'hydrodynamic pressure', respectively and p_o is simply a reference pressure. The thermodynamic pressure is defined as

$$p_o(t) = \frac{1}{V}\int_V p(x,t)\,d\Omega\,, \tag{3.11}$$

where, V is the volume of the solution domain. With this variable decomposition, only the thermodynamic pressure appears in the equations of energy and state. In the momentum equation, the gradient of the thermodynamic pressure vanishes, leaving only the gradient of hydrodynamic pressure.

3.3.2 Pressure-based Methods

The first implementation of pressure-based schemes for compressible flow is widely attributed to the early contribution of Harlow and Amsden [61], based on a semi-implicit finite difference algorithm.

Pressure-correction, or projection methods, are pressure-based fractional-staged schemes with correction for velocity and pressure (see [113]), introduced through the pioneering work of Chorin [28] and Temam [139]. Such methods have been employed effectively within several finite volume implementations, say through the SIMPLE

(Semi-Implicit Pressure Linked Equations) family of schemes [111]. Karki and Patankar [77] developed the SIMPLER method for compressible flows, applicable for a wide range of problem-speeds. These SIMPLE methods are first-order in time. Munz *et al.* [103] extended the SIMPLE scheme for low Mach number flow employing multiple pressure variables, each being associated with different physical response. Similar procedures have been adopted by others [15,96,123]. Pressure-correction was taken forward within finite differences to a second-order by Van Kan [145]. Alternatively, within finite elements, Donea *et al.* [38] introduced a pressure-correction fractional-step method, designed to significantly reduce computational overheads in transient incompressible viscous flow situations. Similarly, Zienkiewicz *et al.* [165,166] have introduced the characteristic-based-split procedure (CBS). This implementation is a Taylor-Galerkin/Pressure-Correction scheme, suitable for both incompressible and compressible flow regimes. The crux here, is to split the equation system into two parts: a part of convection-diffusion type (discretised via a characteristic-Galerkin procedure) and one of self-adjoint type. With the characteristic-based-split scheme, one may solve both parts of the system in an explicit manner. Alternatively, one may use a semi-implicit scheme for the first part, allowing for much larger time-steps, and solve the second part implicitly, with its advantage of unconditional stability. The characteristic-based-split procedure has been tested successfully on a number of scenarios, for example, transonic and supersonic flows, LMN flows with low and high viscosity, and in addition, on shallow-water wave problems.

In the incompressible viscoelastic regime, computational methods have matured significantly over the last two decades or so [10,56,126,150]. Here, it is desirable to extend the methodology into the weakly-compressible regime, and particularly so for viscous/viscoelastic polymeric liquid flows. In this regard, density-based preconditioning or asymptotic methods often demand significant recoding. On the other hand, extending an existing incompressible flow code to accommodate compressibility would appear somewhat more straightforward. Precisely, here the aim is to modify a pressure-correction technique for incompressible polymeric flows to accommodate weakly-compressible, yet highly-viscous/viscoelastic, flows under LMN configurations. This presents a natural extension to earlier incompressible flow studies of Webster and co-workers for viscous [62], inelastic [36, three-dimensional] and viscoelastic [98,150] fluids, where we have developed a hybrid schema to attain second-order accuracy.

3.4 Pressure-Correction scheme for compressible flows

Taylor-Galerkin (TG) schemes have emerged, via Taylor-series expansions, to provide high-order time-stepping schemes of various forms, see Donea [37] and Löhner *et al.* [93]. The principal constructive methodology is to discretise advection-based equations first, in time, and second, in space (Galerkin). Time derivatives may be replaced by spatial equivalents, from the original differential equation (Lax-Wendroff [89]). This introduces explicit or implicit-type schemes, of various orders of accuracy, and of one-step or two-step implementations (see Löhner *et al.* [93]). Such schemes have been used widely to solve model problems to more complex flows [2,31,36,104,165,166]. Recently, Webster and co-workers have advocated various advances in the application of our incompressible second-order, fractional-staged, time-marching pressure-correction procedures. This has accommodated model to complex flows exemplified through free-surface flows [104], wire-coating [105] and dough mixing applications [12]. The present goal is to elaborate the constructive steps to incorporate weak-compressibility upon such a formulation, where we have polymeric viscous/viscoelastic liquid flow applications in mind.

The base formulation-framework is that of a pressure-correction scheme, split into three distinct, fractional-stages. Briefly, at a first stage, which is divided into two sub-stages, the momentum equation is employed to predict the velocity field at a half-stage. Subsequently, the momentum equation is employed to compute the velocity (u^*) at a full-step (two-step Lax-Wendroff style, Taylor-Galerkin phase, [93]. The second stage (pressure-correction) utilises the continuity equation to evaluate a temporal pressure-difference, inserting the approximate velocity field (auxiliary variable, u^*, computed at stage one). Crank-Nicolson averaged treatment for diffusion/source term introduces *semi-implicitness* to the stages and overcomes restrictive diffusive stability limitations. At a third stage, the end-of-step velocity field (u^{n+1}) is corrected, based upon the pressure-difference on the time-step, derived at the second stage. One may draw distinction to the characteristic-based-split procedure of Zienkiewicz *et al.*[165,166], in the retention of pressure gradients, within the representation of the momentum equation over stage one. This ensures the solution at stage two for temporal pressure increments, delivering second-order accuracy to the system and aiding the appropriate setting of boundary conditions throughout. The characteristic-based-split approach, alternatively,

conveys the pressure gradient term to the third fractional-staged equation for velocity-correction. A comparison between the employed scheme in this study and the CBS scheme structure is provided in appendix 3.A.

To extend the incompressible algorithm to deal with compressible flows, one must first appreciate the key role that pressure plays in a compressible flow. In the LMN limit, where density is almost constant, the role of pressure is to influence velocity through the continuity equation, so that conservation of mass is satisfied [102]. In this instance, density and pressure are only weakly-linked variables. To recast the above incompressible scheme into one appropriate for weakly-compressible highly-viscous flows, we follow the ideas of Karki and Patankar [77] and Zienkiewicz *et al.* [165,166]. Here, the temporal derivative of density from the continuity equation is replaced by its equivalent in pressure, appealing to an equation of state. To observe this, we take the equation that defines the auxiliary variable (u^*):

$$u^{n+1} = u^* - \left(\frac{\Delta t}{\rho}\right)\theta\nabla\left(\Delta p^{n+1}\right), \tag{3.12}$$

with constant scheme factor $0 \le \theta \le 1$ and operator $\Delta(\cdot)^{n'} = (\cdot)^{n'} - (\cdot)^{n}$. Here, θ is normally taken as 0.5 for second-order accuracy, as below. By taking the divergence of this equation, one gathers:

$$\nabla.\left(\rho u^{n+1}\right) = \nabla.\left(\rho u^*\right) - \Delta t\theta\nabla^2\left(\Delta p^{n+1}\right), \tag{3.13}$$

from which, by appealing to the compressible form of the continuity equation, one may insert the discrete temporal derivative of density:

$$\frac{\Delta\rho u^{n+1}}{\Delta t} + \nabla\cdot\left(\rho u^*\right) = \Delta t\theta\nabla^2\left(\Delta p^{n+1}\right). \tag{3.14}$$

In addition, in pressure-based methods density increments may be replaced by pressure increments [77]. After rearranging and differentiating the equation of state, we gather:

$$\frac{\partial p}{\partial\rho} = m\rho^{m-1}\frac{\left(\tilde{p}_0 + B\right)}{\rho_0^m} = \frac{m(\tilde{p} + B)}{\rho} = c^2_{(x,t)}, \tag{3.15}$$

where $c_{(x,t)}$ represents the speed of sound. Employing the chain rule upon $\frac{\partial \rho}{\partial t} = \frac{\partial \rho}{\partial p}\frac{\partial p}{\partial t}$ and taking difference operations over the time-step $\Delta t = (t_{n+1} - t_n)$, we may relate density increment to pressure increment at time instant t_{n+1} through,

$$\frac{\Delta \rho^{n+1}}{\Delta t} = \frac{1}{c^2_{(x,t)}}\frac{\Delta p^{n+1}}{\Delta t}. \tag{3.16}$$

Finally, we substitute Eq.(3.16) into Eq.(3.14) to realise a compressible form of the temporal evolutionary expression for pressure:

$$\frac{1}{c^2_{(x,t)}}\frac{\Delta p^{n+1}}{\Delta t} - \Delta t\theta\nabla^2(\Delta p^{n+1}) = -\nabla .(\rho u^*) . \tag{3.17}$$

This is the new Stage-2 equation, introduced to provide the compressible pressure-correction formulation (see below). Note, Eq.(3.17) is obtained under isentropic condition similar to [77,165,166]. Other alternative assumptions may be adopted, such as isenthalpic [91] or homenthalpic [103]. Note, under steady-state conditions, temporal pressure change will vanish and the steady solution will be independent of the above stated assumptions. However, this may affect transient results and convergence properties of the associated schemes.

Briefly, the general framework of the Taylor-Galerkin/pressure-correction (TGPC) scheme is based on a time-stepping procedure, involving two distinct phases within each time step. The *first phase* involves a Taylor-Galerkin scheme, expressed through a two-step, Lax-Wendroff time stepping procedure. This represents a predictor-corrector doublet for velocity and stress, which initially calculates predicted fields $(u,\tau)^{n+1/2}$, prior to computing a non-divergence-free velocity field u^* and an updated stress field τ^{n+1}. The *second phase* is a pressure-correction scheme that ensures second-order accuracy in time. This generates an equation for temporal pressure-difference and a Poisson equation in incompressible flow. A *third and final phase* is a correction stage that recaptures the velocity field u^{n+1} at the end-of-time step loop. By implementing a semi-implicit Crack-Nicolson treatment for diffusion terms, a semi-discrete incremental form of the TGPC scheme may be derived, without heavy stability restriction imposed through diffusion operators. This scheme may be presented in a three-fractional stage form, viz.,

Stage-1a:

$$\frac{2\mathrm{Re}}{\Delta t}\rho^n\left(u^{n+1/2}-u^n\right)-\frac{1}{2}\nabla\cdot\left(\tau_s^{n+1/2}-\tau_s^n\right)=\nabla\cdot\left(\tau_s^n+\tau^n\right)-\rho^n(u\cdot\nabla u)^n-\nabla\left(2p^n-p^{n-1}\right) \tag{3.18}$$

$$\frac{2}{\Delta t}\left(\tau^{n+1/2}-\tau^n\right)=\left[-u\cdot\nabla\tau+\frac{1}{We}\left(\frac{2\mu_e}{\mu}D-\tau\right)+\tau\cdot L+L^T\cdot\tau\right]^n. \tag{3.19}$$

Stage-1b:

$$\frac{\mathrm{Re}}{\Delta t}\rho^n\left(u^*-u^n\right)-\frac{1}{2}\nabla\cdot\left(\tau_s^*-\tau_s^n\right)=\nabla\cdot\left(\tau_s^n+\tau^{n+1/2}\right)-\rho^n(u\cdot\nabla u)^{n+1/2}-\nabla\left(2p^n-p^{n-1}\right) \tag{3.20}$$

$$\frac{1}{\Delta t}\left(\tau^{n+1}-\tau^n\right)=\left[-u\cdot\nabla\tau+\frac{1}{We}\left(\frac{2\mu_e}{\mu}D-\tau\right)+\tau\cdot L+L^T\cdot\tau\right]^{n+1/2} \tag{3.21}$$

Stage-2:

$$\frac{1}{c_{(x,t)}^2}\frac{p^{n+1}-p^n}{\Delta t}-\Delta t\theta\nabla^2\left(p^{n+1}-p^n\right)=-\left[\rho^n\nabla.u^*+\nabla\rho^n.u^*\right] \tag{3.22}$$

Stage-3:

$$\frac{\mathrm{Re}}{\Delta t}\rho^{n+1}\left(u^{n+1}-u^*\right)=-\theta\nabla\cdot\left(p^{n+1}-p^n\right) \tag{3.23}$$

Note, the momentum equations for compressible and incompressible flows are practically identical, bar variation in density. Differences emerge due to the various alternative forms of the continuity equation. Hence, Eq.(3.22) displays some notable features (see [82] for detailed derivation): the first term on the left-hand-side is a first-order time derivative representation, whilst the second term is governed by a Laplacian operator (elliptic properties). In addition, on the right-hand-side, density is a direct function of pressure, that is to be interpreted via the Tait equation of state. When the flow is incompressible, the speed of sound asymptotes to infinity. In this context, the first term on the left-hand-side vanishes along with the second term on the right-hand-side, and elliptic character dominates Eq.(3.22). Alternatively, switching to compressible flows, the balance of equation-type-domination adjusts between elliptic and hyperbolic, the extent of type-mix depending upon the Mach number level (local compressibility).

3.5 Spatial discretisation

In order to analyse the finite element method, it helps to have an understanding of *function spaces*. These are not only sets of functions, but they typically have a *norm* associated with them.

A norm $\|.\|$ on X, where X is a vector space, is a function from X to R^+ such that

$$\|x\| \geq 0 \text{ and } \|x\| = 0 \text{ if and only if } x=0, \tag{3.24}$$

$$\|\alpha x\| = |\alpha| \|x\| \quad \forall x \in X \text{ and scalar } \alpha \in (R,C), \tag{3.25}$$

$$\|x+y\| \leq \|x\| + \|y\| \quad \forall x, y \in X. \tag{3.26}$$

A vector space, equipped with a norm, is termed a normed-vector space. A metric space is a pair (X, h), where X is a set of elements and h a distance (or metric function) $h : X^2 \rightarrow R^+$ such that for all $x, y, z \in X$:

$$h(x,y) \leq 0 \Rightarrow \quad h(x,y) = 0 \quad \Rightarrow x = y, \tag{3.27}$$

$$h(x,y) = h(y,x), \tag{3.28}$$

$$h(x,z) \leq h(x,y) + h(y,z) \tag{3.29}$$

Every normed-space is a metric space, where $h(x,y) = \|x-y\|$.

A sequence x_k is a Cauchy sequence if for every $\varepsilon > 0$ there is an N such that $k,l \geq N$ implies $\|x_k - x_l\| < \varepsilon$.

A metric space (X, h) is called complete, if every Cauchy sequence in X converges. Every complete metric space is called a Banach space.

The first example of a complete function space is the space of continuous functions on $[a,b]$, denoted $C[a,b]$, with norm $\|f\|_\infty = \max_x |f(x)|$.

Let $C^k(\Omega)$ denote the set of functions which together with all derivatives up to and including the k-th derivative are continuous. Let us denote the notation $L^p(\Omega)$ as the set of all functions for which

$$\|f\|_p \equiv \left(\int |f(x)|^p dx \right)^{1/p}. \tag{3.30}$$

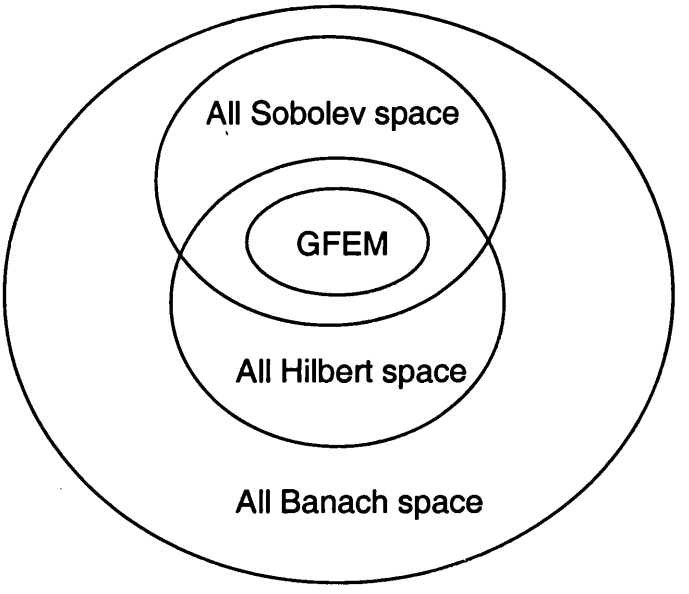

Figure 3.1: GFEM lies in a Banach space that is also in the intersection of two subspaces of it: a Sobolev and a Hilbert space

One of the most important function spaces is the set $L^2(\Omega)$, termed a Hilbert space. A Hilbert space is an inner product space, which is complete with respect to the norm defined by the inner product. Let us denote $L^2(\Omega)$ as the space of square-integrable functions over (Ω), and let $\langle , \rangle$ be the scalar product defined as

$$\langle v, w \rangle = \int_{\Omega} v w d\Omega \text{ for } v, w \in L^2(\Omega), \tag{3.31}$$

where the L^2-norm is given by $\|w\|_{0,\Omega} = \langle w, w \rangle^{1/2}$ (3.32)

One of the more important aspects of $L^2(\Omega)$ is that the norm comes from an inner product.

Sobolev spaces are Banach spaces where the norm involves derivatives. A Sobolev space can be defined as a subspace $H^1(\Omega) \in L^2(\Omega)$, for which the H^1-norm is finite and defined by

$$\|w\|_{1,\Omega} = \left(\langle w,w\rangle + \langle \nabla w, \nabla w\rangle\right)^{1/2}. \tag{3.33}$$

Similarly, a Sobolov space $H^2(\Omega)$ is a space for which the H^2-norm, given by

$$\|w\|_{2,\Omega} = \left(\langle w,w\rangle + \langle \nabla w, \nabla w\rangle + \langle \nabla^2 w, \nabla^2 w\rangle\right)^{1/2}, \tag{3.34}$$

is also finite.

The Galerkin-weighted residual approach applied to each element residual yields

$$\sum_{e=1}^{N_e} \int_{\Omega_e} \phi(x) R(u) du = 0, \tag{3.35}$$

where ϕ represents a weighting/test function belonging to a space of test functions, which may or may not be the space of trial functions, N_e, the total number of elements in the domain, $\Omega = \sum_{e=1}^{N_e} \Omega_e$. In order to be able to find a solution to problem Eq.(3.35), it is necessary for the solution $u \in H^2(\Omega)$, to comply with the second-order differential diffusion terms. The problem can be stated as follows,

$$\text{find } u \in H^2(\Omega) \mid \langle \phi(x), R(u)\rangle = 0, \forall \phi(x) \in L^2(\Omega). \tag{3.36}$$

If however, Eq.(3.35) is integrated by parts, via the Green-Gauss or Divergence theorem, the second order derivative of the velocity will be transformed to obtain a weak formulation of the problem, as

$$\text{find } u \in H^1(\Omega) \mid \langle \nabla\phi(x), \nabla R(u)\rangle = 0, \forall \phi(x) \in L^2(\Omega). \tag{3.37}$$

This means that the weak solution exists in $H^1(\Omega)$, since $H^2(\Omega)$ is densely embedded in $H^1(\Omega)$. The solution is then $u \in H^2(\Omega) \cap H^1$.

3.6 Choice of element

The finite element interpolations are characterised by the shape of the finite element and order of approximations. In general, the choice of a finite element depends on the geometry of the global domain, the degree of accuracy desired in the solution, the case of integration over domain etc. The choice of element is one of the most difficult trails in finite element. This consist of the element geometrical shape and interpolation

functions. The most crucial step in the finite element analysis of a given problem is the choice of adequate interpolation functions. They must meet certain criteria such that convergence to the true solution of the governing differential equation may be attained.

Triangles and quadrilateral are the most popular choice in finite elements for 2-D domain decomposition. They have been employed in various problems successfully. The subdivision of the domain must satisfy the following properties,

1) The number of elements is finite ($\Omega = \sum_{i=1}^{N} \Omega_i$, where N is finite).

2) For any two elements, Ω_1 and Ω_2, they must either have a common vertex or edge, or $\Omega_1 \cap \Omega_2 = \varnothing$.

3) The sets $\{\Omega_i, i = 1,..N\}$ are a partitioning of the total domain Ω.

The interpolation function may suffer some specific criteria, which called inf-sup conditions, which is also known as LBB (Ladyzhenskaya-Babuska-Brezzi) condition. In contrast to the scalar transport equation, the choice of interpolations for Navier-Stokes equations is far from simple. For this reason, Gresho [55] quoted:

> "we emphasize that most of this deep and trouble and muddy water came to be because of the single simplification (!) of the mass conservation equation; i.e., the fluid will be treated as, or assumed to be, incompressible. We also note this alleged simplification has also taken its toll in the finite difference world;... many in this world are also quite confused even today."

It is obvious that viscous flow equations are obtained in the absence of elastic stress terms in the momentum equation. Therefore, these equations should satisfy the inf-sup conditions for viscous flow equations. Moreover, coupling between velocity-stress-pressure, may impose extra constraints for inf-sup conditions. For more details refer to [10]. Here, piecewise linear interpolation is applied for pressure and quadratic interpolation for velocity and stresses (see Figure 3.2).

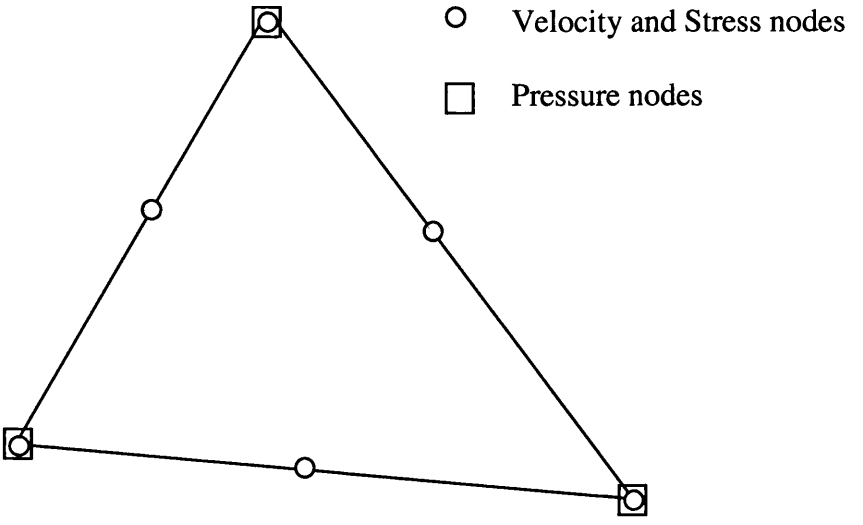

Figure 3.2: Triangular element, quadratic for velocity and stress and linear for pressure

3.7 Shape functions and integration

For triangular element shapes, one may appeal to canonical coordinates to generalize element reference, through area coordinates (also known as natural or barycenteric coordinates) denoted by ξ_i (i=1,...,3). This coordinate system permits exact evaluation of integrals arising from finite element discretisation. As in Figure 3.2, each ξ_i coordinate varies linearly, taking a value zero on one of the sides and varying to a value of unity at the opposite vertex.

Thus, the shape functions for a linear triangular element can be defined as

$$\psi_i = \xi_i, \qquad i=1,2,3, \tag{3.38}$$

with the following consistency relation

$$\sum_{i=1}^{3} \xi_i = 1. \tag{3.39}$$

For a quadratic triangular element (as shown in Figure 3.2 for velocity and stress), the shape functions adopt the form,

$$\begin{aligned} &\phi_1 = \xi_1(2\xi_1 - 1), \quad \phi_2 = \xi_2(2\xi_2 - 1), \quad \phi_3 = \xi_3(2\xi_3 - 1), \\ &\phi_4 = 4\xi_2\xi_3, \quad \phi_5 = 4\xi_1\xi_3, \quad \phi_6 = 4\xi_1\xi_2 \end{aligned} \tag{3.40}$$

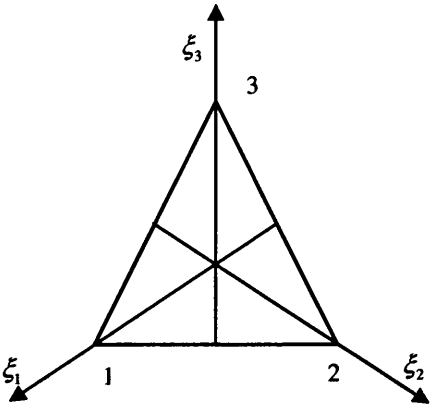

Figure 3.3: Barycentric coordinate systems

A useful feature of the barycentric coordinate system is that exact integration formula apply. These may be generalised for n-dimensional simplex regions, viz

$$\int \xi_i^{m_i} \ldots \xi_{n+1}^{m_{n+1}} d\Omega = n! \frac{\prod_i^{n+1} m_i!}{\left(n + \sum_i^{n+1} m_i \right)!} |\Omega|, \tag{3.41}$$

where the m_i are non-negative integers and $|\Omega|$ denotes the volume of the n-simplex regional element.

Since higher-order interpolation functions, for example quadratic, cubic, etc, may be defined hierarchically upon linear-forms, all orders of function may be accommodated in this fashion. Nevertheless, matrix integrals may be evaluated numerically using quadrature rules, appealing to the inverse coordinate-transformation Jacobian matrix (see below). This is particularly relevant for non-linear integrals, that defy characterisation through polynomial reference to base interpolation functions. Solving two-dimensional problems generates double spatial integrals; equivalently, triple for three-dimensional forms. Mapping a typical 2D-element region onto the canonical unit square, Gauss-Legendre quadrature rules are appropriate of the form:

$$\int_{-1}^{+1}\int_{-1}^{+1} f(x,y)d\Omega = \sum_{i=1}^{N_q}\sum_{j=1}^{N_q} w_i w_j f(x_i, y_i), \tag{3.42}$$

where N_q implies the number of quadrature points to the rule, $\{w_i\}_{i=1}^{N_q}$, the selected set of weights over the quadrature points. For evaluating element matrices integrals, Eq.(3.42), is employed in the local coordinate system as the following form:

$$\int_{\Omega} f(x,y)dxdy = \int_{-1}^{+1}\int_{-1}^{+1} f(\xi,\eta)\det(J)d\xi d\eta \quad , \tag{3.43}$$

where, *det(J)* is the determinant of the coordinate transformation.

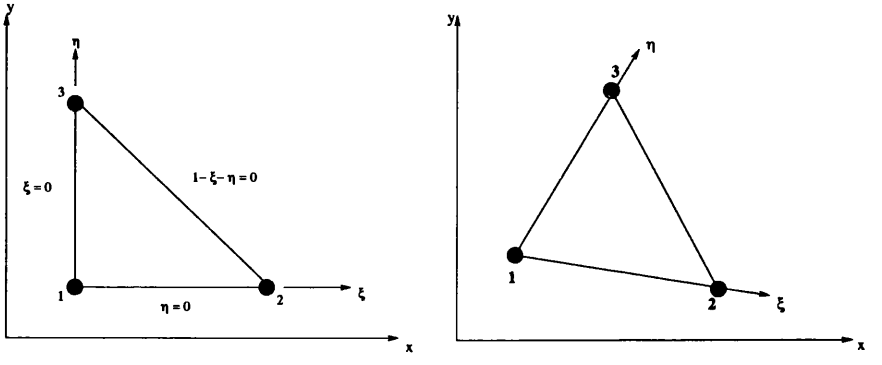

Figure 3.4: (a) Local triangle and (b) global triangle

3.8 Numerical method

For an incompressible viscoelastic fluid, the momentum and continuity equations compose an elliptic saddle point problem for the velocity and pressure fields, while the constitutive equation is a set of first-order hyperbolic equations for the stress tensor. For the elliptic problem the Galerkin discretisation is an optimal choice, in contrast to hyperbolic problems. It is well known that the difficulty in the viscoelastic flow computation mainly comes from the hyperbolic nature of the constitutive equations. Actually, with increasing value of the Weissenberg number, the elastic contribution of the stress component may dramatically increase (in comparison with the viscous part). Hence the importance of convection term $u \cdot \nabla \tau$ grows and Galerkin discretisation is not optimal for this term. Therefore, inaccuracy in evaluating this term may cause inconsistency and deteriorate dramatically the stability and accuracy of the methods. To preclude this situation, mixed finite element methods have found popularity in the evolution of numerical methods for highly elastic flows. This involves Galerkin

discretisation of the equations of motion and appropriate special discretisation suited for hyperbolic type equations. There are two main principles associated with these methods, *stress splitting* and *recovery of velocity gradients* [98]. In recent years, several mixed finite element methods have been developed for the solution of these problems; these include the mixed method of Marchal and Crochet [95], the explicitly elliptic momentum equation (EEME) method of King *et al.* [85], and the elastic-viscous split-stress (EVSS) method of Rajagopalan *et al.* [118]. Several variants of these methods have been published. Each method is based on a different formulation of the original equations set, and on different finite element approximations and weighted residual techniques. A review on these methods may be found in [10].

The selection of the approximation spaces for the field variables hinges on the issue of compatibility conditions between the spaces for velocity and pressure and velocity gradients and stress. Marchal and Crochet [95] emphasized the need for the approximations to satisfy compatibility conditions that are known to exist in the Newtonian fluid limit, where fluid elasticity vanishes. They devised a special mixed element to satisfy this condition. A major question in finite element analysis of viscoelastic flows is whether other compatibility conditions are needed between the velocity and stress approximations because of the introduction of the constitutive equation for the elastic stress. The analysis of the mixed method of Marchal and Crochet [95] by Fortin and Pierre [48] for Newtonian flow, and a similar analysis by Yang and Atluri [162] showed that such conditions are need when the stress is defined by an algebraic equation in terms of the velocity gradients. Constitutive equations in the steady-state reduce to algebraic in near solid boundaries with no-slip conditions for velocity. Qualitatively, the approximations for the stress and the velocity gradients need to be in the same approximating spaces to ensure compatibility of these representations, because the algebraic equation provides no mechanism to smooth the stress approximation [135]. However, when velocity gradients are directly evaluated via differentiation of the velocity over each element, the order of velocity gradients will be one order lower than the velocity field. Therefore, to rectify this position for equal order velocity and stress approximation (the case in this study) it is necessary to recover the order of velocity gradients. For more information about inf-sup conditions for mixed methods, see also [10].

Mixed methods have two main features. First, they use recovery of velocity gradients (or rate of deformation) to improve both inf-sup condition and accuracy for constitutive equations. Second, via operator splitting, they add some artificial numerical ellipticity to the constitutive equations, which are first-order hyperbolic equations without any dissipation term. Within the finite element context, Matallah [98] analysed both aspects of stress-splitting and recovery independently, via a semi-implicit time-stepping fractional-staged finite element method. The framework was a Taylor-Galerkin/pressure-correction procedure, with a choice of Petrov-Galerkin weighting (SUPG) for the constitutive equations. Matallah concluded that, this scheme with recovery is more accurate and stable than without recovery or EVSS alternatives. Here, the same framework is considered as in [98] and extended towards compressible flows.

3.8.1 Recovery scheme

Velocity and velocity gradients appear in the constitutive equations for elastic stress. Consequently, poor quality of these terms may pollute inf-sup condition and accuracy in finite element discretisation, and hence disturb consistency in higher Weissenberg values. Note, near solid boundaries, the velocity is low, whilst, velocity gradients and elastic stress can be large. Moreover, stabilization techniques like SUPG, due to vanishing velocity, cannot affect this region. Therefore, to capture accurate features, it is necessary to evaluate velocity gradients precisely.

Recovery formulation technique is an embellishment upon the conventional scheme, necessitating a technique to recover velocity gradients to furnish the coefficient of the constitutive equation at whatever time stage is necessary. This implies recovering gradient fields prior to a stress equation solution stage. There are a number of techniques that can be employed to provide an accurate discrete representation of these fields from the underlying finite element solution ($u^h \subset H^1(\Omega)$), that itself facilitates piece-wise discontinuous gradients at the element level. This generates velocity gradient approximations that lie in finite dimensional spaces compatible with the choices selected for the primary variables of the finite element solution, namely velocity, pressure and stress. Two techniques are commonly employed, local and global methods, see for example Hawken *et al.* [63], Gresho *et al.* [54]. In Hawken *et al.* [63], the two such methods were compared, a direct local form and a Galerkin global weighted-residual technique. The direct method is based on averaging of the nodal finite element

gradient contributions from the associated triangular elements and takes advantage of the inherent superconvergent properties [164] of the meshes and elements employed. Averaging of gradient values at a mid-side node over the pair of elements in which it lies provides superconvergent values (see for example Hawken *et al.* [63]). Quadratic interpolation on the six recovered nodal quantities per triangle then provides the desired continuous velocity gradient representation. The global approach alternatively fits an appropriate set of nodal gradient values to complete the system. This satisfied an associated weighted residual formulation based on $\left(2D-\left(\nabla u+\nabla u^{T}\right)=0\right)$, with a quadratic interpolation assumed and source function derived from the finite element solution. Localised approaches have the advantage of bias towards the solution properties in the close vicinity of the sample points in question. So that typically in an iterated formulation, intermediate solution fields that are distant from the converged solution in parts of the spatial domain, do not adversely distort the state of recovered gradients elsewhere in the flow. Such an argument may well not apply to a global approach. The local method, being the more robust, is our preferred choice in the present circumstance, where there is coupling within the equation system and dependency on solution evolution [98].

3.8.2 Streamline upwinding

Over the years, basic methods have exhibited shortcomings in particular areas of applications. Particularly, regular (Galerkin) finite elements were unable to provide stable, accurate results for some fluid mechanics problems. This is the case for applications to advection-diffusion types of problems where, mixed results have been produced. Solution often exhibited "spurious" node-to-node oscillations, particularly when convection dominates the flow. Indeed, the source of the problem was that the convection operators are non-symmetric, causing the loss of accurate approximation property. This problem has been observed for space centred (central difference) within the finite difference and finite volume contexts. In finite difference treatments, it was discovered that non-oscillatory solutions can be obtain by employing "upwind" differencing on the convection terms. In essence, upwinding approaches, through the consideration of flow direction, render a non-symmetrical approximation for the convective terms. This rectifies the scheme and precludes oscillation in the solution of convection-dominated flows. Nevertheless, upwinding disturbs second-order accuracy

of space-centred discretisations. However, it has been emphasized that an "optimal" combination of central differencing and upwinding, can improve accuracy. Consequently, some higher order schemes have been proposed to enhance the accuracy of the approximation [90].

The upwinding concept within the finite element context was employed for one dimensional advection-diffusion equation by Christie *et al.* [29]. This was subsequently generalised to the two-dimensional case by Henrich *et al.* [64], and by Brooke and Hughes [19] to convection-dominated flows. The Petrov-Galerkin finite elements formulation describes a wide class of approximations in which mixed function spaces are employed to construct the approximate trial solutions. This feature provides considerable freedom in choosing a pair of spaces in order to improve the computational efficiency of the standard Bubnov-Galerkin method, whilst preserving the order of convergence. This approach has been implemented on the streamline upwinding (SU) method, as a modification of the weighting functions for the convection term. However, implementation of SU for convective terms only disturbs consistency of the method. In contrast, application of this modified weighting function to all terms in the equation gives the desired streamline upwind effect and defines a consistent Petrov-Galerkin formulation. This techniques was first introduced by Brooks and Hughes, with the name of "streamline upwind/Petrov-Galerkin" (SUPG).

For viscoelastic flows, as mentioned earlier, due to the non-symmetric nature of the convective term in the stress equation and large values of stress components (in highly elastic flows), one must consider not only upwinding to overcome instabilities on this severe condition, but also accuracy, which has crucial effect on overall scheme performance.

An expression for SUPG parameters was derived by Shakib [130]. This was implemented by Baaijens [11] and Carew [23] in the viscoelastic context with some additional constraints. The weighting function ϕ_i^p used for SUPG is defined as:

$$\phi_i^p = \phi_i + \alpha^h u \cdot \nabla \phi_i \tag{3.44}$$

where ϕ_i represents the standard Galerkin shape function, and u is the velocity vector. The arbitrary elementwise parameter α^h depends on the size of the mesh and the direction of the velocity.

As in [23,130], the parameter α^h is defined by

$$\alpha^h = \begin{cases} \Delta t^2 \sqrt{g} & if \quad 0 \le g < 1 \\ \dfrac{1}{\sqrt{g}} & if \quad g \ge 1 \end{cases} \tag{3.45}$$

where g is given by

$$g = \frac{\partial \xi_i}{\partial x_j} \frac{\partial \xi_i}{\partial x_k} v_j v_k \tag{3.46}$$

Here, ξ_i represents the local coordinates for triangular elements, and v_j, v_k are the velocity components.

The SUPG method has provided a qualitative jump in the ability of finite element methods to model a wider class of problems. Despite the success of SUPG it has proved to be no panacea; there is still room for improvement. It has been emphasized that, in steep boundary layers or near singularities, the SUPG method may produce oscillatory stress fields [10,95,124]. To circumvent this, Marchal and Crochet [95] proposed a streamline-upwind formulation (SU), where the upwind term is only applied to the convective term of constitutive equation. This formulation may elevate numerical convergence up to high values of Weissenberg number. However, this practice is inconsistent and only first-order accurate with respect to extra stress, as demonstrated by Crochet and Legat [32].

3.9 Finite element discretisation

The momentum and mass conservations equations are discretised via the Galerkin *fe* method, whilst stress equations are approximated via a SUPG method. Galerkin finite element (GFEM) spatial discretisation is adopted, based on triangular elements in two dimensions. This employs a piecewise continuous quadratic interpolation $\phi(x)$ for velocity and stress, and linear interpolation $\psi(x)$ for pressure, of the form:

$$u(x,t) = U_j(t)\,\phi_j(x), \qquad \tau(x,t) = T_j(t)\,\phi_j(x), \quad \text{j=1,6} \tag{3.47}$$

$$p(x,t) = P_k(t)\,\psi_k(x), \quad \text{k=1,3.} \tag{3.48}$$

Time-dependent velocity, stress and pressure nodal-vectors are represented as *U(t)*, *T(t)* and *P(t)*, respectively. For density interpolation, two types of interpolation are considered: piecewise-constant over an element, with recovery for the gradient of density, and piecewise-linear interpolation (as for the pressure field).

The discretised equation for compressible viscoelastic flow may be expressed in fully-discrete matrix form, via TGPC-Stages1-3, viz.

Stage-1a:

$$\left[\mathrm{Re}\frac{2M_\rho}{\Delta t}+\frac{\mu_s}{2}S_U\right]\left(U^{n+\frac{1}{2}}-U^n\right)=\left\{-\left[\mu_s S_U+\mathrm{Re}N_\rho(U)\right]U-BT\right\}^n+L^TP^n, \quad (3.49)$$

$$We\frac{2M}{\Delta t}\left(T^{n+\frac{1}{2}}-T^n\right)=\left[2\mu_e M\left(L+L^T\right)-\left\{M+WeN(U)\right\}T+We\left\{N_e(T)L+\left(N_e(T)L\right)^T\right\}\right]^n \quad (3.50)$$

Stage-1b:

$$\left[\mathrm{Re}\frac{M_\rho}{\Delta t}+\frac{\mu_s}{2}S_U\right]\left(U^*-U^n\right)=\left\{-\left[\mu_s S_U+\mathrm{Re}\,N_\rho(U)\right]U-BT\right\}^{n+\frac{1}{2}}+L^TP^n, \quad (3.51)$$

$$We\frac{M}{\Delta t}\left(T^{n+1}-T^n\right)=\left[2\mu_e M\left(L+L^T\right)-\left\{M+We\,N(U)\right\}T+We\left\{N_e(T)L+\left(N_e(T)L\right)^T\right\}\right]^{n+\frac{1}{2}} \quad (3.52)$$

Stage-2:

$$\left[\frac{M_C}{\Delta t}+\theta\Delta tK\right]\left(P^{n+1}-P^n\right)=-L^\rho U^* \quad (3.53)$$

Stage-3:

$$\mathrm{Re}\,\frac{M_\rho}{\Delta t}\left(U^{n+1}-U^*\right)=\theta\,L^T\left(P^{n+1}-P^n\right) \quad (3.54)$$

where

$$\left(M_\rho\right)_{ij}=\int_\Omega \rho\,\phi_i\phi_j\,d\Omega, \quad (3.55)$$

$$(M)_{ij} = \int_{\Omega} \phi_i \phi_j \, d\Omega, \tag{3.56}$$

$$(\mathrm{M}_{C})_{ij} = \int_{\Omega} \frac{\psi_i \psi_j}{c^2_{(x,t)}} d\Omega \tag{3.57}$$

$$(N_{\rho})_{ij} = \int_{\Omega} \rho \phi_i (U \cdot \nabla \phi_j) \, d\Omega, \tag{3.58}$$

$$(N)_{ij} = \int_{\Omega} \phi_i (U \cdot \nabla \phi_j) \, d\Omega, \tag{3.59}$$

$$(N_e)_{ij} = \int_{\Omega} \phi_i (T \cdot \nabla \phi_j) \, d\Omega \ (22), \tag{3.60}$$

$$(B)_{ij} = \int_{\Omega} \phi_i \nabla \phi_j \, d\Omega, \tag{3.61}$$

$$(K)_{ij} = \int_{\Omega} \nabla \psi_i \cdot \nabla \psi_j \, d\Omega \tag{3.62}$$

$$(L_k)_{ij} = \int_{\Omega} \psi_i \left(\nabla \cdot \phi_j\right)_k \, d\Omega, \tag{3.63}$$

$$(L_k^{\rho})_{ij} = \int_{\Omega} \psi_i \left\{ \psi_l \rho_l \frac{\partial \phi_j}{\partial x_k} + \boxed{\frac{\partial \psi_l}{\partial x_k} \rho_l \phi_j} \right\} d\Omega \tag{3.64}$$

$$(S_U)_{ij} = (S_{lm})_{ij}, \ l, m = 1,2 \tag{3.65}$$

$$(S_{11})_{ij} = \int_{\Omega} \left(2 \frac{\partial \phi_i}{\partial x} \frac{\partial \phi_j}{\partial x} + \frac{\partial \phi_i}{\partial y} \frac{\partial \phi_j}{\partial y} - \boxed{\frac{2}{3} \frac{\partial \phi_i}{\partial x} \frac{\partial \phi_j}{\partial x}} \right) d\Omega \tag{3.66}$$

$$(S_{12})_{ij} = \int_{\Omega} \frac{\partial \phi_i}{\partial y} \frac{\partial \phi_j}{\partial x} \, d\Omega, \tag{3.67}$$

$$(S_{22})_{ij} = \int_{\Omega} \left(\frac{\partial \phi_i}{\partial x} \frac{\partial \phi_j}{\partial x} + 2 \frac{\partial \phi_i}{\partial y} \frac{\partial \phi_j}{\partial y} - \boxed{\frac{2}{3} \frac{\partial \phi_i}{\partial y} \frac{\partial \phi_j}{\partial y}} \right) d\Omega \tag{3.68}$$

These matrices, with their corresponding integrals, may be evaluated analytically or via quadrature on each triangular control element (say with a seven points Gauss quadrature rule).

3.9.1 Density interpolations

Here, the desire is to elucidate the effects of the choice of interpolation employed upon density. For the compressible algorithm, the density term appears inside some element integrals and this elevates the order of the integrals for density. Hence, this increases the computational overhead. Moreover, in the r-z coordinate system due to the r-term in the element integrals, the order of element integrals is one order higher than for the planar case. Therefore, for terms, (like the convection term) one may need to employ higher order of numerical integrations. Here, we considered a piecewise-constant form over an element, and a piecewise-linear form. These are zero and first-order, respectively. The piecewise-constant version looks more attractive, as element integrals are obtained at minimum effort. This is due to the fact, that the density is constant over the integration domain and can be carried out the integration, analytically. This is an important issue in extending incompressible pressure-correction algorithms towards compressible flows. These element integrals for the compressible case can be obtained by scaling incompressible corresponding integrals with density, without extra computational or re-coding effort. Experience has shown that results for the compressible case in implementation of the piecewise-constant form for density are almost identical to those for the incompressible case. By investigating the accuracy of element matrices for both variants of density interpolations, this may be attributed to expression (3.64) and the (L_k^ρ) matrix. When a compressible approach is employed based on a piecewise-constant density interpolation, the element interior contribution of the first term forming the density-gradient representation will vanish. Whilst, on element boundaries and due to discontinuity, the contribution of density-gradients will remain undetermined. Missing this term will cause some loss of information through the continuity equation, due to the variation of density. To expose this issue, one may consider the right hand side of Stage-2, and hence, the (L_k^ρ) matrix which may be expressed viz.

$$\nabla\cdot\left(\rho u^*\right)=u^*\cdot\nabla\rho+\rho\nabla\cdot u^* \tag{3.69}$$

$$\left(L_k^\rho\right)_{ij}U_j=\int_{\Omega_e}\psi_i\nabla\cdot\left(\rho U^*\right)_j d\Omega=\int_{\Omega_e}\psi_i\left\{\nabla\rho\phi_j+\rho\frac{\partial\phi_j}{\partial x_k}\right\}U_j d\Omega \tag{3.70}$$

When density is represented as piecewise-constant, the density on interior of elements is constant. Indeed, this assumption corresponds to considering flow as incompressible over of each element, yet density may vary from one element to another. Consider a Poiseuille 2-D channel flow where, $u = u(y)$, $v=0$, $p=p(x)$. For LMN flows, little deviation in flow pattern from the incompressible case is expected. In addition, if density is considered as only a function of pressure, then $\rho = \rho(x)$. In such circumstances, the term $\nabla \cdot u^*$ in Eq.(3.69) will be small. However, density gradients for piecewise-constant interpolation will vanish. Consequently, effect of density variation across the domain will not appear in the discrete form of the equations.

To remedy this position, during matrix evaluation at Stage-2, a vertex corner nodal density value is assigned, so a representation that equivalent to linear interpolation may be recovered, leading to piecewise-constant gradients. An element averaging (recovery) technique [98] is adequate for this purpose (also see next chapter for more details).

From a computational point of view, matrix evaluation is three-times quicker with ρ-constant than linear, with most work being required for the convection matrix of expression (3.58). Note also, that the solution of each fractional-staged equation is attained via an iterative preconditioned Jacobi solver (see below). That is, with the exception of the temporal pressure-difference equation, which is solved through a direct Choleski procedure [12]. The major difference between the forms of the incompressible and compressible algorithm lies in Stage-2. For compressible instances, density becomes a distributed variable. The incompressible variant emerges, when density is a constant throughout the solution domain and the speed of sound approaches infinity.

3.10 Solution of the algebraic system

The resulting system from a finite discretisation can be linear or nonlinear. Solution of this algebraic system of equations can be expensive both in memory space and computation time. The eigenvalues of the algebraic system can impose some criteria on the selection of an appropriate solver. For the linear system, both direct and iterative method can be employed. However, for the nonlinear system, only iterative solvers are applicable.

Implementation of direct schemes does not imposed any additional criteria upon the system. In contrast, iterative schemes depend on the system condition number, which is

the ratio of the largest to smallest eigenvalue, and this can reduce computation overheads significantly. However, convergence and rate of convergence can suffer from lack of diagonally dominant condition and the condition number of the system, respectively. A general system of the following form emerges

$$Mx = b \ , \tag{3.71}$$

where, M, x and b represent the mass matrix, unknown solution vector over a time step [n,n+1], and the right hand side vector, respectively. For Stage-1 and 3, for velocity and stress, a Jacobi iterative method is employed. In contrast, in stage two for pressure, a direct method (Cholesky decomposition) is adopted. The Jacobi iterative method can be written viz.

$$M_d x^{k+1} = (M_d - wM)x^k + wb \, . \tag{3.72}$$

Here, M_d is a diagonal matrix of the mass matrix, x^k is the unknown vector at iteration k of the Jacobi iteration, and w represents an acceleration parameter, w>0. When w=1, the conventional Jacobi scheme emerges. In contrast, for w>1, the scheme is termed the extrapolated Jacobi iteration. Throughout this thesis, w=1 is selected. For other choices of w and background theory, refer to [35,62]. The diagonal matrix M_d is defined as follow

$$M_d = \left[m_d^{ij} \right] \tag{3.73}$$

$$m_{ij}^d = \begin{cases} 0 & if \quad i \neq j \\ \sum_{k=1}^{n} |m_{ik}| & if \quad i = j \end{cases} \ , \tag{3.74}$$

the diagonals are taken as the absolute row sum. This avoids the singular case and improves the convergence rate over the diagonal choice [53]. For the direct Cholesky decomposition scheme refer to [52].

3.11 Monitoring the solution

To monitor the solution process and in order to emphasize stability and convergence, relative increment norms L_2 and L_∞ are employed. These norms are defined viz.

$$E_r^T(X) = \frac{\left\| X^{n+1} - X^n \right\|_r}{1 + \left\| X^{n+1} \right\|_r} \leq Tol_t \, , \tag{3.75}$$

where, X^n represent the solution vector at time-step n. For r=2, the L_2 error norm, i.e., a root mean square measure of the relative differences between numerical solutions at successive time-steps, is recovered. $L_\infty(r=\infty)$ gives the maximum relative difference in the numerical solution between successive time-step cycles.

3.12 Stream function

Two-dimensional flows (both compressible and incompressible) can be conventionally characterised by introducing a mathematical artifice known as a stream function $\Psi(x,y,t)$. The stream function relates the concept of streamlines to the principle of mass conservation. For a two dimensional incompressible flow, the continuity equation may be expressed as :

$$\frac{\partial u}{\partial x}+\frac{\partial v}{\partial y}=0 \qquad \text{or } \nabla\cdot(V)=0 \ , \tag{3.76}$$

where, $V=(u,v)$ represents the velocity vector with u and v components in the (x,y) directions. This equation is identically satisfied of

$$u=\frac{\partial \Psi}{\partial y}, \qquad \text{and} \qquad v=-\frac{\partial \Psi}{\partial x}. \tag{3.77}$$

In the flow field, lines of constant Ψ and streamlines are identical and the flow rate between two streamlines is proportional to the numerical difference between the two stream functions corresponding to the two streamlines. In the axisymmetric frame of reference (r,z), the stream function is defined as

$$ru=\frac{\partial \Psi}{\partial r}, \qquad \text{and} \qquad rv=-\frac{\partial \Psi}{\partial z}, \tag{3.78}$$

where, u,v are velocity vector components in the (r,z) directions respectively. For a steady-state two-dimensional compressible flow, we have the analogous definitions,

$$u=\frac{\rho_o}{\rho}\frac{\partial \Psi}{\partial y}, \qquad \text{and} \qquad v=\frac{\rho_o}{\rho}\frac{\partial \Psi}{\partial x}, \tag{3.79}$$

where, ρ_o is a reference density, and ρ is the density.

Clearly, the flow problem reduces to finding the solution $\Psi(x,y,t)$ for any particular case. For both Cartesian and cylindrical axisymmetric coordinates, the stream function satisfies a Poisson equation,

$$\frac{\partial^2\Psi}{\partial^2 x}+\frac{\partial^2\Psi}{\partial^2 y}=\frac{\partial v}{\partial x}-\frac{\partial u}{\partial y}=f \qquad \text{for Cartesian reference,} \qquad (3.80)$$

$$\frac{\partial^2\Psi}{\partial r^2}+\frac{\partial^2\Psi}{\partial y^2}=\frac{\partial}{\partial r}(-rv)-\frac{\partial}{\partial z}(-ru)=f \qquad \text{for axisymmetric reference.} \qquad (3.81)$$

For the elliptic equation, at least one essential boundary condition on the stream function is required to specify the problem. A Galerkin weighted residual finite element method with quadratic shape function is employed to compute the stream function.

3.13 Appendix 3.A: A short note on pressure-correction schemes: *TGPC and CBS*

Most numerical methods for solving transient incompressible Navier-Stokes equations, in primitive variable form, apply fractional-step methods. These methods were originally proposed as semi-discrete temporal approximations to the Navier-Stokes equations. The semi-discrete approach discretises equations in time, leaving spatial derivatives as continuous operators. Nevertheless, it has been realised that through discrete representation, some properties of the continuous form may be lost. One prominent advance in the study of pressure-correction schemes has been to realise that these methods should be analysed from a fully discrete point of view [55,112].

Mathematical analysis of the Stokes problem demonstrates that the approximation spaces for velocity and pressure must, *a priori*, satisfy a compatibility condition, known as the inf-sup or LBB condition. The numerical consequence of the lack of satisfaction of this condition often appears as severe node-to-node spatial oscillation across the solution field, particularly arising within the pressure component. The common way to avoid this situation is to employ different spatial approximations for velocity and pressure. To this end, usually the order of approximation for pressure has been considered one order lower than for velocity. Here, we have employed a P2P1 element (quadratic for velocity and linear for pressure) and we refer to [55] for more details of different elements type, employed in the computation of incompressible flows.

In recent years, the suggestion has emerged that the need for LBB conditions stems largely from two different orders of spatial differential operator arising on velocity and pressure, simultaneously. By removing the pressure term from the velocity prediction in the projection procedure, via the momentum equation, and redistributing the same onto the pressure update and velocity correction, one may circumvent the LBB conditions.

One such scheme (characteristic-based splitting scheme, CBS) was introduced by Zienkiewicz and co-workers [165,166], who successfully employed this algorithm for various flow problems. The motivation for developing this scheme has been to employ equal order interpolation for pressure and velocity, particularly in gas dynamical applications, where a huge number of linear elements (P1P1) have been used.

In commencing this study, the philosophy behind CBS was perceived as being attractive for devising numerical algorithm within the viscoelastic context. This was

mainly due to the claim of Zienkiewicz and co-workers [165,166] for unconditional stability overcoming the inf-sup conditions. Nevertheless, it has been noted by ourselves and others [57] that deviation from satisfying the LBB condition is a strong source of instability, particularly in the presence of discontinuity. In these circumstances, capturing sharp discontinuities accurately within the discrete equations, is difficult and violation of continuity provides a source of instability. Our prime interest in studying CBS is to seek robustness and to appreciate how the distribution of pressure and removal of LBB satisfaction from the velocity-pressure coupling may bring this about. This would be taken further in the viscoelastic context to satisfaction of extended inf-sup conditions. In addition, for viscoelastic flows, employing second-order pressure interpolation would appear attractive to elevate spatial accuracy. Though the authors advocated the CBS algorithm, as universal for accommodating various flow problems, Guermond and Quartapelle [57] have demonstrated that CBS-form pressure-redistributing strategies are only conditionally stable. The lack of LBB satisfaction restricts the time-step to a minimum threshold, and for smaller time-steps stability degrades, giving rise to spurious oscillations across the solution field.

3.13.1 Practical implementation

We have constructed the CBS algorithm within the skeleton of our original scheme (TGPC), that in full form realises quadratic P2P1 element interpolation. Here, we have compared and contrasted the two schemes, CBS and TGPC, in the sense of coding and implementation. To this end, we have considered a pure shear flow (inertialess) that does not require a stabilisation treatment to model convection. These schemes can be represented notationally in semi-discrete form, with variables of $(u, p, \tau)^n$ at time-level n, an auxiliary variable u^*, time-step Δt and adaptive parameters $0 \leq \theta_2 \leq 1$ (usually 1/2):

	CBS	*TGPC*
Stage-1:	$\Delta U^* = U^* - U^n = \Delta t[\nabla\cdot\tau]^n$	$\Delta U^* = U^* - U^n = \Delta t[\nabla\cdot\tau - \nabla p]^n$
Stage-2:	$\nabla^2(\theta_2\Delta P + P^n) = -\frac{1}{\Delta t}\nabla\cdot U^*$	$\nabla^2(\theta_2\Delta P) = -\frac{1}{\Delta t}\nabla\cdot U^*$
Stage-3:	$U^{n+1} = U^* - \Delta t\nabla(\theta_2\Delta P + P^n)$	$U^{n+1} = U^* - \Delta t\nabla(\theta_2\Delta P)$

Here, all terms are identical to those of chapter three, where U may be taken to represent ρu. The variational weighted equivalent to the above, on domain Ω with boundary Γ, is derived through weighted functions for velocity (ϕ) and pressure (φ), viz.

Stage-1

$$\text{CBS:}\quad \Delta t^{-1}\int_\Omega \phi(U^* - U^n)d\Omega = -\int_\Omega \nabla\phi\cdot\tau^n d\Omega + \oint_\Gamma \phi\tau^n\cdot n d\Gamma$$

$$\text{TGPC:}\quad \Delta t^{-1}\int_\Omega \phi(U^* - U^n)d\Omega = -\int_\Omega \nabla\phi\cdot(\tau^n + p^n I)d\Omega + \oint_\Gamma \phi(\tau^n + p^n I)\cdot n d\Gamma$$

Stage-2

$$\text{CBS:}\quad \int_\Omega \nabla\varphi\nabla(\theta_2\Delta P + P^n)d\Omega = \frac{1}{\Delta t}\int_\Omega \varphi\nabla\cdot U^* d\Omega + \oint_\Gamma \varphi\nabla(\theta_2\Delta P + P^n)\cdot n d\Gamma$$

$$\text{TGPC:}\quad \int_\Omega \nabla\varphi\nabla(\theta_2\Delta P)d\Omega = \frac{1}{\Delta t}\int_{\Omega\Gamma} \varphi\nabla\cdot U^* d\Omega + \oint_\Gamma \varphi\nabla(\theta_2\Delta P)\cdot n d\Gamma$$

Stage-3

$$\text{CBS:}\quad \Delta t^{-1}\int_\Omega \phi(U^{n+1} - U^*)d\Omega = -\int_\Omega \nabla\phi(\theta_2\Delta P + P^n)d\Omega + \oint_\Gamma \phi(\theta_2\Delta P + P^n)\cdot n d\Gamma$$

$$\text{TGPC:}\quad \Delta t^{-1}\int_\Omega \phi(U^{n+1} - U^*)d\Omega = -\int_\Omega \nabla\phi(\theta_2\Delta P)d\Omega + \oint_\Gamma \phi(\theta_2\Delta P)\cdot n d\Gamma$$

3.13.2 Test problems

The selected test problems are steady-simple shear-flows, with (*a*): Couette flow, of linear velocity and vanishing pressure profiles; and (*b*): Poiseuille flow, of quadratic velocity and linear pressure profiles. Both algorithms (TGPC and CBS) are capable of deriving accurate steady-state solutions commencing from a quiescent state for both test problems. Here, we demonstrate some aspects relating to corresponding spatial discretisation and velocity profiles. We consider analytical steady-state initial conditions, and over a single time-step, we interrogate intermediate stage solutions for both TGPC and CBS algorithms. First, we consider Couette flow, where due to

vanishing pressure, both algorithms reflect identical rhs through the stages, vanishing across the domain. To observe the different nature of these algorithms in discrete form, we consider Poiseuille flow (case *b*), where we have the following analytical solution expressed in rectangular spatial coordinates (x, y):

$$u = 4y(1-y), \quad v = 0.0 \qquad p = p_0 - 8x,$$

where, (u,v) represents the velocity vector; p and p_0 are pressure and pressure reference, respectively. For this test problem, the y-component of momentum vanishes and the x-momentum component, yields

$$(\nabla p)_x = -8\ , \qquad (\nabla \cdot \tau)_x = -8,$$

where subscript x denotes the x-direction component.

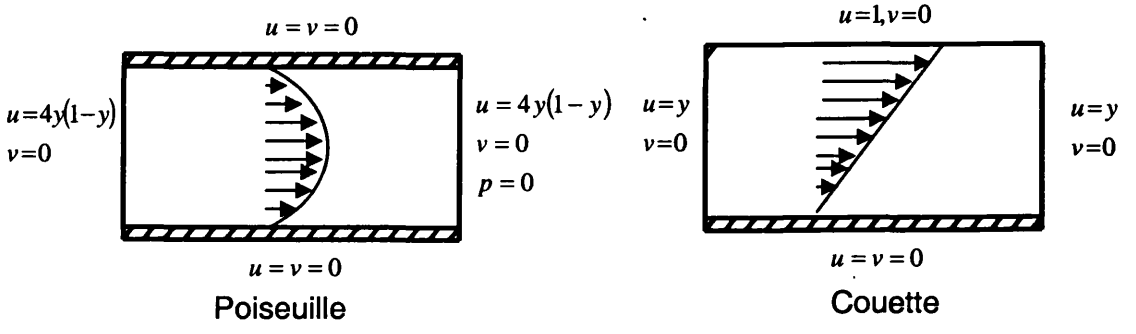

Figure 3.A.1: Steady-simple shear-flows: Poiseuille flow, quadratic velocity and linear pressure profiles (left); Couette flow, linear velocity and vanishing pressure (right)

In Figure 1, we observe rhs of stage-1 field plots for both schemes, with and without boundary integral terms. These plots demonstrate the necessity of boundary integral inclusion for consistent equation evaluation. For CBS, given the nature of U^* and the equation-stage 1 type, it becomes essential to employ boundary integrals. Alternatively, TGPC with or without inclusion of boundary integral terms, is able to derive accurate steady-state solutions. This is due to, *first*, the incremental form of pressure updates within the pressure terms at Stage-2 and Stage-3, which vanish at steady-state. Unfortunately within CBS, absolute pressure references arises, rather than to pressure increments. The effect of inaccurate representation for boundary integrals, with possibly large values of pressure, may stimulate instability, and hence inaccuracy within the solution. *Second*, Stage 1 solution, U^* for TGPC is close to the incompressible velocity field (to a first order in time). So, on stationary boundaries, with strong conditions, one

may impose true end-of-step velocity boundary conditions, hence avoiding the calculation of U^* at the boundary. However, for CBS, U^* does not possess physical meaning and must be calculated on boundaries. Hence, this necessitates the inclusion of boundary integrals.

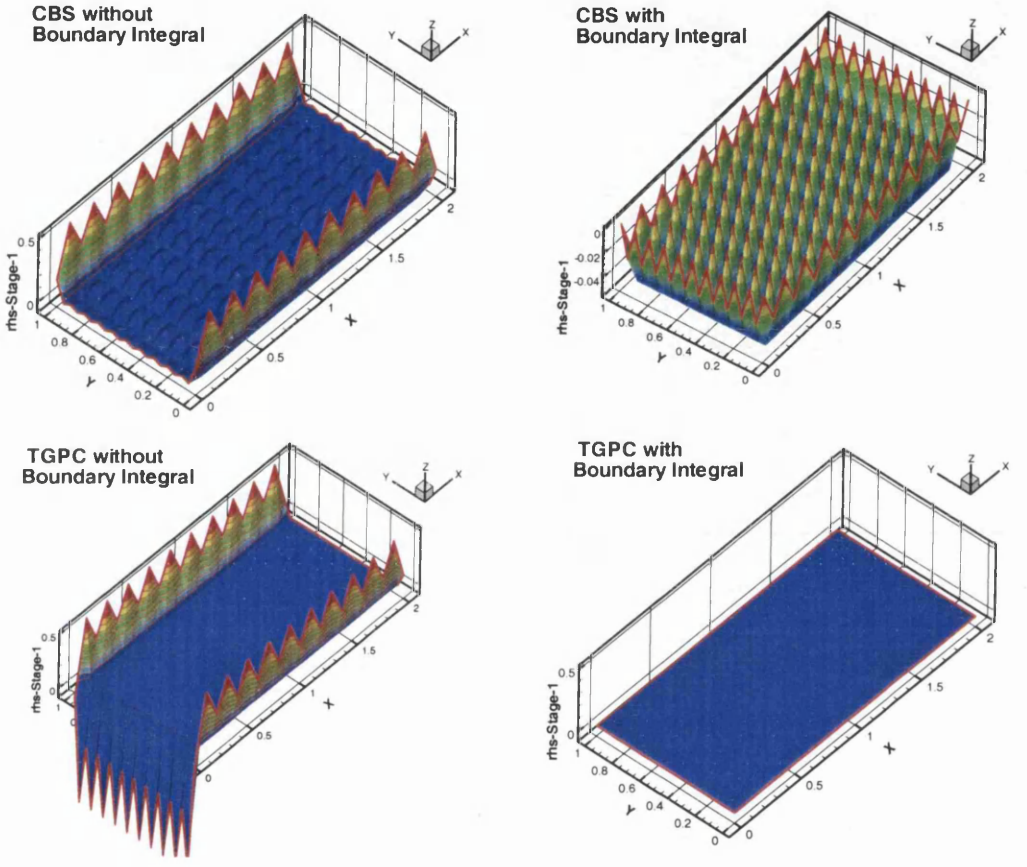

Figure 3.A.2: Field plots of rhs Stage-1 for CBS and TGPC, with/without boundary integral inclusion

The rhs term for TGPC is almost zero, when commencing from the analytical solution as initial conditions. Alternativ ely, for CBS, we observe a bizarre pattern. From the same initial conditions, CBS mimics TGPC at vertex nodes, whilst the mid-side nodes reflect the absence of the pressure term. Here, the rhs-terms over the TGPC stages are much smaller than within the CBS-algorithm, and vanish at steady-state. However, under the CBS-formulation, these terms are often large. The numerical consequence of this fact is observed in solving the corresponding algebraic equations, where for TGPC with a Jacobi-iterative solver, three mass-matrix iterations are found to be sufficient. In contrast, with CBS and under equivalent settings, one must set the

iteration number to $O(10^2)$. The reason for this is clear. With CBS at Stage-1, one forces the removal of any pressure influence upon stage-1 solution (augmented variables). This leaves Stage-3, to enforce the effect of pressure upon the solution. Correspondingly, TGPC achieves the same goal in a superior manner. In Figure 2, we present the effect of the mass-matrix iteration within the solution phase of Stage-1. The analytical solution at this stage adopts the form:

$$\frac{\Delta U^*}{\Delta t} = \frac{U^* - U^n}{\Delta t} = [\nabla \cdot \tau]_x^n = -8.0$$

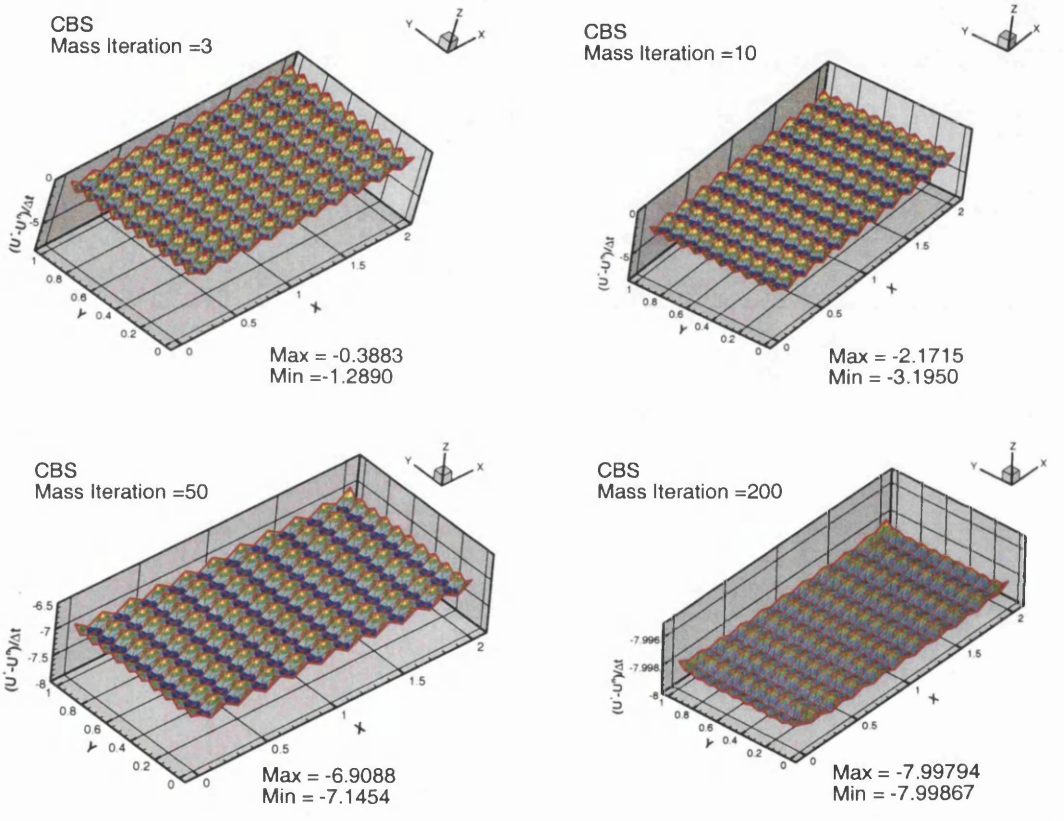

Figure 3: Field plots for $(U^* - U^n)/\Delta t$ solutions (Stage 1), with different mass-matrix iteration numbers

Figure 2 presents the CBS discrete solution ($\Delta U^*/\Delta t$) after Stage-1, with respect to mass-matrix iteration numbers of 3 (top left), 10 (top right), 50 (bottom left) and 200 (bottom right). Such field plots demonstrate that by increasing the mass-matrix iteration

number, the solution eventually converges toward the true solution. In contrast, with the TGPC scheme, 3 mass-matrix iterations delivers accurate results, practically directly.

3.13.3 Concluding remarks

This short study on comparison of pressure-correction schemes illustrates the true incremental character and superior numerical properties of the TGPC-formulation in comparison to its CBS-counterpart. This has become apparent through comparison of discrete form solutions, considering velocity/pressure solution pairings at both linear/linear and quadratic/linear levels. The CBS scheme encountered large numerical discretisation error on quadratic interpolation elements (P2), when employed to represent a flow with a quadratic velocity structure. Nonetheless, in the literature, the CBS scheme has been employed successfully on several flow problems based on linear element representation. In addition, inclusion and accurate representation of boundary integrals is essential for the CBS scheme. In contrast, the TGPC formulation is found to be more flexible and can better accommodate solutions of both linear and quadratic form. Moreover, the inclusion of the pressure term within the velocity prediction structure, enables one to accurately employ Lax-Wendroff type splitting of nonlinear terms, which is particularly useful in the viscoelastic context. On this basis, one seeks to harness the advantageous properties of the TGPC scheme within the extended viscoelastic setting.

CHAPTER 4

Compressible and Incompressible Viscous Flows (*fe*)†

In this chapter under algorithmic development, there is restriction to *Newtonian viscous polymeric liquid flows under isothermal conditions* and where Reynolds and Mach numbers are generally low (viscoelastic alternatives to follow). Within the considered fractional-staged incompressible pressure-correction algorithm, the main modifications in order to deal with weakly-compressible flows are related primarily to the finite element representation of density. Two types of interpolation are adopted: first, a *piecewise-constant* form (incompressible per element), with a nodal recovery for density gradients (second-stage); second, a *linear interpolation* form, similar to that employed for the pressure field. These modifications are confirmed not to degrade second-order accuracy of the original pressure-correction scheme. It is illustrated how the algorithm can tackle weakly-compressible highly-viscous flow at low Mach number, as well as incompressible flows (hence, zero Mach number configurations).

4.1 Numerical examples

To calibrate the algorithm, a number of numerical examples are taken into consideration, regarded as benchmarks in the viscous/viscoelastic regime of interest. Here time-marching procedures are employed to extract steady-state solutions. The first example is a driven cavity problem, considered here to assess the accuracy of the

† Material of this chapter has been shaped in a paper "Computation of Weakly-Compressible Highly-Viscous Liquid Flows" by M. F. Webster, I. J. Keshtiban and F. Belblidia, *Engineering Computations Journal* **21** (2004) 777-804.

algorithms in a complex re-circulating flow. A second example is a contraction flow problem, employed in both planar and axisymmetric configuration. Here, consistency is investigated for compressible algorithms in dealing with various Mach number flows via adjusting Tait equation of state parameters. For density interpolation, both piecewise-constant and linear forms are considered. In all instances, the fluid is assumed to be Newtonian with the laminar flow. Convergence to a steady-state is monitored, via a relative temporal increment L_2 norm on the solution, taken to a tolerance of $O(10^{-8})$ (see [62]).

4.1.1 Cavity flow

Commonly, this problem is employed as a standard incompressible flow benchmark for evaluating stability and accuracy of numerical schemes [51,62,113]. The Flow is enclosed (closed streamlines) and specified within a unit square cavity, where the fluid is driven by the upper-plate (lid) at a given velocity. The problem is characterised by the Reynolds number (*Re*), with velocity-scale, *U*, the lid-velocity, and length-scale, *h*, the height of the cavity. Two cases, with different driving lid-velocity profiles, are considered: case (a) with a variable profile of type $U = 16x^2(1-x)^2$, leading to a continuous solution. This case is well-documented in Hawken *et al.* [62] and Peyret and Taylor [113] references. Case (b) is one of conventional constant profile form, widely reported in the literature, which possesses singularity in the solution at the cavity top-corners.

First, appeal is made to the incompressible form of the pressure-correction algorithm to provide a cross-reference, with flow settings of *Re*=100 and *Re*=400. In Figure 4.1, pressure and stream function profiles are plotted based on case (b) with a regular mesh of 40*40 square sub-divisions, each split into two triangular elements. The contour patterns reflect those shown in Zienkiewicz *et al.* [165], Ghia *et al.* [51], Peyret and Taylor [113] and Hawken *et al.* [62]. Pressure level contours illustrate, maxima (P_A) are at the downstream lid-corner and minima (P_B) at the upstream corner. The stream function contours display the recirculating nature of the flow, with distortion near the singular corners, and a secondary Moffatt-type vortex in the lower right-corner. Streamlines are twisted and distorted with increase of convection (*Re*) towards the downstream corner, and the primary vortex-centre drops within the cavity. Stream function values at the vortex-centre (S_+, primary cell) and (S_*, secondary cell) are also

indicated. The primary vortex intensity is 0.101 under Re=100, for which Ghia *et al.* [51] observed a value of 0.103 employing a fine mesh of 129x129 elements (likewise, Kim and Moin [84] on 65x65 mesh), representing a discrepancy of 2% from the estimated here. For Re=400, the primary vortex intensity rises to 0.107, following the trend established by Ghia *et al.* [51] on a very fine mesh of 257x257 elements (their result being 0.114, a 6% departure from the result here). Kim and Moin [84] provide a value of 0.112 on a 65x65 mesh, again reaffirming general findings with mesh refinement. Figure 4.2 presents the computed incompressible velocity components along the vertical and horizontal centerlines for Re=100 and Re=400. The results are contrasted against those of Ghia *et al.* [51], revealing close agreement and providing confidence in the level of accuracy achieved for incompressible solutions. This position is also reflected in solutions at Re=1, see Hawken *et al.* [62].

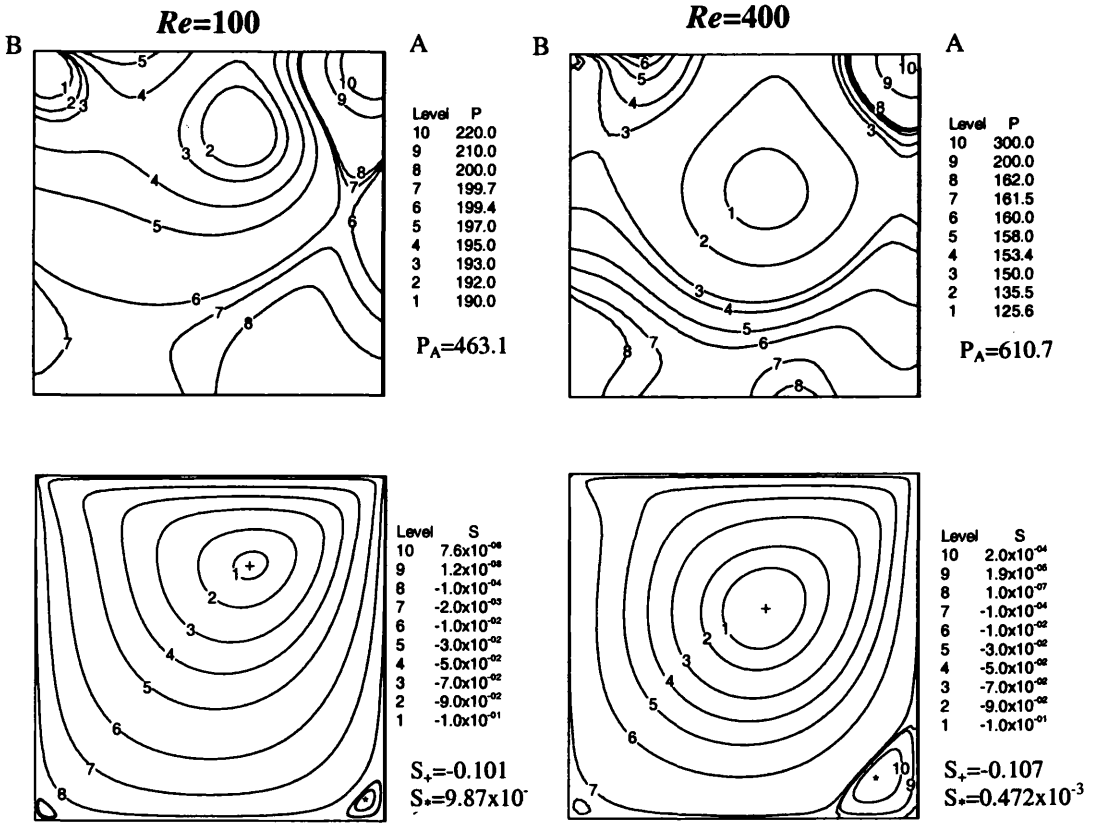

Figure 4.1: Pressure (top) and streamlines (bottom) contours for cavity flow: incompressible, singular case (b), Re=100 (left) and Re=400 (right)

For compressible flow under case (b) condition and Re=100, Tait state equation parameters are fixed to (m,B)=(2,300). This setting, leads to Ma≈0.03 and 21% density increase above the incompressible counterpart. In Figure 4.3, Mach number contours are

presented for piecewise-constant density interpolation (with recovery of the gradients). The figure exhibits the singularity in the solution through the distortion in the Mach number contours near the cavity top corners. In addition, for the compressible case, pressure and streamline contour patterns practically replicate those observed under the incompressible regime, and hence are discarded.

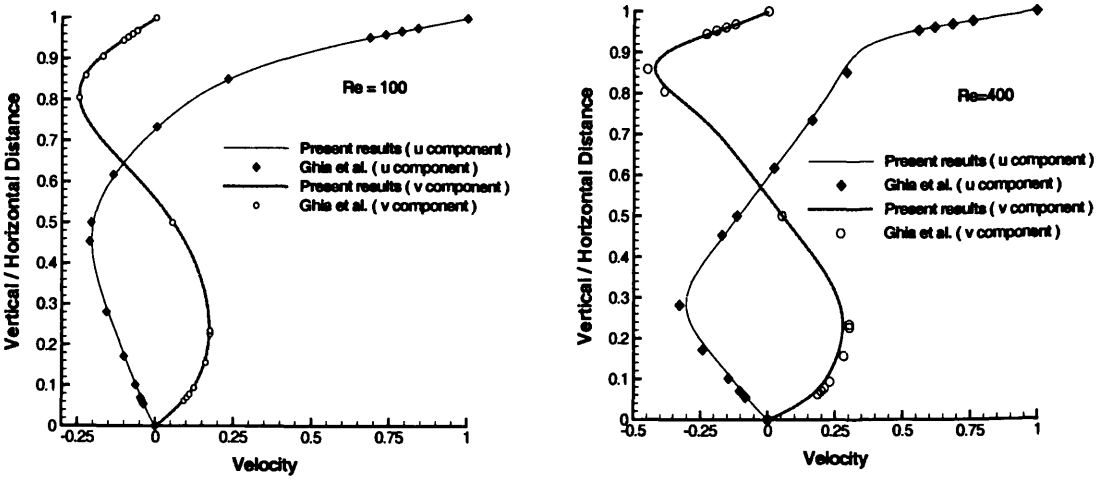

Figure 4.2: (u,v) on vertical or horizontal cavity centrelines, incompressible, singular case (b), Re= 100 and Re= 400

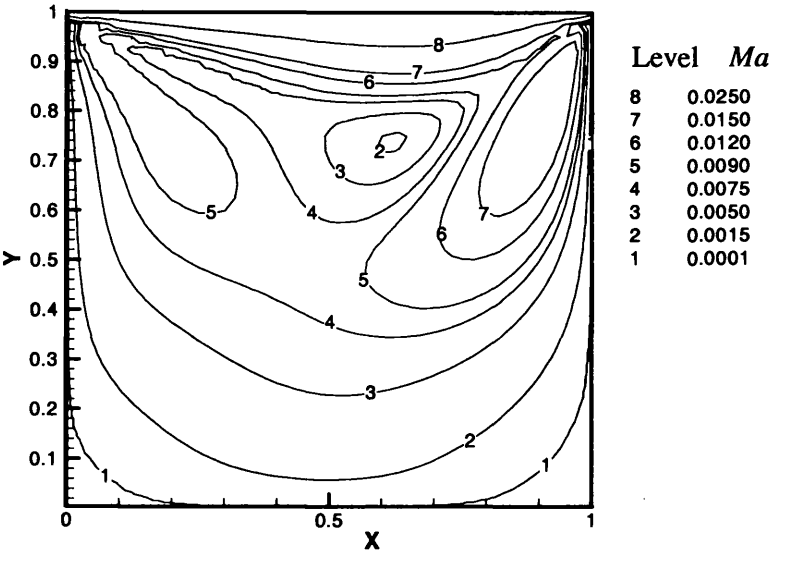

Figure 4.3: Mach number contours for cavity flow: piecewise-constant density interpolation, singular case (b), Re=100, (m,B)=(2,300)

Accuracy is assessed via the infinity norm, ($\|E_h\|_\infty$), on the longitudinal velocity, a maximum norm of the difference from a fine mesh solution (see below), scaled by the maximum of all normed values. This is conducted, under Re=100 and based on both

density interpolations and lid-velocity profiles alternatives. Due to the lack of an analytical solution, a fine mesh solution on 40x40 is taken as a reference, against which three further mesh solutions are compared (5x5, 10x10 and 20x20). Nodal values on both cavity centrelines (X=0.5 and Y=0.5) are sampled for the computation of $\|E_h\|_\infty$. For *Re*=100, trends of infinite velocity error norm, with respect to mesh-size are presented in Figure 4.4(i) for case (a), variable lid-profile, and for case (b), constant lid-profile, in Figure 4.4(ii). For the smooth solution (case (a)), the order of accuracy for the three different implementations is above 2.8, approaching a third-order. This order of accuracy has been achieved in some of earlier works Webster and co-workers for incompressible viscoelastic flows [151]. For case (b), where the solution presents singularities, the order is clearly lowered by about one unit. This is in keeping with expectation, being well known that the presence of singularities in a problem will result in a decline in accuracy if the solution space is not extended to embrace the singularity, see Strang and Fix [132] and Georgiou [50]. Note, the same behaviour in error norm is detected in both case (a) and (b), and for the three algorithmic implementations. This confirms that modifications incorporated within the initial incompressible algorithm, to accommodate weakly-compressible flows, do not degrade the accuracy of the pressure-correction method itself.

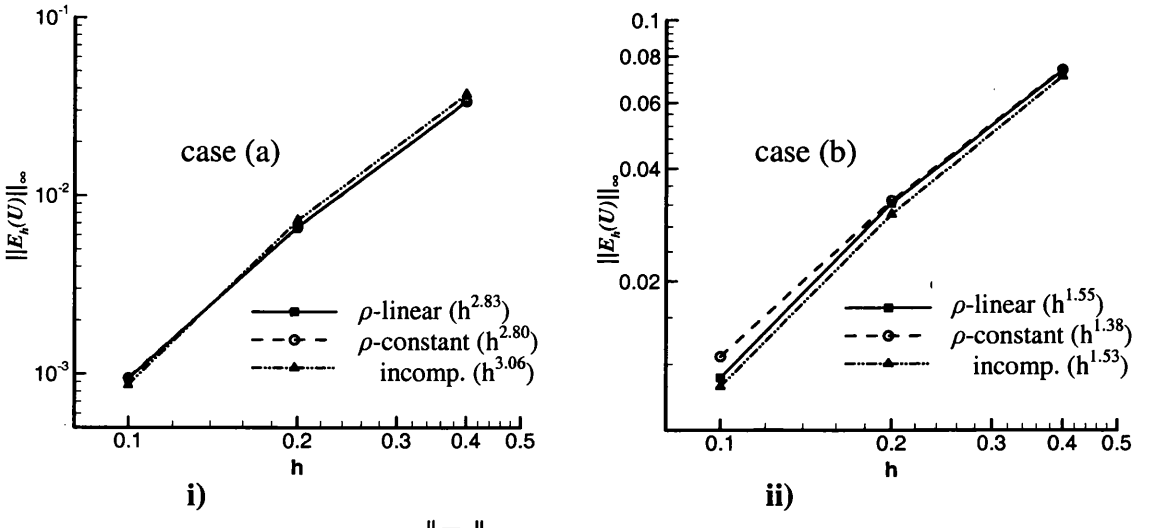

Figure 4.4: Infinity error norm $\|E_h\|_\infty$ on velocity, various algorithms for cavity flow, (i) case (a), *Re*=100; (ii) case (b), *Re*=100, (*m*,*B*)=(2,300)

Assessment of time-convergence to steady-state has been performed on case (b), based on a 40x40 mesh and a time-step of Δt=0.01, with initial conditions assigned as quiescent (see Webster and Townsend [155] for tracking of true transient solutions).

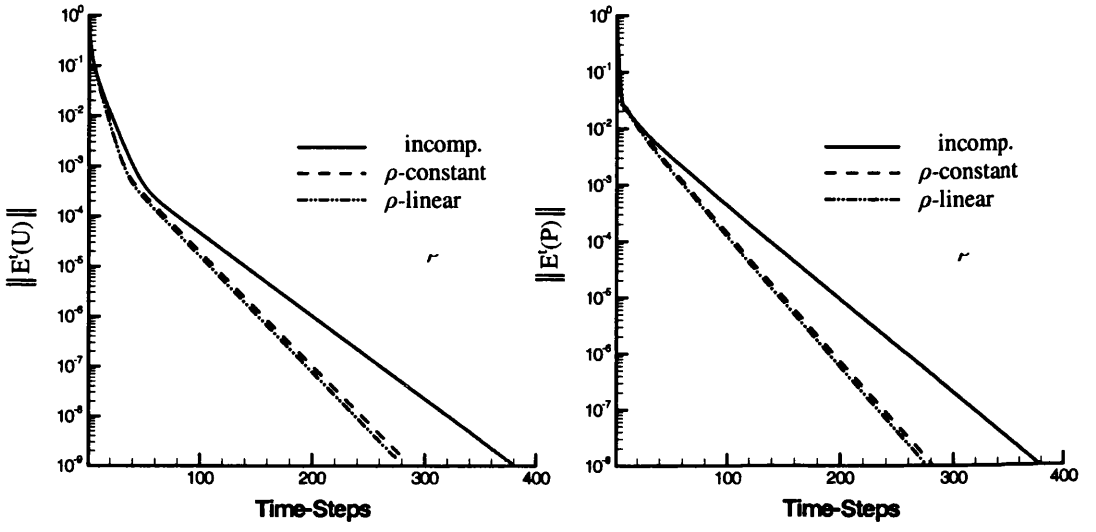

Figure 4.5: Temporal convergence history trends for velocity, $E^t(U)$ (left) and pressure, $E^t(P)$ (right): cavity problem based on Re=100 and Δt=0.01, case (b), (m,B)=(2,300)

There is a need to define a temporal relative-increment L_2-norm to govern time-stepping convergence history, taken here with a standard denominator shift to avoid inappropriate scaling for $\|X^{n+1}\|<1$, (see Shampine [131]):

$$E^t(X)=\frac{\left\|X^{n+1}-X^n\right\|_2}{1+\left\|X^{n+1}\right\|_2}. \tag{4.1}$$

For the three algorithmic variants Figure 4.5, illustrates histories of the relative error norms in velocity ($E^t(U)$) and pressure ($E^t(P)$). The results reflect a superior rate of convergence for the both compressible implementations, as compared to that for the incompressible algorithm: 30% fewer time-steps are required for the compressible implementation to reach an equitable level of tolerance. Here, for compressible settings temporal convergence rate is $O(\Delta t^{2.6})$, as compared to $O(\Delta t^{2.4})$ for the incompressible counterpart. This is associated with the improvement in system matrix condition number, brought about via introduction of the mass-matrix, M_c and right-hand-side adjustment via L_k^{ρ} at stage 2 (see Eq.(3.53)). As a consequence, larger time-steps may

be permitted within the compressible regime, as opposed to the incompressible alternative. Note, in both compressible algorithmic implementations, the same rate of time-stepping convergence is observed.

4.1.2 Contraction flows

In the second benchmark, one may introduce a more complex test problem typical of the industrial setting and with a view to viscoelastic computations to follow. This consists of a contraction flow under both planar and axisymmetric reference, see Figure 4.6a. Here, large pressure-drops are observable, with the significant effects of compressibility.

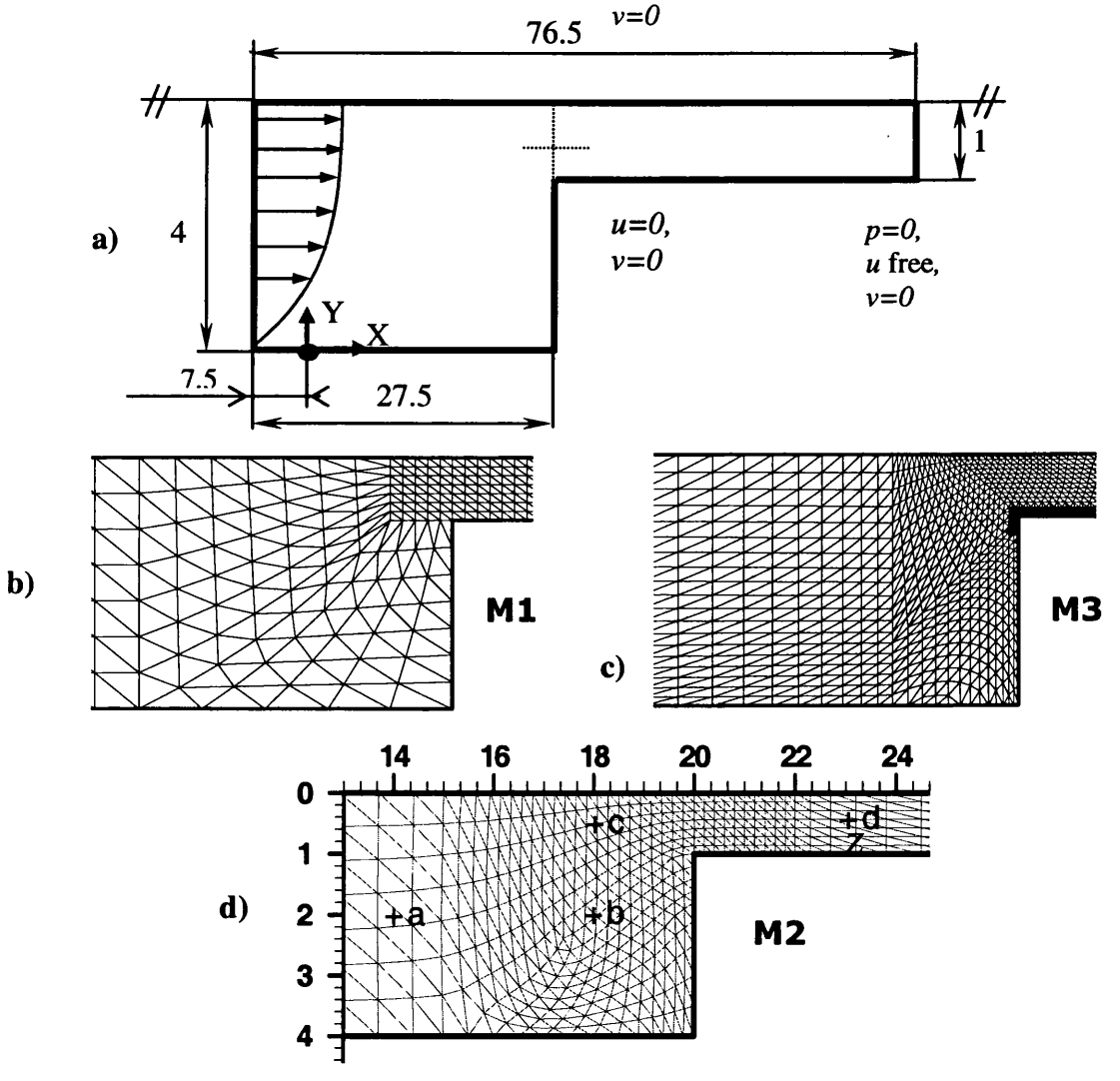

Figure 4.6: Contraction flow:
a) schema, b-d) Mesh refinement around the contraction, M1-M3;
d) sample point locations on mesh M2 for axisymmetric and planar cases (mesh characteristics in Table 4.2)

First, a straight channel (entry/exit) section is considered, two units long by one unit wide, providing a viscous shear flow and analytical solution for incompressible flow. The compressible low Mach number equivalent provides quantitative reference data to be compared against its incompressible counterpart. For velocity, no-slip boundary conditions are imposed on solid boundaries with a parabolic inlet flow profile and at outlet, conditions are treated as natural with a pressure reference at exit. The Tait equation of state parameters (m,B) are assigned as (2,100), to manifest influence of compressibility (Ma≈0.08 and 8% density elevated above the incompressible state). Again, a time-step of Δt=0.01 is found appropriate and the Reynolds number is considered as unity. Based on three levels of regular mesh refinement (10x10, 20x20 and 40x40 rectangular sub-divisions split into triangles), and across each flow regime, the difference between the flow rate entering and leaving the channel is O(0.1%) and less on the finer mesh, demonstrating conservation of mass overall. There is flattening of the parabolic incompressible velocity profile with either piecewise-constant or linear density interpolation.

Table 4.1 presents the values of the pressure, density and Mach number along the centreline of the channel at different X-locations for the various implementations and mesh size. For incompressible flow and with a mesh size 10*10, the exact solution is recovered reflecting a nondimensional inlet-outlet pressure-drop of 16 units. For compressible flow, with either piecewise-constant or linear density interpolation, the pressure-drop is slightly elevated over incompressible flow and increases with mesh-density (5% increase on the finest mesh). Compressibility effects are apparent, with the density of the fluid entering the channel being larger (by about 8% for both density representations) than that departing. As with pressure, density contours degrade slightly from the linear structure span-wise across the flow. Since density at the inlet is larger, the flow-rate is greater in the compressible settings as compared to the incompressible case. This explains the reported corresponding elevation in pressure-drop above. Note that, the speed of sound is infinite for an incompressible liquid, resulting in a vanishing Mach number. Since density is related to pressure through the equation of state, linked via the speed of sound, the Mach number reflects the relationship between velocity and pressure. Thus, for piecewise-constant and linear density interpolation, the differences observed in Mach number may be attributed to variation in pressure and velocity. In addition, these results demonstrate the capability of the compressible implementations

to deal with low Mach number situations ($Ma<8*10^{-2}$). Here, one observes yet again, a reasonable correspondence between results for either density interpolation option (2% difference on the finest mesh).

Table 4.1: Pressure and density values for channel flow under three regimes; centreline various X-locations with mesh-size variation, $(m,B)=(2,100)$

		X-centreline positions	Mesh 10*10	Mesh 20*20	Mesh 40*40
Pressure	Incompressible	0.0	16.000	16.000	16.000
		0.5	12.000	12.000	12.000
		1.0	8.000	8.000	8.000
		1.5	4.000	4.000	4.000
	Piecewise-constant	0.0	16.623	16.656	16.665
		0.5	12.613	12.639	12.647
		1.0	8.506	8.525	8.531
		1.5	4.320	4.331	4.335
	Linear	0.0	16.795	16.812	16.822
		0.5	12.754	12.763	12.774
		1.0	8.627	8.644	8.654
		1.5	4.424	4.444	4.454
Density	Piecewise-constant	0.0	1.075	1.075	1.075
		0.5	1.056	1.056	1.057
		1.0	1.036	1.037	1.037
		1.5	1.016	1.016	1.016
		2.0	0.995	0.995	0.995
	Linear	0.0	1.075	1.075	1.076
		0.5	1.057	1.057	1.057
		1.0	1.037	1.037	1.037
		1.5	1.017	1.017	1.017
		2.0	0.996	0.996	0.996
Mach number $*10^2$	Piecewise-constant	0.0	6.772	6.779	6.783
		1.0	7.186	7.211	7.221
		2.0	7.694	7.729	7.748
	Linear	0.0	6.785	6.785	6.785
		1.0	7.163	7.162	7.162
		2.0	7.580	7.579	7.584

4.1.2.1 Planar contraction flow

For the full problem, the total length of the channel is assumed to be 76.5 units with the contraction ratio of four to one. For this test problem, similar boundary conditions to the channel flow problem above are applied (see Figure 4.6a). The Reynolds number is

set to unity. One must note here, the characteristic velocity scale is the maximum taken over the channel exit where length scale is taken likewise, equating to half-channel width.

a) Mesh refinement: First, mesh refinement is conducted, based on a multi-block meshing strategy to discretised the half-contraction channel-geometry, with conformal mapping in each sub-block and matching of boundary nodes at interfaces. In this manner, three different meshes M1, M2 and M3 with different levels of refinement have been constructed, see Figures 4.6b-d with characteristics quantified in Table 4.2, where details are recorded for total number of elements, nodes, degree of freedom, corner mesh density and minimum element size defined as the radius of the circle inscribed in the smallest triangle element of the mesh considered (see Matallah *et al.* [98]).

Table 4.2: Characteristic mesh parameters for contraction flow

	M1	M2	M3
Elements	980	1140	2987
Nodes	2105	2427	6220
Vertex Nodes	563	644	1617
d.o.f.	8983	9708	14057
R_{min}	0.024	0.023	0.011
Corner mesh density	28	63	201

Figure 4.7 presents plots for temporal convergence history to steady-state on pressure ($E^t(P)$) and velocity ($E^t(U)$) under the planar coordinate system. This covers the three different meshes and algorithmic variants, with Tait parameters set to (m,B)=(5,3000), resulting in $Ma \approx 0.04$ and 4% density variation above the incompressible state, and a time-step of $\Delta t=0.05$. One may observe that both compressible implementations follow practically identical trends, and that once more, as in the channel flow problem, convergence rates are improved by approximately 30% over the incompressible form. As one suppresses oscillations in temporal velocity increments through mesh refinement, one also controls the oscillatory evolutionary patterns for time-increments in pressure. This is anticipated, since convergence history in pressure is constrained in a Lyapunov-norm, see Van Kan (1986). On pressure, for the three meshes considered, one

observes high-frequency/low-amplitude oscillations for the incompressible implementation compared to the compressible counterpart (low-frequency/large-amplitude).

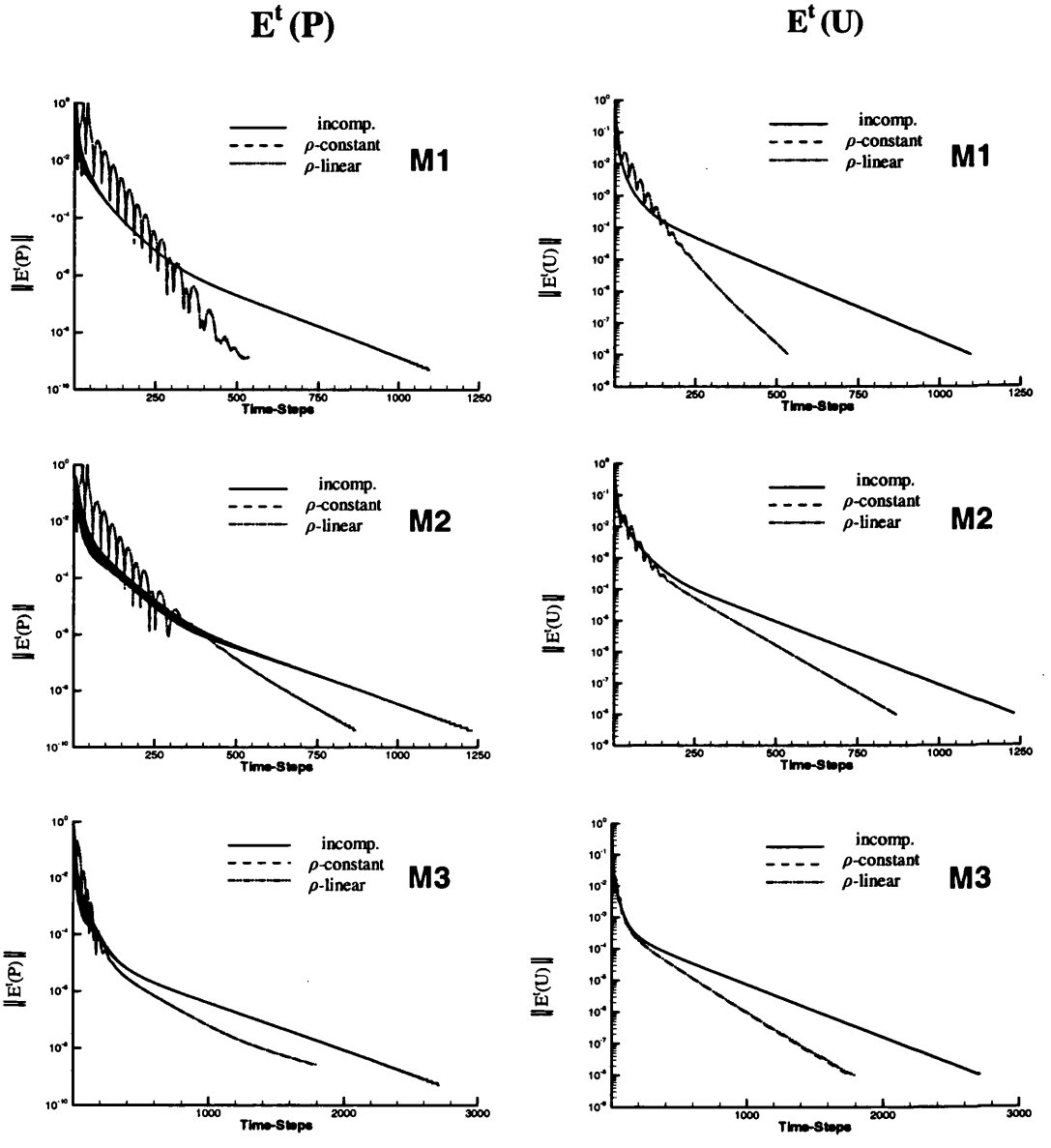

Figure 4.7: Temporal convergence history trends for planar contraction flow, various algorithms: for pressure $E^t(P)$ (left) and velocity $E^t(U)$ (right); (m,B)=(5,3000), mesh refinement M1-M3

Figure 4.8 illustrates pressure and stream function fields, with their relevant contour levels, for the three meshes. Here, only piecewise-constant density interpolation results are illustrated (being representative in these variables of linear density interpolation also). In Table 4.3, values of pressure, velocity components (u,v) and vortex information

are given at the contraction plane (sample location highlighted by a cross '+' in Figure 4.6a). Note, for the same compressibility setting, the piecewise-constant and the linear density interpolations deliver identical results (differing by less than 0.025%) for a particular mesh size (linear form suppressed). The associated contour plots are observed to smooth with refinement. The incompressible vortex size (0.985) is in close agreement with results from [108] (0.988). Furthermore, independent of mesh employed, compressibility effect suppresses the vortex size and elevates its intensity in contrast to incompressible conditions.

Table 4.3. Sample pressure and velocity component values at contraction plane, vortex information; various meshes and ρ-interpolations, planar contraction flow, $(m,B)=(5,3000)$

		M1	M2	M3
Pressure	Incompressible	393.6	393.5	393.5
	ρ-Constant	400.4	400.4	400.3
	ρ-Linear	400.4	400.4	400.4
u	Incompressible	2.957	2.956	2.969
	ρ-Constant	2.953	2.954	2.971
	ρ-Linear	2.953	2.954	2.971
v	Incompressible	0.520	0.516	0.518
	ρ-Constant	0.533	0.526	0.523
	ρ-Linear	0.533	0.526	0.523
S_{min} at vortex (-10^{-3})	Incompressible	0.292	0.437	0.390
	ρ-Constant	0.311	0.439	0.391
Salient Vortex size	Incompressible	0.806	0.976	0.985
	ρ-Constant	0.856	0.954	0.962

b) Solutions at (m,B)=(5,200): Increasing compressible effects, via $(m,B)=(5,200)$, leads to $Ma\approx0.16$. Here, there is variation in density above incompressible by about 27%, to highlight the difference between density representations. Figure 4.9, on mesh M2, illustrates the adjustment across the density field for linear density interpolation, and those in Mach number between piecewise-constant and linear density interpolations around the contraction zone. Solutions point values for velocity, pressure, density and

Mach number are extracted at the sampled spatial locations (a,b,c,d) of Figure 4.6d. In the pressure field, for instance, one observes about 0.04% disparity between both compressible representations.

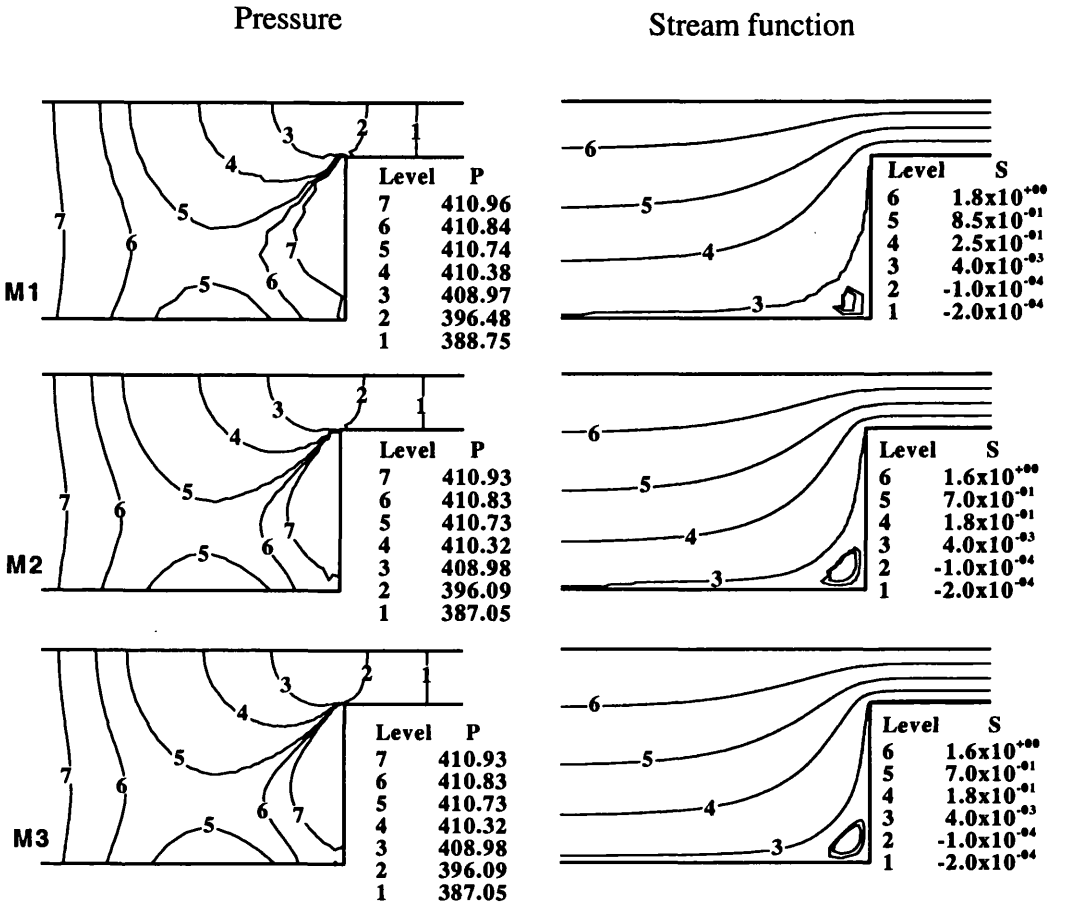

Figure 4.8: Pressure (left) and streamlines fields (right) for planar contraction flow, piecewise-constant density interpolation scheme, (m,B)=(5,3000), mesh refinement M1-M3 (values in Table 4.3)

In Mach number, contour field plots (Figure 4.9) reflect hardly any difference, according to the choice of density interpolation employed. The Mach number is related to the speed of sound, which itself is linked directly to density, via the Tait equation.

Figure 4.10 presents solution profiles for different variables (u-velocity, pressure, density and Mach number) at the contraction channel centreline for both compressible interpolation variants. The results provide clear evidence that low-order density interpolation with gradient recovery, is capable of reproducing results comparable to those with linear density interpolation.

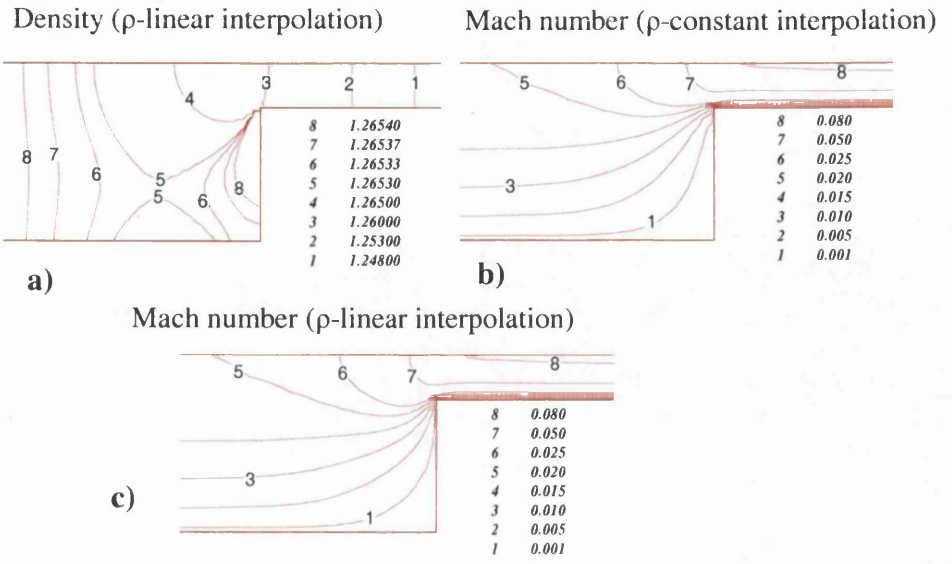

Figure 4.9: Density and Mach number for planar contraction flow, $(m,B)=(5,200)$;
a) density (linear interpolation); Mach number under
b) piecewise density interpolation and c) linear density interpolation

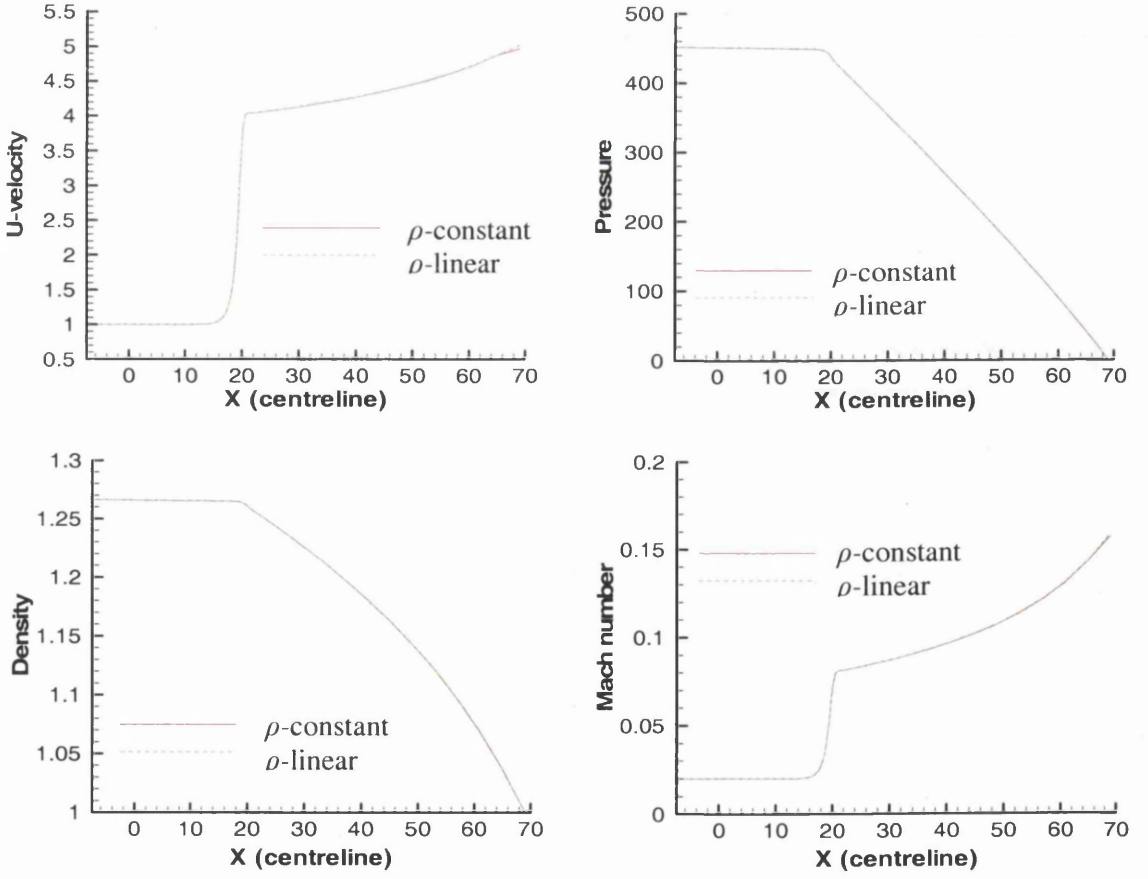

Figure 4.10: Solution profiles at channel centreline (planar case), piecewise-constant and linear density interpolation, $(m,B)=(5,200)$. Top left: velocity, top right: pressure, bottom left: density, bottom right: Mach number

4.1.2.2 Circular contraction flow

Under an axisymmetric frame of reference, pressure-differences exceed those for the planar equivalent. Here, Tait parameters are set to $(m,B)=(5,3000)$, leading to similar compressible influences ($Ma\approx0.16$) as in the planar configuration, and where density is elevated by 17% above the incompressible state. First, as above for planar flow, one confirms that similar trends are observed in field variables based on both forms of density interpolation. Profiles over the contraction channel centreline follow the planar case (as in Figure 4.10). Sampled solutions values for the different variables are extracted at the selected spatial locations of Figure 4.6d. Oncemore, similar results are observed for both compressible representations (ρ-constant or ρ-linear) around this contraction zone (less than 0.1% in pressure). There is about 8% pressure elevation in the compressible regime compared to the incompressible instance (elevation reduced from the planar case by 3%).

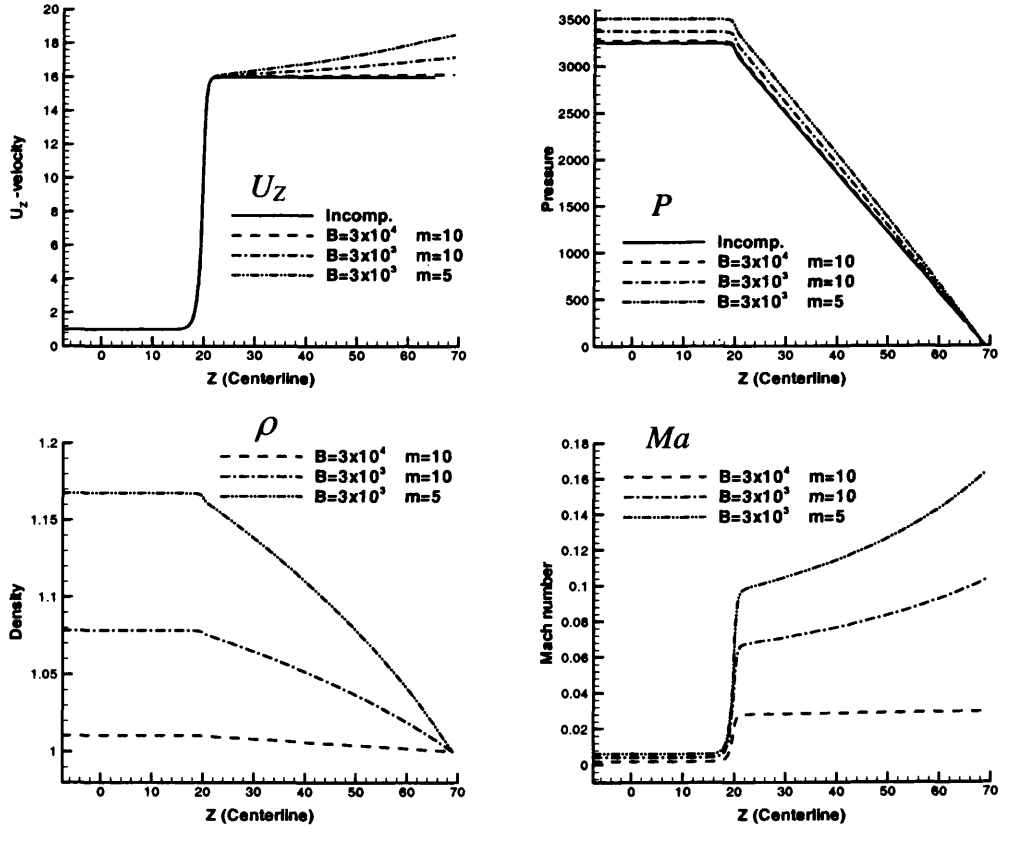

Figure 4.11: Variation in compressibility settings, mildly compressible towards incompressible, trends in solution profiles on channel centreline (circular case), piecewise-constant density interpolation. Top left: U_Z-velocity, top right: pressure, bottom left: density, bottom right: Mach number

a) Tait parameter variation (m,B): A Tait parameter sensitivity analysis is performed to assess variation with the compressibility parameter set (m,B). First, the capability is highlighted of the compressible algorithm to deal with a range of low Mach number ($0<Ma<0.2$), approaching the asymptotic limit $Ma\approx 0$. Figure 4.11 illustrates trends in solution profiles for different variables at the contraction channel centreline, based on variation in compressibility settings, adjusting Tait parameters accordingly. These trends reflect adjustment from the incompressible towards the mildly compressible setting ($Ma<0.2$). In the compressible regime, only piecewise-constant density interpolation has been employed, as both constant and linear representations lead to practically identical results. Centreline solution profiles indicate that the compressibility setting has little influence on the velocity field before the contraction. As the flow becomes more compressible, some effects begin to emerge beyond the contraction zone, once the liquid accelerates (17% faster for $(m,B)=(5,3000)$) above the incompressible instance. At flow-entry, pressure and density are larger for compressible above incompressible flow (8% for pressure and 17% for density for $(m,B)=(5,3000)$). This highlights how much 'compressibility' impacts upon the flow kinematics.

Second, in Figure 4.12, compressible flow history numerical convergence trends are presented to steady-state for variation in the (m,B) parameter set, based upon increasing (Ma,ρ). Experience shows that this is the important paring to extract corresponding convergence behaviour in time. This covers $0.003<Ma<0.12$ and $1.0001<\rho<1.13$. All solutions are pursued to a limiting tolerance of 10^{-8}, though presentation in Figure 4.12 is restricted for comparison purposes, to the first 1000 time-steps at a common time-step value of $5*10^{-2}$. One may comment that where convergence trends are replicated, across (m,B) setting providing similar (Ma,ρ), say (m-variable,$B=10^4$) and ($m=1$,B-variable), almost identical field solutions are obtained at steady-state.

At low Ma, $Ma<0.005$: high-frequency/low-amplitude oscillations are a characteristic in the pressure norm $E^t(P)$ at early time (within the first 100 time-steps). The velocity norm $E^t(U)$ remains smooth. The rate of convergence is higher in pressure ($O(\Delta t^3)$) than in velocity ($O(\Delta t^{2.9})$) up to around 250 time-steps, after which time both norms converge at the same rate (that of velocity, with sustained gap between norms and monotonic linear trends).

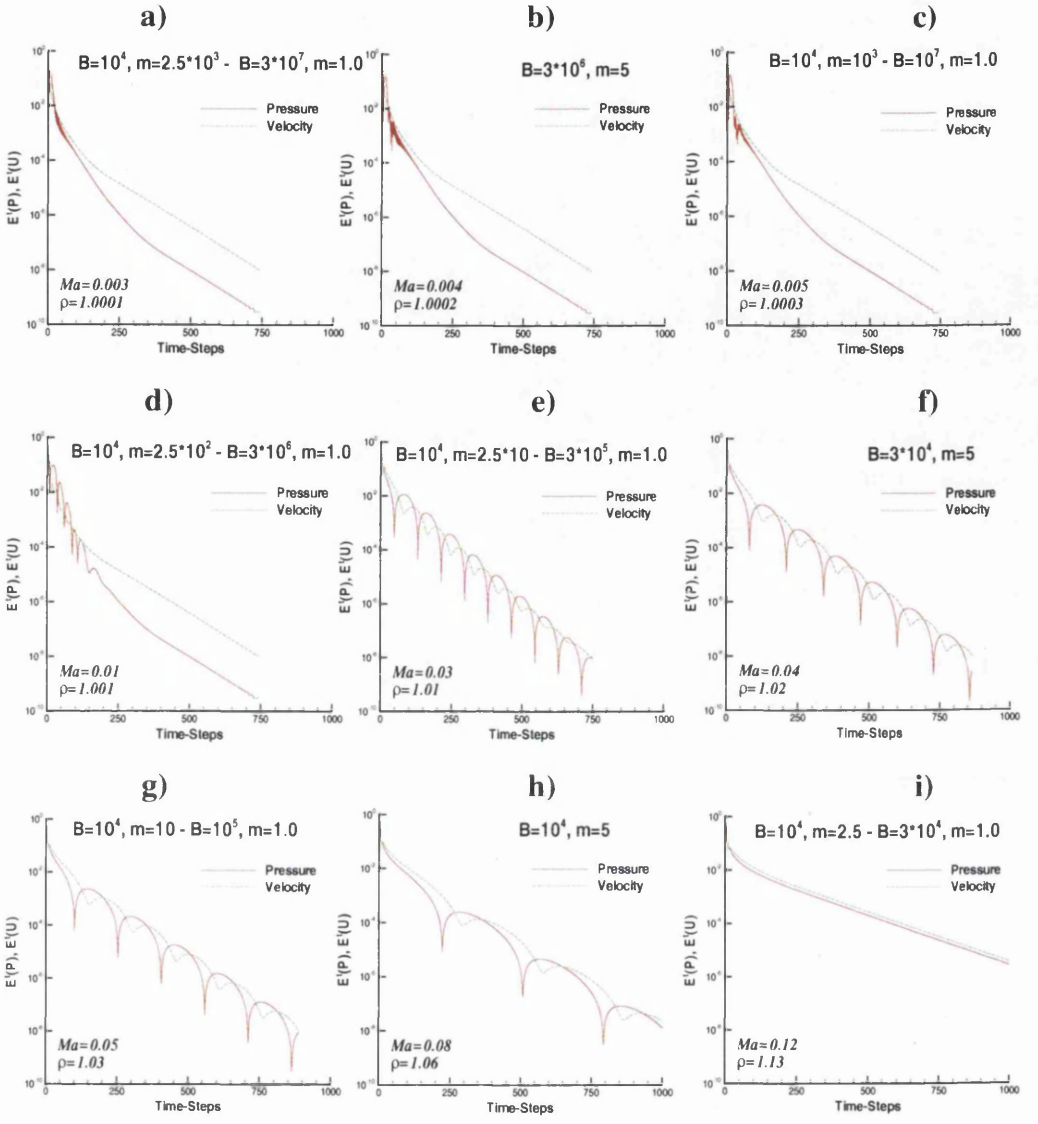

Figure 4.12: Effect of Tait parameter (m,B) variation on convergence history of pressure $E^t(P)$ and velocity $E^t(U)$, piecewise-constant density interpolation, increasing compressibility effect, circular contraction flow

At moderate *Ma* (applicable for liquids), $0.01<Ma<0.08$: there is elongation in pressure norm oscillations, decreasing in frequency with increasing *Ma*. Trends are characterised by lower frequency but larger amplitude pressure norm oscillations than for the low *Ma*-range. Velocity norm oscillations begin to appear at and above $Ma=0.03$, spreading in time with increasing *Ma*. The pressure norm oscillations remain in phase with and some three-times larger than those in velocity, though clearly one drives the other. Equitable convergence rates throughout time now begin to arise in both norms. Averaged rates are linear and monotonic in pattern, being of order $E^t \approx O(\Delta t^{2.1})$.

Oscillatory $E^t(P)$ patterns in m=5 sub-figures (e-g) are typical of convergence in a Lyapnov norm, as the theory would predict (see Van Kan [145]).

For Ma>0.1: oscillations in pressure and velocity norms disappear, so that convergence trends are smooth, with monotonic linear convergence-patterns of equitable order, $E^t \approx O(\Delta t^{1.3})$. The marked difference here is the unification of convergence norm values through time between the two variables of velocity and pressure. Clearly, the overall time to achieve the limiting convergence tolerance of 10^{-8} will imply an increase in the number of time-steps required. In the larger Ma≈0.12 instance, this leads to 1690 time-steps. This adjusts to 865 for Ma≈0.04 and 750 for Ma≈0.005.

One concludes that such trends in numerical convergence behaviour may be used to gather the most preferable form for the instance in hand; speed in steady-state extraction or matching both norms, $E^t(P)$ and $E^t(U)$. Note that, it is the particular level of (Ma,ρ) that dictates the numerical convergence response. Nevertheless, one may be able to take advantage of superior convergence properties in adjusting (m,B) to arrive at a final steady-state for the target pairing. One attributes the linearisation of the $E^t(P)$ norms with increasing Ma to the increased influence of the M_c-matrix in stage 2 (see Eq.(3.53)), an addition which vanishes at steady-state. When only steady-state is sought, convergence behaviour could be enhanced by choosing a large local time-step for stage 2. One notes that by design, the present approach is lacking to describe highly-compressible flow (Ma>>$O(1)$), as amongst other things, this would necessitate consideration of a kinetic equation (which is neglected here). Experience shows that numerical scaling on the pressure time-step at stage 2, ($\Delta t_P=\beta\Delta t$) may be a useful strategy that effectively switches the prevailing numerical value of the speed of sound in the denominator of M_c, thus capturing the temporal convergence trend of an alternative physical (Ma,ρ)-pairing. To demonstrate this for Δt=0.05, (Ma=0.12, ρ=1.13, β=1) are taken and rescaled with β=10 to mimic (Ma=0.03, ρ=1.01, β=10), for which one gathers corresponding history norm convergence plots of Figures 4.12 (i) and (e). This may be repeated with $\beta=10^3$ to mimic (Ma=0.003, ρ=1.0001, $\beta=10^3$) to recover Figure 4.12 (a) convergence pattern. There is a strong similarity here to pseudo-compressible and artificial compressible implementations, employed for incompressible flows, in the sense of stage 2 conditioning on the left-hand-side of the equation.

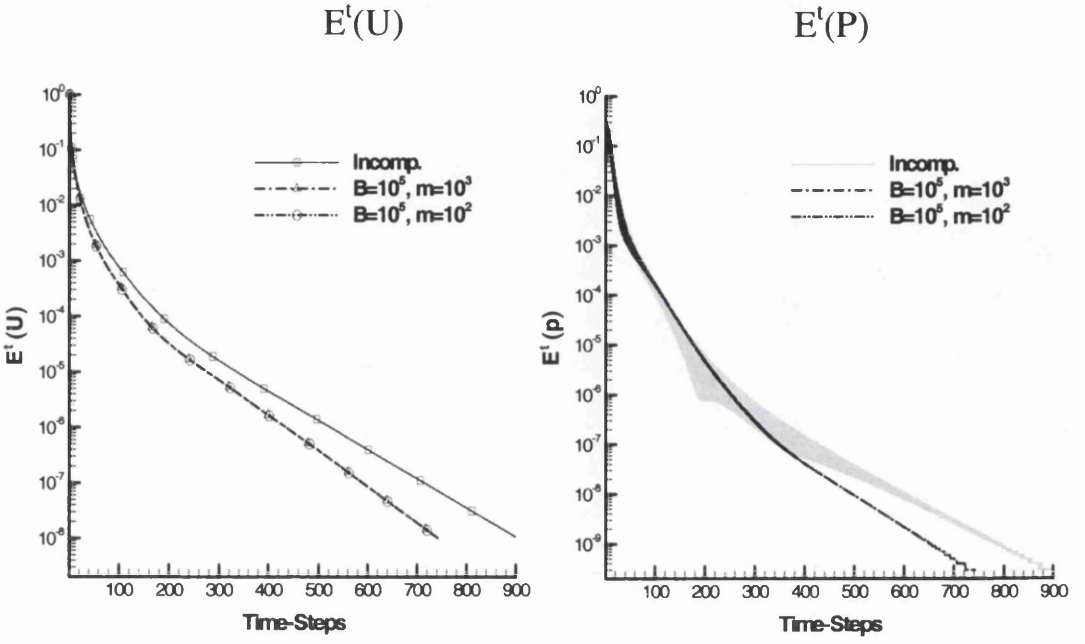

Figure 4.13: Convergence history trends for (left) velocity $E^t(U)$ and (right) pressure $E^t(p)$, circular contraction flow problem, incompressible versus piecewise-constant density interpolation tending to the incompressible limit

b) Tending towards the incompressible limit (Ma→0): Here, the effectiveness of the compressible implementation is addressed to deal with very low Mach number situations ($Ma \approx 0$), via adjustment of the Tait parameter pairing (m, B), to represent such a state. In Figure 4.13, the Tait parameters are elevated to high levels ($m=10^2$ or 10^3 and $B=10^5$), and one observes improvement in stability and convergence-rate of the compressible versus the incompressible implementations. At this level of Tait parameters one observes high-frequency/low-amplitude pressure oscillations for incompressible convergence trends that are practically suppressed in the compressible instance. This is attributed to improvement in system condition number, via inclusion of the stage 2 mass-matrix and right-hand-side terms. Sample solution values for this particular case highlight the match between incompressible and compressible (with $Ma \approx 0$) algorithmic implementations, in all variables and over different regions. Results demonstrate that, in the zero Mach number limiting regime, piecewise-constant density interpolation, with recovery of gradients during the second stage, is equitable to linear density interpolation. On the other hand, there is less than 0.5% overall difference between incompressible and compressible representations. Based on these findings, one

may establish that the compressible algorithmic implementations may be employed effectively to simulate weakly-compressible, as well as incompressible flow scenarios.

4.2 Conclusion

Based on a second order *fe* approximation with a pressure-correction method split into three distinguish fractional stages, two algorithmic representations have been introduced to simulate weakly-compressible highly-viscous liquid flow. The first uses a piecewise-constant density interpolation on the *fe*, with nodal-recovery to compute the gradient of density. The second variant is based on a linear interpolation for the density (hence, piecewise-constant density gradient).

These compressible algorithmic variants have been shown capable of simulating flow with low to zero Mach number. Hence, a zero Mach number limit may be reached by adjusting Tait parameter pairings, where compressibility effects within the liquid flow may be controlled whilst approaching the incompressible limit. Under such circumstances, results match well with those for the compressible algorithm and those for the 'purely' incompressible algorithm. These findings allow the user to apply the compressible algorithm for both compressible and incompressible regimes.

The programming effort required to implement these compressible algorithms within an incompressible software framework has been manageable. The implementation is considerably easier for the piecewise-constant density interpolation (incompressible at the element-level). One may refer to Hawken *et al.*, [62], for operation count analysis indicating linear time complexity on node (or element) counts per time-step, and linear space complexity overall. The piecewise-constant implementation necessitates a recovery technique for density gradients at stage two, with density scaling of all elemental matrices. In addition, low-order density interpolation with gradient recovery, has been found to perform equally as well as a linear density interpolation. Next, attention will be devoted to analysing viscoelastic counterpart flows, seeking to investigate the numerical and physical impact of this methodology there also.

CHAPTER 5

Compressible and Incompressible Viscoelastic Flows (*fe*): Contraction Flows†

In the previous chapter, results have been presented for viscous flows in weakly-compressible and incompressible settings, where the scheme was applied successfully to several benchmark test problems. In the compressible scenario, spatial convergence-rates reach a third-order for continuous problems. At low to vanishing Mach number the algorithm performs well. This leads one to classify a unified scheme for both compressible and incompressible viscous flows. The purpose of the present chapter is to provide extension into the viscoelastic regime. This deals with compressible and incompressible liquid flows, based upon the Oldroyd-B model fluid. For the compressible viscoelastic algorithm, stability, accuracy and performance properties are investigated for low to zero Mach number situations (approaching the incompressible limit). In addition, a parameter sensitivity analysis is conducted to assess convergence history for Weissenberg number levels of order unity and for flows starting from quiescent initial conditions.

5.1 Scheme implementation and numerical solutions

The flow through an abrupt 4:1 contraction for an Oldroyd-B fluid is recognised as an outstanding benchmark test problem. This is, in terms of stability at high Weissenberg number for viscoelastic incompressible flow, well-documented in the literature (see for example [114,150]). Here, this test problem is chosen to validate the

† Material of this chapter has been shaped in a paper "Numerical Simulation of Compressible Viscoelastic Liquids" by I. J. Keshtiban, F. Belblidia and M. F. Webster, *Journal of Non-Newtonian Fluid Mechanics* **122** (2004) 131-146.

asymptotic 'zero' Mach number solutions against published incompressible results. In addition, at high levels of Weissenberg number, consistency, accuracy and behaviour of the more compressible solutions are monitored. The contraction geometry, the meshes employed and no-slip boundary conditions on solid boundaries (see Figure 5.1) are identical to those in chapter four (see Figure 4.6). One notes that in chapter four, fully developed steady-state profiles were consider on open boundaries. Here at the inlet, transient boundary conditions are imposed, reflecting build-up through flow-rate (Waters and King, (W&K) [153]), generating set transient profiles for normal velocity (u) and stress (τ_{xx}, τ_{xy}), displaying vanishing cross-sectional components in velocity (v) and stress (τ_{yy}). The mathematical formulation for these profiles as a function of Weissenberg number is presented in Carew *et a.l* [23]. These settings provide smooth growth of boundary conditions at any particular *We*, and hence improve numerical stability in convergence towards steady-state. In this manner, true transients may be accessed from suitable start-up fields. If incremental continuation through *We*-solutions are employed, step increments would apply correspondingly. In contrast, at the outlet, natural boundary conditions are established, via boundary integrals (B.I.) within weak-form representation of the momentum equations, assuming that v vanishes and a zero pressure reference level is set at the outlet. The Reynolds number is set to unity throughout the system, allowing some inertia to enter the problem. In order to accommodate different flow regimes, here the strategy has been based on adjusting the values of the Tait parameter-set (m,B). These have been adjusted between those representing weakly-compressible flow conditions, say $(4,10^2)$, representative of maximum $Ma=O(10^{-1})$, to a highly incompressible state, typically $(10^4,10^4)$ representative of maximum $Ma=O(10^{-4})$. Then, corresponding solutions may be compared unambiguously to those for incompressible prevailing assumptions.

5.2 Trends in temporal convergence history

The unified framework may be assessed with respect to time-stepping convergence history to steady-state and spatial accuracy properties. To this end, so that as in chapter four, the three different meshes, M1, M2 and M3, are employed. See Figure 4.6 for the multi-block structure of the meshes with increasing levels of refinement around the contraction zone and Table 4.1 for mesh characteristics.

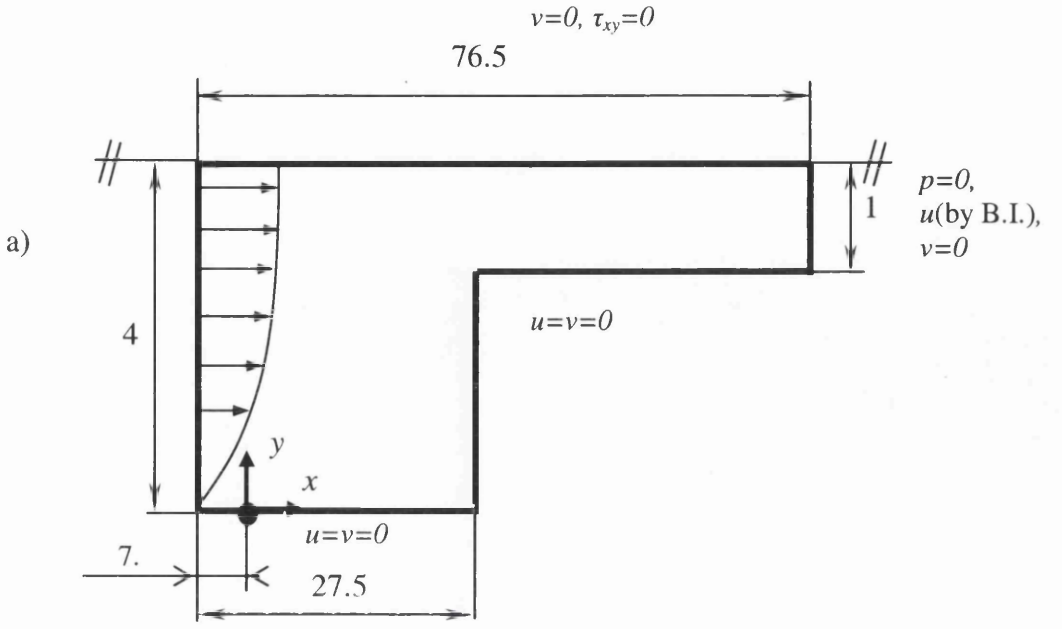

Figure 5.1: Contraction flow schema

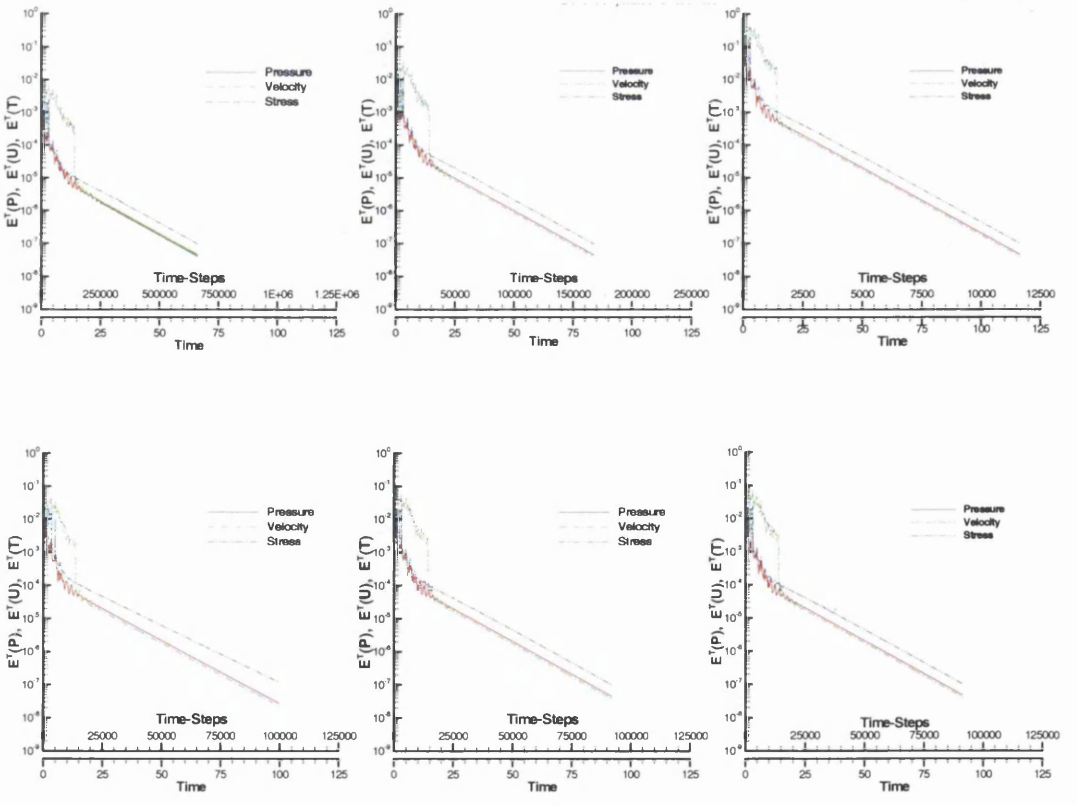

Figure 5.2: Compressible flow error norm convergence history for velocity, $E^T(U)$, pressure, $E^T(P)$, and stress $E^T(T)$, mesh M1; *We*=0.1, W&K, quiescent ic. Top: m_{itn}=5, Δt=10^{-4}, 5x10^{-4}, 10^{-2}. Bottom: Δt=10^{-3}, m_{itn}=1,3,5

5.2.1 Numerical parameter sensitivity analysis (compressible flow)

First, within the compressible context with the Tait parameter pairing of $(m,B)=(4,10^2)$, a numerical parameter sensitivity analysis on time-step (Δt) and mass iteration number (m_{itn}) is conducted. Here, computations are based on mesh M1, with Weissenberg number set to unity and commencing from initial conditions of a quiescent state. History tolerance results for pressure ($E^T(P)$), velocity ($E^T(U)$) and stress ($E^T(T)$) are illustrated in Figure 5.2. The relevant parameter values are those of: $\Delta t = 10^{-2}$, 10^{-3}, 10^{-4}; and m_{itn}=1, 3 and 5. For the compressible flow setting, results demonstrate that history convergence norm increments are relatively insensitive to adjustment in time-step beyond 10^{-3} and mass iteration number greater than 3. As stability is maintained, it is apparent that by increasing the time-step value, fewer time-steps and computational effort are required to achieve a specified relative tolerance level (10^{-7}) equating to steady-state. A monotonic pattern in history tolerance is observed, with an important observation at the start-up phase. There, some oscillation is apparent in history tolerance, as anticipated for the Waters and King kinematic start-up conditions (representative for straight channels). These oscillations are damped away rapidly, whilst the flow evolves to a steady-state, independent of the parameter settings employed.

5.2.2 Incremental continuation in Weissenberg number (incompressible flow)

Next, attention is turned to incompressible viscoelastic computations. Employing *incremental continuation in Weissenberg number* has been recognised as a successful strategy to obtain a stable *steady-state* solution at higher Weissenberg number levels (current target, We=1.0). In this manner, and commencing at the outset from a quiescent state, first a solution at We=0.1 is obtained. Subsequently, the We=0.1 steady-state solution is taken up as the initial starting phase, to derive a solution for We=1.0. This procedure is illustrated through sample results in Figure 5.3 with numerical parameters set throughout of (Δt=10^{-3}, m_{itn}=3, mesh M2). For constitutive models such as the Oldroyd-B, a limiting level of Weissenberg number (We_{crit}) is commonly encountered in such complex flows (see [10,5,46]). Here, in order to draw out and contrast algorithmic properties of the various alternative implementations, there is restriction to the attainable Weissenberg level of unity. Attempting a direct solution procedure (mimicking true time evolution) and starting from a quiescent state, reveals a persistent

periodic non-convergence pattern in convergence history, even at the level of *We*=1.0, as demonstrated in Figure 5.3b. This is a common oscillatory feature at peak *We*-levels with many stable algorithms, where monotonic convergence lies on a stability threshold, dependent upon the size of initial perturbation placed upon the system (given fixed discrete parameters of mesh size and time-step). In like manner, divergence at larger *We*-values would result.

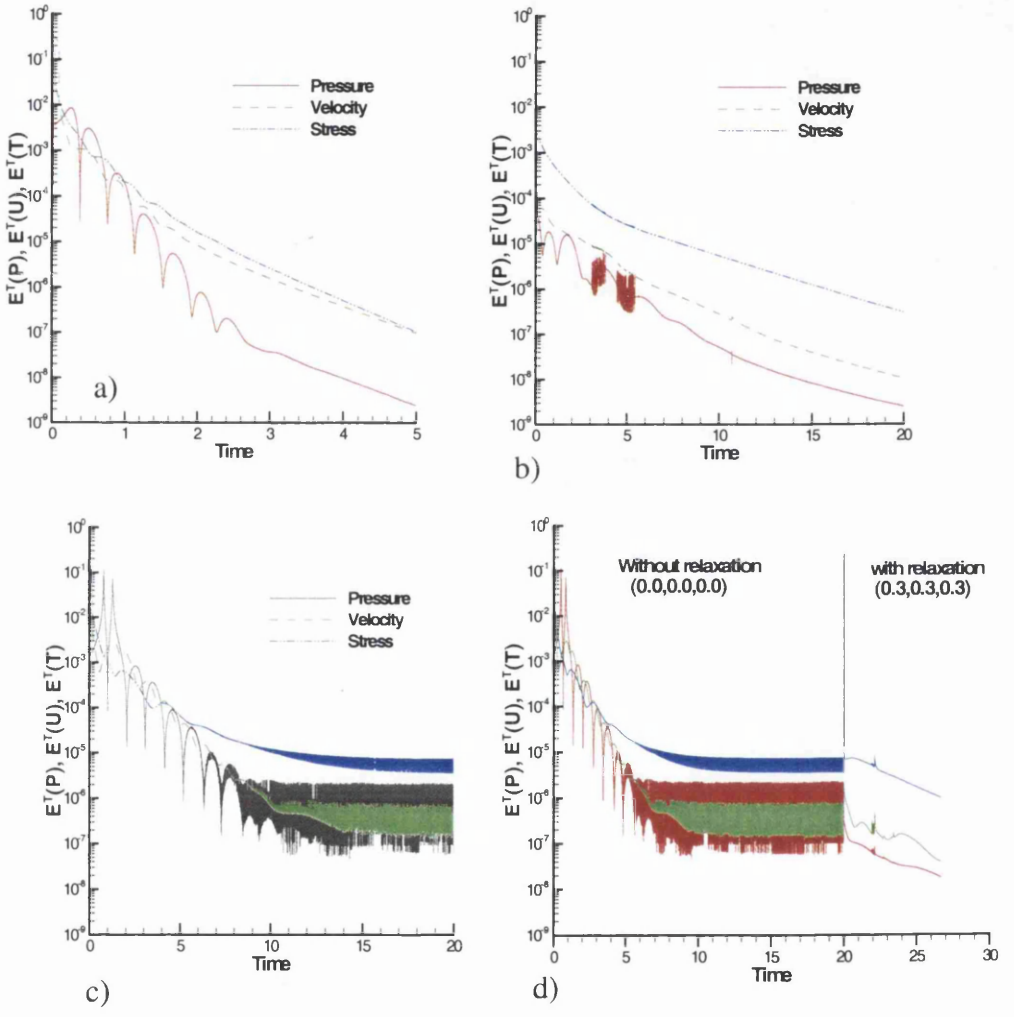

Figure 5.3: Incompressible flow error norm convergence history for velocity, $E^T(U)$, pressure, $E^T(P)$, and stress $E^T(T)$, mesh M2; a): Top left: *We*=0.1, W&K, quiescent ic. b) Top right: *We*=1.0 ic. from *We*=0.1. Bottom left b): *We*=1.0, from quiescent ic. Bottom right c): output of d), introducing under-relaxation

5.2.3 Under-relaxation procedure (incompressible flow)

Numerical instability, exposed through temporal convergence history tolerances, may be attributed to spatial or temporal discretisation error [56]. Here, stabilisation methods,

adequate for a steady equation systems, may prove ineffective for transient systems. Moreover, for fractional-staged procedure, *splitting-error* may itself be a source of instability. Fietier and Deville [46] have investigated numerical stability and presented time-dependent algorithms for viscoelastic flows, employing spectral element methods. In their study, some stabilisation strategies are proposed for flow in simple geometrical configurations. One such proposal is a filtering technique, applied after each time-step in an element-by-element fashion on both velocity and stress fields. Still further suggestions for stabilisation procedures may be found in the literature [10,98].

Through the current implementation, by appealing to solution under-relaxation, numerical stability can be sustained to larger *We*-levels. This may alter the transient representation, to yield the steady-state solution (see pseudo time-stepping, [23]). This is demonstrated starkly in Figure 5.3c, where an under-relaxation procedure is employed equally to all variables (r_U, r_τ, r_P), at the end of a complete time-step loop. Oscillations within convergence history tolerance are dramatically suppressed and monotonic convergence is essentially recovered. It can be realised that such relaxation may be applied on each fractional-stage equation within the time-step loop, so that, solution relaxation may be represented via time-step scaling upon each equation-stage time-step (local time-step, per equation). The reader is referred to Appendix 5.A for more details. Hence, one arrives at the justification for adjustable internal time-steps [106], to be judged as acting on each fractional-stage solution variable and indeed, expressing dependency upon the mesh selected (fraction of the Courant number).

For viscoelastic incompressible counterparts, the consequences of application of under-relaxation are investigated in some greater detail. To this end, again mesh M2 is adopted, and target *We*=1.0 solutions from quiescent initial conditions are sought. Figure 5.4a illustrates the convergence history scenario without relaxation, for ease of comparison. End-of-3-stages relaxation factors (r_i, per variable i) are applied to the solution field χ of the form:

$$\chi_{relax}^{n+1} = r_i \chi^n + (1 - r_i)\chi^{n+1}. \tag{5.1}$$

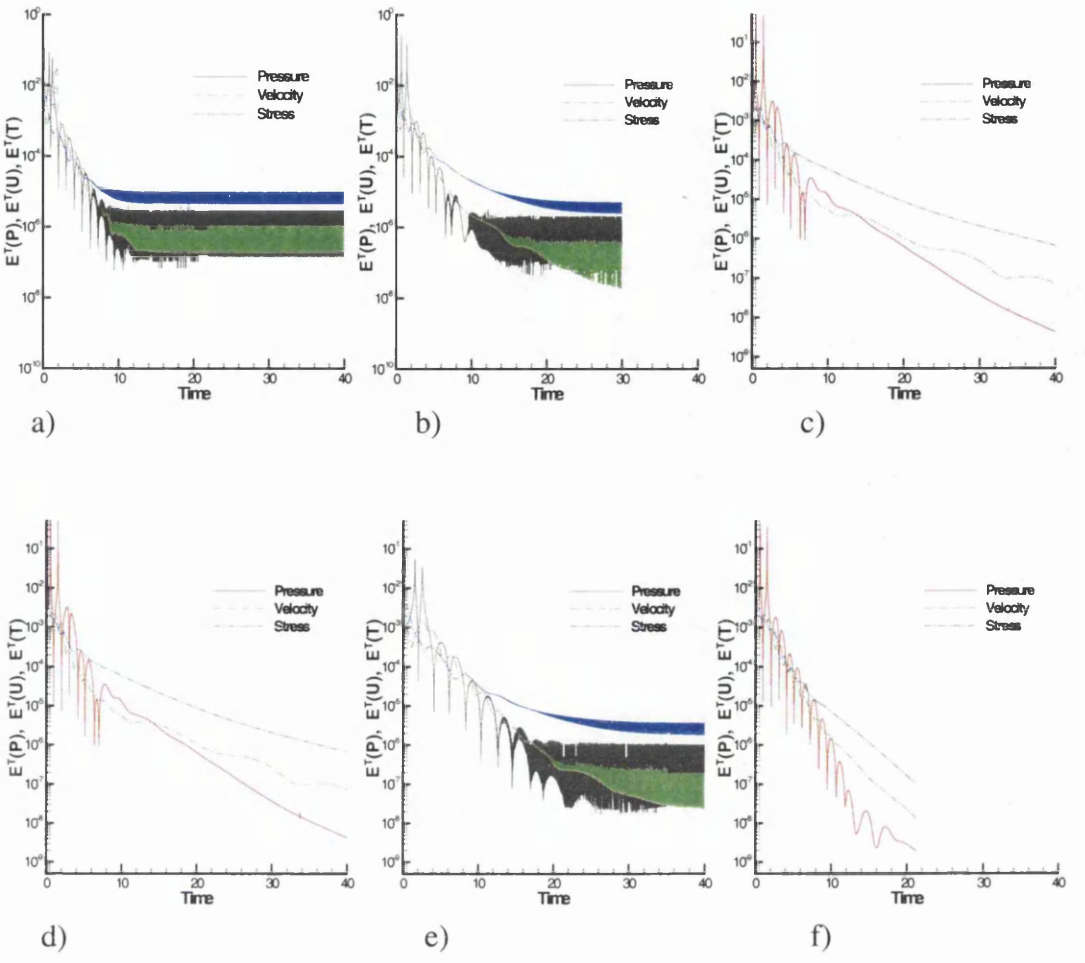

Figure 5.4: Incompressible flow error norm convergence history for velocity, $E^T(U)$, pressure, $E^T(P)$, and stress $E^T(T)$, mesh M2; We=1.0, W&K, quiescent ic., (Δt=10^{-3}, m_{itn}=5) with relaxation parameters (r_U, r_τ, r_P) as a): (0.0,0.0,0.0), b): (0.3,0.3,0.3), c): (0.7,0.7,0.7), d): (0.7,0.7,0.0), e): (0.0,0.7,0.0) and f): (0.7,0.0,0.0)

Convergence histories for constant parameter-setting with (r_U, r_τ, r_P) =(0.3,0.3,0.3) are presented in Figure 5.4b. This level of under-relaxation is not sufficient to damp the persistent oscillatory pattern that has emerged. An optimal level is observed at (0.7,0.7,0.7) in Figure 5.4c, which has the desired suppression and smoothing effect over the prior oscillatory pattern. One may isolate the influence of relaxation to each individual variable (and stage thereby). So, for example, the setting of (0.7,0.7,0.0) of Figure 5.4d exposes insensitivity according to r_P (hence, on Δt_P scaling). As demonstrated in Appendix 5.A, under-relaxing the local time-step (on velocity) at Stage-1 is conveyed to the Stage-2 local time-step, even without under-relaxing the pressure variable. In contrast, removing velocity under-relaxation, with (0.0,0.7,0.0)-

choice, demonstrates in Figure 5.4e, the crucial role of this factor alone: optimal r_U=0.7. suppressing stress under-relaxation with (0.7,0.0,0.0)-setting (as in Figure 5.4f) accelerates temporal convergence rates by fifty percent, achieving the tolerance target in half the time. One concludes that, primarily, only velocity relaxation should be applied. Finally, employing velocity under-relaxation at end-of-first-stage or at end-of-third-stage (end-of-complete-stage cycle) with optimal factors for mesh M2: (0.7,0.0,0.0) delivers identical history tolerance behaviour, as demonstrated in Figure 5.5. This confirms the crucial impact and importance of under-relaxation upon Stage-1 equations, prior to the remaining fractional-stages within the time-step loop.

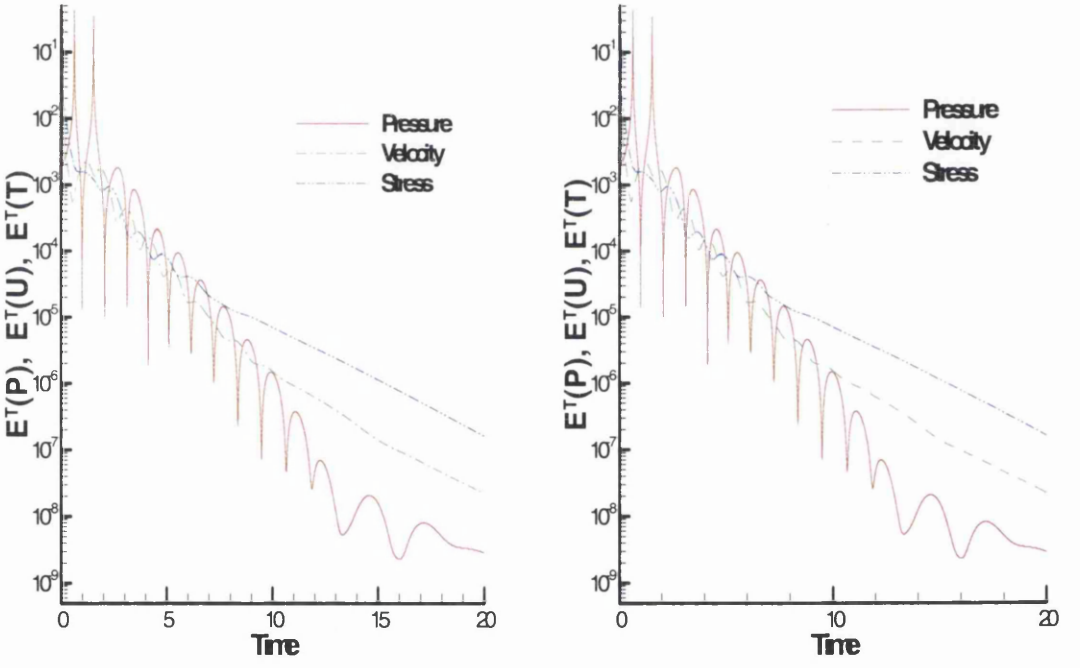

Figure 5.5: Incompressible flow error norm convergence history for velocity, $E^T(U)$, pressure, $E^T(P)$, and stress $E^T(T)$, mesh M2; *We*=1.0, W&K, quiescent ic. ($\Delta t=10^{-3}$, $m_{itn}=5$) with relaxation parameters (r_U, r_τ, r_P) =(0.7,0.0,0.0), a): relaxation at 1st TGPC stage, b): relaxation at 3rd TGPC stage

Weakly-compressible with mesh refinement:

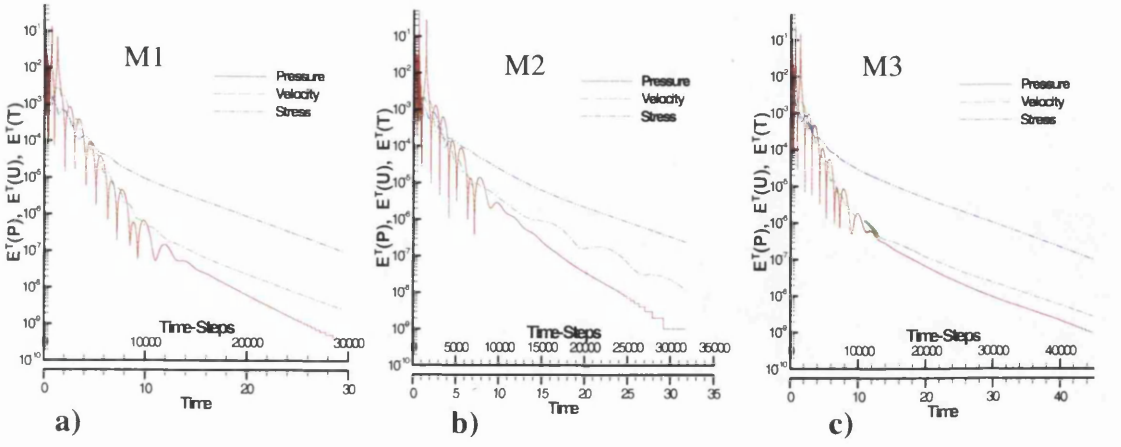

With flow state:

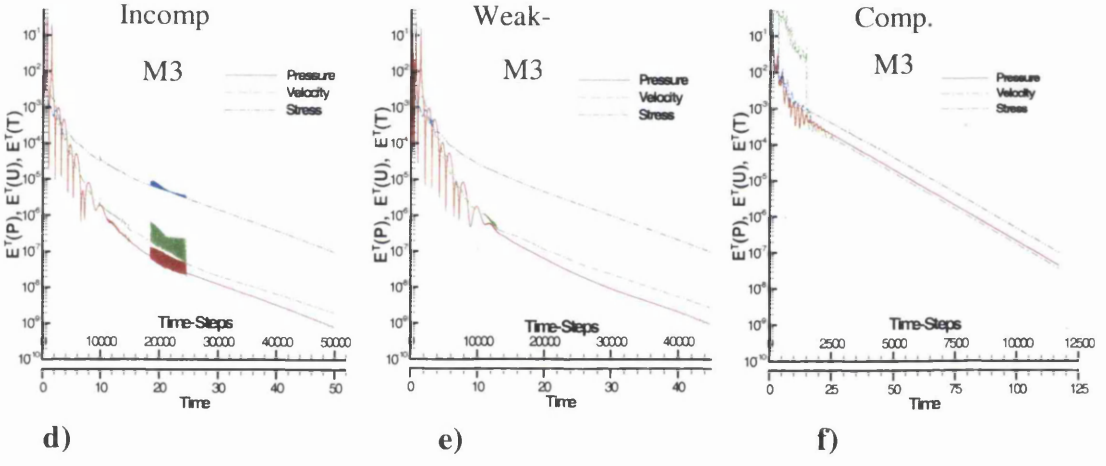

Figure 5.6: Error norm convergence history for velocity, $E^T(U)$, pressure, $E^T(P)$, and stress $E^T(T)$, We=1.0, Re=1.0. h-refinement (a,b and c) for weakly-compressible with $(m,B)=(10^4,10^4)$. Different flow scenarios, based on mesh M3 illustrated in d: incompressible, e: weakly-compressible and f: compressible with $(m,B)=(4,10^2)$

5.2.4 Under-relaxation: incompressible, weakly-compressible, and compressible

Based upon the above remarks, one illustrates, in Figure 5.6a-c, the different history tolerance results across the series of three meshes employed for weakly-compressible ($(m,B)=(10^4,10^4)$) flow. The history convergence tolerances across meshes for incompressible flows are similar in form to those of weakly-compressible and are discarded. Mesh (h) refinement has no noticeable effect on history tolerances for

compressible ($(m,B)=(4,10^2)$) flows, following the form shown for mesh M3 in Figure 5.6f. Results are also illustrated across flow scenarios in Figure 5.6d-f (incompressible, weakly-compressible and compressible flows). For all cases a We=1.0 is targeted from a quiescent initial state. The first observation is that, independent of mesh employed or flow type, convergence history tolerance always commences with an oscillatory pattern, typical of transient start-up conditions. About ten to fifteen time units are necessary to dampen these oscillations and recover a smooth convergence pattern. For weakly-compressible and incompressible flows, based on meshes M2 and M3, under-relaxation is necessary to reach the specified tolerance level. As anticipated by reducing mesh size from M2 to M3, optimum levels of the relaxation factors imply lesser need for relaxation. Note that for these flows, a time–step of 10^{-3} is employed, leading to steady-state solutions within thirty to fifty time units. Here, now that the choice of time-step is not only governed by the Courant number restriction, but also by the level of Weissenberg number. For *compressible flow* conditions, relaxation is unnecessary at this level of Weissenberg number, to reach the specific tolerance and enhanced smoothness in convergence is apparent beyond that of the incompressible case, upon the three test meshes (not shown here). This is due mainly to improved equation conditioning at Stage-2, through the modifications to accommodate for compressibility considerations (see Eq.(3.64), M_c and L^p), so that, a larger time-step is allowed ($\Delta t = 10^{-2}$). Independent of the spatial discretisation employed, a tight window of temporal convergence is observed, displaying a uniform and smooth trend. For compressible flow, independent of meshing, less computational time is demanded to reach a steady-state solution when compared to counterpart incompressible flow settings (30% more rapid). Finally, mesh refinement does not necessarily demand stringent reduction in time-step to reach the desired tolerance level (as is the case in the incompressible/weakly-compressible context). This gives confidence in numerical continuation between the different levels of compressibility.

5.3 Mesh (h) refinement

Through mesh refinement on the series of employed meshes, convergence in all solution component variables has been confirmed. Finally, consistency of the scheme is highlighted by the capability of the scheme to accommodate weakly-compressible flow

scenarios. There similar results are derived for incompressible and weakly-compressible representations.

Having established satisfactory convergence trends, independent of flow type or mesh employed, one interrogates field solution quality through pressure, principal stress N_1 (first normal stress-difference) and shear stress contour plots. All the results thus far have been for We=1.0 and Re=1.0. Each figure represents nine contour plots. Incompressible flow results are displayed on the left, weakly-compressible in the middle and compressible to the right. Solutions based on mesh M1 are illustrated at figure-top, M2 at centre, and M3 over figure-bottom. For each variable, it is practical to contrast scheme accuracy, based on mesh refinement, and scheme consistency whilst increasing Mach number (from the incompressible toward the compressible flow regime). In Figure 5.7, around the contraction zone, similar pressure contour patterns at equitable levels are observed for incompressible and weakly-compressible representations. Pressure-drop increases with mesh-density in all instances, being slightly higher for weakly-compressible as compared to the incompressible flow setting. For the more compressible regime, it is apparent that pressure–drop is higher (about ten percent) than with other flow settings, relating directly to compressibility effects. Similar conclusions may be drawn on principal stress contour plots presented in Figure 5.8. Here, the maximum level of stress is considerably larger upon mesh M3, when compared with M2 or M1, independent of flow representation. This increase is about ninety to ninety-five percent, indicating the strong presence of a singularity located at the re-entrant corner. Field distributions show little disparity between flow settings upon the remainder of the domain, away from the downstream-wall, increasing thereupon. In shear stress, there is a doubling in maximum stress level between mesh M1 and M3 solutions (typical values O(18 units) on M3 compare to O(9 units) on M1), indicating again the significant presence of a singularity. Note, that for each variable, the contour plots display similar patterns through mesh refinement or flow-type under consideration. Incompressible stress fields are corroborated by their close agreement with those in the published literature (see [46,151]).

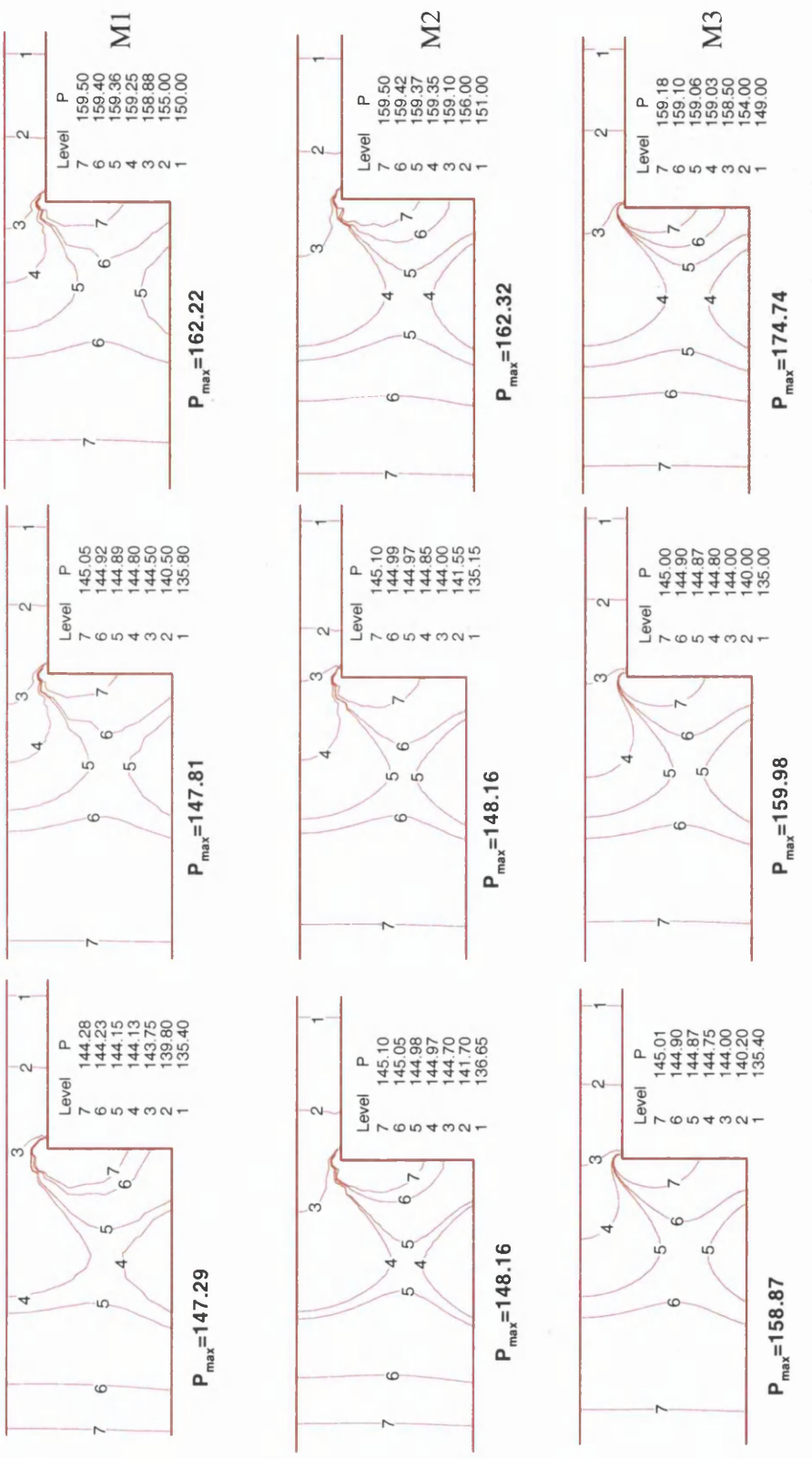

Figure 5.7: Pressure P contours, h-refinement (M1: top, M2: centre, M3: bottom), left: incompressible, middle: weakly-compressible and right: compressible flow. We=1.0, Re=1.0

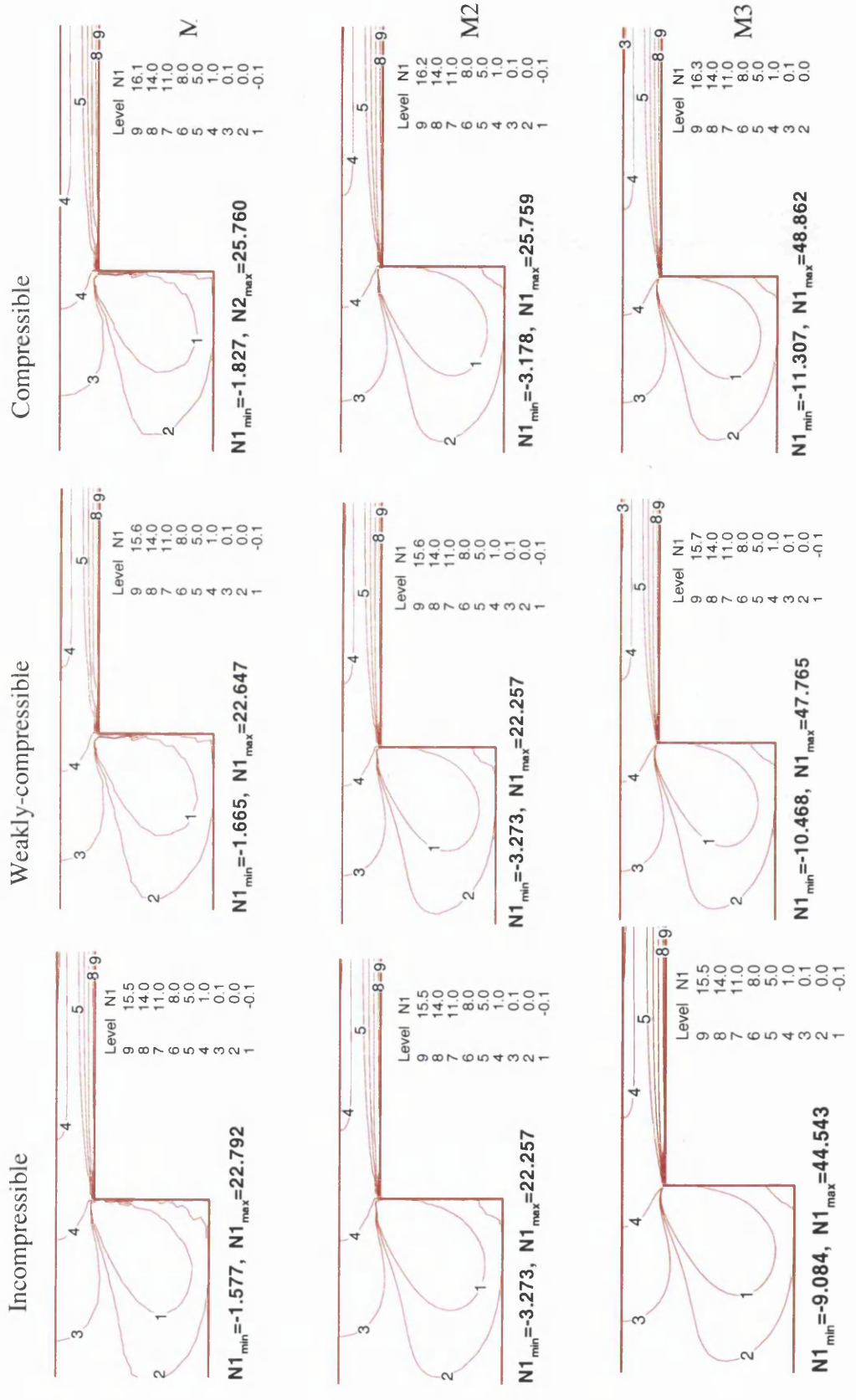

Figure 5.8: Principal stress N_1 contours, h-refinement (M1: top, M2: centre, M3: bottom), left: incompressible, middle: weakly-compressible and right: compressible flow. We=1.0, Re=1.0

Based on the finest mesh M3, streamlines contours plots for incompressible and compressible flows are illustrated in Figure 5.9. Similar incompressible streamlines contours at We=1.0 are presented in reference [151]. Contour profiles demonstrate little disparity between flow settings, except at the centre of the vortex zone, where the stream function peaks ($*10^{-4}$) increase from –1.86 (compressible) to –2.06 (incompressible), and stream function maxima increase from 1.00 (incompressible) to 1.28 (compressible). Finally, for compressible flow based on mesh M3, density and Mach number contours are plotted in Figure 5.10. Note, density contours are non-parallel in the upstream or downstream channel sections (as with pressure). This is due to the fact that under viscoelastic consideration, density is a function of the augmented pressure $\tilde{P}$, which takes into account the trace of stress (see Tait equation Eq.(3.5)). An increase of 28% in density arises between the inlet and outlet. Outlet Mach numbers of Ma=0.093 are approached under such compressible flow conditions.

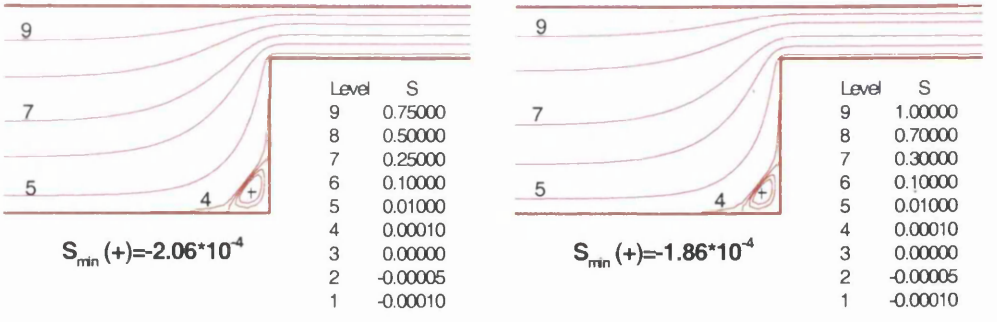

Figure 5.9: Streamline contours, incompressible (left) and compressible flow (right), mesh M3. We=1.0, Re=1.0

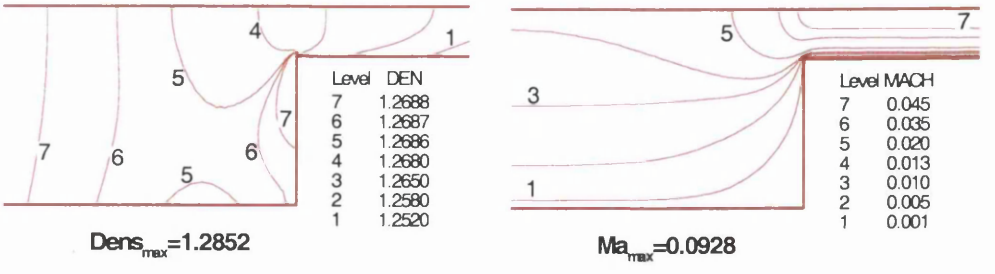

Figure 5.10: Density (left) and Mach number (right) contours for compressible flow setting, mesh M3. We=1.0, Re=1.0

5.4 Stress development

To highlight the nature of flow around the re-entrant corner, for *We*=1.0, stress profiles (τ_{xx}, τ_{xy}, τ_{yy}) at y=0.3 units (see Figure 5.1) are illustrated in Figure 5.11, across the three meshes and flow scenarios. For clarity in plotting, a shift in the position of the re-entrant corner for the different meshes has been applied. As anticipated there are no noticeable differences in stress plot results for incompressible and weakly-compressible representations, and also across all regimes for τ_{yy}; hence these are discarded accordingly. All plots reflect a prominent stress peak at the re-entry corner. The level of this peak increases with mesh refinement, and also, with greater levels of compressibility.

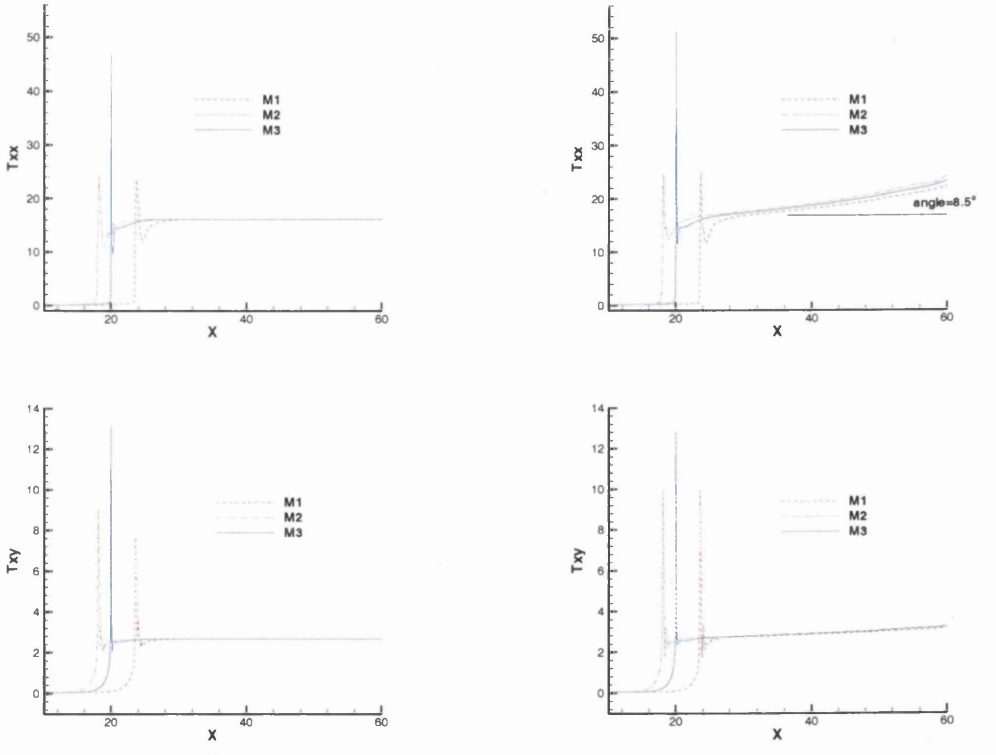

Figure 5.11: Stress profiles (τ_{xx}: top, τ_{xy}: bottom) along y=0.3, different meshes (M1, M2, M3) and flow scenarios (incompressible: left, compressible: right). *We*=1.0, *Re*=1.0

A major feature for the compressible flow lies in the growth of stress, τ_{xx}, near the boundary along the downstream wall (monotonic growth at an angle 8.5°). A corresponding feature arises to a lesser degree in the shear stress component, τ_{xy}. Such an expansion/growth of boundary stress is not present in incompressible or weakly-

compressible flow settings. Finally, note that compressibility does not lessen the strength of the corner solution singularity in stress.

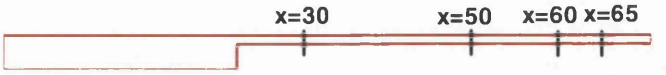

Figure 5.12a: Profile sampling x-positions for principal stress N_1 along downstream channel

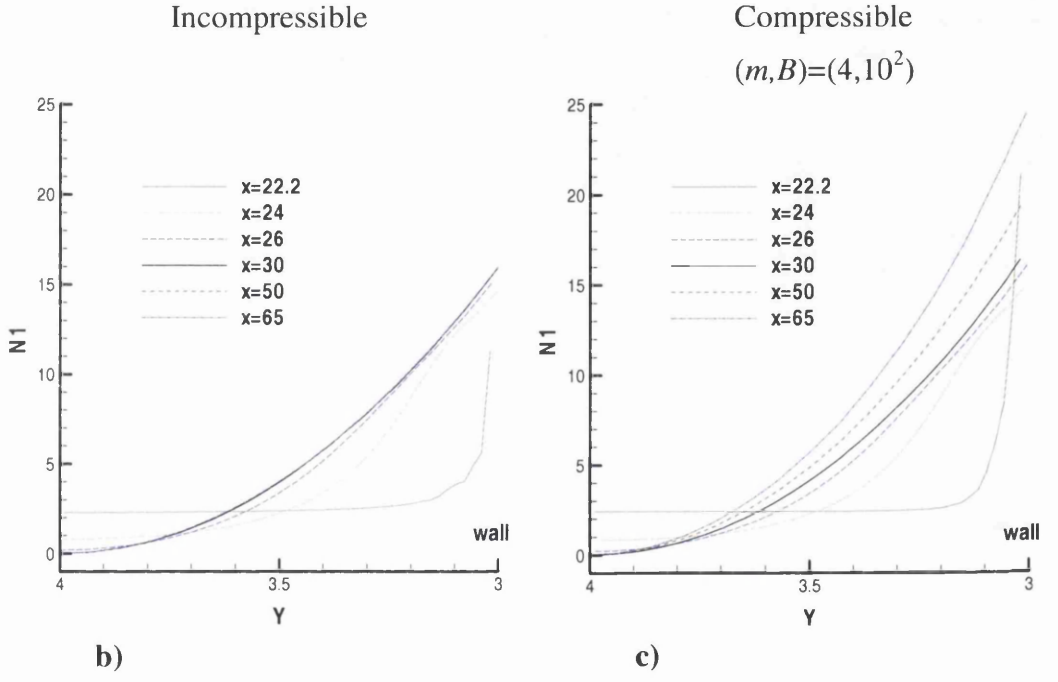

Figure 5.12b-c: Principal stress N_1-profiles across downstream channel section, sampling x-positions, mesh M3, b: incompressible, c: compressible. We=1.0, Re=1.0

Careful analysis of the boundary stress and stress profile development is conducted upon the principal first normal stress-difference, N_1. To this end, variation in stress across the channel, cross-section y=3 to y=4 units, is plotted at different downstream positions (see Figure 5.12). For the incompressible and compressible flow settings, results are illustrated in Figure 5.12b-c based on mesh M3. For the incompressible flows, beyond a downstream position of x=30 units there is hardly any apparent variation in the stress field through the channel cross-section. In contrast, there is more widening and sustain growth of stress-profiles along the wall for the more compressible flow conditions. In Figure 5.13, where for plotting clarity the cross-section dimension

has been zoomed some forty times, three-stress levels (contour values, 1, 5 and 15 units for τ_{xx}, and 0.5, 1.8 and 2.6 units for τ_{xy}) are plotted along the downstream channel wall. One observes the rapid onset of the boundary layer structure just beyond the contraction zone (contraction at x=22 units) for all flows. The sustained growth of stress along the downstream direction is detected off the channel wall into the flow.

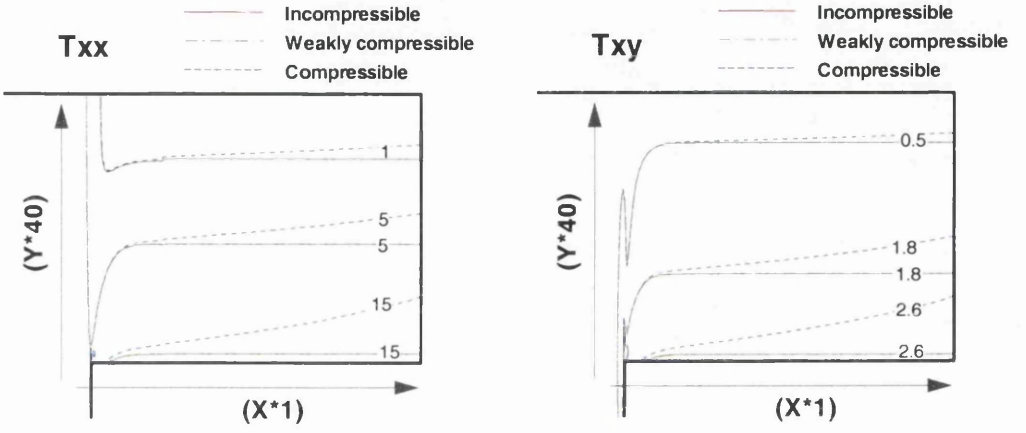

Figure 5.13: Stress profiles: τ_{xx} (right) and τ_{xy} (left) along downstream channel. Boundary layer growth for incompressible, weakly-compressible and compressible flow conditions, mesh M3. We=1.0, Re=1.0 (scaling indicated)

5.5 Conclusions

This study has provided new insight into the finite element modelling of viscoelastic compressible flows, where there is conscious focus upon the Oldroyd model, the Tait equation of state, and planar contraction flows. A fresh look is proposed at pressure-correction type formulations to tackle such a setting, so utilising pressure as a primary variable emanating from conventional incompressible flow representation. In this manner, both evolutionary and steady-state flows have been accurately and consistently resolved, covering the low Mach number regime. A unified (single) finite element scheme is advocated, with flexibility to cover compressible, weakly-compressible, and incompressible flow situations. Various aspects of study have revealed: (*i*) the role and importance of relaxation across fractional-staged equations; (*ii*) sensitivity of the scheme to selection of (Δt, h, m_{itn})-parameters, within the different flow settings; (*iii*) convergence trends and contrast of flow field response.

Pressure-drops rise when greater levels of compressibility are incorporated (here by order 10%). One observes the fact that the solution singularity (stress at re-entrant corner) may actually increase in a more compressible setting, whilst downstream-wall stress profiles broaden along the wall, away from initial inception of the boundary layer, just beyond the re-entrant corner. This is in stark contrast to the incompressible scenario, where wall-stress profiles sustain their initial width far downstream. Stress boundary layers are provoked almost directly beyond the re-entrant corner in all flows studied. Extensions to the current study shall be oriented towards seeking solutions up to critical levels of Weissenberg number, and considering temporal adjustment of the compressible parameter set.

5.6 Appendix 5.A: Fractional staged equations and relaxation procedure

The relaxation procedure may be applied at different TGPC stages and has a direct effect on the local time-step-stage value. To clarify this point, let us consider the first and second stages of TGPC scheme for *incompressible* fluid in compact matrix form:

$$A_U\left(U^* - U^n\right) = \Delta t b_U \tag{5.A.1}$$

$$K\left(P^{n+1} - P^n\right) = \frac{1}{\theta \Delta t} LU^*. \tag{5.A.2}$$

Here, n denotes the time level, Δt the local time-step, U^*, U, P, nodal vectors of non-divergence-free velocity, velocity and pressure, respectively, b_U the right-hand-side of Stage-1b. A_U and K are velocity and pressure governing matrices (mass and stiffness).

In order to relax velocity by α_U at the end of Stage-1, one may introduce a relaxed non-divergence-free velocity $\tilde{U}^*$, viz.:

$$\tilde{U}^* = \alpha_u U^* + (1-\alpha_u)U^n = U^n + \alpha_u\left(U^* - U^n\right). \tag{5.A.3}$$

Note, for convenience of representation one may interpret the relaxation parameter r_U of the text via $\alpha_U = (1 - r_U)$. Taking advantage of Stage-1b equation (Eq.(A.1)), and re-arranging Eq.(A.3), yields:

$$A_U\left(\tilde{U}^* - U^n\right) = \alpha_u \Delta t b_U \tag{5.A.4}$$

an under-relaxed representation for equation Stage-1b, casting velocity solution relaxation onto the local time-step, via scaling with factor α_U.

To enforce relaxation upon Stage-2 alone, a relaxed pressure solution-component is introduced:

$$\tilde{P}^{n+1} = \alpha_P P^{n+1} + (1-\alpha_P)P^n = P^n + \alpha_P\left(P^{n+1} - P^n\right). \tag{5.A.5}$$

Revisiting Stage-2 equation (Eq.(5.A.2)) with relaxation, and taking into account Eq.(5.A.5), a relaxed Stage-2 equation is gathered:

$$K\left(\tilde{P}^{n+1} - P^n\right) = \frac{\alpha_P}{\theta \Delta t} LU^*. \tag{5.A.6}$$

Thus, at this fractional-equation stage, relaxing Stage-2 is equivalent to scaling the local pressure equation time-step by $1/\alpha_P$.

Finally, one may appreciate that relaxing velocity alone (and not pressure), conveys some relaxation into the local time-step at Stage-2, through U^* in the rhs-vector. Reconsidering the relaxed non-divergence-free velocity ($\tilde{U}^*$) of Eq(5.A.3) and applying the discrete matrix equivalent to the divergence operator, L, yields:

$$L\tilde{U}^* = (1-\alpha_u) LU^n + \alpha_u LU^* \tag{5.A.7}$$

which will impact upon the system through the Stage-2 equation accordingly,

$$K\left(P^{n+1} - P^n\right) = \frac{1}{\theta\Delta t} L\tilde{U}^* = \frac{\alpha_U}{\theta\Delta t} LU^* + \frac{(1-\alpha_U)}{\theta\Delta t} LU^n . \tag{5.A.8}$$

Here, one may appeals to the continuity equation to neglect the term $LU^n \approx 0$ on the right-hand-side of Eq.(5.A.8), giving:

$$K\left(P^{n+1} - P^n\right) \approx \frac{\alpha_U}{\theta\Delta t} LU^* . \tag{5.A.9}$$

Therefore, one appreciates that by relaxing velocity at Stage-1, scaling is imparted on local time-steps at both Stage-1 and Stage-2. Similar arguments hold for the compressible flow context.

CHAPTER 6

Viscoelastic Liquids Flow: Hybrid Finite Element/Volume Scheme†

In the previous chapters (see also [14,79,80,154]), a numerical scheme has been developed for Newtonian and viscoelastic weakly-compressible liquid flows based on a pure *fe* methodology. There, the capability of this method has been demonstrated to deal with complex flows. In this chapter, a hybrid finite element/finite volume (*fe/fv*) algorithm is introduced to handle such flows at low Mach number and Reynolds number. The finite volume (*fv*) sub-cell scheme is incorporated for the hyperbolic constitutive equation, considered here of Oldroyd-B form. The continuity/momentum balance is accommodated through a semi-implicit fractional-staged/pressure-correction *fe*-formulation.

The fundamental idea behind this scheme lies in the fact that the equations of motion (continuity and momentum) in low Reynolds regimes (main interest in the Rheology community) display elliptic-dominated character. Whilst, for the stress constitutive equation the type is hyperbolic. Standard Galerkin *fe*-approximations are optimal for self-adjoint (elliptic) problems in the sense that the discretisation error is bounded by the error in the best approximation of the solution via functions in the trial space (see [3]). Therefore, standard Galerkin *fe*-methods are ideal for the discretisation of

† Material of this chapter has been shaped in a paper "Computation of Incompressible and Weakly-Compressible Viscoelastic Liquids Flow: finite element/volume schemes" by I. J. Keshtiban, F. Belblidia and M. F. Webster, and accepted for publication in *Journal of Non-Newtonian Fluid Mechanics* (2004).

diffusion-based problems. However, in circumstances where Péclet numbers are high, non-symmetric convective terms introduce some hyperbolic solution character into the system; this deteriorates the optimal properties of a standard Galerkin *fe*-approximation. Similarly space-centred schemes display spurious oscillations for high mesh Péclet numbers. For example, GLS schemes have been proposed to stabilise the Galerkin formulation for convection-dominated flows. The SUPG-variant has been successfully employed in the approximation of these constitutive equations (see chapter five and also [23]). In addition, some strategies have emerged via stress-splitting formulation, in order to artificially include some ellipticity into the system of equations, wherever these equations physically express hyperbolic character, lacking any diffusion term (see [10]). Furthermore, it has been observed that *fv*-schemes display reasonably good performance characteristics in approximating hyperbolic equations; offering significantly less computational overheads, compared to their *fe*-counterparts.

Wapperom and Webster [151,152] employed a Galerkin *fe*-formulation for the equations of motion (mass and momentum) and a *fv*-form for the constitutive equation alone. One may find close similarity between this scheme and the so-called *4x4* stress sub-elements, introduced by Marchal and Crochet [95] in the mid-1980's. For the choice of element, a six-node (P2P1) (see [55]) element was considered, with quadratic interpolation for velocity and stress, and linear for pressure based on vertex nodes. The *fe*-grid is used as a platform for the *fv*-grid, from which control volumes are constructed. Each *fv*-cell is one of four sub-triangles formed by connecting the mid-side nodes of the parent element (see Figure 6.1a). Stress variables are located at the vertices of the *fv*-cells, and may be used directly without interpolation, as *fe*-nodal values. Selecting this type of element, supports some important features. For the calculation of velocity under low Reynolds number regimes, employing a quadratic element is well-suited in capturing the flow pattern near solid boundaries. This enhances the quality of velocity-gradient representation, which has a major impact upon the performance of the numerical scheme within boundary layers. The parent *fe*-element structure has advocated a recovery-type technique (see Matallah *et al.* [98]) and has enhanced the quality of velocity gradients to second-order. In comparison, Aboubacar and Webster [4] have observed that linear-form elements (sub-cell) for stress are more suitable in damping numerical noise, and hence, prove more successful in attaining higher *We*-solutions (recall Basombrío *et al.* [13] likewise, for quadratic to linear stress

interpolation results). Subsequently, the hybrid *fe/fv*-scheme enjoys improved quality of velocity gradients, obtained via recovery applied over the parent *fe*-element, with linear-form elements for stress over sub-cells.

6.1 Numerical Discretisation

Over the last ten years a family of cell vertex finite volume methods for the solution of the two-dimensional scalar advection equation has evolved, collectively known as multidimensional upwind fluctuation distribution schemes, see for example [68,69]. For the approximation of steady state flows on unstructured triangular grids, these have reached a degree of maturity whereby the multidimensional schemes reproduce most of the advantages of upwind schemes in one dimension: second-order approximation of smooth solutions, monoticity in the presence of discontinuities, and rapid necessity for additional artificial viscosity. A distinctive and attractive feature of these schemes is that they are computationally compact. They can be written as loops over elements and when processing an element no reference is made to data outside that element. This makes for efficient parallelisation. A theoretical attraction is that the update schemes can incorporate insights derived from the nature of the multidimensional physics.

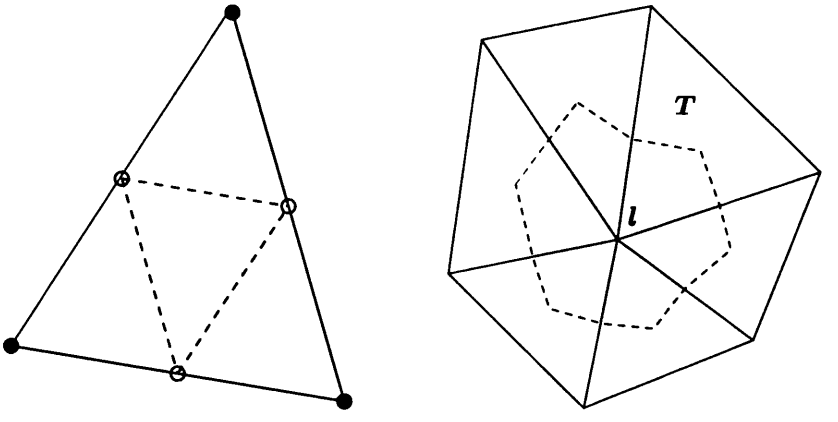

Figure 6.1: (a) *fe* with 4 *fv* sub-cells, (b) MDC area for node *l*

6.1.1 Advection scheme

Before attempting to model the stress equations one should consider the numerical solution of the linear advection equation, which is expressed as follows:

$$\frac{\partial \phi}{\partial t} + \vec{a} \cdot \vec{\nabla} \phi = 0, \tag{6.1}$$

where $\vec{a} \in R^2$ is a constant vector. This is to be solved numerically over an arbitrary triangulation of a region Ω, with appropriate conditions being imposed on the boundary of the domain, $\partial\Omega$. The fluctuation associated with this equation is a cell-based quantity, which is given by

$$R_T = \iint_{\Omega_T} \frac{\partial \phi}{\partial t} dxdy = -\iint_{\Omega_T} \vec{a} \cdot \nabla \phi dxdy = \oint_{\partial\Omega_T} \phi \vec{a} \cdot d\vec{n}, \tag{6.2}$$

where $\partial\Omega_T$ is the boundary and Ω_T the area of triangle T (Figure 6.2a), and $d\vec{n}$ is the inward normal to the boundary of the element. The numerical scheme is constructed from a discretisation of the integrated form of Eq.(6.2) by evaluating the quantity defined in within each cell and then distributing it to the nodes of the grid, for example, a distribution of the fluctuation is carried out.

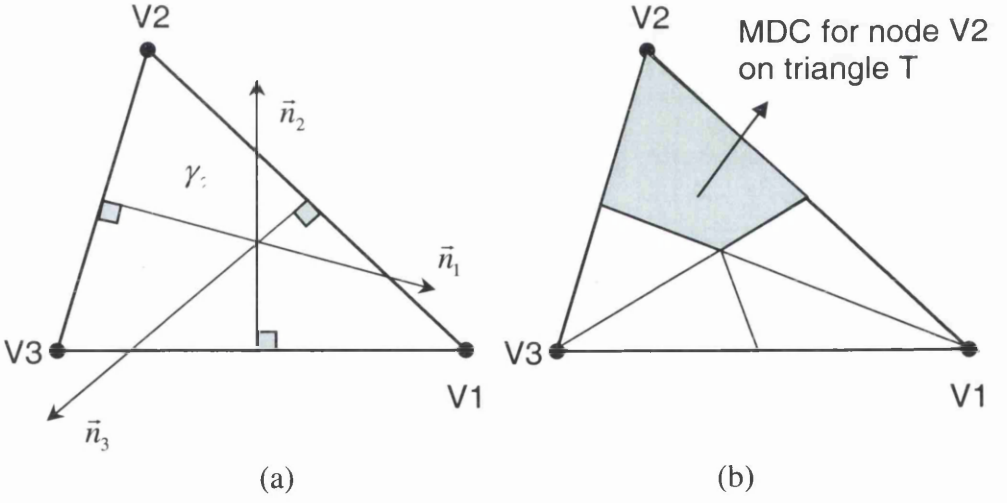

Figure 6.2: (a) A *fv* sub-cell with vertices V*i*, (b) MDC area for node V2

The discrete form for R_T is evaluated by employing appropriate linearisation. Here we consider ϕ varies linearly along each side, so the fluctuation can be easily evaluated viz.

$$\begin{aligned} 2R_T &= (\phi_1 + \phi_2)\vec{a} \cdot \vec{n}_3 + (\phi_2 + \phi_3)\vec{a} \cdot \vec{n}_1 + (\phi_3 + \phi_1)\vec{a} \cdot \vec{n}_2 \\ &= -\phi_1 \vec{a} \cdot \vec{n}_1 - \phi_2 \vec{a} \cdot \vec{n}_2 - \phi_3 \vec{a} \cdot \vec{n}_3, \end{aligned} \tag{6.3}$$

where $\vec{n}_i$ is the inward normal to edge i scaled by the length of edge i. Thus, the fluctuation can be expressed simply as:

$$R_T = -\sum_{i=1}^{3} k_i \phi_i \text{ , where } k_i = \frac{1}{2}\vec{a}\cdot\vec{n}_i. \tag{6.4}$$

The k_i are important because they can be adapted to determine the direction of flow through an edge: if $k_i > 0$ then flow enters the triangle through edge i but if $k_i < 0$, edge i is an outflow edge. It is clear that one has

$$\sum_{i=1}^{3} k_i = 0. \tag{6.5}$$

The temporal term in Eq.(6.2) may be discretised via the forward Euler scheme as follow:

$$\iint_{\Omega_T} \frac{\partial \phi}{\partial t} dxdy = \frac{1}{\Delta t}\iint_{\Omega_T} \left(\phi^{n+1} - \phi^n\right) dxdy = \frac{1}{\Delta t}\sum_{l=1}^{3} \left(\phi^{n+1} - \phi^n\right)_l \hat{\Omega}_l^T \text{ ,} \tag{6.6}$$

where $\hat{\Omega}_l^T$ is the area of the median dual cell (see Figure 6.2b) corresponding to node l (one third of the total area of the triangle T).

Within the FD scheme, the flux R_T is calculated over the individual finite volume cell T and then distribution to the nodes of that cell. The update form of triangle T to vertex l on that triangle is:

$$\hat{\Omega}_l^T \left(\phi_l^{n+1} - \phi_l^n\right) = \Delta t \alpha_l^T R_T \text{ ,} \tag{6.7}$$

the coefficients α_l^T are weights which determine the distribution of the flux R_T to vertex l of triangle T (see below).

Properties of FD schemes are closely related to how the fluctuation within each triangle should be distributed to its vertices. For a suitable choice of α_l^T, the theory associated with variants of FD schemes possess some criteria such as *conservation*, *positivity* and *linear preservation*.

Conservation yields the requirement that the sum of the coefficient α_l^T over the each triangle T should satisfy:

$$\sum_{l=1}^{3} \alpha_l^T = 1. \tag{6.8}$$

Positivity means that each ϕ_l^{n+1} is a convex combination of nodal values at the previous time-step, ϕ_j^n:

$$\phi_l^{n+1} = \sum c_j \phi_j^n, \tag{6.9}$$

where the coefficients c_j are positive. Positivity guarantees a maximum principle for the discrete steady solution of the linear advection equation, thus prohibiting the occurrence of new extrema and imposing stability on the explicit scheme [133]. A stronger, but more easily verifiable condition, is local positivity, which requires that the contribution of each triangle, taken separately, is positive. A linear positive scheme is TVD [151]. For non-linear schemes, the positivity criterion is less stringent than TVD, whilst still maintaining the favourable properties of suppression of new extrema in the solution and guaranteeing stability of the explicit time-stepping scheme. Ensuring positivity of the flux distribution has been only an issue for the flux terms and may not be an appropriate criterium for source term treatment; the presence of sources may produce new, physically meaningful extrema that should not be suppressed.

Linear preservation requires that the scheme preserves the exact steady state solution whenever this is a linear function in space for an arbitrary triangulation of the domain. This is closely related to the notion of second-order accuracy, commonly discussed under finite difference schemes, although it is an accuracy on the spatial discretisation only.

A linear scheme does not have to be linearity preserving. For a linear scheme, ϕ_l^{n+1} is a linear combination of solution values at the previous time-step *n*, so that the coefficients c_j in Eq.(6.9) are constant. When written in the form Eq.(6.7), the two possibilities of having a linear scheme, are either for the coefficient α_l^T to be independent of ϕ, in which case it is linearly preserving, or for

$$\alpha_l^T = \frac{\beta_l^T}{R_T}, \tag{6.10}$$

where the coefficient β_l^T depends linearly on ϕ summing to R_T. This fact can be used to prove that linear schemes cannot be both positive and linearly preserving [151]. For certain flux distribution schemes, notably linear positive schemes, it is more convenient to express the distribution of the coefficients β_l^T.

At this point, it is convenient to divide linear schemes into two class, those that satisfy positivity and the remainder that satisfy linear preservation. Only a non-linear scheme can satisfy both these properties simultaneously.

6.1.2 Fluctuation distribution schemes

In this section, some choices are discussed for the coefficient α_l^T and β_l^T. Henceforth, superscript T is dropped in the α and β coefficients, for the reason of clarity.

For flux distribution schemes, it is important to distinguish between instances of triangles with one (Figure 6.3a) and two inflow (Figure 6.3b) sides. The inflow sides are determined by the sign of the coefficient k, which has been defined in Eq.(6.4). A positive k_l indicates that the advection speed a is inflowing across the side opposite vertex l. Due to Eq.(6.5), it is ensured that each triangle has a maximum of two inflow or two outflow sides.

By sending the flux of the *fv*-cell to the downstream node, triangular cells with only one inflow side can satisfy both the positivity and linearity preservation properties simultaneously. For example with $k_i > 0$, $k_j < 0$, $k_k < 0$, (see Figure 6.3a), we would have:

$$\alpha_i = 1, \quad \alpha_j = 0, \quad \alpha_k = 0. \tag{6.11}$$

The various flux distribution schemes only differ for the case of two inflow sides, as illustrated in Figure 6.3, for which the flux is distributed over the nodes i and j ($\alpha_k = 0$). One deliberates here to discuss briefly two specific flux distribution schemes that we shall consider. A linear LDB-scheme, that satisfies linearity preservation, and the PSI-scheme, a non-linear scheme that is both positive and linearity preserving.

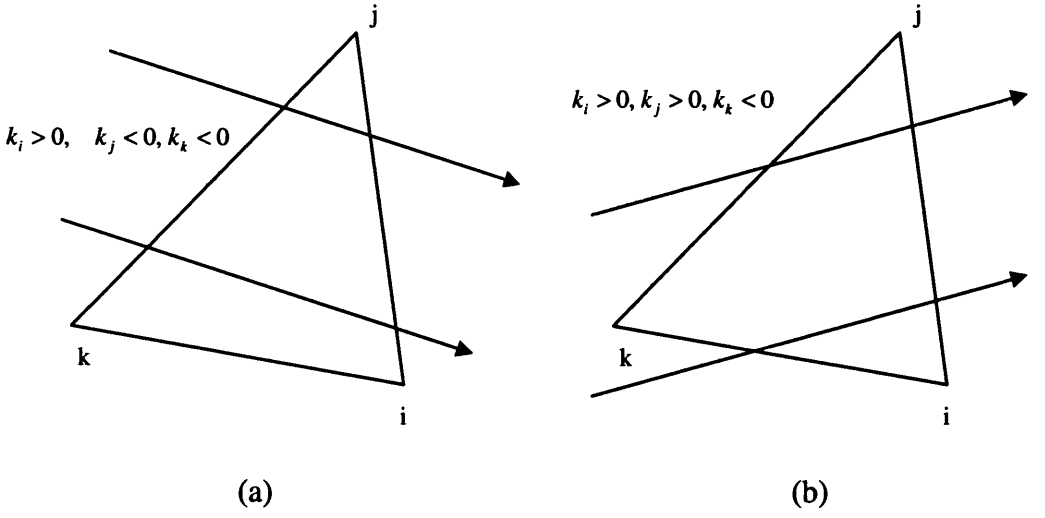

Figure 6.3. Triangular cells: (a) with one, (b) two inflow sides

6.1.3 The LDB-scheme

The Low Diffusion B (LDB) scheme is a linear α-scheme that is linearity preserving, which demonstrates a relatively small amount of numerical diffusion in comparison with a linear positive scheme. Based on our previous experience for model problems, this LDB-scheme is based on the angles in the triangle on both sides of the advection speed vector *a*. The alternative LDA-scheme is based on the corresponding area split of the triangle. With the angles γ_1 and γ_2, defined in Figure 6.4, the α-coefficients are expressed viz.

$$\begin{aligned} \alpha_i &= (\sin\gamma_1 \cos\gamma_2)/\sin(\gamma_1+\gamma_2), \\ \alpha_j &= (\sin\gamma_2 \cos\gamma_1)/\sin(\gamma_1+\gamma_2), \\ \alpha_k &= 0. \end{aligned} \tag{6.12}$$

The closer the advection speed *a* is to being parallel to one of the boundary sides, the larger is the contribution to the downstream node at that boundary.

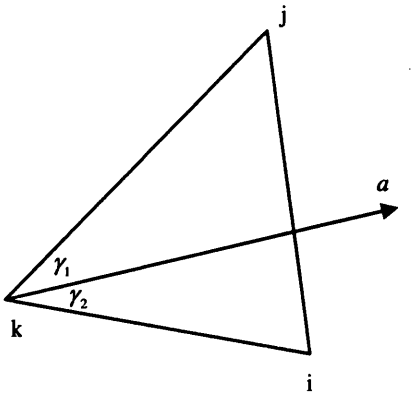

Figure 6.4: Graphical representation of LDB-parameters; constant advection speed, *a*

6.1.4 PSI-scheme

The PSI-scheme is a non-linear scheme that is both positive and linearity preserving. With definitions

$$\beta_i = -k_i(\phi_i - \phi_k)$$

$$\beta_j = -k_j(\phi_j - \phi_k),$$

we have for $\beta_i + \beta_j > 0$,

$$\alpha_i = \beta_i / (\beta_i + \beta_j),\ \alpha_j = \beta_j / (\beta_i + \beta_j),$$

and for $\beta_i + \beta_j < 0$,

$$\alpha_i = 1,\quad \alpha_j = 0 \quad \text{for} \quad |\beta_i| > |\beta_j|,$$

$$\alpha_i = 0,\quad \alpha_j = 1 \quad \text{for} \quad |\beta_i| < |\beta_j|.$$

For $\beta_i = -\beta_j$ (zero flux), the default setting of $\alpha_i = \alpha_j = 1/2$ prevails.

6.1.5 Employing FD-schemes for discretisation of stress equations

In the hybrid *fe/fv* approach of Wapperom and Webster [151], momentum and continuity equations are discretised via the Galerkin finite element method whilst stress constitutive equations are discretised via a finite volume FD-scheme. The Galerkin discretisation has been presented in chapter 3. Here, discretisation of the stress equations is discussed. To this end, Eq.(3.3) may be expressed in the following form

$$\frac{\partial \tau}{\partial t} = -R + Q \tag{6.13}$$

$$R = u \cdot \nabla \tau , \tag{6.14}$$

$$Q = \frac{1}{We}\left(2\frac{\mu_e}{\mu} d - \tau \right) + L \cdot \tau + \tau \cdot L^T \tag{6.15}$$

where R and Q are the flux and the source terms, respectively. It is common practice to refer to a single scalar component τ of the stress tensor, in correspondence with the flux and the source terms. With the aid of the Gauss divergence theorem on the flux term, integration of Eq.(6.13) over a control volume Ω for each stress component τ yields:

$$\frac{\partial}{\partial t} \iint_{\Omega} \tau d\Omega = \oint R \cdot n d\Gamma + \iint_{\Omega} Q d\Omega . \tag{6.16}$$

The flux and temporal terms may be evaluated as discussed in section 6.2.1. Correspondingly, the source term integral is evaluated from the linear velocity and stress representation per *fv*-cell. Velocity gradients may be approximated via linear consideration of velocity on a *fv*-cell or quadratic representation of velocity per parent *fe*-element or furthermore via recovery schemes to obtain higher order approximations for this term. When source terms are involved, the standard treatment advocated widely in the literature consists in dealing separately with the flux and the source terms (inconsistent approach). As the source terms are of a similar form to temporal terms, likewise, the appropriate choice of control volume for these terms would be the median dual cell (MDC) as explained in the previous section. However, this approach is inconsistent: there is incompatibility due to the selection of different areas for the source and flux terms. This is particularly important for stress equations where source terms can be large in comparison to the convection term. A remedy for this is to treat source terms as for the flux terms. Therefore two different alternatives for evaluating source terms may be considered as follows:

$$Q_{\Omega_l} = \iint_{\Omega_l} Q d\Omega , \qquad \text{where } \Omega_l = \begin{cases} \Omega_T \\ \Omega_{MDC} \end{cases} . \tag{6.17}$$

Henceforth, we will express evaluated integral terms over Ω_T and Ω_{MDC} with subscripts of *T* and *MDC* respectively.

The *inconsistent* variant of the discrete form of Eq.(6.16) may be written as follow:

$$\hat{\Omega}_l^T \frac{\tau^{n+1}-\tau^n}{\Delta t} = \alpha_l^T R_T + Q_{MDC}, \tag{6.18}$$

here $\hat{\Omega}_l^T$ is the MDC of the triangle T around node l. This standard provides inaccurate results, even for simple model problems (steady sink flow [24] and channel flow [152] for Oldroyd-B model). As a consequence, a consistent approach has been proposed by Wapperom and Webster [152]. With this formulation, both flux and source terms are calculated over the same control volume, and distributed together, via factors α .The *consistent* form formulation may be expressed as follow:

$$\hat{\Omega}_l^T \frac{\tau^{n+1}-\tau^n}{\Delta t} = \alpha_l^T \left(R_T + Q_T\right). \tag{6.19}$$

The difference between Eq.(6.18) and Eq.(6.19) lies in the control volume area of reference for a source term Q. The consistent form based on Eq.(6.19) performed well. It has provided second-order accurate results for particular steady-state problems: sink flow [24] and Cartesian test problems [152]. Unfortunately, such schemes lack stability. For example, the consistent approach was unable to reach a convergence steady-state solution beyond *We*=1 for the channel flow [152], a pure shear flow. This is may due to the non-consistency in discretisation of the temporal term. For a time-marching algorithm, consistency in the transient state is crucial for reaching higher *We*-solutions. Aboubacar and Webster [4] proposed CT2-scheme variant, to include consistent area-weighting for fluctuation-distribution and MDC-term. This, in turn enhanced stability significantly in complex flows (attaining levels $We \approx O(3)$ on highly refined meshes for the benchmark 4:1 contraction flow of an Oldroyd-B model fluid [4]).

Webster and co-workers [156] have generalised these formulations to resolve transient problems. The starting point is to consider separately the FD and MDC contributions to the nodal update. For a single *fv*-subcell T, and a given node l in T, the segregated contributions read:

$$\frac{\alpha_l^T \Omega_T}{\Delta t}\left(\tau^{n+1}-\tau^n\right) = \alpha_l^T \left(R_T + Q_T\right) \quad \text{on } \Omega_T, \tag{6.20}$$

and

$$\frac{\hat{\Omega}_l^T}{\Delta t}\alpha_l^T \left(\tau^{n+1}-\tau^n\right) = \left(R_{MDC} + Q_{MDC}\right)_l \text{ on } MDC. \tag{6.21}$$

Blending equations Eq.(6.20) and Eq.(6.21) with adjustable parameters δ_T and δ_{MDC}, and summing over all *fv*-subcells surrounding node l yields the present CT3-scheme

$$\left(\Omega_{FD}+\Omega_{MDC}\right)\frac{\tau^{n+1}-\tau^{n}}{\Delta t}=\sum_{\forall T_l}\delta_T\alpha_l^T b_T+\sum_{\forall MDC_{ll}}\delta_{MDC}^T b_{MDC}^l\,, \tag{6.22}$$

where $b_T=\left(R_T+Q_T\right)$, $b_{MDC}^l=\left(R_{MDC}+Q_{MDC}\right)^l$, $\Omega_{FD}=\sum_{\forall T_l}\delta_T\alpha_l^T\Omega_T$ and $\Omega_{MDC}=\sum_{\forall MDC_l}\delta_{MDC}^T\hat{\Omega}_l^T$.

Theoretically, δ_T and δ_{MDC} are mutually linked and complementary. One notes, Eq.(6.22) is reorganised as

$$\frac{\tau^{n+1}-\tau^{n}}{\Delta t}=\frac{\sum_{\forall T_l}\delta_T\alpha_l^T b_T}{\Omega_1}+\frac{\sum_{\forall MDC_{ll}}\delta_{MDC}^T b_{MDC}^l}{\Omega_2}\,, \tag{6.23}$$

The CT3-scheme is obtained by setting $\Omega_1=\Omega_2\equiv\Omega_{FD}+\Omega_{MDC}$. The CT2-scheme variant is obtained with the combination of $\Omega_1=\Omega_{FD}$ and $\Omega_2=\Omega_{MDC}$, whilst the CT0-scheme of [152] would correspond to $\Omega_1=\Omega_2=\hat{\Omega}_l$ .Wapperom and Webster [152] defined $\delta_T=\xi/3$ if $|\xi|\le 3$ and 1 otherwise, and $\delta_{MDC}=1$. Here one may consider, $\xi=We(a/h)$, with a the magnitude of the advection velocity per *fv*-cell and h the square-root of the *fv*-subcell in question.

With the above parameter combinations, both CT0 and CT2 variants have proved inadequate in tracking transient solution evolution in a start-up Poiseuille flow [157]. There, significant improvement in transient accuracy was achieved with the CT2-scheme by appealing to a dynamic δ_{MDC} factor, in the form $\delta_{MDC}=1-\delta_T$. This simply recognises the complementary nature of the relative strength between flux (better discretised through FD, δ_T-weight) and source terms (optimally represented via MDC, δ_{MDC}-weight). The dependence of δ_T upon local averaged-velocity provides an estimate of the local flux-magnitude. In contrast, the CT3-scheme is relatively insensitive to the dynamic setting of δ_{MDC} for this shear flow problem, being well-reproduced with the full inclusion of the MDC contribution ($\delta_{MDC}=1$). This is a clear indication of the superior consistency in the formal derivation of the CT3-scheme. Indeed, the CT3-

scheme includes consistent control-volumes for flux and source terms on the rhs, and consistent area-weighting for the time-terms on the lhs of the equations.

6.2 Discussion of results

Flow through an abrupt contraction for an Oldroyd-B fluid is well-documented in the literature, where it is recognised as a valuable benchmark problem, useful to qualify numerical stability of schemes at high *We*-levels. Here, a literature review is presented for this problem.

6.2.1 Literature review

A challenging feature of the abrupt contraction (non-smooth) flow problem is the presence of a stress singularity at the re-entrant corner, which impacts upon stability properties of numerical schemes. Many fluid models suffer a limiting Weissenberg number (*We*), beyond which numerical solutions fail. This issue has become known as 'the high *We* problem-HWNP', drawing considerable attention over the last two decades or so. In *the incompressible context*, one may cite those based on the 'pure' *fe*-framework, from Carew et *al.* [23] and Matallah et *al.* [98], providing literature reviews and common findings on vortex behaviour. Subsequently, Wapperom and Webster [151,152] introduced a hybrid *fe/fv*-methodology. This was developed further in Aboubacar and Webster [4]. There, mesh refinement was conducted for an Oldroyd-B model. Extension of this work in Aboubacar *et al.* [1,2], focused on alternative geometries (planar and axisymmetric, sharp- and rounded-corners) and several viscoelastic models (Oldroyd-B and PTT-variants). An overview of experimental and numerical studies was also documented there.

Elsewhere, Guénette and Fortin [56] proposed a stable and cost-effective mixed *fe*-method, a variant of the EVSS formulation. Numerical results were presented for the PTT fluid model. Yurun [163] compared two variants of EVSS *fe*-schemes on this benchmark problem (discontinuous Galerkin DG and continuous SUPG). The DG/EVSS scheme was observed to reflect significant improvement over the SUPG/EVSS variant at higher *We*-levels (smoothness in solutions and enhanced robustness, see on for *fv*-solutions). The above subject matter is covered in the comprehensive literature review of Baaijens [10].

In *the context of fv-formulations*, Phillips and Williams [114,115] investigated the differences in vortex structure and development, with and without inertia. This work covered planar and axisymmetrical configurations, and was based on a semi-Lagrangian *fv*-method. Similarly, Mompean [101] proposed an approximate algebraic-extra-stress fluid model, via a second-order *fv*-scheme, employing a staggered-grid technique. Likewise, Alves *et al.* [5] invoked an extremely refined mesh to chart in detail the development of both vortex-size and intensity for Oldroyd-B and PTT fluids. Similarly to Aboubacar *et al.* [1,2], their work† highlighted that suitable mesh refinement is necessary in the re-entrant corner zone to sharply capture the singularity there. This often reduces the critical level of *We* (We_{crit}) attained, when compared to that gained on poorer quality meshes. Predominantly, the above cited studies are restricted to steady-state solutions and the incompressible flow domain.

Under *compressible liquid flow considerations*, Webster and co-workers [14,79,80,154] have extended an incompressible viscoelastic *fe*-scheme to handle weakly-compressible flows. The emerging new scheme has been validated on several benchmark problems, including that of present interest of an abrupt four-to-one contraction flow. Over its incompressible counterpart, no loss of accuracy was observed, and convergence properties were enhanced, in seeking steady-state solutions.

6.2.2 Problem specification

The compressible *fe* and hybrid *fe/fv*-volume schemes are compared and contrasted, focusing on the sharp-corner 4:1 planar contraction flow. Employed meshes, imposed boundary conditions and Tait equation of state parameters are selected in a similar fashion that of chapter five. A suitable dimensionless time-step is adopted throughout (typically, $O(\Delta t=10^{-4})$), satisfying local Courant number conditions [23]. Convergence to steady-state is monitored, via a relative L_2 increment norm on the solution, taken to a time-stepping termination tolerance of $O(10^{-6})$.

Numerical simulations to steady-state are performed for both *fe* and hybrid *fe/fv*-schemes under incompressible (Ma=0.0), limiting ($Ma\approx0$), and weakly-compressible (Ma=0.1) settings. To investigate numerical stability and accuracy properties through time-stepping of each variant, a continuation solution strategy is employed through increasing *We*, to extract steady-state solutions. This procedure is implemented as

† Ellipticity, via diffusion smoothing, was introduced into the stress equation in Alves et al. [6].

follows: each simulation is commenced at *We*=0.1 from a quiescent state in all field variables. Next, the solution is sought incrementing directly to *We*=1.0, commencing from the solution at *We*=0.1. This is followed by successive computations, elevating the *We*-level incrementally in steps of 0.1, until the selected scheme fails to converge (encountering numerical divergence or oscillatory non-convergence to a unique state).

In presenting results through field data and profiles, one proceeds for each scheme variant through three sub-sections. The first compares scheme variants at a fixed and moderate *We*-level (here, *We*=1.5). In the second sub-section, critical *We*-levels are sought, highlighting numerical stability properties for each individual flow/scheme setting. In the last sub-section, trends are analysed in vortex behaviour, through parameterisation in vortex-size and intensity. Comparison with the literature is given throughout. The convention for presentation across schemes is to display corresponding plots for the *fe*-scheme to the left and the hybrid *fe/fv*-counterpart to the right of each figure.

With respect to detailed analysis on the accuracy of the various schemes proposed here, and for brevity, there is cross-reference with some related earlier work. In Matallah *et al.* [98], mesh refinement for the *fe*-scheme was dealt with; following this similarly in the *fe/fv*-context under Aboubacar and Webster [1,2,4], drawing out scheme construction and extending beyond Oldroyd considerations. Transient and higher-order aspects are covered within Webster *et al.* [157] and Aboubacar *et al.* [3], where the current *fe/fv-CT3*-scheme is discussed noting the impact of FD/MDC methodology. Pertinent to the present compressible context and extensions numerically, one may cite recent studies under Webster and co-workers [14,79,154], covering *fe*-discretisations, accuracy over various classical benchmark problems with mesh refinement, and introducing the under-relaxation technique. Notably in [79], mesh refinement was confirmed on a fixed *We*-level of unity across a series of meshes (M1-M3), both in field states and temporal convergence rates. The present study bears out such correspondence across *fe* and *fe/fv*-schemes on the finest mesh (M3) as a starting point. Earlier findings are reaffirmed of Matallah *et al.* [98] and Keshtiban *et al.* [79], based on the *fe*-scheme. Likewise, for those of Aboubacar and Webster [18] with the *fe/fv*-scheme variant, looking at solution convergence in stress fields across these series of meshes, covering

both incompressible [2,98] and compressible [79] flow settings. This evidence is provided in Figure 6.5 under inertial flow setting at *We*=1.0.

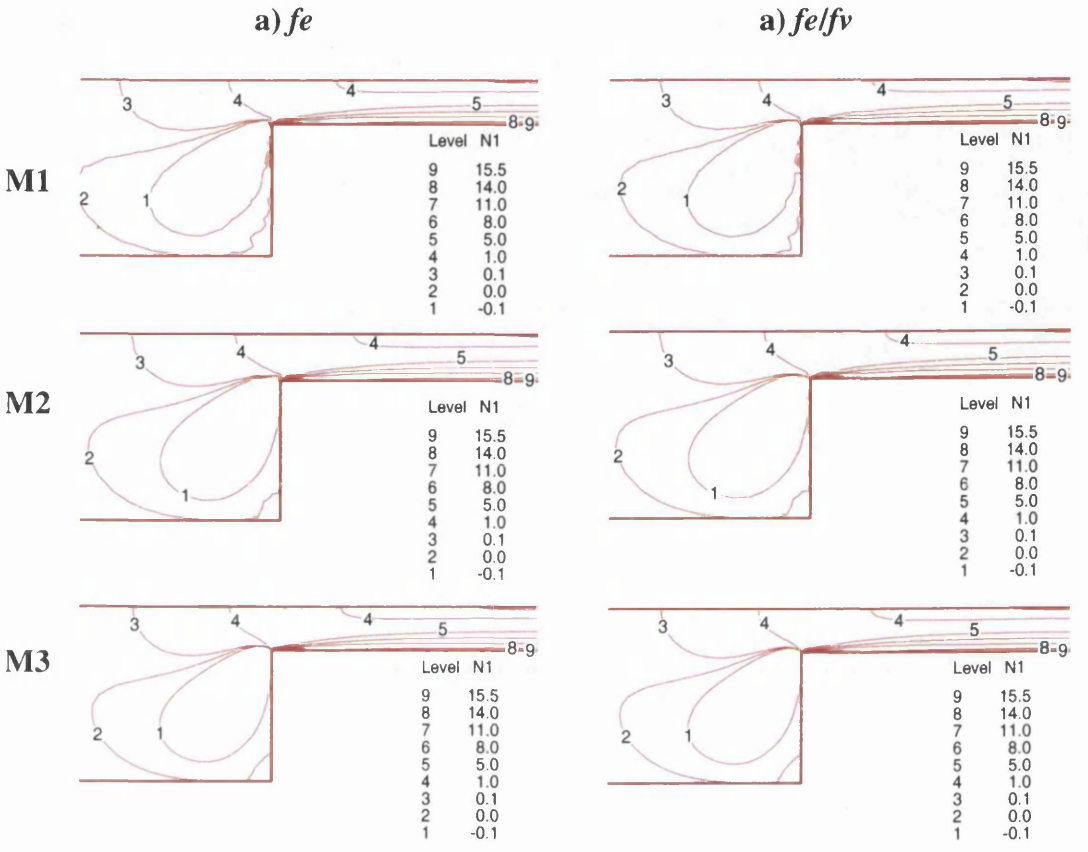

Figure 6.5: Principal stress N_1 contours, h-refinement; a) *fe*, b) *fe/fv* implementations; *We*=1.0, *Re*=1.0

Computations presented in this study were performed on a single-user/single job, Intel Pentium 4 (2.5GHz speed, 512MB memory) processor on a UNIX platform. As an indication of CPU time required for each analysis, only about 200 minutes were required to extract a solution at *We*=1.5, starting from *We*=1.4. About 110 CPU-hours were needed to reach the critical *We* of 3.0, starting from a quiescent state and based on the solution continuation strategy (steps of 0.1 to We_{crit}) for the *fe/fv* incompressible non-relaxed scheme. This takes into account the post-processing time for each *We*-solution step.

6.2.3 Numerical solutions at *We*=1.5 - across scheme variants

First, one commences by investigating consistency and accuracy across numerical schemes (*fe* and *fe/fv*) under the three Mach number settings quoted above. For this part

of the investigation, one selects for comparison purposes the level of We=1.5 and creeping flow. Numerical assessment of scheme variants is made on field variable representation, streamline patterns and stress profiles. For incompressible implementations (*fe* and *fe/fv*), under-relaxation (R) is called upon to enhance numerical stability. This relaxation procedure may be interpreted as time-step scaling upon each individual equation stage (see chapter five and also [79] for more details). Here, one finds it effective to retain a uniform under-relaxation factor of $\beta = 0.7$.

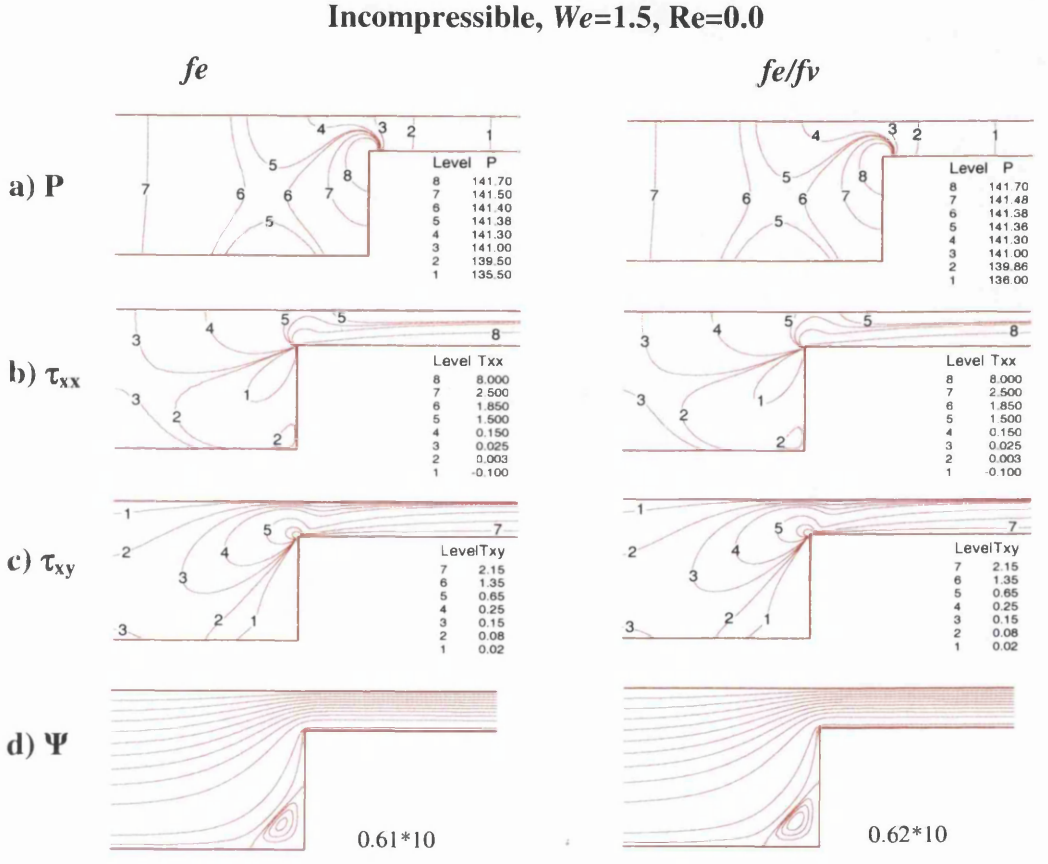

Figure 6.6: Incompressible field contours, We=1.5, Re=0.0: a) P, b) τ_{xx}, c) τ_{xy}, d) Ψ; (left) *fe*, (right) *fe/fv* implementations

Incompressible liquid flow: Field solution plots are provided in Figure 6.6, concentrating on the contraction zone. This data includes pressure (top), stress components τ_{xx} and τ_{xy} (middle), and stream-function (bottom). Note, in all streamline plots, a total of fifteen levels are spread as: ten equal levels, from 1.0 to 0.1, followed by two levels at 0.01 and 0.001; plus four levels to illustrate the salient-corner-vortex (inclusive from a minimum level to the zero, separation-streamline). Similar field

contour patterns at equivalent levels are observed for both scheme variants, both with under-relaxation (R) and without relaxation (nR). Only minor discrepancy is noted between schemes; about 0.7% in pressure and 2.6% in stream-function. Solutions are observed to faithfully reproduce those presented elsewhere [1,5,98,114].

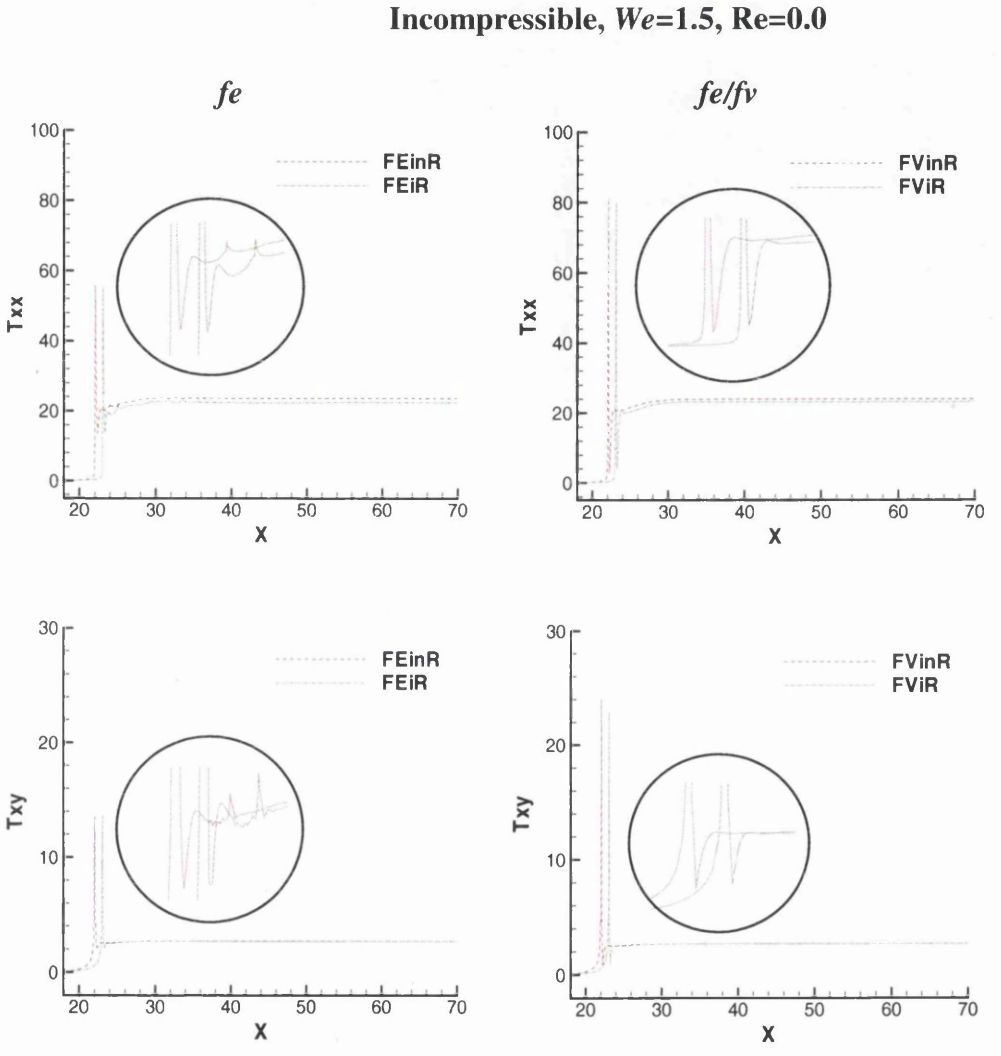

Figure 6.7: Incompressible (without relaxation, nR; with relaxation, R) stress profiles at horizontal line y=3.0, *We*=1.5, Re=0.0: (top) τ_{xx}, (bottom) τ_{xy}; (left) *fe*, (right) *fe/fv* implementations

Figure 6.7 quantifies the above via stress profiles, for τ_{xx} (top) and τ_{xy} (bottom), at y=3.0 along the downstream boundary-wall (see Figure 5.1). For plotting clarity, a shift in the position of the re-entrant corner is introduced in under-relaxed (R)-plots. There are practically no differences detected, with or without under-relaxation. Levels in both stress component (τ_{xx},τ_{xy})-peaks at the re-entrant corner, are larger for the hybrid *fe/fv*

above the *fe*-form (by about 1.4 times for τ_{xx} and twice for τ_{xy}). One may attribute this to the deeper interpolation quality of the hybrid form (refinement in mesh through sub-cells). Beyond the re-entrant corner and along the wall, there is no growth of stress, reaching equitable levels independently of the scheme employed. Scheme comparison, provides a level of confidence in the validity of these incompressible solutions.

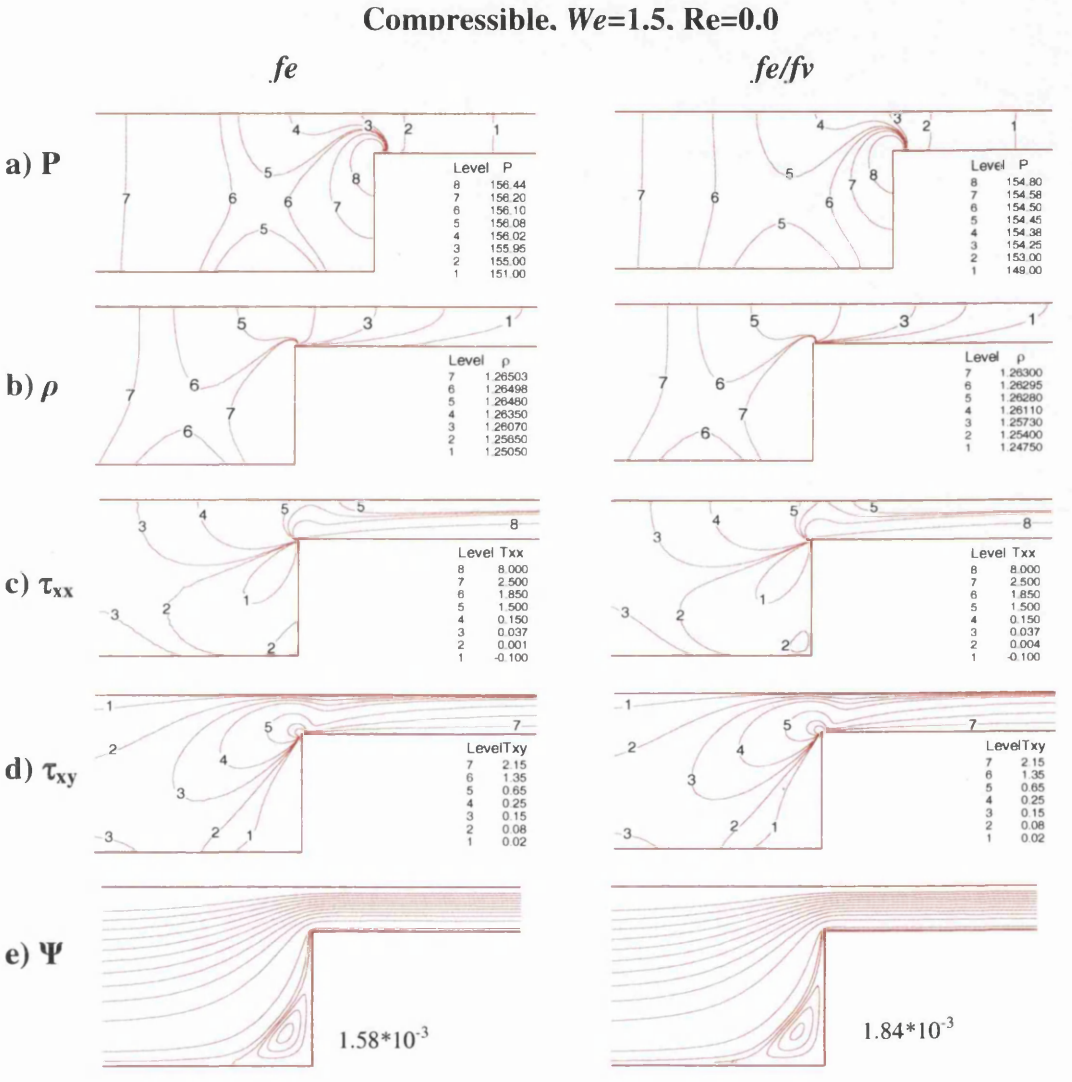

Figure 6.8: Compressible (*Ma*=0.1) field contours, *We*=1.5, Re=0.0: a) P, b) ρ, c) τ_{xx}, d) τ_{xy}, e) Ψ; (left) *fe*, (right) *fe/fv* implementations

Weakly-compressible liquid flow: Results are presented for both schemes in a similar fashion to the foregoing, though field variable plots (Figure 6.8 as Figure 6.6) and stress profiles (Figure 6.9 as Figure 6.7). Additionally, field plots are now provided for density variation (Figure 6.8b). Note, no under-relaxation is necessary for compressible

implementations, as numerical stability is found to be satisfactory without such measures. Once more, similar contour patterns at equitable levels are observed for both schemes (discrepancy in pressure is 1%; in density, 0.2%). Conspicuously, density representation, across the channel section (x=constant), declines from the centreline to the wall, due to the relationship between density and pressure, upheld via the Tait equation of state (Eq.(3.5)). In this instance, τ_{xx} (and hence trace τ) is larger at the wall than the centreline. Note, under Newtonian conditions, density contours mimic those of pressure.

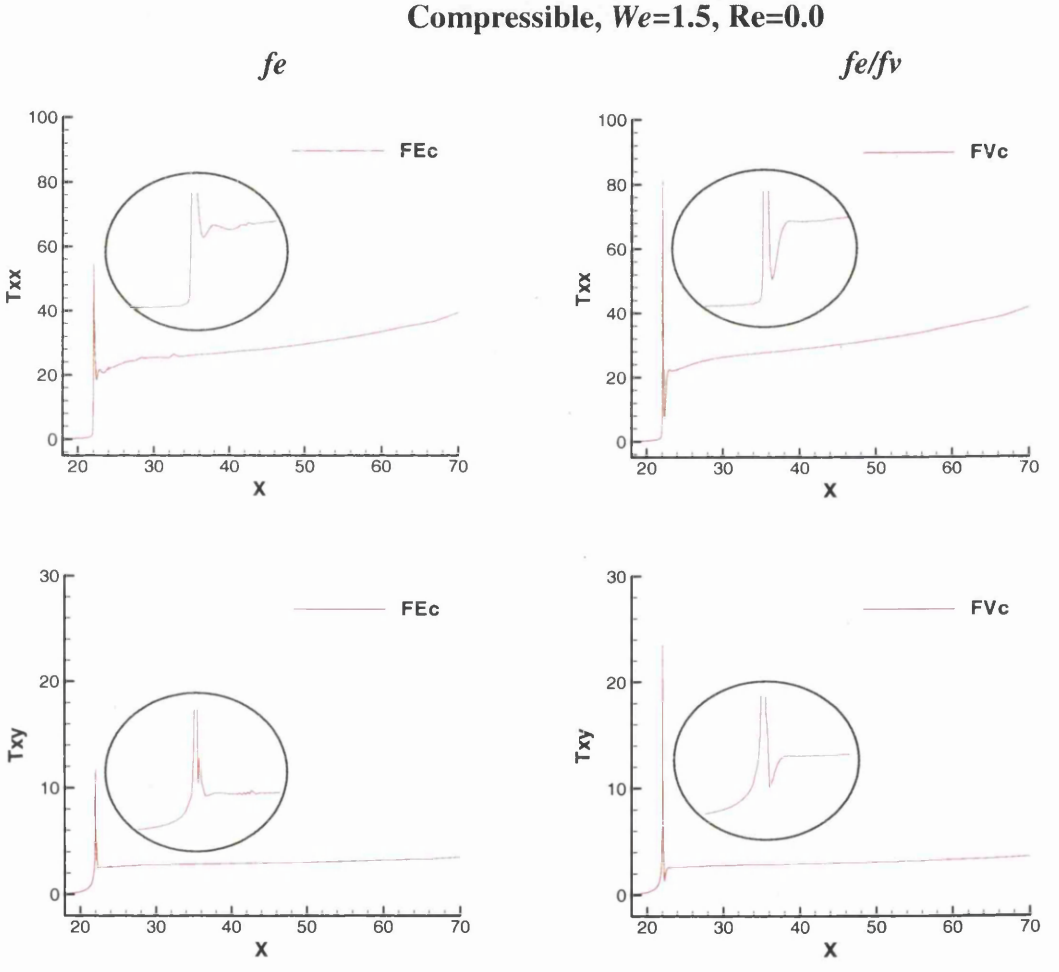

Figure 6.9: Compressible (*Ma*=0.1) stress profiles at horizontal line y=3.0, *We*=1.5, Re=0.0: (top) τ_{xx}, (bottom) τ_{xy}; (left) *fe*, (right) *fe/fv* implementations

Figure 6.9 illustrates solution profiles in τ_{xx} (top) and τ_{xy} (bottom), for both schemes at the boundary wall (y=3.0). The levels of stress-peak are comparable to those of the incompressible instance of Figure 6.7, when comparing both *fe* to *fe/fv*-solutions. The

main differences to observe against incompressible counterparts lie in the sustained growth in both stress components along the boundary wall. This growth rate is constant, described by its angle. These angles are larger for τ_{xx} (12° for τ_{xx} compared to 4° for τ_{xy}), and reflect independence of the specific spatial discretisation employed. At *We*=1.5, one notices oscillatory patterns, behind the singularity corner, in the *fe*-stress plots, which disappear in the *fe/fv*-profiles. This is due to the ability of the *fe/fv* to deal with sharp solution gradients and superior upwinding characteristics on numerical cross-stream diffusion. By design, this is not the case with the SUPG/*fe*-implementation, as observed by others [163].

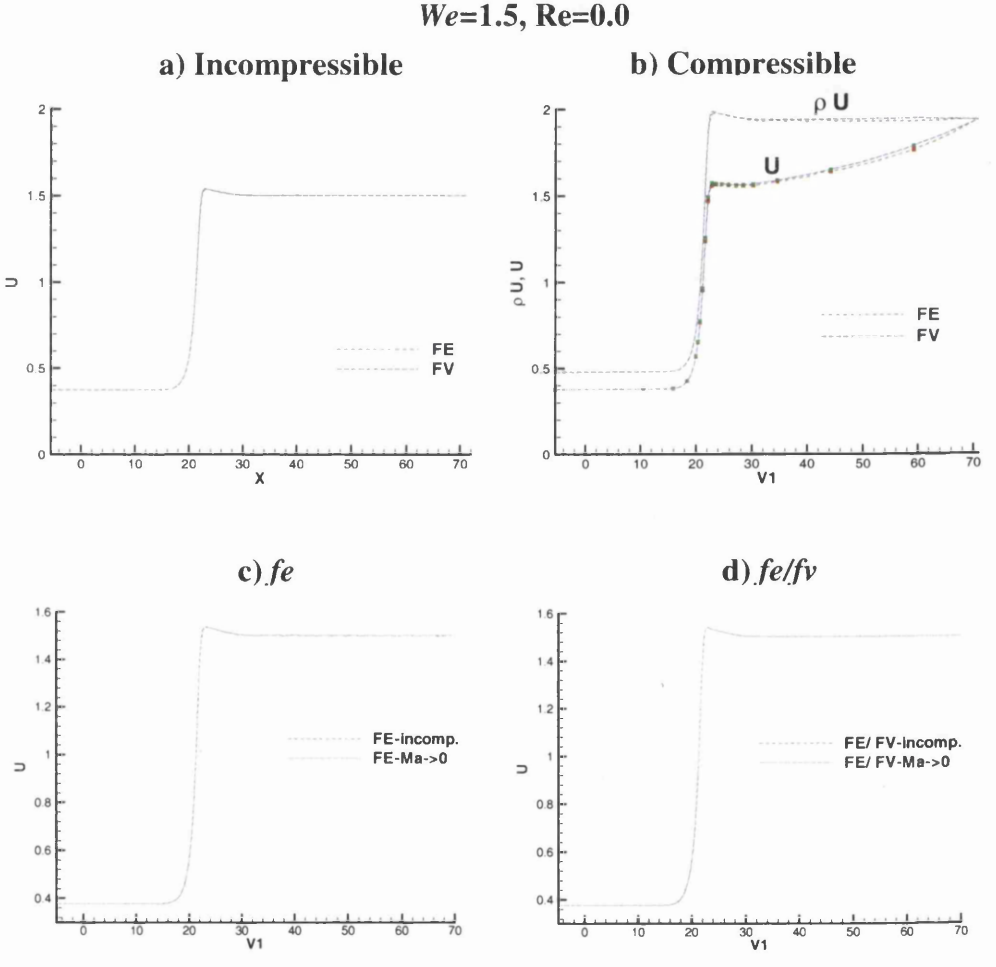

Figure 6.10: U-velocity profiles at centreline, *We*=1.5, Re=0.0: (top) *fe* vs. *fe/fv*: a) incompressible, b) compressible; (bottom) incompressible vs. *Ma*≈0 limit: c) *fe*, d) *fe/fv* implementations

Scheme and flow setting comparison: Quantitative comparison of U-profiles along the centreline (y=4, see Figure 5.1) is undertaken, in Figure 6.10. This includes

assessment of *fe* and *fe/fv*-algorithmic implementations for both incompressible (*Ma*=0.0, Figure 6.10a) and weakly-compressible (*Ma*=0.1, Figure 6.10b) variants. In addition, we provide *Ma*≈0 limit and incompressible (*Ma*=0) comparison (Figure 6.10c, *fe*; Figure 6.10d, *fe/fv*). At this *We*-level, close agreement is observed between implementations, under these alternative flow configurations. The U-profile remains flat beyond the re-entrant corner plane for incompressible flow, whilst it increases monotonically for compressible flow. This maintains a balance in mass-flow rate (ρU, see Figure 6.10b) overall, as density at the inlet is some 30% larger than that at the exit†. Furthermore, as with stress above and for both schemes, *Ma*≈0 solutions lie within less than 0.1% of their incompressible equivalents.

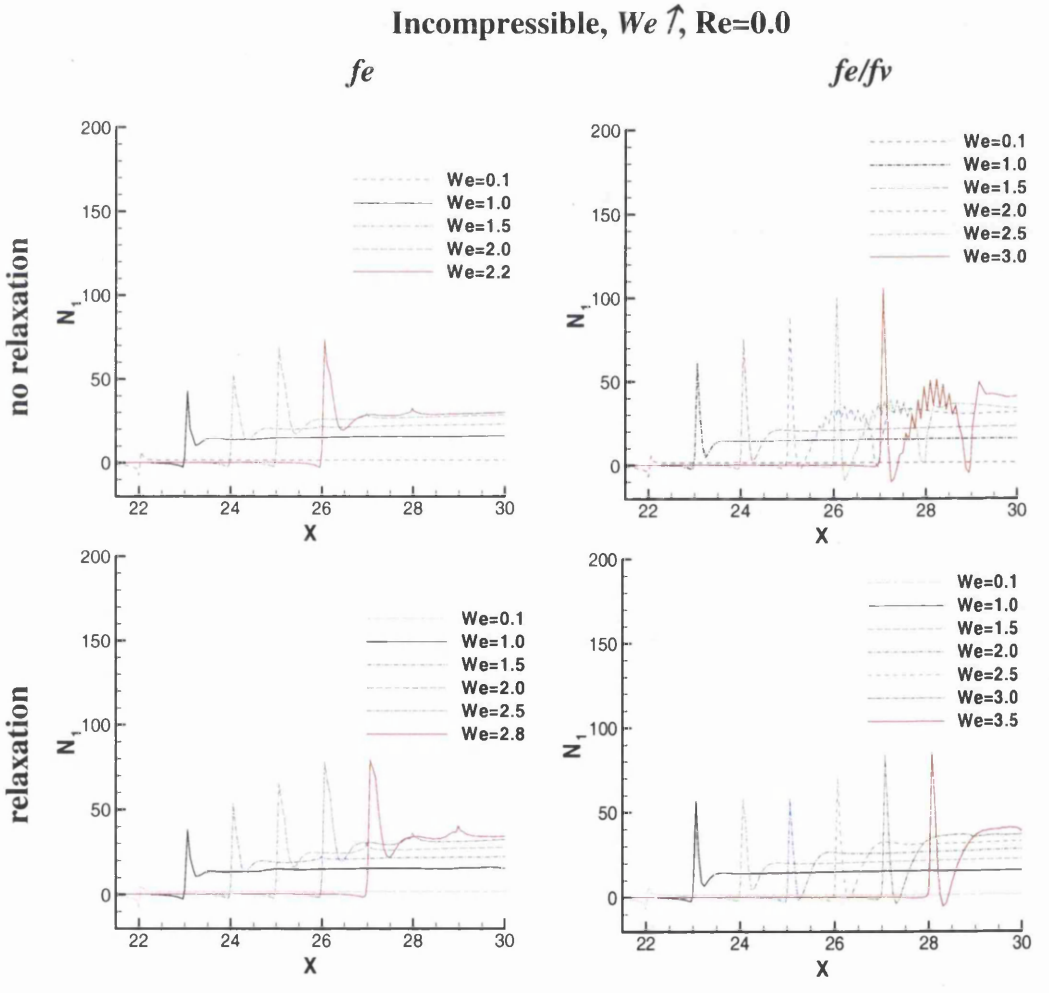

Figure 6.11: N_1-profiles at horizontal line y=3.0 increasing *We*, Re=0.0. Incompressible: (left) *fe* and (right) *fe/fv* implementations; (top) without relaxation, (bottom) with relaxation

† This suggests that (ρU) may be the more appropriate conserved variable with which to operate in the compressible context. One may accommodate for this presently via the ρ-constant interpolation offered.

6.2.4 Increasing We-solution strategy

Here, both *fe* and *fe/fv*-solutions are sought under the three *Ma*-flow settings for increasing *We* up to critical limiting levels. Initially, liquid inertia is omitted in these calculations.

6.2.4.1 Incompressible liquid flow

In Figure 6.11, solution profiles for principal stress N_1 are plotted across each scheme. The effect of introducing under-relaxation (bottom) is also highlighted. We comment upon critical levels of *We* attained, in passing, recorded for immediate comparison in Table 6.1.

Table 6.1: Critical *We* level for different scheme variants and flow configurations

	Re=0.0								Re=1.0	
	Incompressible				Compressible				Compressible	
	fe		*fe/fv*		*fe*		*fe/fv*		*Fe*	
	nR	R	nR	R	*Ma*≈0	*Ma*=0.1	*Ma*≈0	*Ma*=0.1	*Ma*≈0	*Ma*=0.1
Critical *We*	2.2	2.8	3.0	3.5	1.5	1.7	3.3	3.1	1.5	2.0
Peak N_1	73.7	79.1	105.9	85.1	53.3	54.4	194.0	200.8	51.1	68.6

a) Without relaxation: Stress-peaks are larger for the *fe/fv*-scheme (peak We_{crit}=3.0) compared to their *fe*-counterpart (peak We_{crit}=2.2). At the same *We*-level, say *We*=2.0, there is about 30% increase in the stress-peak for the *fe/fv* above the *fe*-form. With the *fe/fv*-scheme, at *We*=2.0 and above, in a small region beyond the corner, the principal stress-peak is followed by two short duration oscillations, that are rapidly damped away travelling further downstream. Similar oscillatory behaviour has been observed earlier by both Yurun [163] and Phillips and Williams [115].

b) With under-relaxation: At *We*=2.5, there is about 12% decrease in the stress-peak for the *fe/fv* below the *fe*-variant. In contrast to the non-relaxed results at *We*=2.0, there is hardly any difference in stress-peak level with the *fe*-scheme, whilst there is about 30% reduction with the relaxed *fe/fv* result. Downstream oscillations are also reduced for the relaxed *fe/fv*-scheme compared to its non-relaxed form. Overall, under-relaxation enhances scheme stability, when compared to its non-relaxed counterpart. On We_{crit}-

levels, with the *fe*-scheme, there is increase from 2.2 to 2.8; a position matched with the *fe/fv*-scheme, demonstrating increase from 3.0 to 3.5.

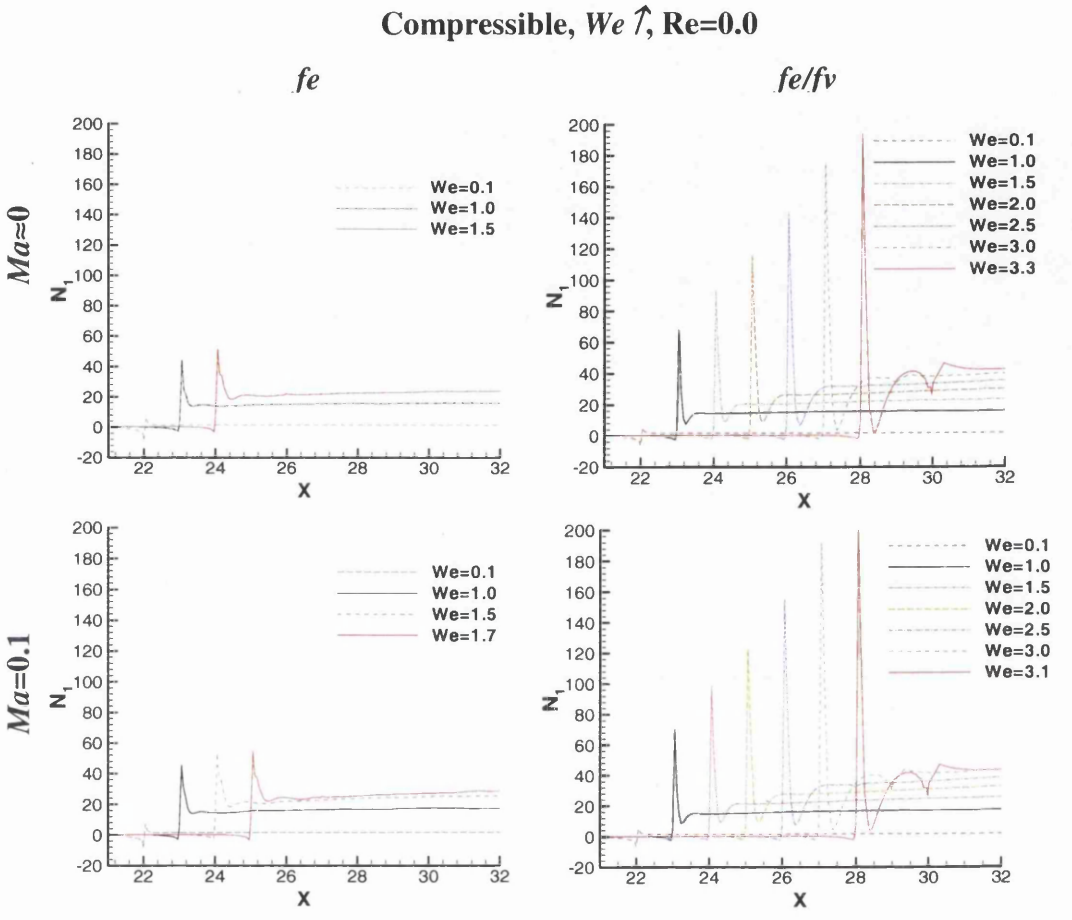

Figure 6.12: N_1-profiles at horizontal line y=3.0, increasing *We*, Re=0.0. Compressible: (left) *fe* and (right) *fe/fv* implementations; (top) incompressible limit, *Ma*≈0; (bottom) compressible *Ma*=0.1

6.2.4.2 Weakly-compressible flow

Figure 6.12 illustrates corresponding N_1-profiles for both *Ma*≈0 and *Ma*=0.1 settings (discarding relaxation). Independent of flow scenario and across schemes, stress-peaks for the *fe/fv*-scheme may amount to some four times larger than those of their *fe*-counterparts (at *We*=1.5, the *fe/fv*-stress peak is about 40% larger for *Ma*≈0 and double that for *Ma*=0.1 compared to its *fe*-counterpart). This is mainly due to sub-cell refinement and the particular reduced corner integration technique applied: a discontinuity-capturing treatment for the corner solution-singularity unique to the hybrid scheme [4]. When evaluating unrelaxed compressible *Ma*≈0 solutions against their truly incompressible counterparts (*Ma*=0) for the *fe*-scheme, equitable stress-levels

are observed at We_{crit}=1.5. This is not the case for the corresponding *fe/fv*-scheme, as stress-peak levels are somewhat elevated from around 105 units for *Ma*=0, to 180 units for *Ma*≈0, see back to Figure 6.11. One may attribute these discrepancies to the alternative *fe/fv*-discrete implementation in the corner neighbourhood (as above); and also, to the additional sharp velocity gradient contributions made there within the compressible formulation $\left(L^T_{kk}\,\delta_{ij}/3\right)$. Under the compressible configuration (*Ma*=0.1), the We_{crit}-level is about twice as large for the *fe/fv*-implementation (peak We_{crit}=3.1), when compared to that for the *fe*-form (peak We_{crit}=1.7). Nevertheless, when comparing compressible, *Ma*≈0, We_{crit}-levels against their incompressible counterparts, the compressible *fe*-scheme implementation reduces We_{crit} (from *We*=2.2 to 1.5). The reverse is true for the sub-cell *fe/fv*-scheme, as here the We_{crit}-level actually increases (from *We*=3.0 to 3.3). Overall, larger We_{crit}-levels are achieved with the *fe/fv*-scheme throughout all the various flow scenarios investigated. This is a strong argument to advocate the *fe/fv*-scheme over the alternate *fe*-scheme. This elevated level of *We* (*We*=3.1) for *fe/fv*, in compressible implementations, gives rise, again, to post-corner oscillation, as noted above at earlier *We*-levels for incompressible flow.

6.2.4.3 Three-dimensional field plots

Surface plots presented in Figure 6.13 highlight the significant differences in solutions across the domain for the *fe/fv*-scheme at *We*=3.0. Viewing angles are displayed at the top of the figure. This covers incompressible (*Ma*=0, without relaxation, the extreme level) and compressible (*Ma*=0.1) flow configurations, along with variables of U-velocity (Figure 6.13a and c, viewing angle-1), stress τ_{xx} (Figure 6.13b and d, viewing angle-2), Mach number (Figure 6.13e, viewing angle-1) and density (Figure 6.13f, viewing angle-1). In contrast to the incompressible flow configuration, for the weakly-compressible flow, there is a sustained increase in U-velocity along the exit-channel, corresponding to the reduction in density there (see Figure 6.13f and 6.10b). In stress-peaks, both flows settings manifest the presence of the re-entrant corner singularity, yet with larger peaks in the compressible (τ_{xx}^{Peak}=196.3) over the incompressible solutions (τ_{xx}^{Peak}=113.9). For the incompressible solution, beyond this position, along the exit-channel boundary wall, there is no growth in the stress-level. In the compressible solution, the stress sustains a monotonic growth along the wall, so that at the exit, the compressible-τ_{xx} doubles its incompressible counterpart

(see Figure 6.12). This may be gathered from the more excessive cross-stream exit-flow curvature in the compressible τ_{xx}-surface plot.

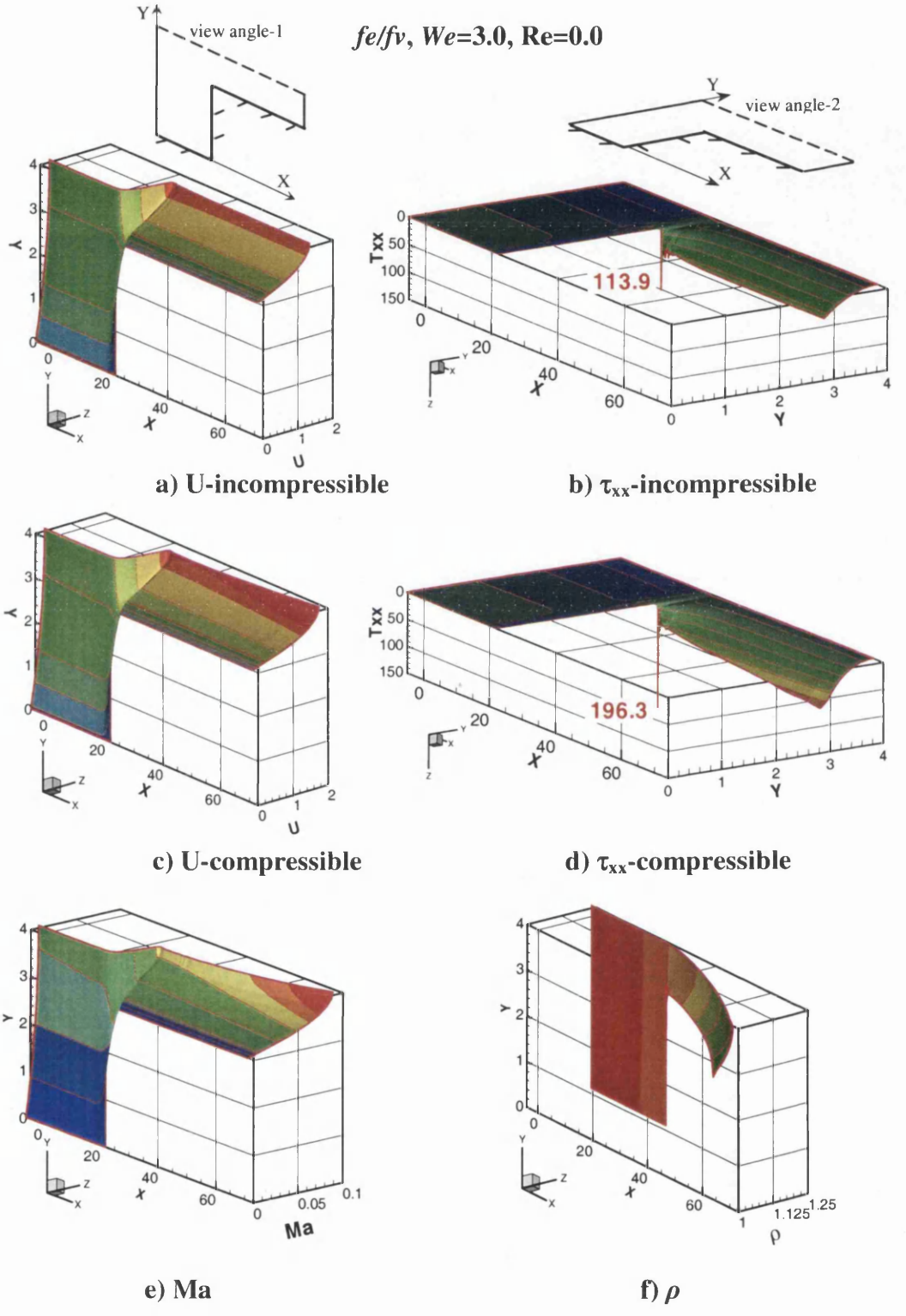

Figure 6.13: 3D contour plots, *fe/fv* scheme, *We*=3.0, Re=0.0. Incompressible a) U-velocity, b) stress τ_{xx}; Compressible c) U-velocity, d) stress τ_{xx}, e) *Ma* and f) ρ

Mach number contour patterns mimic those in velocity, confirming the acceleration of the flow throughout the exit-channel. Density patterns expose the influence of stress, in relating pressure to density. The three-dimensional surface plot at exit of Figure 6.13f is not straight, but curves towards the centerline, see also Figure 6.8b. Correspondingly, contours are straight at channel-entry, where density variation is negligible.

6.2.5 Flow patterns and vortex activity

In the contraction flow problem, salient-corner vortex-size and strength are major characteristics used to quantify numerical solutions, often judged against experimental observations. First, we summarise the position in the literature. In their experimental work, Evans and Walters [42] reported on both lip and salient-corner vortex behaviour. They attributed the complex characteristics encountered under vortex enhancement to several factors: material properties, type of geometric contraction (sharp or rounded), contraction ratio, fluid inertia and breakdown of steady flow. Prunode and Crochet [117] performed a qualitative numerical comparison against these experimental results. Matallah *et al.* [98] presented a comprehensive literature review on vortex activity, indicating the difficulty of accurate prediction of lip-vortex activity. The Matallah *et al.* study was based on new features in the *fe*-scheme, with velocity-gradient recovery applied within the constitutive equation. There, for the creeping flow of an Oldroyd-B fluid, a lip-vortex appeared as early as We=1.0, which grew in intensity with increasing We. This lip-vortex strength was found to be larger than the salient-corner counterpart, from a We-level of unity and beyond. Likewise, based on *fv*-discretisation, Aboubacar and Webster [4], Xue *et al.* [161], Oliveira and Pinho [108], also observed the appearance of a lip-vortex at We 2.0 in [4] and We=1.6 in [161]. Oliveira and Pinho [108] claimed to detect the appearance of a lip-vortex for an UCM model at We=1.0. Furthermore, the authors highlighted the need for a high degree of mesh refinement required for an accurate and reliable representation of vortex activity. The influence of inertia inclusion was also interrogated by Xue *et al.* [161], who concluded that although fluid inertia had some influence on the upstream flow field, no evidence linked the appearance (or absence) of lip-vortices with inertia. On the contrary, Phillips and Williams [115] found that the inclusion of inertia for an Oldroyd-B model, delayed the appearance of the lip-vortex till We=2.5 (appearing at We=2.0 for Re=0) and the salient-corner vortex-size and intensity shrank (falling by about 20% below that for Re=0).

Subsequently, Phillips and Williams [114] observed that the size of the salient-corner vortex decayed slowly over a range, $0 \leq We \leq 1.5$, where growth in vortex-intensity was independent of Re-level (0.0 or 1.0). Their results agreed closely with those of Sato and Richardson [127], Matallah *et al.* [98] and Xue *et al.* [161]. They also recognised the sensitivity of their results to the quality of mesh employed. Likewise, many authors have been aware of the impracticability to refine the mesh towards the corner beyond a certain threshold, due to the consequence of approximating the singularity. These findings demonstrate that trends in salient-corner vortex activity are better characterised and predicted than is the case for lip-vortex activity. In a more recent study, Alves *et al.* [5] have catalogued a set of benchmark solutions, for Oldroyd-B and PTT models, again under planar creeping flow conditions. Solutions were produced based upon mesh refinement strategy. On the finest mesh of $O(10^5)$ *fv*-cells, resulting in over one million degrees of freedom, their numerical scheme was able to reach $We=2.5$. Once more, these authors demonstrated that vortex characteristics (size and intensity) were sensitive to the particular mesh employed. Alves *et al.* also observed salient-corner vortex reduction with increasing *We*, and the appearance of a lip-vortex at around $We=1.0$ (Re=0). They found that, by extrapolating mesh refined data on lip-vortex intensity through diminishing mesh-size, for $We=0.5$ and 1.0, the lip-vortex would vanish. Yet, at $We=1.5$, a finite lip-vortex intensity ($0.02*10^3$) was predicted to survive, as mesh-size tended to zero. These findings are based on the assumption that extrapolation has some meaning, when applied to spatially shifting phenomena across meshes.

As above, in our current study, the focus has been on flow patterns as a function of increasing *We*, emphasising steady-state salient vortex behaviour. Trends in vortex-size and intensity for both *fe* and *fe/fv*-schemes are presented under incompressible ($Ma=0$, without and with relaxation) and compressible ($Ma \approx 0$ and $Ma=0.1$) flow configurations. In addition, creeping (Re=0.0) and inertial (Re=1.0) conditions are considered. Extrema (minima) in stream-function intensity may be located either in the salient-corner vortex or lip-vortex depending on the particular *We*-level. Corner-vortex cell-size, X_S, is defined by convention as the non-dimensional vortex-length from the salient-corner to the separation streamline along the upstream wall (see Figure 5.1).

One commences with *scheme and flow setting comparison* for creeping flow. Under incompressible liquid flow, one illustrates in Figure 6.14 (as elsewhere to follow),

vortex reduction trends in salient-corner vortex-size (top) and vortex-intensity (bottom, $*10^{-3}$), under both schemes and increasing *We*-level. Solutions are based on three alternative settings (incompressible flow, both with relaxation (R) and without (nR), and compressible flow with $Ma \approx 0$). Less than 1% difference is noted between the nR- and R-vortex-size data. This rises to one order more in vortex-intensity, due to the solution size $O(10^{-3})$ and the nature of this measure. For the compressible implementation, $Ma \approx 0$, and in contrast to its incompressible counterpart ($Ma=0$), discrepancies are uniformly around 2%.

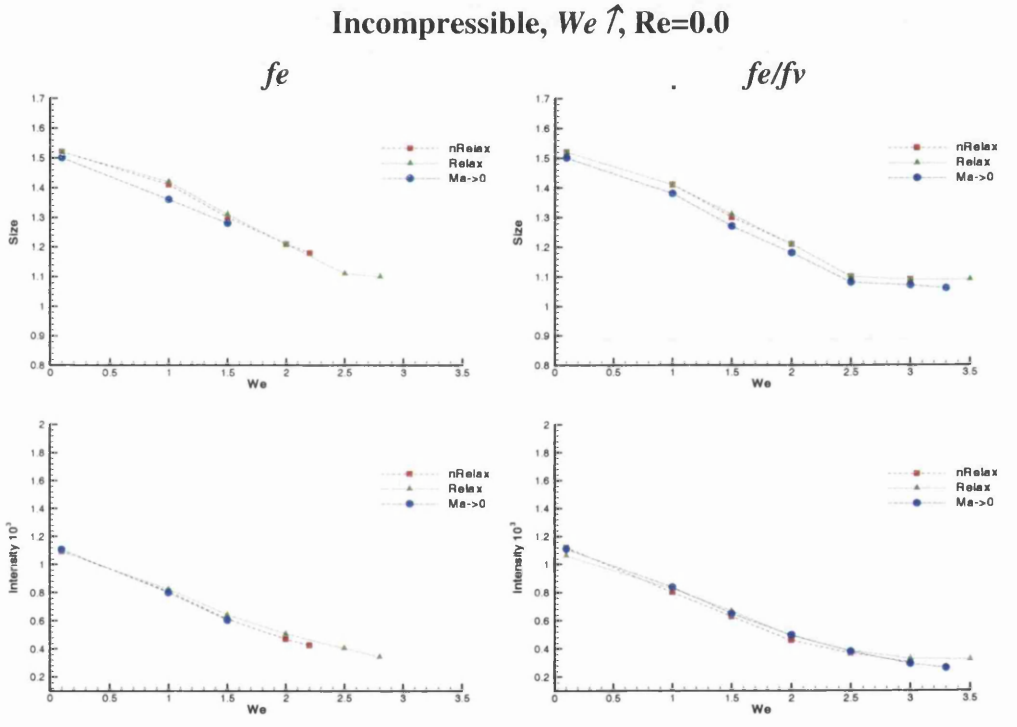

Figure 6.14: Vortex size (top) and intensity (bottom, $*10^{-3}$), increasing *We*: incompressible creeping flow; *fe* (left) and *fe/fv* (right) schemes; relaxed, non-relaxed and $Ma \approx 0$ variants

Similarly, in Figure 6.15, one turns attention to observing trends with switch in flow setting, detecting differences under scheme variants (*fe* and *fe/fv*), for flow settings nR-incompressible $Ma=0$ (left) and $Ma=0.1$-compressible (right). Again, vortex reduction is generally observed throughout all scenarios. Under incompressible considerations, there is hardly any difference in solutions between the two numerical schemes (differences of about 2% in intensity and less than 0.1% in size). Close agreement is found between the solutions and those of Alves *et al.* [5] (included in plot) up to relatively high levels of

We of 2.5. For compressible flow conditions, *fe* and *fe/fv*-solutions differ by about 3% in size. Under any particular *We*-value, compressible conditions increase vortex characteristics compared to those for equivalent incompressible considerations (about 15% increase in size and intensity triples). As the characteristic compressible velocity scale (defined at the outlet) is larger than its incompressible counterpart (by about 30%, see Figure 6.10b), this will have an effect on the *We*-scale employed. To equilibrate comparison, a transformed equivalent incompressible *We*-scale (We^*) is also included within the compressible plots. Even on this basis, compressibility exaggerates vortex characteristics.

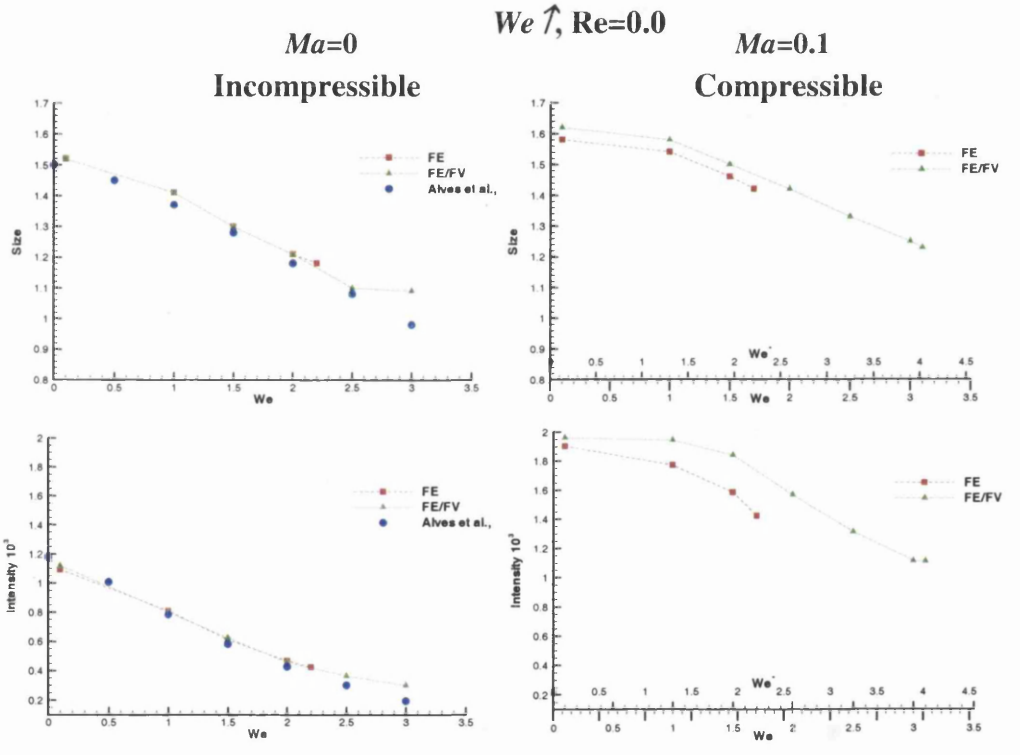

Figure 6.15: Vortex size (top) and intensity (bottom, $*10^{-3}$), increasing *We*: incompressible (nR) (*Ma*=0, left) and compressible (*Ma*=0.1, right); creeping flow, comparison of *fe* and *fe/fv* solutions

Streamline patterns with increasing *We*-level are plotted for each scheme, *fe* and hybrid *fe/fv*, and flow conditions, incompressible and weakly-compressible. For incompressible flow, relaxation is considered to reach elevated levels of We_{crit}†.

† Experience generally points to the fact that We_{crit} decreases upon mesh refinement for any scheme or setting, particularly in the context of non-smooth flows displaying sharp singularities, see [5]. Also, vortex trends are observed to be consistent with mesh refinement.

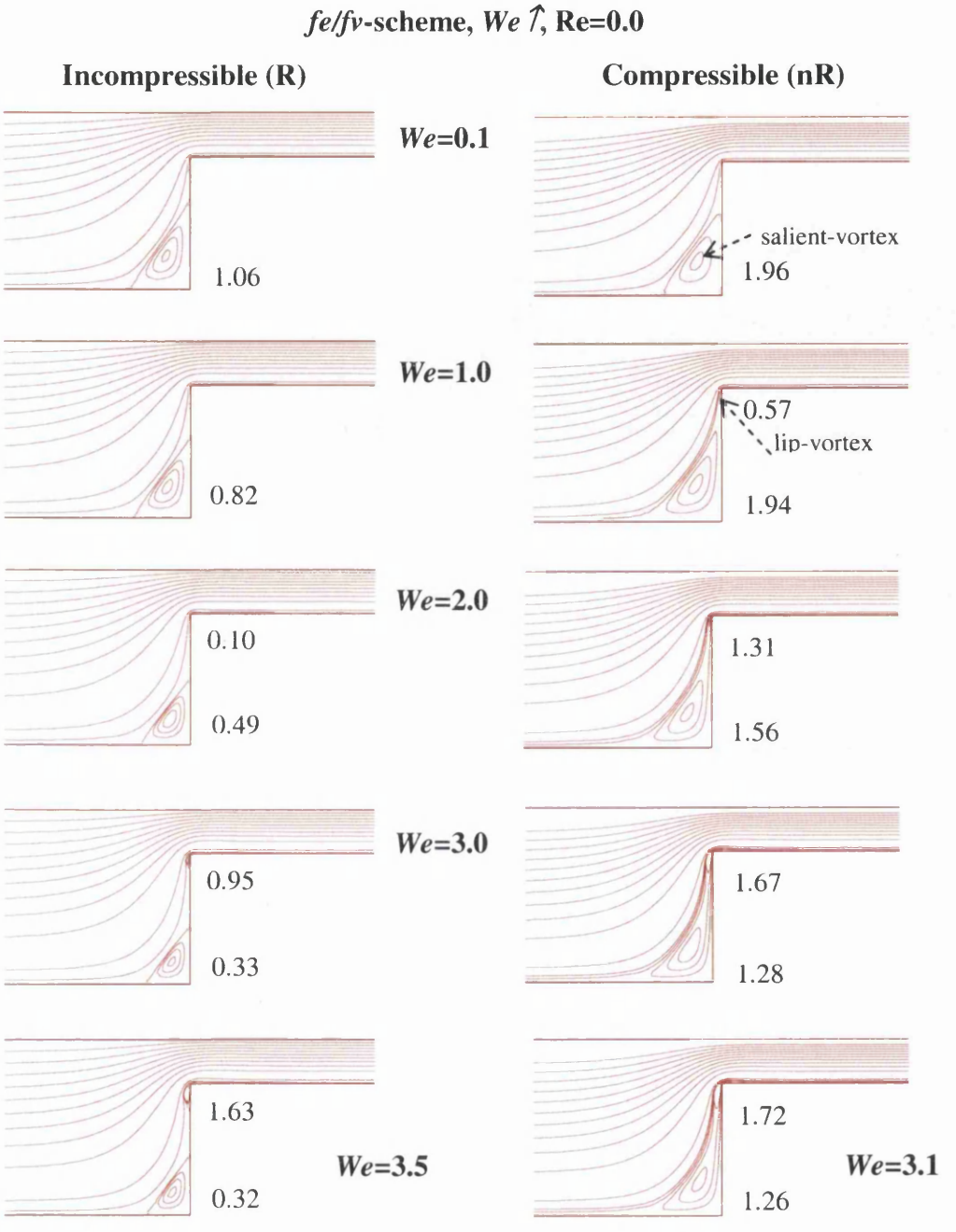

Figure 6.16: Streamline contours, increasing *We*: (left) incompressible (R) and (right) compressible (nR); creeping flows, *fe/fv* scheme, vortex intensity*10^{-3}

In Figure 6.16, under the *fe/fv*-scheme and creeping flow, streamlines contours are illustrated in steps of *We* (from 0.1 to We_{crit}) for incompressible (left) as well as compressible *We*=0.1 (right). We note, as stated above, the larger salient-corner-vortex, as well as the lip-vortex, in the compressible flow solutions above their incompressible counterparts. For incompressible flow solutions with the *fe*-scheme (not presented here), the lip-vortex first appears beyond *We*=2.5 ($1.9*10^{-4}$ at *We*=2.8). Alternatively, under

the *fe/fv*-variant, the lip-vortex emerges earlier at *We*=2.0. This was the case in [3], there attributed to the characteristics of the hybrid scheme. In the compressible context, a lip-vortex first appears earlier (at *We*=1.0). Lip-vortex intensity becomes larger, in absolute value, for both flow configurations from the *We*=3.0-level onwards. Note, that for the compressible *fe*-scheme, not illustrated here, the lip-vortex also appears at *We*=1.0, with intensity of $3.7*10^{-4}$, increasing to $4.3*10^{-4}$ at We_{crit}=1.7. Salient-corner vortex reduction is clearly apparent with increasing *We* under any flow configuration; whilst once present, lip-vortex size grows. For compressible flow, the shape of the salient vortex changes from its equivalent incompressible shape at *We*=0.1 (same in the Newtonian case) to a more stretched, and convex form joining the lip-vortex at high *We*.

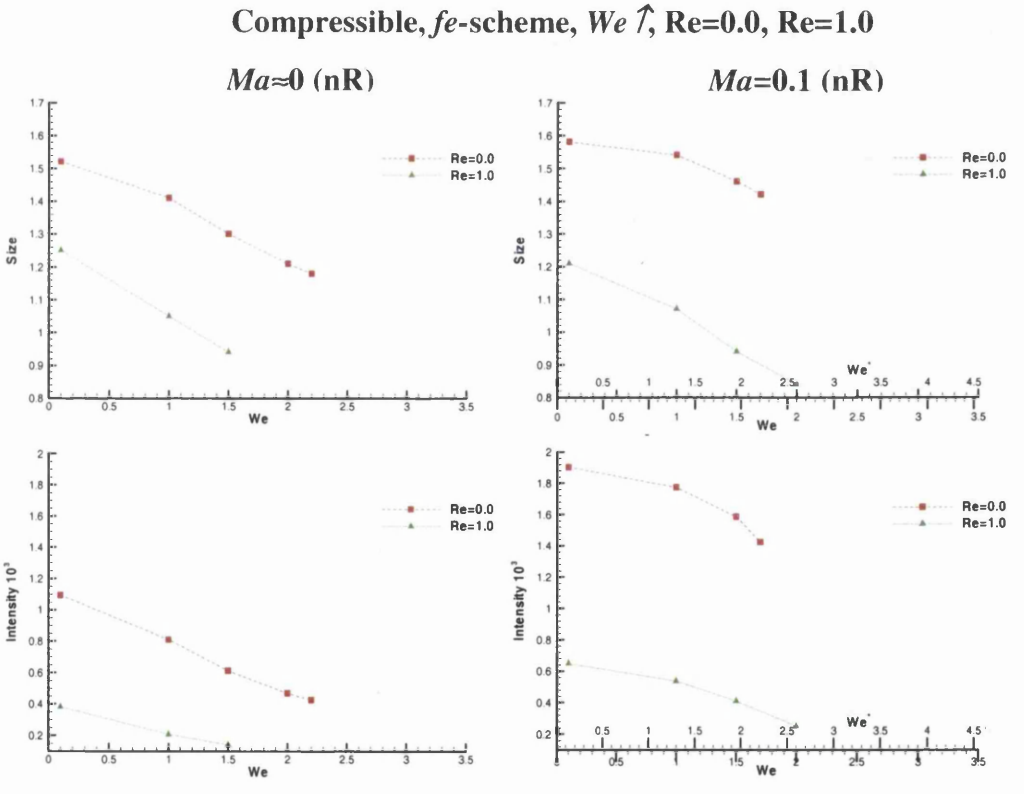

Figure 6.17: Vortex size (top) and intensity (bottom, $*10^{-3}$), increasing *We*, compressible *fe*-scheme: *Ma*≈0 (left) and *Ma*=0.1 (right); creeping vs. inertial flow

Inertia inclusion: With restriction to *fe*-solutions henceforth, Figure 6.17 follows Figure 6.15, to demonstrate the influence of inclusion of inertia against increasing *We*-level. Such data address *Ma*≈0 (left) as well as *Ma*=0.1 (right) compressible flow configurations. As anticipated, introducing inertia reduces vortex-size and intensity, a

consistent trend noted across configurations. This reduction in size for incompressible flow ($Ma \approx 0$) varies between 17% for We=0.1, to 26% over the higher range at We of 1.5 (intensities following in a similar form). Such trends in vortex-size are amplified for the compressible context (Ma=0.1) to 23% at low We of 0.1, up to 36% at We=1.5.

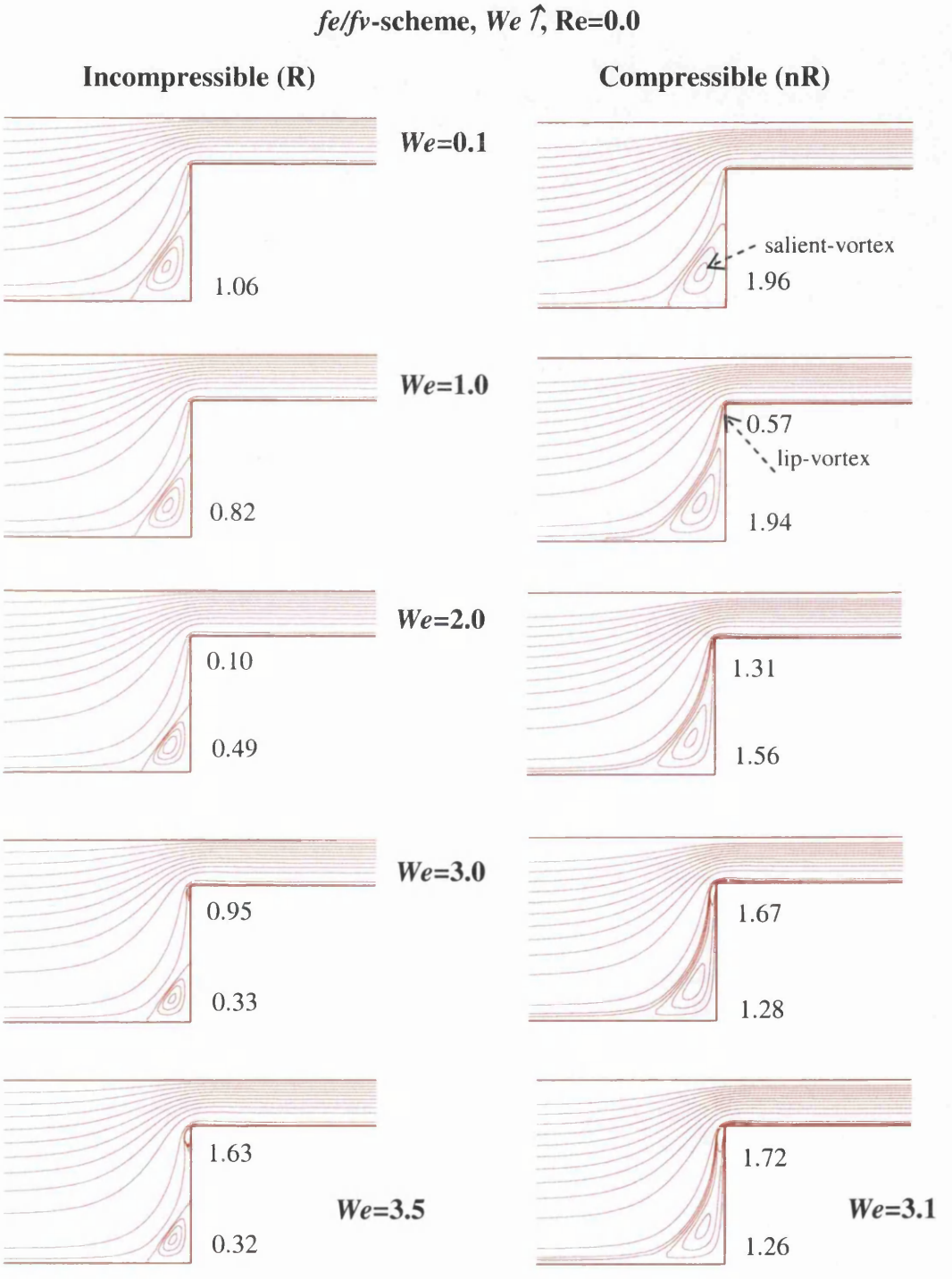

Figure 6.18: Streamline contours, increasing We: (left) incompressible and (right) compressible; inertial flows, *fe* scheme, vortex intensity$*10^{-3}$

Following Figure 6.17, Figure 6.18 charts the equivalent compressible stream-function field solutions for inertial flow, under increasing *We*. The shrinkage of vortices (salient and lip) is clearly apparent compared to those in creeping flow. For the more disputed lip-vortex activity, *fe*-solutions display no lip-vortex in the incompressible limit ($Ma \approx 0$), whilst one does appear at $We=1.0$ in the compressible ($Ma=0.1$) configuration, as was the case for compressible creeping flow. Again, at the relatively high limiting *We* of 2.0, lip-vortex intensity overtakes that of the salient-corner vortex. It has already been established [43,117], that in inertial flow there is delay in the onset of lip-vortex activity, compared to that under creeping flow. Its absence in the incompressible instance ($Ma \approx 0$) is due to the low We_{crit} (1.5) achieved by the $Ma \approx 0$-*fe*-scheme (a lip-vortex appears at $We=2.0$ for creeping flow). Based on such observations, and specifically with respect to capture of corner solution characteristics, the sub-cell *fe/fv*-scheme is advocated over the parent-*fe*-variant.

6.3 Conclusions

The abrupt four-to-one contraction benchmark problem has been investigated for an Oldroyd-B model, two numerical schemes (*fe* and hybrid *fe/fv*), and three flow settings (incompressible-$Ma=0$, weakly-compressible-$Ma \approx 0$ and $Ma=0.1$). Solutions for both creeping and inertial flows conditions have been presented.

For each implementation, on We_{crit} and corresponding vortex activity (size and intensity), the main differences one observes against incompressible counterparts lie in the sustained growth at constant rate, in both wall-stress components beyond the re-entrant corner. This is independent of the specific spatial scheme employed. Under the incompressible context, relaxation elevates the We_{crit}-levels for both scheme implementations, as numerical stability is enhanced. Larger We_{crit} levels are reached under all three flow settings, for the *fe/fv*-scheme compared to the *fe*-variant. This, may be attributed to the discretisation differences between schemes approaching the re-entrant corner: sub-cells and use of discontinuity capturing in the hybrid case. One notes also the property of the *fe/fv*-scheme to display some control on cross-stream solution variation, particularly in the presence of sharp solution gradients. On vortex behaviour, at equitable *We*-level and flow settings, both schemes produce comparable vortex characteristics. One has observed larger salient-corner and lip-vortices in compressible

flow above its incompressible counterpart. Independently of flow setting, salient-corner vortex-size decays with increasing *We* (vortex reduction), whilst lip-vortex size is enhanced. For compressible flow, the shape of the salient vortex adopts a curved and stretched form (separation line becomes curved), uniting with the lip-vortex at high *We*. Upon introducing inertia into the problem, all aspects of vortex (salient and lip) activities are reduced.

CHAPTER 7

Stabilised Computations for Weakly-Compressible and Incompressible Viscoelastic Flows (*fe/fv*)†

The main propose of this chapter is to investigate stabilised computations for slightly compressible to incompressible viscoelastic flows. This is conducted through extensive studies upon an incremental pressure-correction (*PC*) fractional-staged hybrid *fe/fv* method. The particular interest in the present context is to draw together some of the established stabilisation methodologies, used to gain numerical convergence for highly-elastic steady-state viscoelastic solutions. That is, in achieving high Weissenberg number (*We*) solutions to classical benchmark problems. To illustrate this, Oldroyd-B model solutions have been considered in planar 4:1 abrupt contraction flows.

The key issues dealt with involve: (*i*) the stabilisation of *PC*-schemes in application to the coupled velocity-pressure-stress system via a fractional-staged procedure; (*ii*) the improved satisfaction of extended LBB compatibility conditions within the spatial representation, and (*iii*) some miscellaneous stabilisation aspects particular to the stress equation, such as capturing discontinuities and steep stress gradients. The second aspect involves the compatibility of function spaces, improving the quality of velocity gradients and appending an elliptic dissipation function. New theoretical findings in this area are appealed to associated within the coupled velocity-pressure system. Fortunately, the equivalence of various stabilisation mechanisms has already been

† Material of this chapter appears in paper "Stabilised computations for incompressible and mildly compressible viscoelastic flows" by F. Belblidia, I. J. Keshtiban, and M. F. Webster, and submitted for publication in *Journal of Non-Newtonian Fluid Mechanics* (2004).

established theoretically. For example, in associating the stabilisation parameter of the *Galerkin-Least-squares* (GLS) method with the proper choice of time-step in a *PC*-approach [30]. Similarly in [57], the necessity of satisfying the inf-sup (LBB) conditions is confirmed, if superior temporal error bounds are to be realised. Admissible trial spaces result and specific incremental pressure-correction schemes (three time-levels) are advocated to realise these advantageous properties.

It is through these alternative stabilisation procedures, that one is able to access new levels of stable *We*-solutions. This presents novel solution features in terms of vortex activity, stress field structure around abrupt corners and in stress boundary layers (SBL), and cross-stream solution representation. Likewise, one may consider the specific effect that inclusion of compressibility may have, contrasting this against its incompressible counterpart, notably through vortex activity. The merits of coupled and fractional-staged problem statements are commented upon in Appendix 7.A.

7.1 Aspects of stabilisation

Computation of viscoelastic flow with *PC*-methods has been investigated by several authors. The overall numerical performance of such schemes may be influenced by three main issues. The *first* such stabilisation issue to consider upon the introduction of elasticity, is that pressure-correction methods not only inherit properties associated with the computation of Stokes flow, but go beyond this phase, with the increased complexity of the problem. As such, decoupling the calculation of stress (over each time-step) from the momentum and continuity equations may reduce convergence rates, affect stability, and hence, lower the maximum attainable *We* (We_{crit}) for steady-state solutions [9,10]. Generally, additional stabilisation procedures are required to improve numerical convergence, particularly in more complex non-smooth flows. To date, much work has been devoted to the study of Stokes flow and the properties of pressure-correction methods, in developing accurate and stable numerical schemes [8,20,25,57,83]. Codina and Zienkiewicz [30] have established a generalised PC-framework which demonstrates the unification of *GLS*-constructs with those of stable projection methods. This is achieved through stabilisation factors, introduced into the fractional-staged approach, which mimic time-step scaling (*TSS*) across individual equations. Laterly, these ideas have matured, see Zienkiewicz and co-workers [165,166]. Utilising such formalism in the viscoelastic context, for example by Carew *et*

al. [23] and furthermore by Keshtiban *et al.* [79], have shown that under-relaxation over each equation time-step (or variable) reproduces identical structures to the generalised PC- framework of [30]. This effectively smoothes oscillations and improves stability towards higher *We*-level solutions.

A *second* aspect of stabilisation concerns the compatibility conditions on function (trial) spaces for spatial discretisation [18,56]. The mathematical analysis of Stokes flow indicates that the approximation spaces for velocity and pressure must *a priori* satisfy a compatibility condition known as the inf-sup or LBB condition (see [18]). In recent years, the stabilising influence of Poisson-based *PC*-methods has gained in appeal, questioning the need to satisfy such compatibility relationships within the spatial interpolation employed (see [166]). However, recent theoretical analysis has shown, that within either a *fe*, or spectral framework (Guermond and Quartapelle [57]), lack of satisfaction of LBB conditions may impose additional stability restrictions resulting in a lower bound on permissible time-step. Under such circumstances, when time-steps exceed this threshold, spurious oscillations may emerge that are most prominent in the pressure field. Furthermore for viscoelastic flows, the addition of a weak-form stress constitutive equation, imposes supplementary compatibility conditions on admissible interpolation spaces for velocity-gradients, ($S(\nabla u) \subset S(\tau)$) (see Fortin and Fortin [47], Baaijens [10], re DG-schemes). Nevertheless, extended inf-sup type conditions for such flows are less well-developed. The numerical consequence of deviation from such conditions appears in the form of numerical oscillations and poor stability response. The order of accuracy in representation for velocity gradients could appear to play a significant role in the satisfaction of LBB conditions. In addition, the presence of an elliptic operator, introduced via operator-splitting through the rate-of-deformation (see *SRS* below), has been found to considerably enhance LBB satisfaction for viscoelastic flows. This has been implemented in various forms of EVSS (stress-splitting) schemes. An alternative approach has been to employ recovery techniques [98] for velocity gradients, to accurately approximate the rate-of-deformation. Matallah *et al.* [97] concluded, that utilising recovery when applied to velocity gradients, may yield a more accurate and stable implementation than a conventional form (without recovery), proving competitive with other stress-splitting formulations (EVSS, DEVSS/SUPG and DEVSS/DG, see [10,98]). In [3], it was concluded that the single most important factor was the treatment of velocity gradients (weak or strong form), as opposed to the stress-

splitting *per se*. Identical vortex trends (size and intensity) for the 4:1 contraction flow were gathered across these various implementations. As above within the *SRS* method, an elliptic smoothing function may be derived, based on the residue between the continuous and discontinuous spatial representations for solvent stress term. This is achieved by introducing a differed-correction term, $\alpha(2\mu_s/\mu)(D-D_c)$, within the weak-form expression for momentum. The continuous representation, D_c, is derived from recovery procedures, whilst the discontinuous form, D, emerges via the *fe*-approximation. Here, α adopts the role of an adjustable scalar parameter, an optimal setting of which is gathered from empirical observation as extra-stress compatible: $\alpha = \mu_e/\mu_s = 8$. For this auxiliary viscosity and with the XPP-model, Verbeeten *et al.* [147] adopted the form $\alpha(\mu_s/\mu) = \sum_{i=1}^{M} G_i\lambda_i$, where $(G,\lambda)_i$ represents the (plateau modulus, relaxation time)$_i$ per mode i, with M the number of modes. Locally adaptive alternatives may also suggest themselves, see [97,134].

A third stabilisation issue, is related to the difficulties encountered within the computation of stress itself, via the constitutive equation. These equations display hyperbolic character, often reflecting large components in elastic extra-stress, which may support steep/discontinuous stress gradients in the vicinity of solution singularity. Under such circumstances, particular treatment is necessary for effective discretisation. Sharp discontinuity capturing procedures stabilise the solution locally about singular field locations, to suppress non-physical oscillations. In this respect, Aboubacar and Webster [4] employed discontinuity capturing, based on a reduced corner integration (*RCI*) technique applied in elements adjoining the re-entrant corner (six-point Newton-Cotes rule reduced to three-point rule). The rationale behind such a treatment lay in reflecting low-order local approximation, tightly capturing sharp gradients, whilst suppressing propagation of numerical noise away from singular solution zones. Resolving stress boundary layers (SBL) near singular locations is an important issue in gathering numerical stability and retaining accuracy in viscoelastic computations. As it described below, within such boundary layers the quality of velocity gradients has a major influence upon stability and accuracy (notably affecting shear stress, τ_{xy}). In addition, by including a system mollifier (such as in the *SRS*-form), oscillations are smoothed, which provides better velocity description to assist the accurate computation of stress. Upwinding procedures suppress crosswind propagation, and thereby, avoid

dispersion of the boundary layer throughout the solution domain. Note, the transverse boundary layer convection term is generally low, whilst cross-stream gradients may be large. The *SRS*-variant, via a Galerkin approximation, provides a handle on crosswind dispersion, thereby suppressing numerical oscillations near solid-wall boundaries. To achieve a similar objective within the SUPG-context, Matallah *et al.* [97] employed variational discontinuity capturing (*DC*) for the constitutive equation, and various alternative forms of strain-rate stabilisation, adaptive/local and global (see also, [134]). In the *consistent* DC-method, an additional term was appended to the streamline upwinding Petrov-Galerkin (SUPG) weighting function, to act in the direction of solution gradients (normal to the flow) and to introduce control upon crosswind solution propagation. Similar results were extracted for an *inconsistent DC*-implementation. Consistent discretisation of the constitutive equation is a major issue demanding upwinding procedures. In the present study, one appeals to a revised form of the *fe/fv* (*CT3*) scheme and derivations thereby (see [3]), which invoke a form of velocity-gradient recovery over each parent triangular finite element. One may advance to compressible algorithm representations throughout, with comparison across stabilised scheme variants and flow settings (Ma=0, $Ma \approx 0$, Ma=0.1), commenting upon the respective stabilisation properties derived thereupon.

7.2 Numerical method

The numerical method employed within this study is discussed extensively in chapter six. For the sake of completeness, in this section key aspects involved are recalled. The stabilisation employed has emerged via modification of momentum equation (*Stage 1a* and *Stage 1b*). The stabilised form of the momentum equation is revealed by appending the SRS differed-correction term (see above), as follows:

$$\frac{2\mathrm{Re}}{\Delta t}\rho^n\left(u^{n+1/2}-u^n\right)-\frac{1}{2}\nabla\cdot\left(\tau_s^{n+1/2}-\tau_s^n\right)=\nabla\cdot\left(\tau_s^n+\tau^n\right)-\rho^n\left(u\cdot\nabla u\right)^n-\nabla\left(2p^n-p^{n-1}\right)+2\alpha\mu_s\nabla\cdot\left(D-D\right)^n, \quad (7.1)$$

The same stencil is employed for *Stage 1b*. This fractional-staged procedure accommodates second-order accuracy in time, noting the new incremental *PC*-structure

of Guermond and Quartapelle [57], which introduces a three-time level reference on pressure[†].

7.3 Problem description and solution strategy

In the present study, the creeping flow of an Oldroyd-B fluid through a planar 4:1 abrupt contraction is chosen as the test-problem. This is widely recognized as a valuable benchmark to assess stability, accuracy and convergence properties, particularly at elevated levels of *We*. Such a non-smooth flow, poses a stress singularity at the re-entrant corner and a downstream-wall SBL to resolve, with provocative trends to cover in vortex behaviour and stress-field development. See chapter four for the meshing employed, and chapter five for imposed boundary conditions.

Pursuing steady-state solutions for both incompressible and compressible flows, optimal properties are sought in achieving unpoluted solutions at elevated critical levels of *We* (We_{crit}) for each stabilisation scheme attempted: *TSS*, *RCI* and *SRS*. It has been demonstrated that a combination of such stabilisation techniques may significantly improve numerical convergence properties (see below). Stress profiles, stress and pressure field plots are presented up to critical levels of *We*, around the contraction zone and along the downstream wall. The solutions are charted through the boundary layer, and structures in salient-corner and lip-vortices. Under compressible flow considerations, the generalised Tait equation of state is considered (see [154]), with a scalar parameter set of (m,B)=(4,10^2). At *Ma*-level of 0.1, this leads to an exaggerated rise in density, of about 30% above that experienced in an equivalent incompressible flow.

Two alternative solution continuation strategies have been considered. One, more stringent, of *true-time* evolution from rest at any appointed *We*-level (adjustment in time). The second follows the more conventional *incrementation* (continuation) in *We* itself (say in steps of 0.1), stepping through a series of *We* steady-state solutions (a perturbation approach). Through either solution approach, a steady-state is acknowledged by satisfying a terminating preset temporal-solution increment-tolerance (set typically as 10^{-6} with a time-step size of 10^{-4}).

[†] Multi-time level reference ties further implicitness into the system and stronger enforcement of continuity satisfaction through time.

7.4 Numerical results

To start, one may present a general overview and snapshot of the basic findings, as tabulated in Table 7.1 for incompressible flow (Ma=0.0) across each stabilisation scheme, based on We_{crit} and first normal stress-peak (N_1-peak) levels. With the *SRS*-implementation, significant elevation is observed beyond We_{crit} levels for *CT3*-scheme. Stress-peak (τ_{peak}) levels confirm agreement in solution at each We-stage reached, with rise as We increases for each scheme. The *RCI*-scheme captures steep stress gradients sharply and has larger stress-peak values compared to alternative schemes. In contrast, the *SRS*-form reduces stress-peak levels significantly. Comparatives for combinations of various stabilisation strategies are also presented in Table 7.1. In Table 7.2 the comparable results are presented for compressible scenarios (Ma≈0.0 and Ma=0.1) with stabilisation schemes. Once more, significant elevation in We_{crit} with *SRS* is observed. Introducing *RCI* to the *CT3*-structure shows some slight improvement in stability, marginally increasing We_{crit}.

Table 7.1: Incompressible: We_{crit} and principal τ_{peak}, various scheme

	Ma=0.0						
	Alone				*combinations*		
	CT3	*TSS*	*RCI*	*SRS*	*+TSS + RCI*	*+ RCI +SRS*	*+TSS + RCI +SRS*
Critical *We*	2.8	2.8	3.0	5.9	3.5	6.1	6.4
Peak N_1	91.5	91.5	105.9	133.4	85.1	157.8	171.2
N_1 at *We*=2.0	81.3	81.3	67.2	77.5	58.2	72.9	72.9
N_1 at *We*=2.8	-	-	103.1	86.7	81.4	85.8	85.8
We_{crit} salient-vortex (size,intensity*10^3)	1.05, 0.325	1.04, 0.324	1.02, 0.299	0.69, 0.114	0.97, 0.270	0.68, 0.114	0.67, 0.115
We_{crit} lip-vortex (intensity*10^3)	0.107	0.107	0.855	-	2.634	-	-

7.4.1 Incompressible-stabilised schemes results (*CT3, TSS, RCI* and *SRS*)

The neutral incompressible *CT3*-scheme is the basis for comparative evaluation across the stabilisation techniques explored. From Table 7.1, the *CT3*-scheme provides solutions up to the We_{crit} level of 2.8. Note that under the *TSS*-scheme (or any *TSS*-combination) to cope with equitable comparison in time-step scaling or solution relaxation (factor r=0.3), the time-stepping tolerance is reduced from 10^{-6} by an

equivalent factor (to say $3x10^{-7}$), so that the ratio of time-step to tolerance remains constant. The application of the *TSS*-scheme alone has little influence on high-*We* stabilisation, as We_{crit} attained is identical to that observed with *CT3*-scheme, reaching the same level of stress-peak. The incompressible *RCI*-scheme promotes We_{crit} from 2.8 (*CT3*) to 3.0. Clearly, introduction of the incompressible *SRS*-variant has promoted We_{crit} significantly, doubling its value from 2.8 (base-*CT3*) to 5.9. This finding lies in broad agreement with the observation of others who have employed similar strategies (see DEVSS/DG with GLS of Baaijens [9,10]). Referring to Table 7.1, the *SRS*-scheme offers the lowest stress-peak at *We*=2.8, when compared to alternative scheme variants (*CT3*, *TSS*, *RCI*).

Table 7.2: Compressible (*Ma*≈0.0 and *Ma*=0.1): We_{crit} and principal τ_{peak}, various scheme

	Ma≈0.0					*Ma*=0.1				
	Alone			*combination*		*alone*				*Comb.*
	CT3	*RCI*	*SRS*	*+TSS +RCI*	*+RCI +SRS (±TSS)*	*CT3*	*TSS*	*RCI*	*SRS*	*+RCI +SRS*
Critical *We*	2.0	3.3	5.4	3.6	6.3	2.0	2.2	3.1	4.9	6.1
Peak N_1	102.2	194.0	103.1	171.1	154.0	99.1	82.9	200.8	107.6	183.5
N_1 at *We*=2.0	102.2	116.2	70.3	110.4	69.5	99.1	79.1	122.8	73.4	73.5
We_{crit} sal.-vortex (size,intens.*10^3)	1.20, 0.496	0.98, 0.260	0.73, 0.119	0.94, 0.244	0.68, 0.116	1.49, 1.496	1.41, 1.384	1.28, 1.261	1.04, 0.841	0.87, 0.644
We_{crit} lip-vortex (intensity*10^3)	0.063	0.163	-	1.862	-	1.105	0.505	1.719	1.561	3.209

a)- Incompressible stress (τ_{xx}, τ_{xy}) profiles: These are illustrated in Figure 7.1 through increasing *We* and scheme-variants plotted along the horizontal line along the downstream wall (y=3.0) at the level of the re-entrant corner. Note, in the comparative in-place presentation for stress profiles, a lateral shift has been applied for each *We*-solution plot (all τ_{peak} actually occur at the re-entrant corner), that displays a rising trend in peak values as *We* increases. There is a sharp rise in stress at the re-entrant corner to τ_{peak} and decay to a trough in each *We*-solution. Beyond this state and in the τ_{xx} extensional stress, build-up is apparent to a *We*-dependent plateau level. *TSS*-stress profiles are identical to those of *CT3* up to We_{crit}=2.8. This indicates that temporal stabilisation with the *TSS*-form does not affect the *CT3* steady-state solution. For *CT3* and *TSS*-schemes, solution structure is practically oscillation-free, even at We_{crit}, as

shown in Figure 7.1a,b. Under the *RCI*-scheme in Figure 7.1c at We_{crit}=3.0, there is a 12% increase in τ_{xx} stress-peak compared to that for *CT3*-scheme. Here, one observes large oscillations associated with the generation of a secondary vestigial stress-peak in both component profiles: an indicator of looming instability, largely absent at sub-critical *We*-levels. For *CT3* and *TSS*-profiles at We_{crit}=2.8, there are also slight signs of this vestigial peak appearing. Stress (τ_{xx},τ_{xy}) profiles with *SRS* of Figure 7.1d display smooth patterns up to *We*=3.0, that revert to oscillatory form beyond *We*=4.0. Note, this level of *We* has not been attained by *CT3*, *TSS* or *RCI*-schemes. Subsequently, these oscillatory patterns gather greater amplitude with increasing *We*, until ultimately the *SRS*-scheme fails to converge beyond the super-elevated level of *We*=5.9. At this *We*-level, the principal stress-peak value has risen to 133.4, representing an increase of some 46% above the corresponding value for *CT3*-scheme at We_{crit}=2.8 (value 91.5). At *We*=3.0, the vestigial peak of the *RCI*-variant is removed with the *SRS*-form, where the solution is smooth and devoid of such features. One may relates this response to the dissipative nature of the strain-rate treatment.

b) Pressure and stress fields: Next, for each scheme-alternative, pressure and stress (τ_{xx},τ_{xy}) field contour plots are analysed within the contraction zone at sub-critical *We*=2.5 (in Figure 7.2) and We_{crit} (in Figure 7.3). For *We*=2.5 and *CT3*-scheme, Figure 7.2a illustrates sharp gradients in the vicinity of the singular solution point and the downstream boundary layer. A comparison between *CT3* and *TSS*-stress profiles and contours up to We_{crit}=2.8 (see Figure 7.2b and 7.3b) shows no noticeable disparity; see also Figures 7.3a and 4a for *CT3*-scheme. With *RCI*, at *We*=2.5 (Figure 7.2c) and for higher *We* (Figure 7.3c), oscillatory patterns begin to emerge in pressure and shear stress, close to and along the downstream wall. This is clear evidence of the *We* build-up of a SBL beyond the re-entrant corner, from which loss of stability results, concomitant with that reported in Renardy [121]. At *We*=2.0, there are no oscillations apparent and solutions with *RCI* mimic those following the *CT3*-scheme (not shown). Primary elongational stress (τ_{xx}) remains relatively smooth on the field for all schemes up to We_{crit} (noting local profile behaviour as above). With respect to pressure and shear stress, trends are smoother for *SRS* compared to *RCI*-forms (see Figure 7.2c,d at *We*=2.5). The oscillatory response within the boundary layer is particularly prominent in shear stress. Compared against *RCI*-solutions at We_{crit}=3.0 (Figure 7.3c), relatively smooth τ_{xy} *SRS*-patterns are extracted and beyond in *We* (see on to Figure 7). This

position adjusts in approaching the limit We_{crit}=5.9, when oscillations have reappeared in pressure and shear stress (Figure 7.3d).

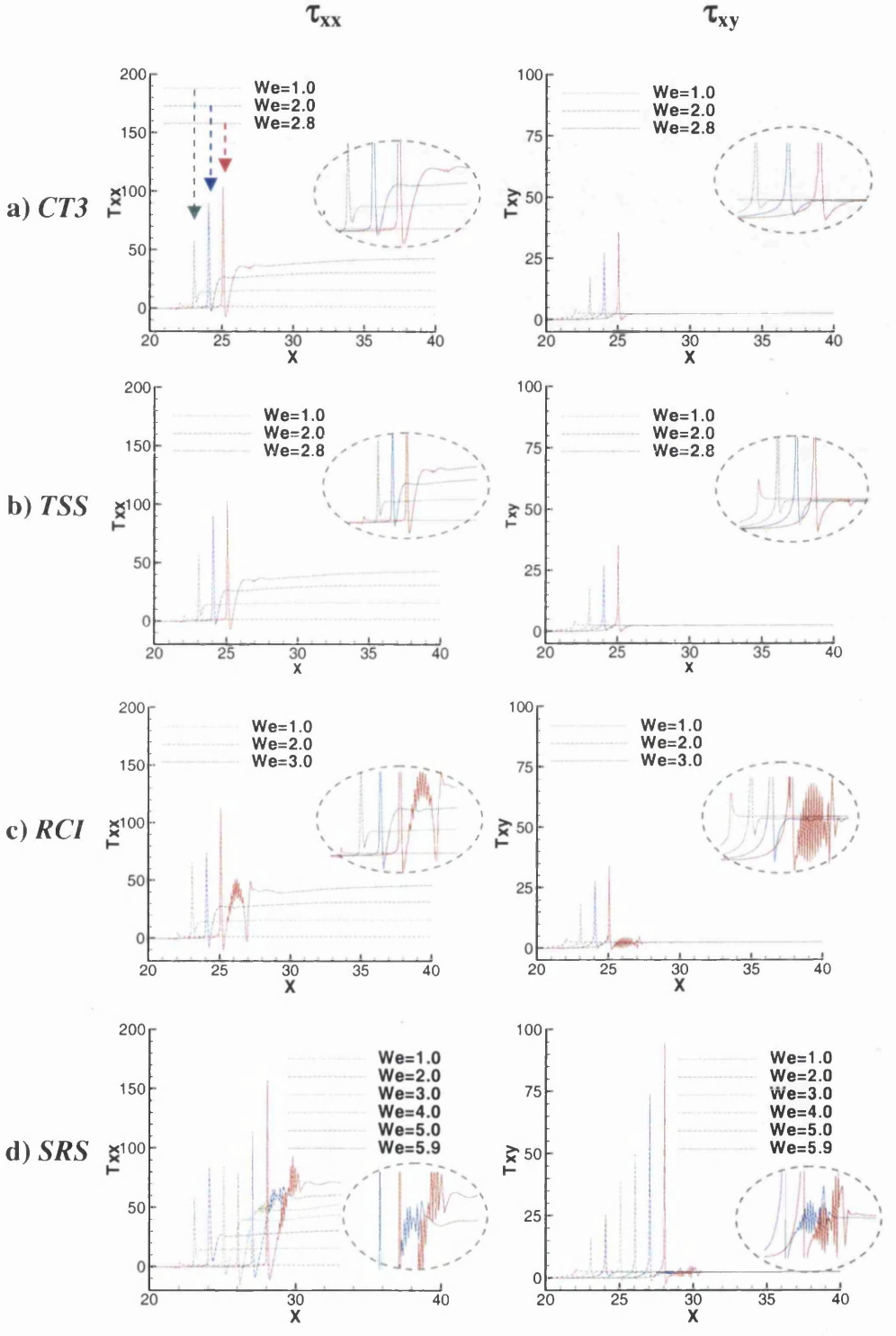

Figure 7.1: Incompressible (τ_{xx},τ_{xx})-profile, downstream-wall, increasing *We*: (left) τ_{xx} and (right) τ_{xy}; under schemes a) *CT3*, b) *TSS*, c) *RCI* and d) *SRS*

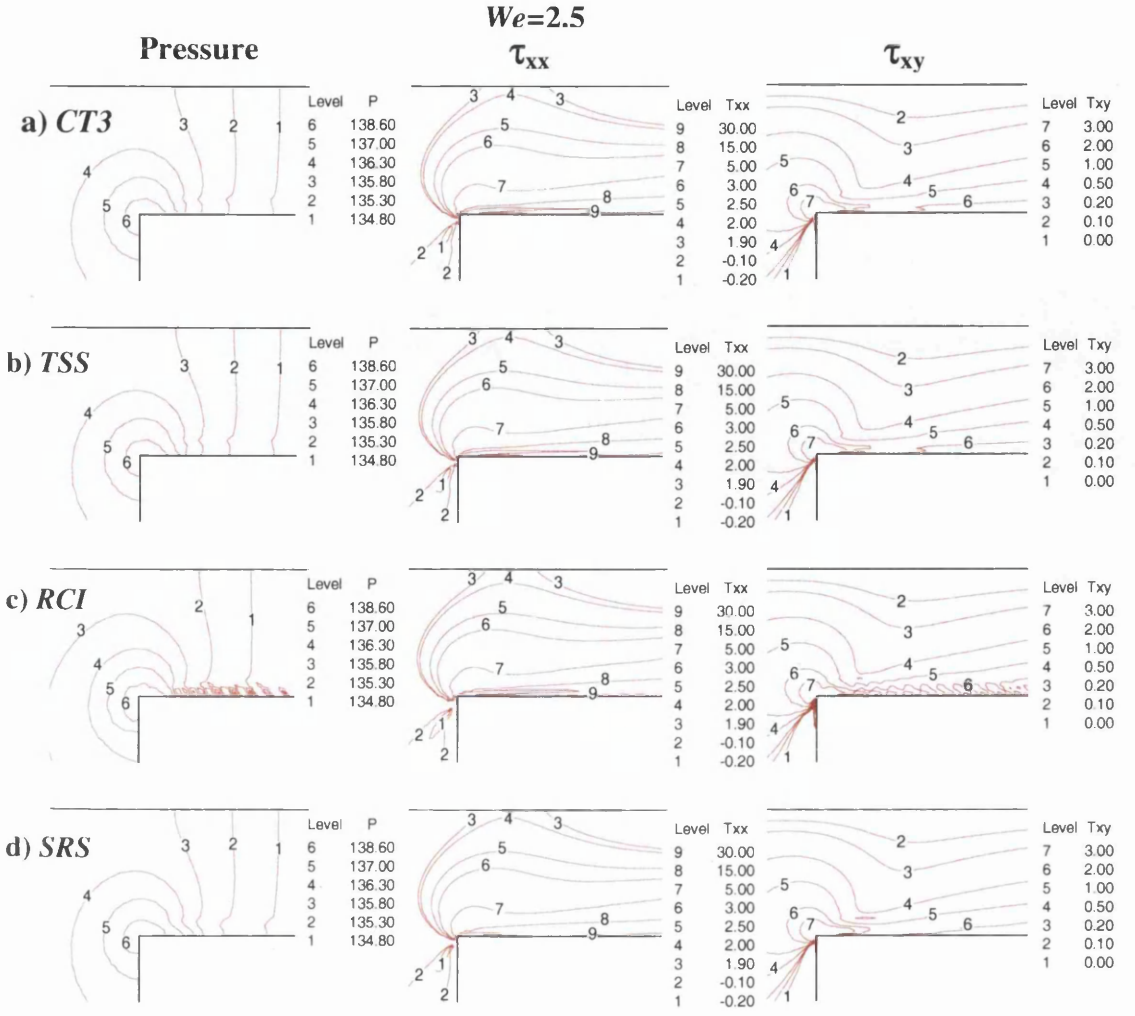

Figure 7.2: Incompressible variable fields, *We*=2.5: (left) pressure, (middle) τ_{xx} and (right) τ_{xy}; under schemes a) *CT3*, b) *TSS*, c) *RCI* and d) *SRS*

To identify the influence of *SRS* upon the flow field, Figure 7.4 contrasts solution fields extracted for the base *CT3*-scheme, both with *SRS*-inclusion and without. This corresponds to a relatively low level of *We*=2.0, where oscillations are absent in either form (see Figure 7.2). Figure 7.4 demonstrates that one may extract similar behaviour across schemes (*CT3* against *SRS*) at such a moderate level of *We* (problem-dependant), reflecting correspondence in vortex characteristics (see Figure 12 below). One can deduce that the influence of *SRS* is negligible when the solution is sufficiently smooth in the boundary layer (also confirmed on plane channel shear flow). One may gather from Figure 7.4, a connection to the use of dissipative terms in shock capturing, which are based on second and fourth-order gradients of pressure. These terms become active near sharp gradients, yet are suppressed in smooth flow zones (see Carew *et al.* [22] and Jameson [73]).

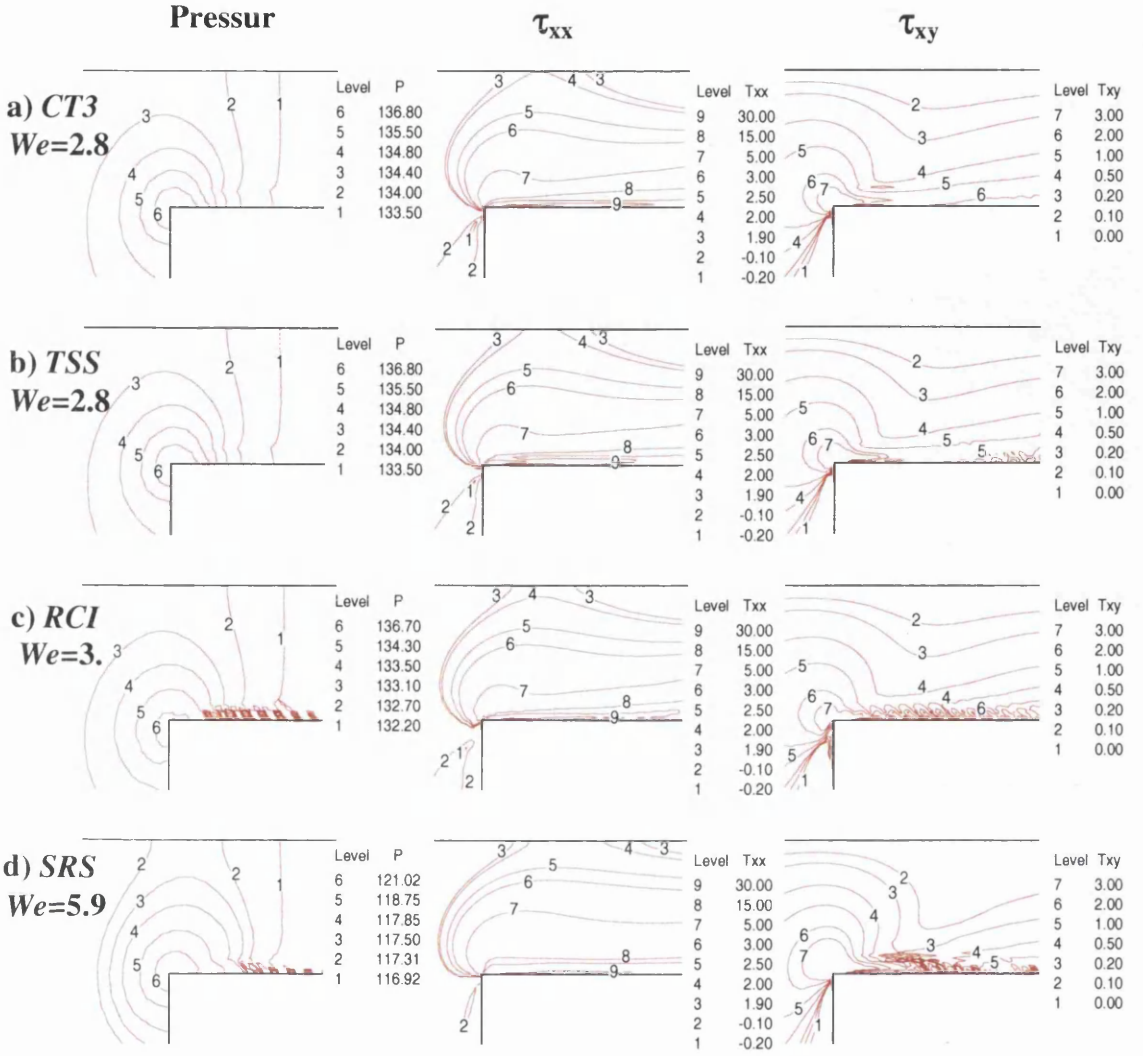

Figure 7.3: Incompressible variable fields, We_{crit}: (left) pressure, (middle) τ_{xx} and (right) τ_{xy}; under schemes a) *CT3*, b) *TSS*, c) *RCI* and d) *SRS*

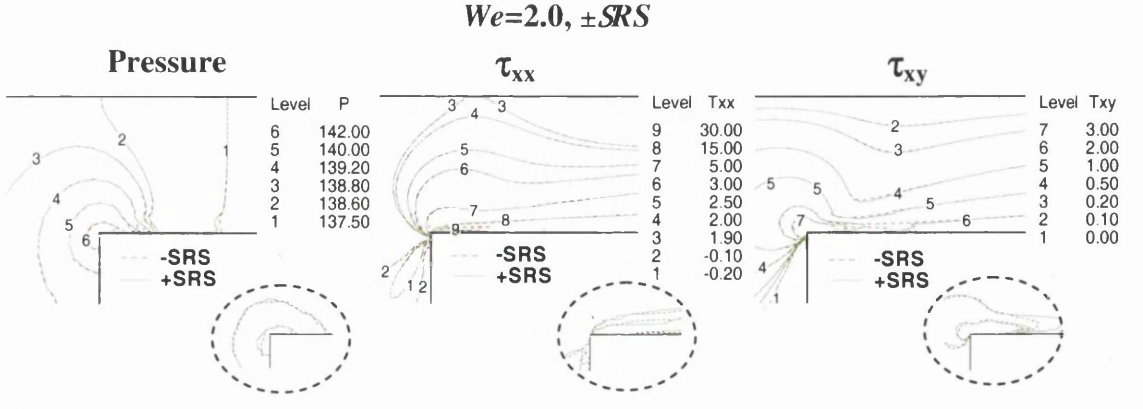

Figure 7.4: Incompressible variable fields, *We*=2.0: (left) pressure, (middle) τ_{xx} and (right) τ_{xy}; variable contour fields, *We*=2.0; (left) pressure, (middle) stress τ_{xx} and (right) stress τ_{xy}; comparison of *+SRS* and *-SRS*

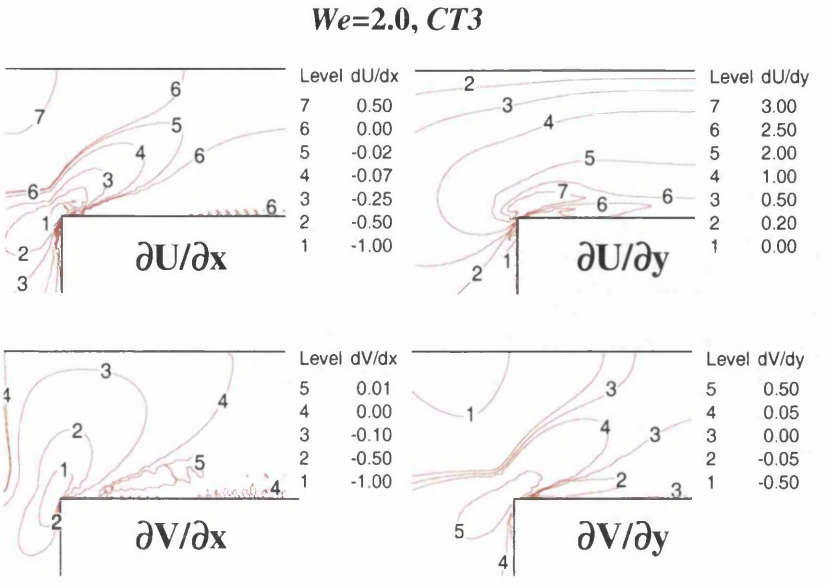

Figure 7.5: Velocity gradient contour plots at *We*=2.0, (top) U-gradients, (bottom)) V-gradients, (left) streamwise $\partial U/\partial x$, (right) cross-stream $\partial U/\partial y$, under *CT3*-incompressible schemes

c) Velocity-gradients and SBL: Boundary layer analysis plays a key role in the understanding of viscoelastic flows near walls and corners. In Newtonian flows, when inertial terms in the momentum equation are dominant, viscous terms may be neglected, except within thin fluid layers along no-slip solid boundaries. Boundary layers in the viscoelastic context are discussed in Rallison and Hinch [119] and Hagen and Renardy [59], and relevant references therein. In numerical computations on flow about singularities (where the flow supports large stress levels with steep gradients), non-physical oscillations may appear in the solution. Beyond such a singular location, the shear (velocity) boundary layer is also active. Within SBLs, convective derivatives vanish, forcing stress to be viscometric and determined completely by velocity gradients (both being large and balancing). The effect of numerical noise within the SBL often poses severe discretisation and convergence difficulties. The resolution of these boundary layers has proved a major obstacle to successful viscoelastic computations at high *We*, in for example, flows past a sphere and abrupt re-entrant corners [57]. In these regions and in the boundary layer beyond, local levels of *We* can be excessively large (see [119]), as a consequence of large velocity gradients ($We = \lambda|\nabla u|$).

One may proceed to clarify the dynamics of the SBL by interrogating the nature of the solution in the vicinity of the re-entrant corner and beyond, with back-reference to the discussion above on pressure and shear stress fields. The distortion noted in the

pressure field contours, beyond the re-entrant corner and across the SBL, vanishes as *We* reduces. This identifies that such distortion (away from level lines) is not due to a numerical pressure boundary layer, but rather to the consequence of the SBL itself. Correspondence amongst the results with *fe/fv*, and *fv*-results in references [5,41], confirms consistency in predicted solutions across different schemes. Close agreement in salient-corner vortex activity (see Figure 12 below) lends added confidence in the quality of solutions generated. To extract the impact of the various terms on the SBL, in Figure 7.5 velocity-gradient contour plots at *We*=2.5 are presented for *CT3*-scheme. This illustrates the most active (largest) velocity gradient component $\partial u/\partial y$, being present in both τ_{xx} and τ_{xy}-equations. Also, the numerical noise observed in $\partial u/\partial x$ (streamwise gradient) is highlighted, while $\partial u/\partial y$ (transverse gradient) remains relatively smooth. Importantly, the accurate determination of this dominant ($\partial u/\partial y$) component strongly influences both τ_{xx} and τ_{xy}-fields beyond the singular solution point, but more particularly τ_{xy}.

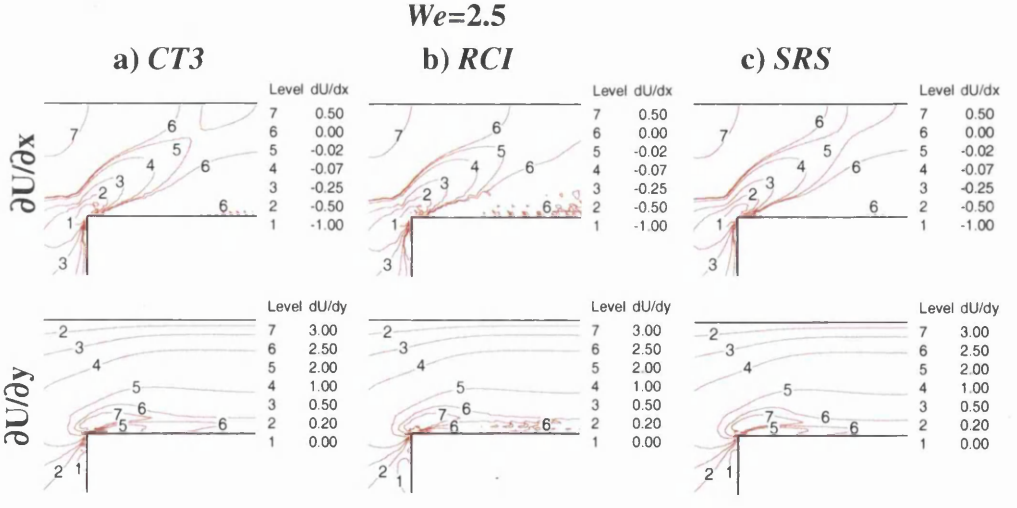

Figure 7.6: Incompressible longitudinal velocity gradient fields, *We*=2.5: (top) streamwise $\partial U/\partial x$, (bottom) cross-stream $\partial U/\partial y$; under schemes a) *CT3*, b) *RCI* and c) *SRS*

In Figure 7.6, velocity-gradient contour plots at the higher level of *We*=2.5 are presented for *CT3*, *RCI* and *SRS*-schemes. As with the *CT3*-scheme (also *TSS*) in Figure 7.6a, no oscillatory behaviour is observed and stress fields are smooth. Equivalently, for the *RCI*-scheme, one observes degradation in velocity-gradient contours, as clearly demonstrated in Figure 7.6b. Note that, at the lower level of *We*=2.0, corresponding

contours remain smooth. This may be a consequence of heavy oscillation within the τ_{xy}-field, noting that in comparison, the primary elongation stress τ_{xx} retains reasonable smoothness. The removal of numerical noise in Figure 7.6c, indicates the enhanced stability of the *SRS*-scheme at this level of *We*, in contrast to that inherent within the *RCI*-implementation. The *SRS*-contour plots for the dominant $\partial u/\partial y$-term retain smoothness up to *We*=4.5, beyond which oscillatory τ_{xy}-profiles emerge through the boundary layer. This is clearly demonstrated in Figure 7.7, where stress profiles with increasing *We* are illustrated for the *SRS*-scheme.

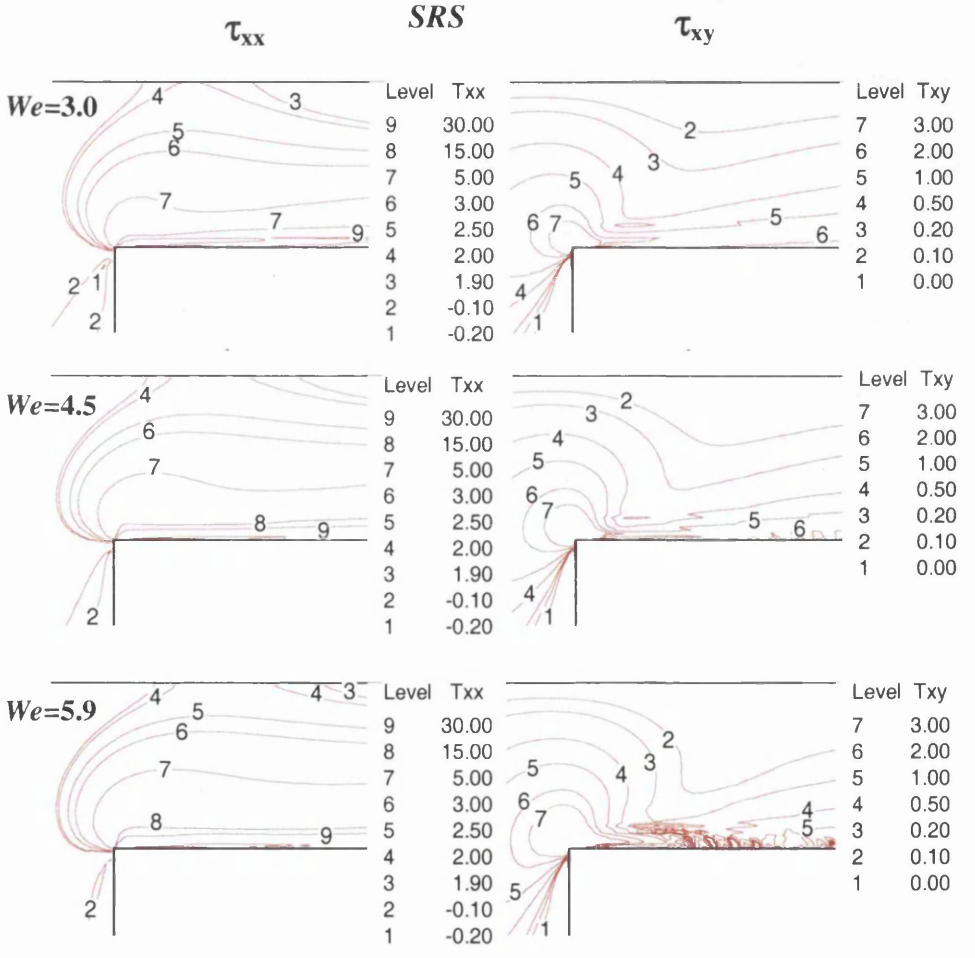

Figure 7.7: Incompressible variable fields, increasing *We*: (left) τ_{xx} and (right) τ_{xy}; under *SRS*-scheme

Boundary layer evolution with increasing *We* is illustrated in Figure 7.8 for the three variants, *CT3*, *RCI* and *SRS*-schemes. Here, the SBL profile is characterised by the vanishing $\partial\tau_{xx}/\partial y$ contour and build-up of boundary layer length is apparent with increasing *We* over all scheme variants, as annotated by arrow. The boundary layer

profile for the *CT3*-scheme (and *TSS*) is smooth up to We_{crit}=2.8 (Figure 7.8a). At We_{crit}=3.0 with the *RCI*-scheme, the boundary layer profile has clearly become numerically 'polluted' and disjoint, as shown in Figure 7.8b, reflecting once again oscillatory patterns in stress. Figure 7.8c, provides further evidence of the enhanced stability, enjoyed with the *SRS*-scheme, through the evolution of the boundary layer with increasing *We* up to We_{crit}=5.9. Hence, one observes the consequence of *RCI*-adjustment is the propagation of noise into the downstream-wall SBL†, generating oscillatory field patterns thereby (see Renardy [121]). In addition, the *SRS* may be used as a mechanism to stabilise the *RCI*-strategy (see below). Conversely, one would attribute the considerable elevation of We_{crit} under the *SRS*-implementation as being mainly due to the tight capturing of the SBL, via the inclusion of weak-form dissipative terms in the formulation, $2\alpha\mu_s\left(D-D_c\right)$. This has the dual effect of controlling cross-stream solution prolongation, and at the same time, eases the compatibility relationship between function spaces adopted for velocity-gradients and stress (also pressure, as a result).

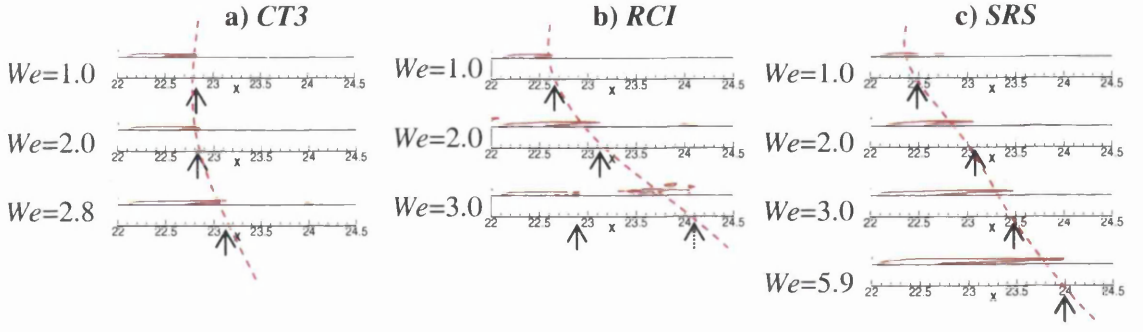

Figure 7.8: Incompressible boundary layer growth, increasing *We*: under schemes a) *CT3*, b) *RCI* and c) *SRS*

7.4.2 Temporal convergence rates

Here, *CT3*, *RCI* and *SRS*-schemes are analysed under a *true-transient* setting at the sub-critical level *We*=1.5, to provide indications of scheme behaviour, and particularly for the *SRS*-variant. Temporal convergence plots on history tolerance through solution components (pressure, velocity and stress) are analysed via the three levels of mesh refinement (M1, M2 and M3 of Figure 4.6) and three levels of time-step (Δt=5*10^{-4}, 10^{-4}, 5*10^{-5}). Time-stepping termination tolerance levels remain fixed at 10^{-6}. Figure 7.9 illustrates the associated temporal convergence tolerances for stress across scheme and

† A link is established between lip-vortex activity stimulated and consequent degradation observed within the SBL, which may prove to be primarily responsible for subsequent failure in numerical convergence.

mesh refinement for $\Delta t=10^{-4}$. Overall, the same temporal convergence trends are observed across mesh and scheme in stress (likewise in velocity and pressure). Under the finest mesh M3, testing across schemes reveals that the *SRS*-scheme gathers the most rapid ultimate convergence rate, followed by the *RCI*-variant (see Figure 7.9d).

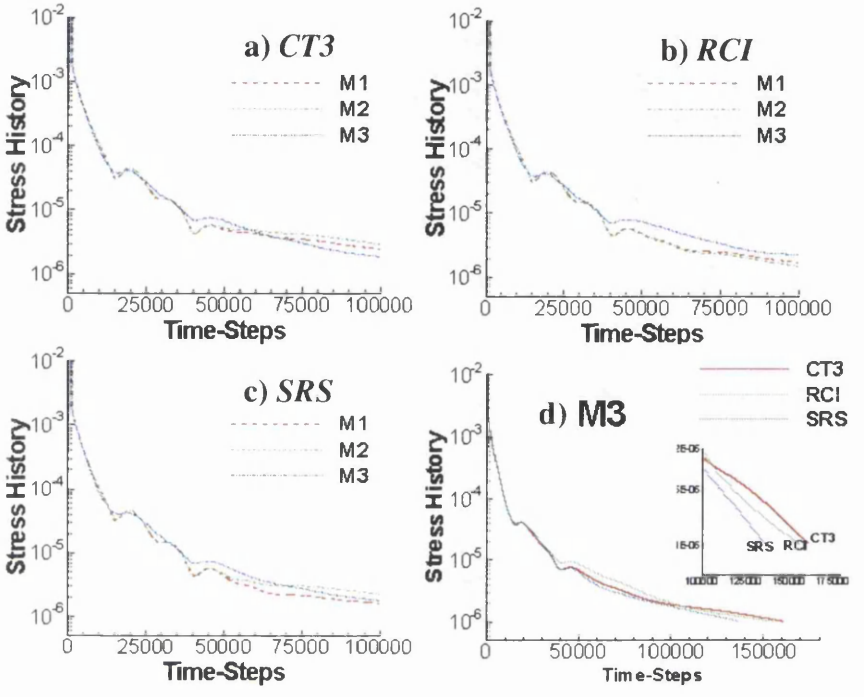

Figure 7.9: Incompressible temporal convergence patterns for stress with mesh refinement; *We*=1.5, $\Delta t=10^{-4}$: under schemes a) *CT3*, b) *RCI* and c) *SRS*; d) across schemes M3-mesh

Temporal rates of convergence for the *SRS*-scheme for various solution components are illustrated in Figure 7.10, through different levels of time-step and the finest mesh M3. Under the smallest time-step, where spatial discretisation error is minimal, less time is required than with the other time-step settings to attain the specified tolerance level, with more rapid early convergence in stress. Large amplitude oscillatory convergence patterns are observed in pressure, being larger for the larger time-steps, yet frequencies are similar. This is indicative of the improved temporal stability response with incremental pressure-correction. Comparatively, oscillatory patterns are reduced in velocity and smoothed in stress. In Figure 7.10d, temporal evolution of the 'differed-correction term', denoted as $(D-D_c)$, is plotted indicating its reduction through time. One may note that through this 'differed-correction term', temporal convergence rates follow faithfully those in stress, independent of time-step selection. This mechanism

acts as a temporal control-monitor to solution evolution, whilst achieving a steady-state under a specified tolerance.

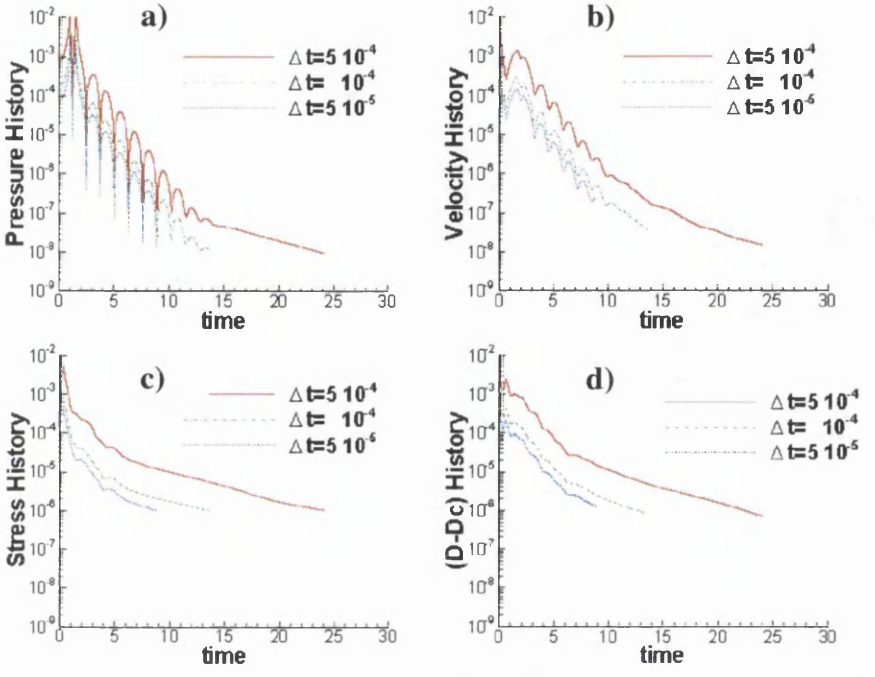

Figure 7.10: Incompressible temporal convergence patterns with temporal refinement; *We*=1.5, mesh M3 under *SRS* scheme: for variables a) pressure, b) velocity, c) τ and d) *D-Dc*

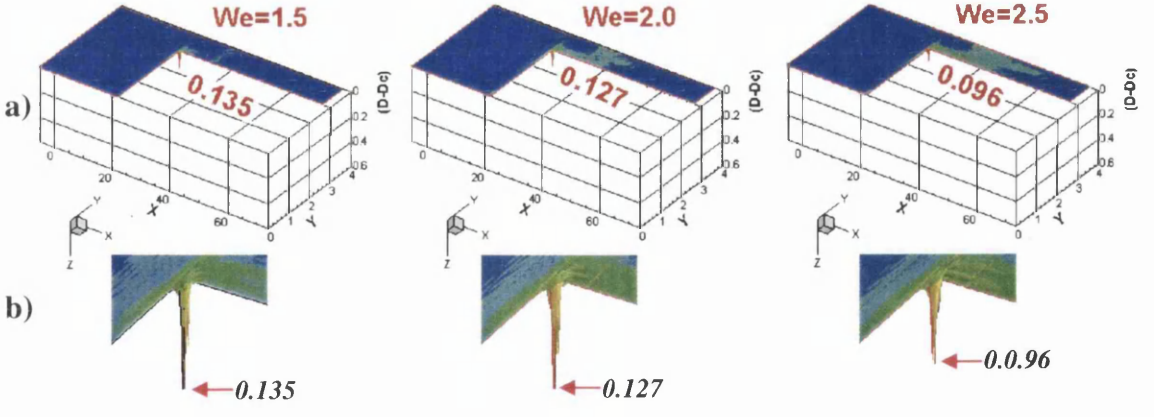

Figure 7.11: Development of $(D\text{-}Dc)_{incomp}$ under increasing *We*; *SRS*-scheme, mesh M3: a) whole domain, b) re-entrant corner zone

Steady-state three-dimensional plots of the $(D-D_c)$ term are provided in Figure 7.11 for the refined mesh M3, at *We*=1.5, 2.0 and 2.5 and Δt=5*10^{-4}. This figure starkly exposes the localised nature of the stabilisation term, which takes affect principally at the re-entrant corner in the form of a singular-valued function (usefully characterising

the singularity). By increasing the *We*-level, the contribution of this term is slightly reduced through dissipation (by 30% from *We*=1.5 through to *We*=2.5). This evidence identifies that *SRS*-implementation does not disturb the solution field away from the localised re-entrant corner neighbourhood.

7.4.3 Vortex behaviour

Vortex enhancement and reduction are important aspects in the study of contraction flows, being associated with both salient-corner and lip-vortices, where both physically and through prediction, trends in vortex behaviour have been quantified via size, shape and strength. The literature base is broad, being evidenced by works: experimentally of Evans and Walters [42,43], McKinley and co-workers [99] and Boger [11]; and from simulation/theory, Matallah *et al.* [98], Aboubacar and Webster [4], Xue *et al.* [161], Oliveira and Pinho [108], Alves *et al.* [6], Renardy [121] and Keshtiban *et al.* [79]. Usefully, Alves *et al.* [5] and Aboubacar *et al.* [1,2] have catalogued many of the published results. A review on vortex activity is provided in Appendix 7.B.

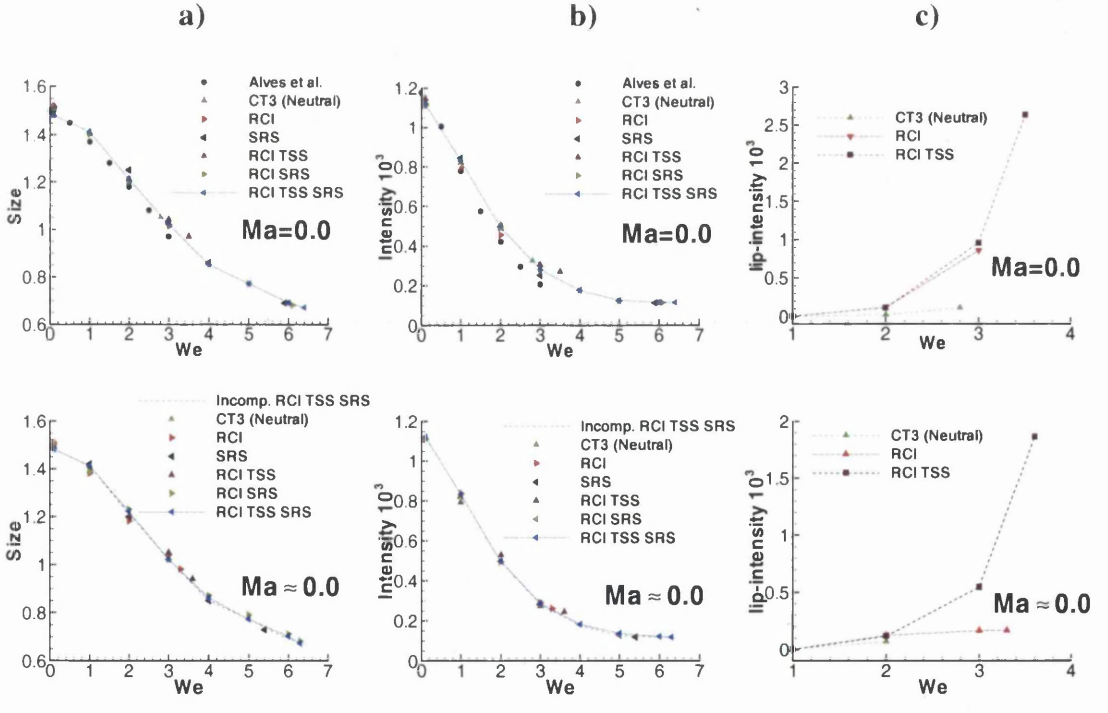

Figure 7.12: Incompressible vortex trends, increasing *We*: (top) Ma=0.0, (bottom) Ma≈0; salient-corner vortex a) size, b) intensity; and c) lip-vortex intensity

Figure 7.12 provides a summary of the incompressible vortex activity results, displaying salient-corner vortex size and intensity (Figure 7.12a,b), and lip-vortex intensity (Figure 7.12c). Close agreement is observed amongst the various stabilisation

strategies adopted and comparatively against the results of Alves *et al.* [5]. There is reduction in salient-corner vortex intensity in a continuous form towards a threshold value. The *CT3*-scheme displays a lip-vortex, and introducing *RCI,* promotes lip-vortex presence further. In contrast, *SRS* removes this flow feature completely. Hence, this feature is linked directly to the numerical scheme and its treatment of the singularity.

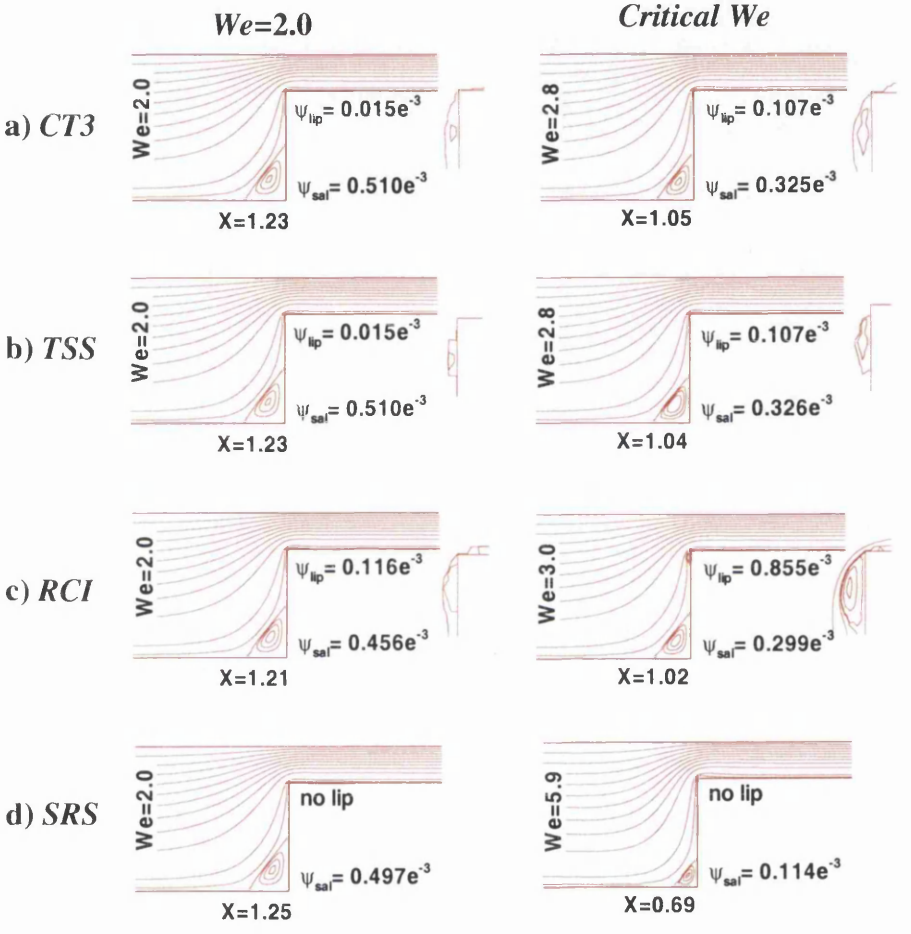

Figure 7.13: Incompressible streamlines: (left) *We*=2.0 and (right) We_{crit}; under schemes a) *CT3*, b) *TSS*, c) *RCI* and d) *SRS*

Here attempt is to enumerate the findings on vortex activity through finest mesh M3 solutions, as a consequence of the additional stabilisation procedures outlined above. Note, in all streamline plots, a total of sixteen levels are dispatched covering core-flow: ten equitable levels, from 0.1 to 1.0, followed by two levels at 10^{-2} and 10^{-3}; plus four levels to illustrate the salient-corner-vortex (inclusive from the minimum level to that of the separation-streamline). At the lower *We*-levels, a large salient-corner vortex is present, both in size and intensity[†]; vortex reduction is clearly apparent with increasing

[†] No lip-vortex with *CT3* for *We* < 2.0; Ψ_{sal}=-1.115 10^{-3} at *We*=0.1; Ψ_{sal}=-0.838 10^{-3} at *We*=1.0.

We. This trend of salient-corner vortex behaviour is observed for all stabilised schemes under consideration (identical size and intensity). In Figure 7.13, streamline contour plots for all scheme-variants are presented at *We*=2.0 (left) and at We_{crit}-levels for each scheme (right). A lip-vortex emerges at *We*=2.0 and once present, the lip-vortex grows in size. With respect to the *TSS*-scheme and vortex activity, a minute lip-vortex appears at *We*=2.0: intensity of $0.015*10^{-3}$, identical to its *CT3*-counterpart. This growth continues in intensity, to reach $0.107*10^{-3}$ at We_{crit}=2.8 (comparable to *CT3*). At *We*=1.5, there is no indication of lip-vortex presence with either *CT3* or *TSS*. Considering *RCI*-vortex activity, lip-vortices display exaggerated increase in size and intensity, when compared to their equivalent solutions with either *CT3* or *TSS*. In addition, the *RCI* lip-vortex is stimulated somewhat earlier at *We*=1.5: intensity $0.095*10^{-3}$. At *We*=2.0, its intensity is about 1.5 times larger than its *CT3*-counterpart.

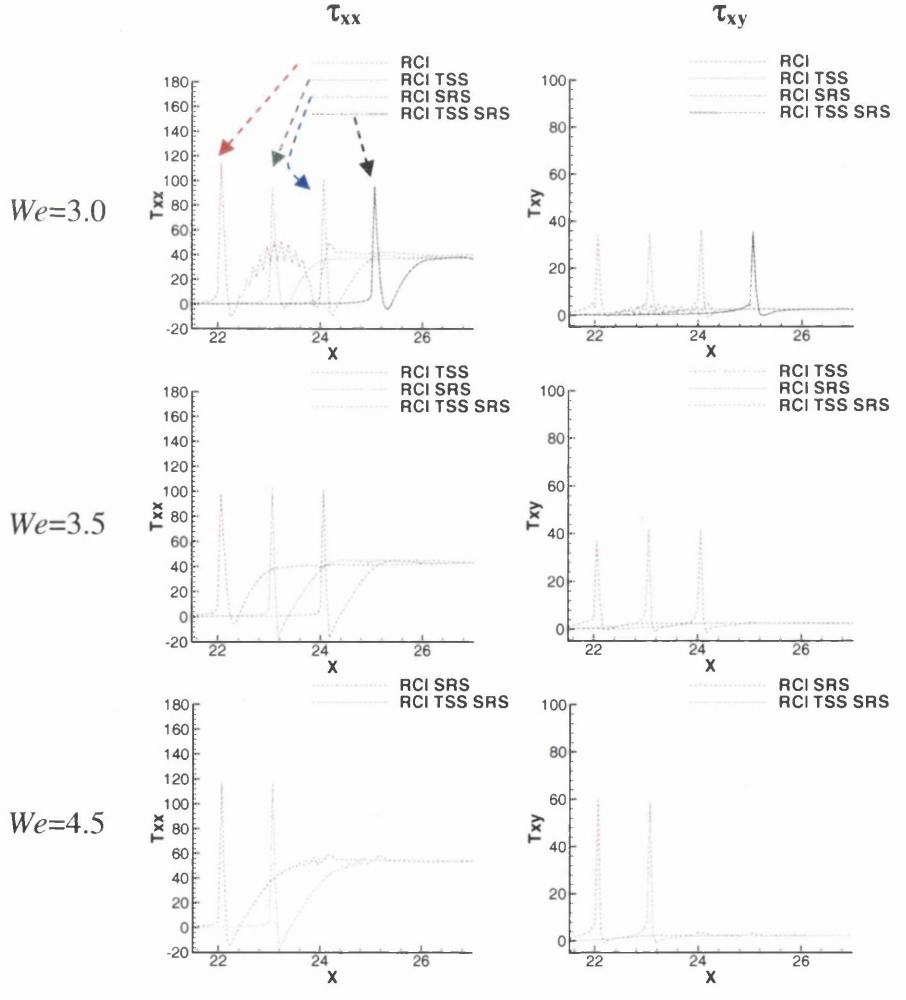

Figure 7.14: Incompressible τ-profiles, downstream-wall, scheme combinations: (left) τ_{xx} and (right) τ_{xy}; (top) *We*=3.0, (middle) *We*=3.5, and (bottom) *We*=4.5

7.4.4 Stabilised scheme combination results (RCI/TSS/ SRS)

After investigating the effect of application of each individual stabilisation scheme when layered upon the incompressible *CT3*-variant, one is in a position to consider optimal scheme combinations. First, the *RCI*-scheme, with results tabulated in Table 7.1, has been found to produce heavy-side oscillation beyond We=2.5 (We_{crit}=3.0). Note, introducing *TSS* upon the *RCI*-form, reduces τ_{peak} levels (see Table 7.2), yet elevates lip-vortex intensity. Stability properties for *RCI*-scheme are improved by appealing to either the *TSS*-scheme, or the *SRS*-scheme, or both. This is demonstrated in stress profiles in Figure 7.14, where *RCI*-oscillations are completely removed at We=3.0. Note that no oscillations are observed up to We=3.5 for any scheme combination with *RCI*. Oscillations appear once more at We=4.5 and beyond, for (*RCI+SRS*) and (*RCI+TSS+SRS*)-scheme combinations. Also, We_{crit} is progressively elevated from the level of 3.0 for *RCI*-scheme, to 3.5 under (*RCI+TSS*)-scheme, to 6.1 with (*RCI+SRS*)-scheme, and to an impressive level of 6.4 with (*RCI+TSS+SRS*)-scheme combinations. Up to We=6.1, both (*RCI+SRS*) and (*RCI+TSS+SRS*)-scheme solutions mimic one another. By combining all approaches under (*RCI+TSS+SRS*)-form, a remarkable level of We=6.4 may be reached. The benefit of the *SRS*-scheme is again highlighted, in stabilising the numerical algorithm and promoting the We_{crit}-level crafted: the introduction of the *SRS*-technique has doubled We_{crit} over those forms without *SRS*. In Figure 7.15, velocity-gradient profiles ($\partial u/\partial x$ and $\partial u/\partial y$) are compared at We=3.0 on the downstream-wall horizontal line (y=3.0) for *RCI* and (*RCI+SRS*)-variants. This figure illustrates the appearance of streamwise oscillations under the *RCI*-scheme, particularly prominent in the transverse gradient $\partial u/\partial y$, so vital to the accurate description of the SBL. Such oscillations are identified as being completely removed through combinations with *SRS*-inclusion.

Independent of stabilisation approach or scheme combination applied, similar salient-corner vortex response is preserved (see Figure 7.12). Regarding lip-vortex response, any combination where the *SRS*-scheme is employed, removes the lip-vortex completely for the incompressible setting. It is prominent that, the *RCI*-scheme (or combinations thereof) promotes lip-vortex activity when compared to other scheme combinations. One may comment, in passing, that at the less stringent time-stepping

convergence tolerance/time-step pairing† of (10^{-6},10^{-4}), the *TSS*-scheme combined with *RCI* proved considerably more stable. Thereby, We_{crit} of 11.6 was extracted, bearing out the realisation of improved stability properties (see earlier to equivalence with GLS). Unfortunately, this proves to be at the expense of degradation in accuracy within this hyperbolic-parabolic context, which demands greater care in precision. One notes similar comments in Alves *et al.*[5].

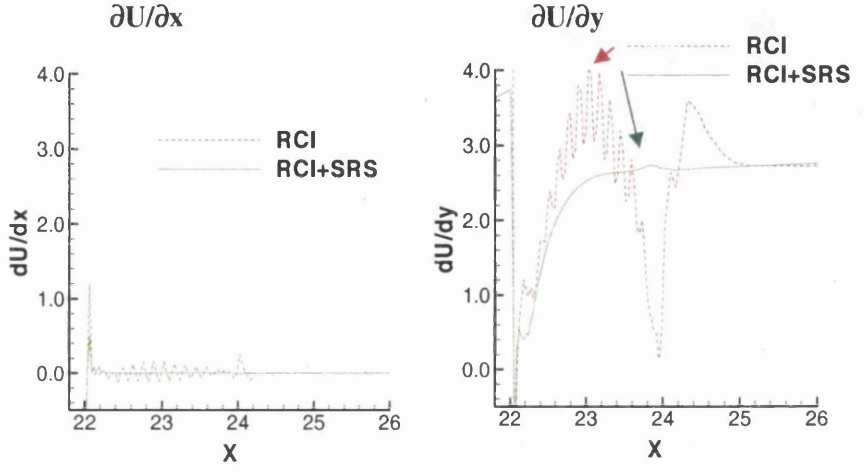

Figure 7.15: Incompressible ∇u-profiles, downstream-wall, *RCI*-scheme ±SRS-inclusion, We=3.0: (left) streamwise $\partial U/\partial x$ and (right) cross-stream $\partial U/\partial y$

7.4.5 Compressible algorithm results

The compressible version of the algorithm with $\rho \neq$constant ($Ma>0$) is the more general classification, collapsing to the incompressible form with ρ=constant (Ma=0). This may be emulated practically by setting the Tait parameter pairing (m,B) to high levels asymptoting to $Ma \approx 0$. From a numerical perspective, introducing compressibility may convey residual from the continuity equation into the momentum equation (see Eq.(2.5)), whereupon residuals may be minimised simultaneously. Thereby, violation of local mass conservation may be reduced. In chapter four, the improved stabilisation characteristics of the compressible above the incompressible algorithm, in terms of temporal convergence history (reducing the bandwidth between variables through time) has been demonstrated. Here, one may follow the above incompressible analysis, reporting results across the same three forms of stabilisation scheme.

† Normally enforced as ($3*10^{-7}$,10^{-4}) for *TSS*-combinations.

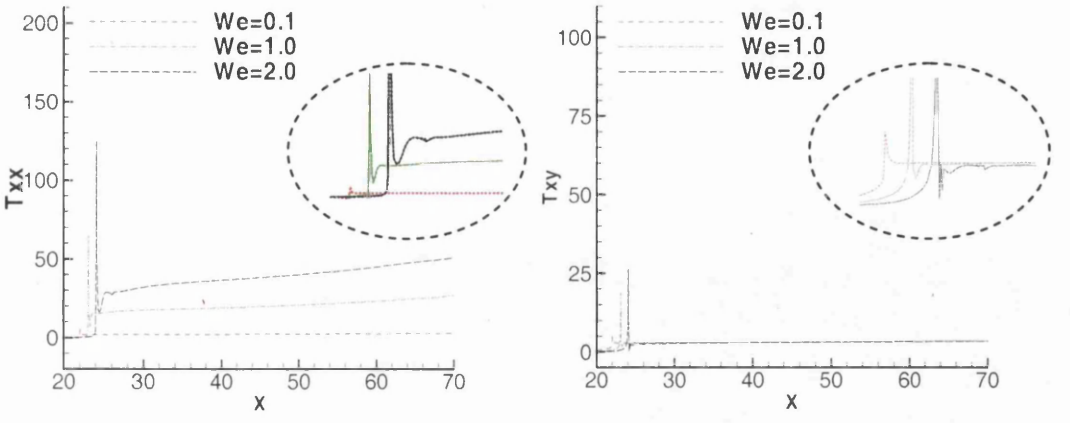

Figure 7.16: Compressible τ-profiles, downstream-wall, increasing *We*, *CT3*-scheme: (left) τ_{xx} and (right) τ_{xy}

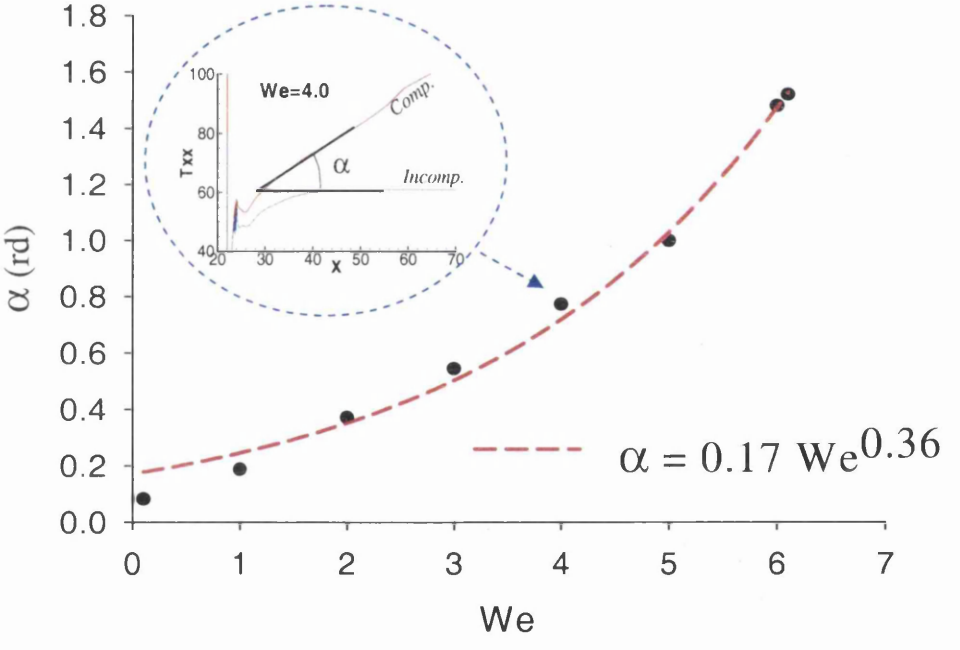

Figure 7.17: Compressible τ-growth rate α, downstream-wall, increasing *We*; under *RCI+SRS*-scheme; zoomed plot, α at *We*=4.0

a) Mildly compressible schemes under Ma=0.1

Here, the Mach number is set to 0.1 through the selection of Tait parameter pairing $(m,B)=(4,10^2)$, with Table 7.2 covering We_{crit} and principal stress level (N_1-peak) reached for each scheme. The neutral $CT3_{comp}$-scheme achieved $We_{crit}=2.0$. This level is promoted to $We_{crit}=2.2$ under TSS_{comp}-scheme, and further to $We_{crit}=3.1$ under RCI_{comp}-scheme. The most effective stabilisation scheme (SRS_{comp}) has elevated the We_{crit} level

above $CT3_{comp}$ by some 2.5 times, whilst the combination $(RCI+SRS)_{comp}$ has more than tripled We_{crit} to 6.1. For each scheme, one may observe a lowering of critical We_{comp} by about a unit below its incompressible correspondent (see below, due to $\nabla.u$ inclusion). That is, with the exception of RCI_{comp} (and its combinations), where We_{crit} levels are maintained. With regard to τ_{peak} at a selected *We*-level, SRS_{comp}-scheme displays the lowest value, whilst RCI_{comp} claims the largest.

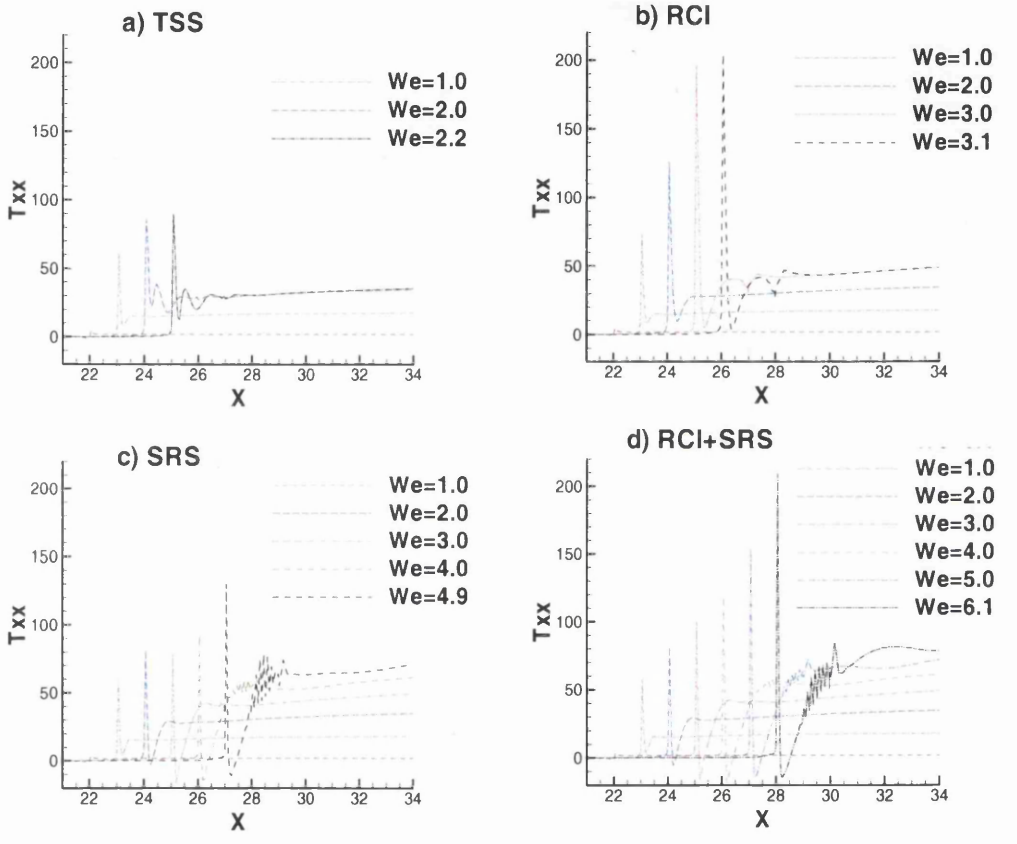

Figure 7.18: Compressible τ_{xx}-profiles, downstream-wall, increasing *We*: (left) τ_{xx} and (right) τ_{xy}; under schemes a) *TSS*, b) *RCI*, c) *SRS*, and d) *RCI+SRS*

Compressible stress (τ_{xx},τ_{xy}) profiles are illustrated along the downstream wall in Figure 7.16 through increasing *We* for $CT3_{comp}$-scheme. Even at We_{crit}=2.0, both stress component profiles are practically oscillation-free. After the re-entrant corner, one observes monotonic streamwise stress build-up along the solid wall, principally in τ_{xx} (much less so in τ_{xy}, which is practically *We*-independent). The growth rate of τ_{xx} along the downstream wall increases as *We* increases (initial rate/angle in radians, empirically estimated as a function of We^k, k=0.36, see Figure 7.17). This feature is attributed to the velocity field, reflecting dependence upon density (see Eq.(3.5)), which impacts upon the stress field accordingly. Furthermore at *We*=2.0, the TSS_{comp}, SRS_{comp} and

$(RCI+SRS)_{comp}$-schemes maintain their τ_{peak} level, within 5%, of their respective incompressible values. At the same We=2.0 level, the $\tau_{peak\text{-}comp}$ rises by 20% for $CT3_{comp}$ above $CT3_{incomp}$, and doubles for RCI_{comp} above RCI_{incomp} (see Figures 7.1 and 7.18). Figure 7.18 illustrates compressible τ_{xx}-profiles with increasing We for schemes TSS_{comp}, RCI_{comp}, SRS_{comp} and $(RCI+SRS)_{comp}$. At We=2.0, TSS_{comp} τ_{xx}-profiles show the emergence of the telltale subsequent vestigial peak/trough followed by an oscillatory pattern. This pattern grows further up to We_{crit}=2.2. RCI_{comp} removes such oscillations below We=3.0, with rebirth thereafter. At We=3.0, RCI_{comp} has smoothed stress profiles and doubled τ_{peak} over RCI_{incomp}. With SRS_{comp}, smaller oscillations are observed at We=3.0 and stronger stability is enjoyed up to We_{crit}=4.9, though oscillations begin to amplify between these two We-levels. At We_{crit}=4.9, the SRS_{comp}-τ_{peak} is some 8% larger than that for $CT3_{comp}$, at its We_{crit}=2.0. The response for both *SRS* and *RCI* is reflected in their combination, $(RCI+SRS)_{comp}$, delivering an impressive level of We_{crit}=6.1. As anticipated under this combined scheme, τ_{peak} for any particular We-solution is bounded by the lower limit of the *SRS*-solution and the upper limit of the *RCI*-solution. Note that *TSS*-combinations are excessive in computational expense requiring lower termination tolerance, and are avoided subsequently on practical grounds.

Following the presentation of above incompressible results, Figure 7.19 presents compressible τ_{xy}-contours considering schemes $CT3_{comp}$, RCI_{comp}, SRS_{comp} and $(RCI+SRS)_{comp}$ at We=2.0, 3.0, 4.5 and 5.5. This shows the lack of smoothness in $(RCI+SRS)_{comp}$-solutions is delayed to beyond We=4.5. Around the contraction zone, a region of low Ma, one observes little difference in compressible pressure and stress fields, in comparison to their incompressible alternatives, recalling the irregularity in $\tau_{xy\text{-}incomp}$-contours at large We-levels. One notes the smooth structure with RCI_{comp}-scheme in contrast to RCI_{incomp} (see Figures 7.2 and 7.3). Under RCI_{comp}, velocity-gradient contours (not shown) are also smooth. Again, τ_{xx}-contours are smooth for all Ma=0.1-variants, as for Ma=0.0. Along the downstream solid wall, the compressible SBL is a region subject to relatively low Ma-levels (typically, Ma<0.001). Therefore, compressibility has little impact upon the SBL, and hence, compressible-SBL development follows that of its incompressible counterpart. As the RCI_{comp}-scheme maintains solution smoothness up to We_{crit}=3.1, the SBL for this We-level is also smooth (see RCI_{incomp} at We=3.0).

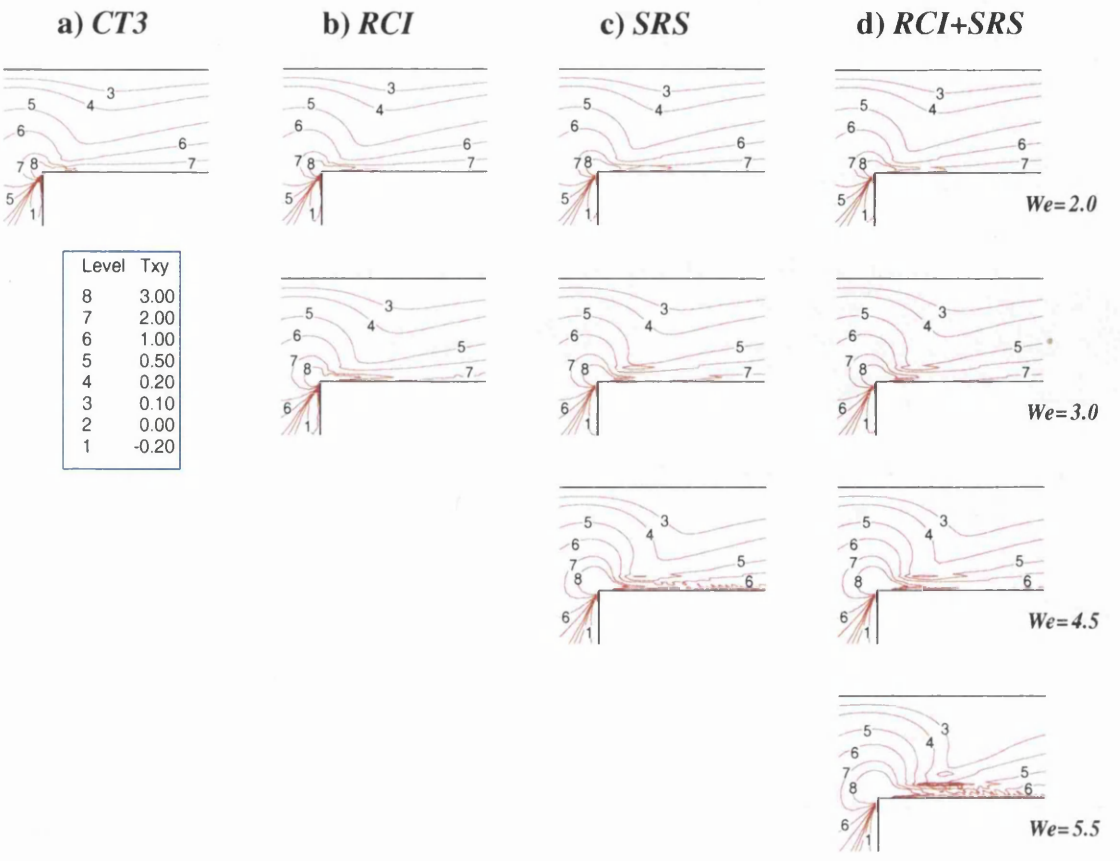

Figure 7.19: Compressible τ_{xy}-fields, *We*=2.0 to 5.5: under schemes a) *CT3*, b) *RCI*, c) *SRS* and d) *RCI+SRS*

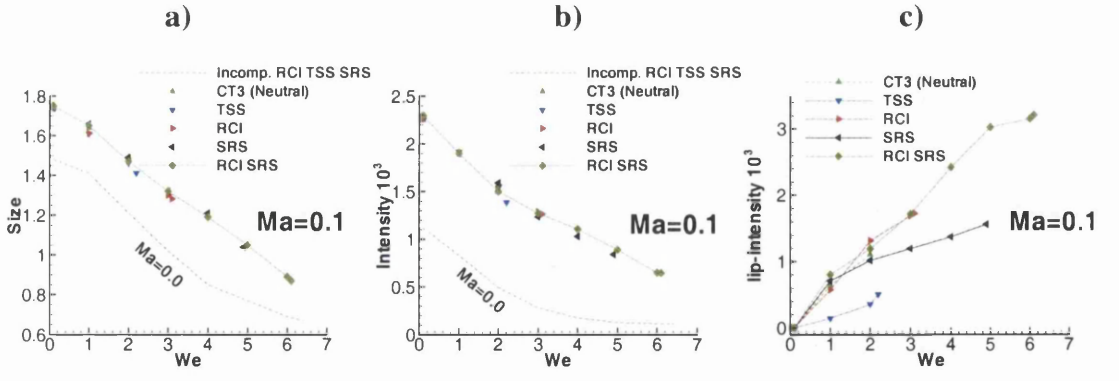

Figure 7.20: Compressible vortex trends, increasing *We*: salient-corner vortex a) size, b) intensity; and c) lip-vortex intensity

To our knowledge and in the style adopted here, the consideration of compressibility upon vortex activity in these viscoelastic flows is novel in this domain. Figure 7.20 summarises trends in vortex behaviour, with increasing *We* for different stabilised compressible implementations. As under incompressible constraints and at equitable *We*-levels, stabilised schemes produce comparable salient-corner vortex characteristics.

One observes larger salient-corner and lip-vortices in compressible flow above their incompressible counterparts, following similar evolution characteristics: salient-corner vortex-size decays with increasing *We* (vortex reduction), whilst lip-vortex size is enhanced. A well-developed compressible lip-vortex emerges as early as *We*=1.0 and continues in its growth as *We* rises. Now, the compressible SRS_{comp}-scheme does not remove the lip-vortex as was the case under the incompressible setting (see on). Again, RCI_{comp} or $(RCI+SRS)_{comp}$-versions, promote the lip-vortex feature somewhat further in comparison to other scheme variants. Figure 7.21 illustrates $CT3_{comp}$-streamline patterns with increasing *We*-levels. Here, one observes shape adjustment in salient-corner vortices from their equivalent incompressible form at *We*=0.1 (same in the Newtonian case) to a more stretched, and convex form (separation line becomes curved). At *We*=2.0, $CT3_{comp}$-vortex characteristics are elevated compared to their incompressible forms by about 20% in size, tripling intensity in the salient-corner vortex. Similarly, lip-vortex intensity is about thirteen times larger. In Figure 7.22, streamline plots for $CT3_{comp}$, RCI_{comp}, SRS_{comp} and $(RCI+SRS)_{comp}$- variants are presented at *We*=2.0 (left) and at We_{crit}-levels for each scheme (right). At elevated *We*-levels the curved shape of the separation line is confirmed, which becomes more convex as *We* increases further. From *We*=3.0-level onwards, one notes that lip-vortex intensity becomes larger in absolute value than that of its salient-corner partner. At large *We*-level, the emergence of a second trailing-edge vortex on the downstream-wall, just beyond the re-entrant corner, is a specific feature new to the compressible setting.

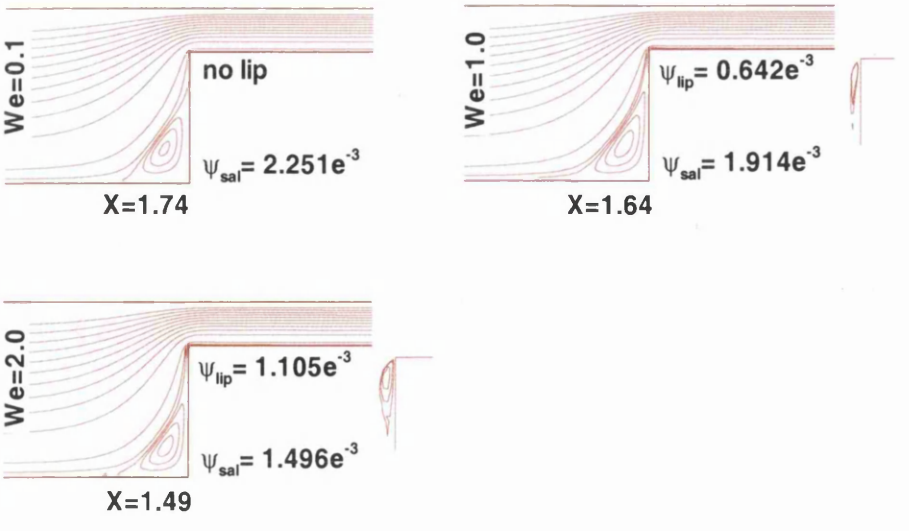

Figure 7.21: Compressible streamlines, increasing *We*; under *CT3*-scheme

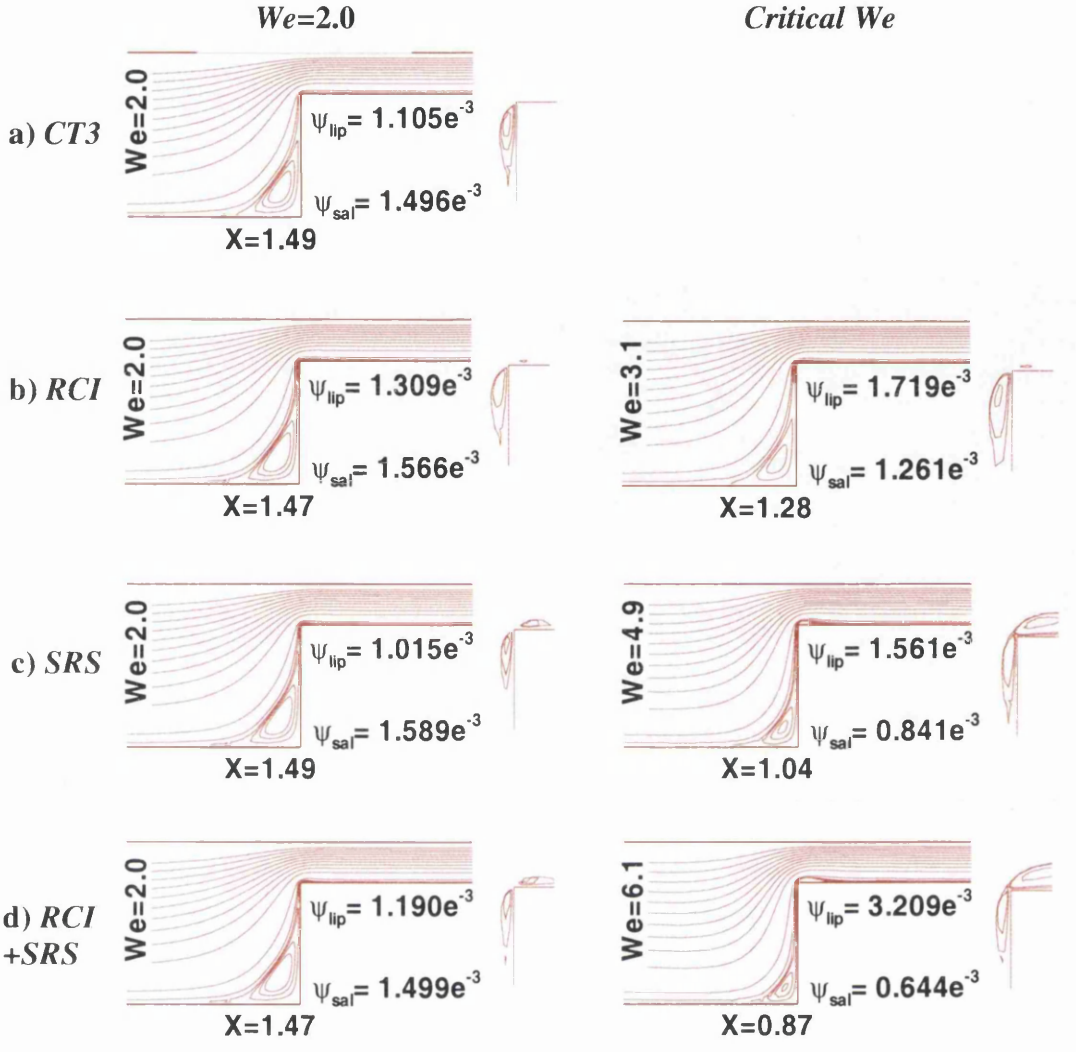

Figure 7.22: Compressible streamlines: (left) increasing *We* and *We*=2.0, (right) We_{crit}; under schemes a) *CT3*, b) *RCI*, c) *SRS* and d) *RCI+SRS*

b) Limiting compressible schemes under Ma≈0.0

In this limiting state, Tait parameters may be set to $(m,B)=(10^5,10^5)$ with $Ma=O(10^{-5})$, to emulate incompressible conditions via the compressible algorithmic structure. In contrast to $CT3_{Ma\approx0}$ (We_{crit}=2.0) and Table 7.2 results, $RCI_{Ma\approx0}$ elevates We_{crit} to 3.3 and doubles equivalent τ_{peak} at respective We_{crit}. Likewise, $SRS_{Ma\approx0}$ promotes We_{crit} from 2.0 to 5.4, whilst maintaining the same $CT3_{Ma\approx0}$ level of τ_{peak}. *TSS* brings modest stabilisation to $RCI_{Ma\approx0}$ (We_{crit} rises from 3.3 to 3.6 for $(TSS+RCI)_{Ma\approx0}$); whilst *SRS* provides major impact upon $RCI_{Ma\approx0}$ (We_{crit} increases from 3.3 to 6.3 for $(RCI+SRS\pm TSS)_{Ma\approx0}$), tripling the state for $CT3_{Ma\approx0}$. Here, *TSS* inclusion has no effect;

SRS presence dominates to maintain the lowest levels of τ_{peak} (observed say, at *We*=2.0). *RCI* without *SRS* attains the largest τ_{peak}-levels, so that scheme combinations with *RCI* and *SRS* are limited between the bounds of each, as observed in incompressible and more compressible settings. Vortex trends for *Ma*≈0 and *Ma*=0 are shown comparatively in Figure 7.12 across schemes with increasing *We*, showing identical salient-corner vortex response.

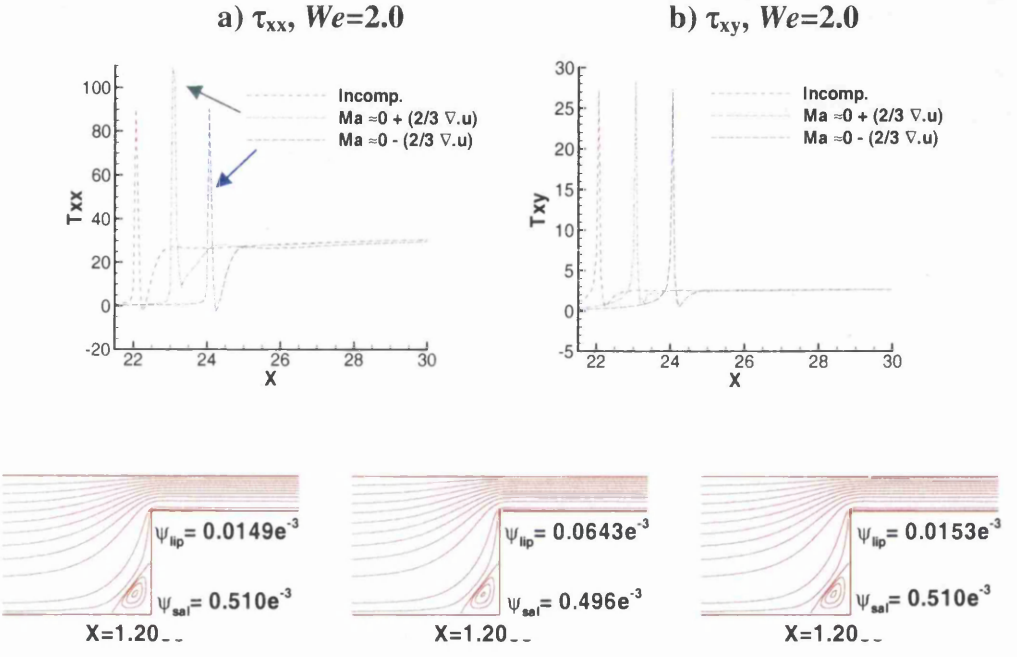

Figure 7.23: '*∇.u*' term influence, *We*=2.0, CT3 scheme: on τ-profiles, downstream-wall, a) τ_{xx}, b) τ_{xy}; on streamline patterns, c) *Ma*=0, no added term, d) *Ma*≈0, added term, e) *Ma*≈0, no added term

Ma≈0 versus Ma=0: Here, one may compare compressible results in Table 7.2 with conventional incompressible values of Table 7.1. Overall, at a fixed *We*=2.0 and under most schemes, one notes elevated τ_{peak} that occur with the *Ma*≈0-scheme, when compared to their *Ma*=0.0-equivalents, as rationalised below. Correspondingly on We_{crit}, $CT3_{Ma\approx0}$ and $SRS_{Ma\approx0}$ provide lower values than $CT3_{Ma\approx0}$ and $SRS_{Ma\approx0}$, respectively. Alternatively, $RCI_{Ma\approx0}$ improves We_{crit} above $RCI_{Ma=0}$ (3.3 above 3.0), which is also true for *RCI*-combinations. At *We*=2.0, there is slight adjustment in τ_{peak} for *CT3* and *SRS* versions, with increase for $CT3_{Ma\approx0}$ above $CT3_{Ma=0}$, and decrease for $SRS_{Ma\approx0}$ from $SRS_{Ma\approx0}$; τ_{peak} values double with $RCI_{Ma\approx0}$ above $RCI_{Ma\approx0}$. In general terms, one observes that lowering τ_{peak} has the corresponding effect of lowering We_{crit}. Overall, the

compressible '$\nabla.u$' extra-term inclusion within the momentum equation (see Eq.(2.5)) has caused reduction in We_{crit} attained for *CT3* and *SRS*, whilst it is maintained for *RCI* and its combinations, see below.

Ma≈0 versus Ma=0.1: Likewise, one may contrast findings across settings with variation in *Ma* covered in Table 7.2. Overall at *We*=2.0, all schemes maintain their allotted levels of τ_{peak}, when comparing *Ma*≈0.0 to *Ma*=0.1 setting (discussed above). We_{crit} levels are maintained for *CT3* (2.0) and *RCI* (3.3) and deteriorate for *SRS* from *Ma*≈0.0 (5.4) to *Ma*=0.1 (4.9). In particular, $CT3_{Ma\approx0}$-scheme reaches We_{crit} of 2.0, similar to $CT3_{Ma=0.1}$ case, with an identical τ_{peak}.

Discarding '$\nabla.u$' extra-term (Ma≈0, κ=0): Here the influence of the '2/3* $\nabla.u$' term in Eq.(2.5) is analysed in greater detail. This term vanishes under an incompressible (*Ma*=0) setting. As suggested by Oliveira and Pinho [32], this two-third term inclusion can improve numerical accuracy and steady-state convergence properties with *We* rise. This feature was observed in the chapter four for viscous and chapter five for viscoelastic, where the compressible algorithm with *Ma*≈0 displayed better temporal convergence characteristics over its incompressible alternative. Note, the inclusion of this $\nabla.u$ term is natural to the compressible (*Ma*=0.1) setting. To interrogate dependency and response to term inclusion under the compressible *CT3*-scheme, *Ma*≈0 setting, three numerical tests have been conducted. In the first, test (a), the 'conventional' incompressible scheme is employed for comparison. The second, test (b), consists of appending the extra-term to the momentum equation through Eq.(2.5). In the third, test (c), this term is discarded, whilst the scheme remains compressible otherwise (equivalent to setting $\kappa=2\mu_s/3=0.074$). Findings are illustrated in Figure 7.23a,b for *We*=2.0, through stress (τ_{xx},τ_{xy})-profiles and comparison against its true-incompressible counterpart (namely, case (a), *Ma*=0.0). At *We*=2.0, the extra-term inclusion has the effect of increasing τ_{peak}-levels (particularly in τ_{xx}) by about 20% above the *Ma*=0 case. Identical *Ma*=0 solutions to the incompressible case are retrieved when the extra-term is nullified, with We_{crit}=2.8 solution reached for case (c), mirroring that for incompressible case (a). For case (b), We_{crit} is lowered to 2.0 (as with *Ma*=0.1 case). Hence, in the present algorithmic framework, one may conclude that this extra-term inclusion for *Ma*≈0, is actually responsible for the early *loss of stability* beyond *We*=2.0. A closer look at streamline patterns for *We*=2.0 illustrated in Figure 7.23 c-e, shows that identical

salient-corner vortex characteristics are obtained for each variant. However, lip-vortex intensity is magnified some *four times* above the incompressible form under $Ma \approx 0$ setting (case (b)). The same level of lip-vortex intensity is observed for cases (a) and (c). Overall, this confirms that differences are localised to the re-entrant corner, affecting lip-vortex intensity and τ_{peak}-levels, which have a direct influence on the level of We_{crit} reached. The evidence is unequivocal. The extra inclusion of $\nabla.u$ (continuity residual) alone is responsible for these flow features. Any local discrepancy in continuity representation immediately impacts on lip-vortex generation, which in this respect and context must be taken as numerical and spurious.

7.5 Conclusions

This study has quantified the enhanced stabilisation characteristics of a time-marching incremental pressure-correction formulation, in solving the abrupt four-to-one planar contraction benchmark for incompressible ($Ma=0$ and $Ma \approx 0$), and mildly compressible ($Ma=0.1$), Oldroyd-B viscoelastic flows. To do this, *three* separate additional stabilisation strategies have been investigated, embedded upon a hybrid *fe/fv*-implementation (base neutral scheme), reporting on levels of stable Weissenberg number solution; vortex activity, stress field structure about abrupt corners and in boundary layers; and cross-stream solution prolongation.

The temporal stabilisation scheme applied through time-step relaxation (*TSS*), effective in true transient scenarios [79], is observed to have little relative influence in promoting *high-We* stability. In contrast, a second stabilisation strategy of reduced corner integration (*RCI*), has promoted considerable stabilisation, particularly under compressible ($Ma \approx 0$ and $Ma=0.1$) considerations. Under *RCI*, large stress peaks have been extracted at the re-entrant corner, alongside large lip-vortex structures. Nevertheless, greatest improvement has been encountered with the third stabilisation strategy, that of strain-rate stabilisation (*SRS*). With *SRS*, We_{crit}-levels for stable solutions have more than doubled above the neutral variant. Theoretically, the weak dissipative terms in the *SRS*-formulation have the dual effect of: (*i*) controlling cross-stream solution propagation (absent in most currently favoured schemes) and (*ii*) easing compatibility relationships between function spaces on stress and velocity gradients (extended LBB-condition satisfaction). In practice, stress peaks have been constrained, whilst lip-vortices have been completely removed under incompressible settings ($Ma=0$

and $Ma \approx 0$). Combinations of these three stabilisation variants have recorded optimal stability properties. An unexpected result was that the *SRS* 'differed-correction term', $(D - D_c)$, was found to characterise temporal error-norm stress convergence patterns, and thereby, the nature of the stress singularity at the re-entrant corner, yet without solution degradation elsewhere. Hence, this may be appreciated as a derived mechanism to incorporate singularity within the solution at the re-entrant corner. One may attribute the considerable elevation of We_{crit} under *SRS* to the tight capturing of the stress boundary layer (SBL).

Overall, with increasing *We*, for each scheme and independent of flow conditions, salient-corner vortex reduction and lip-vortex growth has been observed. At a selected *We*-level and under a specific flow setting, all scheme variants have produced similar salient-corner vortex trends. In contrast, lip-vortex features are found to be significantly affected by the particular re-entrant corner treatment. Surprisingly, at $Ma=0$ and $Ma \approx 0$ levels, it has been observed that continuity residual error may spark off purely numerical (false) lip-vortex response, assuming uniqueness of solution (non-bifurcation [121]). This generates exaggerated re-entrant corner stress peaks that distinguish between $Ma=0$ and $Ma \approx 0$ solutions. The absence of lip-vortices under SRS-solutions has clearly identified this erroneous position. Nevertheless, this lip-vortex feature is certainly present under the compressible *Ma=0.1* setting, with or without *SRS*. This leaves some open questions of general algorithms/codes and of the quality of their respective solutions about such singularities. Under certain numerical approximations, the experience here is that mere global satisfaction of continuity (common to many continuous pressure-interpolations, for example), may stimulate considerable continuity residual, which may itself dictate the local nature of the solution predicted. This lays still greater demands upon localised mesh resolution and iterative/time-stepping convergence states to more precisely approximate steady-state and transient dynamics. Noting continuity satisfaction also raises the issue of bulk viscosity in compressible computations. Its role and numerical influence, are left as a subject open for future study.

7.6 Appendix 7.A: Pressure-correction approach

A coupled statement of the problem for transient incompressible viscous flow, leads to elliptic-parabolic equations, becoming hyperbolic–parabolic in the compressible configuration. The pressure acts as a Lagrange multiplier within the system. As pressure is absent in the continuity equation, pressure must be updated implicitly for incompressibility to be satisfied. This aspect renders the numerical solution of such a problem a severe challenge. In addition, the resulting discrete system of equations for pressure and velocity is normally large and generally difficult to solve efficiently [25]. Furthermore, the viscoelastic context, introduces a first-order space-time hyperbolic constitutive equation in stress. The computation costs soar dramatically in this context through additional unknowns and increasing complexity.

Pressure-correction (also termed projection) methods were conceived to overcome the above difficulties, reducing system size and breaking down complexity. In this respect, pressure-correction methods were system designed, based around fractional-staged procedures, solving the system through a series of segregated equations for each variable, and armed with predictor-corrector schemes. Strictly, this idea may be related to a fundamental theorem of Helmholtz-Hodge classifying the orthogonal decomposition of a vector over a finite domain (see [71])[†]. The introduction of the *PC*-approach has proven to be a significant advance in the computation of incompressible (transient) flows. Still, it is not a complete panacea, and there is room for improvement covering aspects of treatment of numerical boundary layers, boundary conditions, '*splitting error*', and change of mathematical type of the system. For example, it has been shown by Webster *et al.* [154] that changing eigenvalues within the present *PC*-scheme via artificial compressibility, can affect convergence patterns in the computation of Stokes flow. *Splitting errors* arise from the fact that, solution error per time-step is minimised in a sequential manner for each consecutive equation, as opposed to the whole. One must guard against the loss of any benefit gained via pressure-correction; ensuring that this is not outweighed through degradation in temporal accuracy [25],

[†] The Helmholz decomposition theorem states that a smooth vector field is uniquely determined, in a bounded regular domain, when its divergence, curl and normal (or tangential) component on the boundary, are assigned. Consequently, it is implied that every smooth vector field decomposes into the sum of a gradient field component and one, which is divergence-free.

convergence rate and stability. For implementation within the viscoelastic context, these aspects may be hidden within the representation of stress.

PC-schemes have been applied in the approximation of a large number of flows, comprising incompressible, chemically reactive, viscoelastic and compressible flows. For compressible flow, *PC*-schemes have shown superior merits in the computation of zero-Mach number to large Mach number flows, extending to flows with mixed Mach number. With $Ma \approx 0$, singular regions must be resolved for compressible solvers. For variable range *Ma*-flows, it may be the case that some highly compressible regions coexist alongside almost incompressible zones. Consequently, significant effort has been devoted to developing efficient and accurate variants of pressure-correction methods, particularly in the context of *fv* (most common) and *fe*-discretisation (see, for example [3]). The greater power, flexibility and consistent analysis lies within the *fe*-context, which subsumes all variational and strong formulations.

7.6 Appendix 7.B: Review on vortex activity studies

Experimentally in planar configurations, Evans and Walters [42,43] established the link between salient-corner vortex growth, and the onset and growth of a lip-vortex. Likewise, lip-vortex activity itself may be responsible for salient-corner vortex enhancement [43]. In their experimental study, the dominant driving force behind vortex activity was attributed to fluid properties and contraction geometry ratio. For example, with a shear-thinning polyacrylamide solution, a lip-vortex was apparent for a 4:1 contraction ratio, whilst for a constant viscosity Boger fluid, such a feature was only beginning to emerge once the contraction ratio had reached 80:1. The data of McKinley and co-workers [99] in axisymetric configurations would point to the fact that lip-vortices for Boger fluids are present and dynamically stable for contraction ratios beyond 4:1 (critical ratio), below which temporal instabilities and 3D-effects begin to have an influence, so that stable steady-states are elusive to capture; see the results of Boger similarly [17].

From the numerical standpoint, many authors have highlighted the need for a high degree of mesh refinement, required for an accurate and reliable representation of vortex activity. One might note the impracticality to pursue mesh refinement towards the corner beyond a certain critical threshold, due to the consequence of approximating

the singularity too closely. Under creeping flow conditions, Matallah *et al.* [98] presented a comprehensive literature review on vortex activity, indicating some of the obstacles in accurately predicting lip-vortex activity. In their study for Oldroyd-B fluids, based on a *fe*-scheme and an unstructured triangular tessellation, the authors introduced a SUPG/velocity-gradient-recovery technique to solve the constitutive equation. Findings reflected the appearance of a lip-vortex as early as We=1.0, which grew in intensity with increasing We. This lip-vortex strength was found to be larger than that for its salient-corner counterpart. Similarly, based on *fv*-discretisation, Aboubacar and Webster [4], Xue *et al.* [161], Oliveira and Pinho [108], also observed the appearance of a lip-vortex: at We=2.0 in [4] and We=1.6 in [6]. Oliveira and Pinho [108] detected the appearance of a lip-vortex for an UCM model at We=1.0. Notably, Aboubacar and Webster [108] observed a reducing trend towards a practically vanishing lip-vortex with mesh refinement, for *CT3* and *RCI* scheme-variants.

We have investigated this scenario further in the present study, under even more stringent steady-state tolerance settings and via additional stabilisation constructs. Once more, the sensitivity of lip-vortex response to the precise form of the discretisation employed is highlighted. Alves *et al.* [6] applied a differencing procedure (MINMOD) for their stress solver to improve the accuracy of their *fv*-implementation. Through a mesh refinement strategy and increasing We up to the critical level of We=5.0, they managed to observe a reduction in salient-corner vortex characteristic cell-size, with enhancement of the lip-vortex. In a more recent study, the same authors (Alves *et al.* [5]) have catalogued many of these published results on vortex activity (size and intensity), recognizing some clear discrepancies. They have demonstrated close agreement with predictions from the hybrid *fe/fv* algorithm [4]. In their study, they have employed a new *fv*-scheme for steady flows, termed CUBISTA. The scheme incorporates total-variation diminishing (TVD) constraints within an implicit time-marching method. In this manner, they have been able to achieve an Oldroyd-B solution for Oldroyd-B at We=2.5 on their finest mesh. Alves *et al.* [5] also observed salient-corner vortex reduction with increasing We. By extrapolating data on lip-vortex intensity through mesh refinement for We=0.5 and 1.0, they have established that the lip-vortex would vanish. Yet, at We=1.5, a finite lip-vortex would survive with vanishing mesh-size (intensity: $0.02*10^{-3}$ and size: 0.062). Based on these findings, Alves *et al.* [5] conclude that 'although minute, the lip-vortex is not an artefact of the

computation'. One may reflect on this position in the light of the *SRS*-stabilisation offered here.

All such findings demonstrate that trends in salient-corner vortex characteristics are better predicted than is the case for lip-vortices. It is now widely accepted for planar contraction flows, both experimentally and numerically, that upon increasing *We* and for constant viscosity fluids (such as those represented by Oldroyd models), one anticipates reduction in salient-corner vortex-size and intensity. In this case, the particularly intriguing question, concerning the existence and behaviour of a lip-vortex, remains unresolved. As suggested by Renardy [121], it is possible that the lip-vortex may appear as a result of bifurcation, and that solutions with and without lip-vortices may exist. Any lip-vortex mechanism tends to vary with mesh refinement and the manner of handling convection terms. In the present study and with increase of *We,* under certain implementations some growth in lip-vortex activity have been observed. One can also point to the fact that this is influenced particularly by the type of treatment employed to deal with the stress singularity and any solution dissipation operator introduced.

CHAPTER 8

Concluding remarks

The objective of this thesis has been to establish accurate numerical methods for the simulation of compressible flow with complex fluids. An extensive review on flows has been provided at low Mach numbers (LMN), pointing to the severe difficulties which compressible flow solvers encounter in dealing with such flows. The literature has advocated extending pressure-based incompressible schemes to accommodate compressible flows. This is particularly so at low to vanishing Mach numbers, where these types of schemes demonstrate robustness and efficiency in character. Consequently, a high-order, time-marching, fractional-staged, incremental pressure-correction scheme has been adopted, to accommodate viscous/viscoelastic flows. For this propose, the pressure update equation (*Stage-2*) has been modified, by appealing to the compressible form of the continuity equation along with an equation of state to link density to pressure. The compressible form of the pressure update equation, brings some interesting new features into the algorithm. This form can adapt itself with the changing nature of the flow, with respect to local Mach number. Within the incompressible regime, this equation has elliptic character, consistent with the nature of the flow. Nevertheless, upon increasing Mach number, the pressure update equation introduces hyperbolic character to the system of equations, now consistent with the changing flow-type. This important feature, enables pressure-based schemes to deal with flows over a range of Mach numbers, particularly tending toward the zero limit. In addition, this local adaptation is important in dealing with flows of mixed Mach number, where some compressible regions coexist alongside incompressible ones.

For the discrete representation of density, two alternative forms of interpolations have been adopted, a piecewise-constant form with nodal-recovery to compute gradients of density, and a piecewise-linear form. One may notice that employing piecewise-constant interpolation has provided less accurate results. To rectify this position, a recovery technique is implemented to incorporate density gradients within the rhs of *Stage-2*. With this treatment, both interpolation alternatives reflect practically identical numerical solutions.

Consistency, accuracy and convergence have been assessed on a series of benchmark problems to highlight the performance of both interpolation variants. There is no apparent loss of accuracy incurred through these compressible interpolation variants, as compared to their incompressible counterpart. This is anticipated to reach a third-order for continuous problems. The convergence-rate to steady state of both interpolation-forms is improved upon, as compared to that of the incompressible flow algorithm. This finding is associated with the improvement in system condition number, through the mass-matrix and right-hand-side contributions to the second-stage equation (for pressure).

Altering the temporal terms within the pressure-update equation has crucial influence upon the transient solution path toward steady-state. However, theoretically steady-state solutions are thought to be independent of the solution path, as temporal terms vanish under steady-state conditions. This is similar to the situation for pseudo-compressible algorithms, where it is possible to enhance numerical convergence properties by adjusting the eigenvalues of the system, via altering preconditioning-matrix parameters. This scenario can be shown to be effective in extracting steady-state solutions for viscous flows. However, for viscoelastic flows, accuracy during transient stages is crucial for extracting steady-state solutions, and employing such procedures may not be practical.

A test has been conducted on scheme sensitivity under the variation of Tait parameters, and hence, through the form of the equation of state. For the scheme, the value of the Tait parameters (m,B) are unimportant: what matters is how much the equation of state includes compressibility within the flow (values of Ma and variation within density). In other words, for different settings of Tait parameters, which deliver the same amount of Ma and ρ, the scheme reflects similar temporal convergence

patterns and steady-state solutions. Hence, this scheme can be employed in the simulation of various material flows with such adjustment in the equation of state.

Consistency is an important aspect of the numerical scheme as Mach number approaches the zero limit. This has been demonstrated through adjusting the Tait equation pairing parameters. As Mach number approaches zero, the solution converges toward the incompressible solution.

The main novelty of this study has been in the numerical simulation of compressible viscoelastic flows, being a pioneering study in this context. A significant observation has been the heavy-side influence that the compressible equation structure has on temporal convergence patterns, proving of monotonic in-phase form across the various variables. This extends equally to the asymptotic weakly-compressible limit, that mimics (slightly) incompressible liquid flow ($Ma \approx 10^{-4}$). Hence the important outcome that, the weakly-compressible assumption may be usefully employed to numerically improve convergence properties for incompressible viscoelastic solutions.

As an overall remark, the main disparity between incompressible and compressible flow representations is related to the level of stress-peak at the re-entrant corner and within the downstream stress boundary layer. It has been observed that solution singularity (stress/velocity gradient at re-entrant corners) may actually increase in strength under a more compressible setting, whilst downstream-wall stress profiles broaden along the wall, away from the initial inception just beyond the re-entrant corner. This observation lies in marked contrast to the incompressible scenario, where wall-stress profiles sustain their initial width far downstream. For compressible flow settings, density elevates at flow inlet and mass flow-rate rises accordingly. Consequently, higher pressure-drops can be observed (here by $O(10\%)$). The impact of the link between density and trace of stress, in combination with the continuity equation, arises through changing velocity profiles, particularly around the contraction zone (area with large stress-peaks) and along the downstream channel. Here, one observes sustained growth in velocity streamwise and deviation from parabolic fully-developed form cross-stream. Consequently, a boundary-integral form has been adopted for computing the solution at flow outlet.

The structure of the compressible algorithm has better properties, in the sense of splitting error, and hence, stability and convergence. As a consequence, one is able to

reach higher *We* true-transient solutions. This algorithm variant, has kept most of these properties when the Tait parameters were adjusted to mimic incompressible flow. However, as a consequence of higher stress-peaks level for compressible settings, the We_{crit} is smaller than for its incompressible counterpart. This is believed to be due to the shortcomings of the SUPG formulation in capturing sharp stress-gradients and stress boundary layers beyond the contraction point. There for compressible flow, stress peaks are larger and the boundary layer is more active. To rectify this effect, a sub-cell finite volume implementation has been employed, a hybrid *fe/fv* scheme acting upon the full system.

For vortex activity, steady-state salient and corner-vortex patterns have been studied through increasing *We*. Results for both *fe* and hybrid *fe/fv* algorithmic schemes have been presented under compressible (Ma=0.1) and incompressible ($Ma\approx0$ and Ma=0) flow settings. In addition, the effect of inclusion of inertia (Re=1.0) has been studied, contrasting this against creeping flow (Re=0.0) results. Findings reveal that at equitable *We*-level and flow settings, both *fe* and hybrid *fe/fv*-schemes produce consistent and comparable vortex characteristics. Compressible solutions provide larger vortices (in size and intensity, salient and lip) over their incompressible counterparts: important if vortex enhancement is sought. Inertia tends to suppress such phenomena in all instances. Trends with increasing *We* and independent of flow setting, indicate that salient-corner vortex-size decays (vortex reduction), whilst lip-vortex size is enhanced. For compressible flow, the shape of the salient-corner vortex separation-line becomes curved and stretched, uniting with the lip-vortex at high-*We*. Compressible-flow stress patterns are larger in the re-entrant corner zone, with sustained constant growth-rate in stress along the downstream wall. There is close agreement between results with and without relaxation. The hybrid *fe/fv*-scheme is clearly more robust, in that it captures the stress singularity more tightly than the *fe*-form at comparable Weissenberg numbers, reaching higher We_{crit}-levels. The sub-cell structure, the control of cross-stream numerical diffusion in the presence of sharp solution gradients, and corner discontinuity capturing features of the hybrid *fe/fv*-scheme, are all perceived as fresh, attractive and additional strengths.

Several stabilisation techniques have been considered based on the hybrid *fe/fv* scheme. For incompressible (Ma=0 and $Ma\approx0$), and mildly compressible (Ma=0.1)

viscoelastic flows, a minor improvement is observed in stabilisation properties with the *TSS* scheme. Introducing *TSS* does not alter the steady-state solution, and its stabilisation effect has been demonstrated in true transient scenarios. In contrast, reduced corner integration (*RCI*), is related directly to spatial stress discretisation, employed to suppress non-physical oscillations and to capture sharp gradients in the solution. This strategy has promoted considerable stabilisation, particularly under compressible ($Ma \approx 0$ and $Ma=0.1$) considerations. Under *RCI*, large stress peaks have been extracted at the re-entrant corner, alongside large lip-vortex structures.

Greatest improvement has been encountered with strain-rate stabilisation (*SRS*). With *SRS*, *We*-levels for stable solutions have more than doubled above the neutral variant. This strategy is interpreted as aiding with: (i) easing compatibility relationships between functional spaces on stress and velocity gradients (extended LBB condition satisfaction); (ii) offering some control upon cross-stream solution prolongation (absent in many currently favoured schemes). In this manner, stress peaks have been maintained at their lowest levels, whilst any lip-vortex is completely removed under $Ma=0$ and $Ma \approx 0$ settings. Combinations of these stabilisation variants have recorded optimal stability properties. The 'differed-correction term' is found to characterise temporal stress convergence patterns and the nature of the stress singularity at the re-entrant corner. This is without degradation of the solution field elsewhere. The considerable elevation of We_{crit} under *SRS* is attributed to the tight capturing of the SBL.

Overall with increasing *We*, under response for each scheme and independent of flow conditions, salient-corner vortex reduction and lip-vortex growth have been observed. At a selected *We*-level and under a specific flow setting, all scheme variants have produced similar salient-corner vortex trends. In contrast, lip-vortex features have been found to be significantly affected by the particular re-entrant corner treatment. At $Ma=0$ and $Ma \approx 0$ levels, lip-vortex response has been observed, which vanishes under SRS-implementation. The absence of lip-vortices under SRS-solutions has clearly identified the smoothing character of this term. Nevertheless, this lip-vortex feature is certainly present under the compressible $Ma=0.1$ setting. This leaves some open questions of general algorithms/codes and of the quality of their respective solutions about such singularities. Under certain numerical approximations, our experience is that mere global satisfaction of continuity (common to many continuous pressure-interpolations,

for example), may stimulate considerable continuity residual error, which may itself dictate the local nature of the numerical solution predicted. This has raised the issue of bulk viscosity, its role and numerical influence, a subject open for future study.

We have established a profound base for the computation of compressible highly viscoelastic flows. Subsequently, this work may be extended to deal with more complex rheological models. The superior numerical structure of these compressible algorithms, offers simulation capability for truly compressible complex flows. This is seen as helpful particularly in rheometry, where in many circumstances, compressibility should be taken into account. The structure of pressure-correction schemes and the impact of splitting-error, have been observed to have a significant influence upon the performance of numerical schemes. As such and with the aid of recent advances within the application of pressure-correction schemes, one may hope to devise robust and accurate schemes for effective future use in this domain.

List of figures

List of tables

Bibliography

1 M. Aboubacar, H. Matallah, H.R. Tamaddon-Jahromi, M.F. Webster, Numerical prediction of extensional flows in contraction geometries: hybrid finite volume/element method, *Journal of Non-Newtonian Fluid Mechanics* **104** (2002) 125-164.

2 M. Aboubacar, H. Matallah, M.F. Webster, Highly elastic solutions for Oldroyd-B and Phan-Thien/Tanner fluids with a finite volume/element method: planar contraction flows, *Journal of Non-Newtonian Fluid Mechanics* **103** (2002) 65-103.

3 M. Aboubacar, T.N. Phillips, H.R. Tamaddon-Jahromi, B.A. Snigerev, M.F. Webster, High-order finite volume methods for viscoelastic flow problems, *Journal of Computational Physics* **199** (2004) 16-40.

4 M. Aboubacar, M.F. Webster, A cell-vertex finite volume/element method on triangles for abrupt contraction viscoelastic flows, *Journal of Non-Newtonian Fluid Mechanics* **98** (2001) 83-106.

5 M.A. Alves, P.J. Oliveira, F.T. Pinho, Benchmark solutions for the flow of Oldroyd-B and PTT fluids in planar contractions, *Journal of Nonnewtonian Fluid Mechanics* **110** (2003) 45-75.

6 M.A. Alves, F.T. Pinho, P.J. Oliveira, Effect of a high-resolution differencing scheme on finite-volume predictions of viscoelastic flows, *Journal of Non-Newtonian Fluid Mechanics* **93** (2000) 287-314.

7 P.W. Atkins, Physical chemistry. In, Freeman, New York, 1999.

8 F. Auteri, J.L. Guermond, N. Parolini, Role of the LBB condition in weak spectral projection methods, *Journal of Computational Physics* **174** (2001) 405-420.

9 F.P.T. Baaijens, An iterative solver for the DEVSS/DG method with application to smooth and non-smooth flows of the upper convected Maxwell fluid, *Journal of Non-Newtonian Fluid Mechanics* **75** (1998) 119-138.

10 F.P.T. Baaijens, Mixed finite element methods for viscoelastic flow analysis: a review, *Journal of Non-Newtonian Fluid Mechanics* **79** (1998) 361-385.

11 F.P.T. Baaijens, Numerical analysis of unsteady viscoelastic flow, *Computer Methods in Applied Mechanics and Engineering* **94** (1992) 285-299.

12 A. Baloch, P.W. Grant, M.F. Webster, Parallel computation of two-dimensional rotational flows of viscoelastic fluids in cylindrical vessels, *Engineering Computations* **19** (2002) 820 - 853.

13 F.G. Basombrio, G.C. Buscaglia, E.A. Dari, Simulation of highly elastic fluid flows without additional numerical diffusivity, *Journal of Non-Newtonian Fluid Mechanics* **39** (1991) 189-206.

14 F. Belblidia, I.J. Keshtiban, M.F. Webster, Novel schemes for steady weakly compressible and incompressible flows. In: ACME-UK conf, University of Strathclyde, Glasgow, UK, 2003.

15 H. Bijl, P. Wesseling, A unified method for computing incompressible and compressible flows in boundary-fitted coordinates, *Journal of Computational Physics* **141** (1998) 153-173.

16 R.B. Bird, *Dynamics of polymeric liquids*,Wiley,New York, (1987).

17 D.V. Boger, Viscoelastic flows through contractions, *Annual Review of Fluid Mechanics* **19** (1987) 157-182.

18 F. Brezzi, M. Fortin, *Mixed and hybrid finite elements methods*,Springer-Verlag,New York, (1991).

19 A.N. Brooks, T.J.R. Hughes, Streamline-upwind/Petrov-Galerkin formulations for convective dominated flows with particular emphasis on the incompressible Navier-Stokes equations, *Computer Methods in Applied Mechanics and Engineering* **32** (1982) 199-259.

20 D.L. Brown, R. Cortez, M.L. Minion, Accurate projection methods for the incompressible Navier-Stokes equations, *Journal of Computational Physics* **168** (2001) 464-499.

21 E.A. Brujan, A first-order model for bubble dynamics in a compressible viscoelastic liquid, *Journal of Non-Newtonian Fluid Mechanics* **84** (1999) 83-103.

22 E.O.A. Carew, P. Townsend, M.F. Webster, On a discontinuity capturing technique for Oldroyd-B fluids, *Journal of Non-Newtonian Fluid Mechanics* **51** (1994) 231-238.

23 E.O.A. Carew, P. Townsend, M.F. Webster, A Taylor-Petrov-Galerkin algorithm for viscoelastic flow, *Journal of Non-Newtonian Fluid Mechanics* **50** (1993) 253-287.

24 M.S. Chandio, K.S. Sujatha, M.F. Webster, Consistent hybrid finite volume/element formulations: model and complex viscoelastic flows, *Internationa Journal for Numerical Methods in Fluids* **45** (2004) 945-971.

25 W. Chang, F. Giraldo, B. Perot, Analysis of an exact fractional step method, *Journal of Computational Physics* **180** (2002) 183-199.

26 Y.H. Choi, C.L. Merkle, The application of preconditioning in viscous flows, *Journal of Computational Physics* **105** (1993) 207-223.

27 A.J. Chorin, A numerical method for solving incompressible viscous flow problems, *Journal of Computational Physics* **2** (1967) 12-26.

28 A.J. Chorin, Numerical solution of the Navier-Stokes equations, *Mathematics of Computation* **22** (1968) 745-762.

29 I. Christie, D.F. Griffiths, A.R. Mitchell, O.C. Zienkiewicz, Finite element methods for second order differential equations with significant first derivatives, *International Journal for Numerical Methods in engineering* **10** (1976) 1389--1396.

30 R. Codina, O.C. Zienkiewicz, CBS versus GLS stabilization of the incompressible Navier-Stokes equations and the role of the time step as stabilization parameter, *Communications in Numerical Methods in Engineering* **18** (2002) 99-112.

31 O. Colin, M. Rudgyard, Development of High-Order Taylor-Galerkin Schemes for LES, *Journal of Computational Physics* **162** (2000) 338-371.

32 M.J. Crochet, V. Legat, The consistent streamline-upwind/Petrov-Galerkin method for viscoelastic flow revisited, *Journal of Non-Newtonian Fluid Mechanics* **42** (1992) 283-299.

33 D.L. Darmofal, P.J. Schmid, The Importance of Eigenvectors for Local Preconditioners of the Euler Equations, *Journal of Computational Physics* **127** (1996) 346-362.

34 T. De Mulder, The role of bulk viscosity in stabilized finite element formulations for incompressible flow: A review, *Computer Methods in Applied Mechanics and Engineering* **163** (1998) 1-10.

35 D. Ding, P. Townsend, M.F. Webster, The Iterative Solution of Taylor-Galerkin Augmented Mass Matrix Equations, *International Journal for Numerical Methods in engineering* **35** (1992) 241-253.

36 D. Ding, P. Townsend, M.F. Webster, On computation of two and three-dimensional unsteady thermal non-Newtonian flows, *International Journal of Numerical Methods in Heat and Fluid Flow* **5** (1995) 495-510.

37 J. Donea, A Taylor-Galerkin method for convective transport problems, *International Journal for Numerical Methods in Engineering* **20** (1984) 101-119.

38 J. Donea, S. Giuliani, H. Laval, L. Quartapelle, Finite element solution of the unsteady Navier-Stokes equations by fractional step method, *Computer Methods in Applied Mechanics and Engineering* **30** (1982) 53-73.

39 D. Doraiswamy, The origins of rheology: a short historical excursion, *American society of rheology, rheology bulletin.* **71** (2002).

40 L.F.A. Douven, F.P.T. Baaijens, H.E.H. Meijer, The computation of properties of injection-moulded products, *Progress in Polymer Science* **20** (1995) 403-457.

41 S.S. Edussuriya, A.J. Williams, C. Bailey, A cell-centred finite volume method for modelling viscoelastic flow, *Journal of Nonnewtonian Fluid Mechanics* **117** (2004) 47-61.

42 R.E. Evans, K. Walters, Flow characteristics associated with abrupt changes in geometry in the case of highly elastic liquids, *Journal of Non-Newtonian Fluid Mechanics* **20** (1986) 11-29.

43 R.E. Evans, K. Walters, Further remarks on the lip-vortex mechanism of vortex enhancement in planar-contraction flows, *Journal of Non-Newtonian Fluid Mechanics* **32** (1989) 95-105.

44 J. Ferguson, Z. Kemblowski, *Applied Fluid Rheology*,Kluwer Academic Publishers, Dordrecht, (1991).

45 J.E. Field, ELSI conference: invited lecture: Liquid impact: theory, experiment, applications, *Wear* **233-235** (1999) 1-12.

46 N. Fietier, M.O. Deville, Time-dependent algorithms for the simulation of viscoelastic flows with spectral element methods: applications and stability, *Journal of Computational Physics* **186** (2003) 93-121.

47 M. Fortin, A. Fortin, A new approach for the FEM simulation of viscoelastic flows, *Journal of Non-Newtonian Fluid Mechanics* **32** (1989) 295-310.

48 M. Fortin, R. Pierre, On the convergence of the mixed method of Crochet and Marchal for viscoelastic flows, *Computer Methods in Applied Mechanics and Engineering* **73** (1989) 341-350.

49 G.C. Georgiou, The time-dependent, compressible Poiseuille and extrudate-swell flows of a Carreau fluid with slip at the wall, *Journal of Non-Newtonian Fluid Mechanics* **109** (2003) 93-114.

50 G.C. Georgiou, L.G. Olson, W.W. Schultz, S. Sagan, A singular finite element for stokes flow: the stick-slip prooblem, *International Journal for Numerical Methods in Fluid* **9** (1989) 1353-1367.

51 U. Ghia, K.N. Ghia, C. Shin, High-Re solutions for incompressible flow using the Navier-Stokes equations and a multigrid method, *Journal of Computational Physics* **48** (1982) 387-411.

52 G.H. Golub, C.F. Van Loan, *Matrix computations*,Johns Hopkins University Press,Baltimore, (1996).

53 P.M. Gresho, R.L. Lee, R.L. Sani, Advection-dominated flows with emphasis on the sequences of mass lumping., *Finite Element in Fluids* **3** (1978) 745-756.

54 P.M. Gresho, R.L. Lee, R.L. Sani, M.K. Maslanik, B.E. Eaton, The consistent Galerkin FEM for computing derived boundary quantities in thermal and/or fluids problems, *International Journal for Numerical Methods in Fluids* **7** (1987) 371-394.

55 P.M. Gresho, R.L. Sani, M.S. Engelman, NetLibrary Inc., *Incompressible flow and the finite element method advection-diffusion and isothermal laminar flow*,Wiley,Chichester England; New York, (1999).

56 R. Guénette, M. Fortin, A new mixed finite element method for computing viscoelastic flows, *Journal of Non-Newtonian Fluid Mechanics* **60** (1995) 27-52.

57 J.L. Guermond, L. Quartapelle, On stability and convergence of projection methods based on pressure Poisson equation, *International Journal for Numerical Methods in Fluids* **26** (1998) 1039-1054.

58 H. Guillard, C. Viozat, On the behaviour of upwind schemes in the low Mach number limit, *Computers & Fluids* **28** (1999) 63-86.

59 T. Hagen, M. Renardy, Boundary layer analysis of the Phan-Thien-Tanner and Giesekus model in high Weissenberg number flow, *Journal of Non-Newtonian Fluid Mechanics* **73** (1997) 181-189.

60 K.H. Han, Y.T. Im, Compressible flow analysis of filling and post-filling in injection molding with phase-change effect, *Composite Structures* **38** (1997) 179-190.

61 F.H. Harlow, A. Amsden, Numerical calculation of almost incompressible flow, *Journal of Computational Physics* **3** (1968) 80-93.

62 D.M. Hawken, H.R. Tamaddon-Jahromi, P. Townsend, M.F. Webster, A Taylor-Galerkin based algorithm for viscous incompressible flow, *International Journal for Numerical Methods in Fluids* **10** (1990) 327-351.

63 D.M. Hawken, P. Townsend, M.F. Webster, A comparison of gradient recovery methods in finite element calculations, *Communication in applied numerical methods* **7** (1991) 195-204.

64 J.C. Henrich, P.S. Huyakorn, O.C. Zienkiewicz, An upwinding finite element scheme for two-dimensional convective transport equation, *International Journal for Numerical Methods in engineering* **11** (1977) 134-143.

65 C. Hirsch, *Numerical computation of internal and external flows*, Wiley, Chichester, England; New York, (1988).

66 R. Hooke, De potentia restitutiva, *Journal Martyn, London* (1678).

67 Y.K. Huang, C.Y. Chow, The generalized compressibility equation of Tait for dense matter, *Journal of Physics D: Applied Physics* **7** (1974) 2021-2023.

68 M.E. Hubbard, R. P.L., Multidimensional upwind fluctuation distribution schemes for scalar time dependent problems. Numerical Analysis Report 1:98, Department of Mathematics, University of Reading.

69 M.E. Hubbard, P.L. Roe, Compact high-resolution algorithms for time-dependent advection on unstructured grids, *Internationa Journal for Numerical Methods in Fluids* **33** (2000) 711-736.

70 T.J.R. Hughes, L.P. Franca, G.M. Hulbert, A new finite element formulation for computational fluid dynamics: VIII. The Galerkin Least-Squares method for advective diffusive equations, *Computer Methods in Applied Mechanics and Engineering* **73** (1989) 173–189.

71 P. Iannelli, F.M. Denaro, Analysis of the local truncation error in the pressure-free projection method for incompressible flows: a new accurate expression of the intermediate boundary conditions, *International Journal for Numerical Methods in Fluids* **42** (2003) 399-438.

72 M.J. Jackson, J.E. Field, Liquid impact erosion of single-crystal magnesium oxide, *Wear* **233-235** (1999) 39-50.

73 A. Jameson, W. Schmidt, E. Turkel, Numerical solutions of the Euler equations by finite volume methods using Runge-Kutta time-stepping schemes. In: AIAA, 14th Fluid and Plasma Dynamic Conference, Palo Alto, 1981, pp. 1259-1276.

74 P. Jenny, B. Muller, Convergence acceleration for computing steady-state compressible flow at low Mach numbers, *Computers & Fluids* **28** (1999) 951-972.

75 J.W. Kang, J.H. Lee, K.P. Yoo, C.S. Lee, Evaluation of equations of state applicable to polymers and complex systems, *Fluid Phase Equilibria* **194-197** (2002) 77-86.

76 S.M.H. Karimian, G.E. Schneider, Pressure-based control-volume finite-element method for flow at all speeds, *AIAA journal* **33** (1995) 1611-1618.

77 K. Karki, S.V. Patankar, Pressure based calculation procedure for viscous flows at all speeds in arbitrary configurations, *AIAA journal* **27** (1989) 1167-1174.

78 M.A. Kelmanson, S.B. Maunder, Modelling high-velocity impact phenomena using unstructured dynamically-adaptive Eulerian meshes, *Journal of the Mechanics and Physics of Solids* **47** (1999) 731-762.

79 I.J. Keshtiban, F. Belblidia, M.F. Webster, Numerical simulation of compressible viscoelastic liquids, *Journal of Non-Newtonian Fluid Mechanics* **122** (2004) 131-146.

80 I.J. Keshtiban, F. Belblidia, M.F. Webster, Numerical simulation of compressible viscoelastic liquids, *XIIIth International Workshop on Numerical Methods for non-Newtonian Flows*, Lausanne, Switzerland, (2003).

81 I.J. Keshtiban, F. Belblidia, M.F. Webster, Computation of Incompressible and Weakly-Compressible Viscoelastic Liquids Flow: finite element/volume schemes, *Journal of Non-Newtonian Fluid Mechanics* (2004), in press.

82 I.J. Keshtiban, F. Belblidia, M.F. Webster, Second-order Schemes for Steady Weakly Compressible Liquid Flows, *Report No.*: **CSR 4-2003**: Computer Science Dept., University of Wales Swansea, UK (2003),.

83 I.J. Keshtiban, M.F. Webster, Comparison of pressure-correction schemes: TGPC and CBS, *Report No.*: **CSR 11-2004**: Computer Science Dept., University of Wales Swansea, UK, (2004),.

84 J. Kim, P. Moin, Application of a fractional-step method to incompressible Navier-Stokes equations, *Journal of Computational Physics* **59** (1985) 308-323.

85 R.C. King, M.R. Apelian, R.C. Armstrong, R.A. Brown, Numerically stable finite element techniques for viscoelastic calculations in smooth and singular geometries, *Journal of Non-Newtonian Fluid Mechanics* **29** (1988) 147-216.

86 S. Klainerman, A. Majda, Compressible and incompressible fluids, *Communications on Pureand Applied Mathematics* **35** (1982) 629-651.

87 H.O. Kreiss, J. Lorenz, M.J. Naughton, Convergence of the solution of the compressible to the solution of the incompressible Navier-Stokes equation, *Advancess in Applied Mathematics* **12** (1991) 187-214.

88 R.G. Larson, *Constitutive equations for polymer melts and solutions*, Butterworths, Boston, (1988).

89 P.D. Lax, B. Wendroff, Systems of conservation laws, *Comm. Pure Applied Math* **13** (1960) 217-237.

90 B.P. Leonard, Order of accuracy of QUICK and related convection-diffusion schemes, *Applied Mathematical Modelling* **19** (1995) 640-653.

91 F.S. Lien, M.A. Leschziner, A pressure velocity solution strategy for compressible flow and its application to shock boundary layer interaction using second-moment turbulance closure, *Journal of Fluid Engineering* **115** (1993) 717-725.

92 C. Liu, Z. Liu, High order finite difference and multigrid methods for spatially evolving instability in a planar channel, *Journal of Computational Physics* **106** (1993) 92-100.

93 R. Löhner, K. Morgan, O.C. Zienkiewicz, The solution of non-linear hyperbolic equation systems by the finite element method, *International Journal for Numerical Methods in Fluids* **4** (1984) 1043-1063.

94 A. Majda, *Compressible fluid flow and systems of conservation laws in several space variables*,Springer-Verlag,New York, (1984).

95 J.M. Marchal, M.J. Crochet, A new mixed finite element for calculating viscoelastic flow, *Journal of Non-Newtonian Fluid Mechanics* **26** (1987) 77-114.

96 I. Mary, P. Sagaut, M. Deville, An algorithm for low Mach number unsteady flows, *Computers & Fluids* **29** (2000) 119-147.

97 H. Matallah, P. Nithiarasu, M.F. Webster, Stabilisation techniques for viscoelastic flows. In: ECCOMAS conf., Swansea, Wales, 2001.

98 H. Matallah, P. Townsend, M.F. Webster, Recovery and stress-splitting schemes for viscoelastic flows, *Journal of Non-Newtonian Fluid Mechanics* **75** (1998) 139-166.

99 G.H. McKinley, Raiford, W.P., Brown, R.A. and Armstrong, R.C., Nonlinear Dynamics of Viscoelastic Flow in Axisymmetric Abrupt Contractions, *Journal of Fluid Mechanics* **223** (1991) 411-456.

100 S. Mittal, T. Tezduyar, A unified finite element formulation for compressible and incompressible flows using augmented conservation variables, *Computer Methods in Applied Mechanics and Engineering* **161** (1998) 229-244.

101 G. Mompean, On predicting abrupt contraction flows with differential and algebraic viscoelastic models, *Computers & Fluids* **31** (2002) 935-956.

102 F. Moukalled, M. Darwish, A High-Resolution Pressure-Based Algorithm for Fluid Flow at All Speeds, *Journal of Computational Physics* **168** (2001) 101-133.

103 C.D. Munz, S. Roller, R. Klein, K.J. Geratz, The extension of incompressible flow solvers to the weakly compressible regime, *Computers & Fluids* **32** (2003) 173-196.

104 V. Ngamaramvaranggul, M.F. Webster, Computation of free surface flows with a Taylor-Galerkin/pressure-correction algorithm, *International Journal for Numerical Methods in Fluids* **33** (2000) 993-1026.

105 V. Ngamaramvaranggul, M.F. Webster, Simulation of coating flows with slip effects, *International Journal for Numerical Methods in Fluids* **33** (2000) 961-992.

106 P. Nithiarasu, O.C. Zienkiewicz, On stabilization of the CBS algorithm: Internal and external time steps, *International Journal for Numerical Methods in Engineering* **48** (2000) 875-880.

107 J.G. Oldroyd, On the formulation of rheological equations of state, *Proc. R. Soc. Lond* **A200** (1950) 523-541.

108 P.J. Oliveira, F.T. Pinho, Plane contraction flows of upper convected Maxwell and Phan-Thien-Tanner fluids as predicted by a finite-volume method, *Journal of Non-Newtonian Fluid Mechanics* **88** (1999) 63-88.

109 H. Orbey, C.C. Chen, C. Bokis, An extension of cubic equations of state to vapor-liquid equilibria in polymer-solvent mixtures, *Fluid Phase Equilibria* **145** (1998) 169-192.

110 R.L. Panton, *Incompressible flow*, J. Wiley, New York, (1996).

111 S.V. Patankar, *Numerical heat transfer and fluid flow*, McGraw-Hill, New York, (1980).

112 J.B. Perot, Comments on the fractional step method, *Journal of Computational Physics* **121** (1995) 190-191.

113 R. Peyret, T.D. Taylor, *Computational Methods for Fluid Flow*,Springer-Verlag, New York, (1983).

114 T.N. Phillips, A.J. Williams, Comparison of creeping and inertial flow of an Oldroyd B fluid through planar and axisymmetric contractions, *Journal of Non-Newtonian Fluid Mechanics* **108** (2002) 25-47.

115 T.N. Phillips, A.J. Williams, Viscoelastic flow through a planar contraction using a semi-Lagrangian finite volume method, *Journal of Non-Newtonian Fluid Mechanics* **87** (1999) 215-246.

116 J.M. Prausnitz, R.N. Lichtenthaler, E.G. Azevedo, *Molecular thermodynamics of fluid-phase equilibria*,Prentice-Hall, Englewood Cliffs, N.J., (1986).

117 B. Purnode, M.J. Crochet, Flows of polymer solutions through contractions Part 1: flows of polyacrylamide solutions through planar contractions, *Journal of Non-Newtonian Fluid Mechanics* **65** (1996) 269-289.

118 D. Rajagopalan, R.C. Armstrong, R.A. Brown, Calculation of steady viscoelastic flow using a multimode Maxwell model: application of the explicitly elliptic momentum equation (EEME) formulation, *Journal of Non-Newtonian Fluid Mechanics* **36** (1990) 135-157.

119 J.M. Rallison, E.J. Hinch, The flow of an Oldroyd fluid past a reentrant corner: the downstream boundary layer, *Journal of Non-Newtonian Fluid Mechanics* **116** (2004) 141-162.

120 M. Ranganathan, M.R. Mackley, P.H.J. Spitteler, The application of the multipass Rheometer to time dependent capillary flow measurements of a Polyethylene melt, *Journal of Rheology* **43** (1999) 443-451.

121 M. Renardy, Current issues in non-Newtonian flows: a mathematical perspective, *Journal of Non-Newtonian Fluid Mechanics* **90** (2000) 243-259.

122 P.A. Rodgers, Pressure-Volume-Temperature Relationships for Polymeric Liquids: A Review of Equations of State and Their Characteristic Parameters for 56 Polymers, *Journal of Applied Polymer Science* **48** (1993) 1061.

123 S. Roller, C.D. Munz, A low Mach number scheme based on multi-scale asymptotics, *Computing and Visualization in Science* **3** (2000) 85-91.

124 J. Rosenberg, R. Keunings, Numerical integration of differential viscoelastic models, *Journal of Non-Newtonian Fluid Mechanics* **39** (1991) 269-290.

125 C.C. Rossow, A Flux-Splitting Scheme for Compressible and Incompressible Flows, *Journal of Computational Physics* **164** (2000) 104-122.

126 P. Saramito, J.M. Piau, Flow characteristics of viscoelastic fluids in an abrupt contraction by using numerical modeling, *Journal of Non-Newtonian Fluid Mechanics* **52** (1994) 263.

127 T. Sato, S.M. Richardson, Explicit numerical simulation of time-dependent viscoelastic flow problems by a finite element/finite volume method, *Journal of Non-Newtonian Fluid Mechanics* **51** (1994) 249-275.

128 T. Schneider, N. Botta, K.J. Geratz, R. Klein, Extension of Finite Volume Compressible Flow Solvers to Multi-dimensional, Variable Density Zero Mach Number Flows, *Journal of Computational Physics* **155** (1999) 248-286.

129 J. Sesterhenn, B. Muller, H. Thomann, On the Cancellation Problem in Calculating Compressible Low Mach Number Flows, *Journal of Computational Physics* **151** (1999) 597-615.

130 F. Shakib, Ph.D. Dissertation. In: Stanford Uiniversity, 1987.

131 L.F. Shampine, Implementation of implicit formulas for the solution of ODEs, *Vol1, of Scientific Statistical Compututation* **1** (1980) 103-118.

132 G. Strang, G.J. Fix, *An Analysis of the Finite Element Method*, Englewood Cliffs, N.J.: Prentice-Hall, (1973).

133 R. Struijs, H. Deconinck, P.L. Roe, Fluctuation splitting for the 2D Euler equations. Technical Report Lecture series 1990–01, Von Karman Institute for Fluid Dynamics.

134 J. Sun, N. Phan-Thien, R.I. Tanner, An adaptive viscoelastic stress splitting scheme and its applications: AVSS/SI and AVSS/SUPG, *Journal of Non-Newtonian Fluid Mechanics* **65** (1996) 75-91.

135 M.J. Szady, T.R. Salamon, A.W. Liu, D.E. Bornside, A new mixed finite element method for viscoelastic flows governed by differential constitutive equations, *Journal of Nonnewtonian Fluid Mechanics* **59** (1995) 215.

136 P.G. Tait, HSMO, *London* **2** (1888).

137 R.I. Tanner, Engineering Rheology, *Oxford Engineering Science Series* **52** (2000) ALL.

138 R.I. Tanner, K. Walters, *Rheology: An Historical Perspective*,Elsevier,Oxford, (1998).

139 R. Temam, Sur l'approximation de la solution de Navier-Stokes par la méthode des pas fractionnaires, *Archiv. Ration. Mech. Anal.* **32** (1969) 377-385.

140 A.G. Tomboulides, S.A. Orzag, A quasi-two-dimensional benchmark problem for low Mach number compressible codes, *Journal of Computational Physics* **146** (1998) 691-706.

141 E. Turkel, Preconditioned Methods for solving the incompressible and low speed compressible equations, *journal of computational physics* **72** (1987) 277-298.

142 E. Turkel, Review of Preconditioning Methods for Fluid Dynamics, *Review of Preconditioning Methods for Fluid Dynamics* **12** (1993) 257-284.

143 E. Turkel, R. Radespiel, N. Kroll, Assessment of preconditioning methods for multidimensional aerodynamics, *Computers & Fluids* **26** (1997) 613-634.

144 D.R. van der Heul, C. Vuik, P. Wesseling, A conservative pressure-correction method for flow at all speeds, *Computers & Fluids* **32** (2003) 1113-1132.

145 J. Van Kan, A second-order accurate pressure-correction scheme for viscous incompressible flow, *SIAM Journal of Scientific and Statistical Computing* **7** (1986) 870-891.

146 B. Van Leer, W.T. Lee, L. Roe, Characteristic time-stepping or local preconditioning of the Euler equations, *AIAA journal* **91** (1991).

147 W.M.H. Verbeeten, G.W.M. Peters, F.P.T. Baaijens, Numerical simulations of the planar contraction flow for a polyethylene melt using the XPP model, *Journal of Non-Newtonian Fluid Mechanics* **117** (2004) 73-84.

148 G.V. Vinogradov, A.Y. Malkin, *Rheology of polymers*, Mir publisher, Moscow, (1980).

149 K. Walters, M.F. Webster, The distinctive CFD challenges of computational rheology, *International Journal for Numerical Methods in Fluids* **In press** (2003).

150 K. Walters, M.F. Webster, The distinctive CFD challenges of computational rheology, *International Journal for Numerical Methods in Fluids* **43** (2003) 577-596.

151 P. Wapperom, M.F. Webster, A second-order hybrid finite-element/volume method for viscoelastic flows, *Journal of Non-Newtonian Fluid Mechanics* **79** (1998) 405-431.

152 P. Wapperom, M.F. Webster, Simulation for viscoelastic flow by a finite volume/element method, *Computer Methods in Applied Mechanics and Engineering* **180** (1999) 281-304.

153 N.D. Waters, M.J. King, Unsteady flow of an elastico-viscous liquid, *Rheology Acta* **9** (1970) 245-355.

154 M.F. Webster, I.J. Keshtiban, F. Belblidia, Computation of weakly-compressible highly-viscous liquid flows, *Engineering Computations* , **21** (2004) 777-804.

155 M.F. Webster, Townsend P., Developement of a transient approach to simulate Newtonian and non-Newtonian flow. In: G.N.M. by Pandle, J. (Ed.), Numerical Methods in Engineering: Theory and applications- NUMETA, London & New York: Elsevier, 1990.

156 M.F. Webster, H.R. Tamaddon-Jahromi, M. Aboubacar, Time-dependent algorithm for viscoelastic flow-finite element/volume schemes, *Numerical Methods for Partial Differential Equations,* **21** (2004), 272-296.

157 M.F. Webster, H.R. Tamaddon-Jahromi, M. Aboubacar, Transient viscoelastic flows in planar contractions, *Journal of Non-Newtonian Fluid Mechanics* **118** (2004) 83-101.

158 P. Wesseling, Principles of Computational Fluid Dynamics, *Springer Series in Computational Mathematics* **29** (2000) ALL.

159 J.S. Wong, D.L. Darmofal, J. Peraire, The solution of the compressible Euler equations at low Mach numbers using a stabilized finite element algorithm, *Computer Methods in Applied Mechanics and Engineering* **190** (2001) 5719-5737.

160 Y.S. Wu, K. Pruess, Integral solutions for transient fluid flow through a porous medium with pressure-dependent permeability, *International Journal of Rock Mechanics and Mining Sciences* **37** (2000) 51-61.

161 S.C. Xue, N. Phan-Thien, R.I. Tanner, Three dimensional numerical simulations of viscoelastic flows through planar contractions, *Journal of Non-Newtonian Fluid Mechanics* **74** (1998) 195-245.

162 C.T. Yang, S.N. Atluri, An assumed 'Deviatoric Stress-Pressure-Velocity' mixed finite element method for unsteady, convective, incompressible viscous flow:- Part I-Theoretical Development, *International Journal for Numerical Methods in Fluids* **3** (1984) 377-398.

163 F. Yurun, A comparative study of the discontinuous Galerkin and continuous SUPG finite element methods for computation of viscoelastic flows, *Computer Methods in Applied Mechanics and Engineering* **141** (1997) 47-65.

164 Z. Zhanga, J.Z. Zhub, Analysis of the superconvergent patch recovery technique and a posteriori error estimator in the finite element method (II), *Computer Methods in Applied Mechanics and Engineering* **163** (1998) 159-170.

165 O.C. Zienkiewicz, K. Morgan, B.V.K. Sataya Sal, R. Codina, M. Vasquez, A general algorithm for compressible and incompressible flow - Part II. Test on the explicit form, *International Journal for Numerical Methods in Fluids* **20** (1995) 887-913.

166 O.C. Zienkiewicz, P. Nithiarasu, R. Codina, M. Vazquez, P. Ortiz, The characteristic-based-split procedure: An efficient and accurate algorithm for fluid problems, *International Journal for Numerical Methods in Fluids* **31** (1999) 359.